# Study of magnetic, magneto-transport and magnetocaloric properties in bulk and nanocrystalline manganites

*By*

SANJIB BANIK

PHYS05201204018

Saha Institute of Nuclear Physics

*A thesis submitted to the*

*Board of Studies in Physical Sciences*

*In partial fulfillment of requirements*

*For the Degree of*

DOCTOR OF PHILOSOPHY

*of*

HOMI BHABHA NATIONAL INSTITUTE


April, 2018

# Homi Bhabha National Institute

## Recommendations of the Viva Voce Board

As members of the Viva Voce Board, we certify that we have read the dissertation prepared by **Sanjib Banik** entitled " **Study of magnetic, magneto-transport and magnetocaloric properties in bulk and nanocrystalline manganites** " and recommend that it maybe accepted as fulfilling the dissertation requirement for the Degree of Doctor of Philosophy.

Chandan Mazumdar Date: 13/8/18

Chair - Prof. Chandan Mazumdar, SINP

Indranil Das Date: 13/8/2018

Guide/Convener - Prof. Indranil Das, SINP

Date: 13/8/18

Examiner - Dr. Rajeev Rawat, UGC-DAE CSR, Indore

Date: 13/08/2018

Member 1 - Prof. Bilwadal Bandhyopadhyay, SINP

Date: 13/8/2018

Member 2 - Prof. Arti Garg, SINP

Gayathri N. Date: 13/8/18

Member 3 - Dr. Gayathri N. Banerjee, VECC

Final approval and acceptance of this dissertation is contingent upon the candidate's submission of the final copies of the dissertation to HBNI.

I hereby certify that I have read this dissertation prepared under my direction and recommend that it may be accepted as fulfilling the dissertation requirement.

**Date:** 13/8/2018

**Place:** SINP- Kolkata

Guide: Indranil Das

Prof. Indranil Das

## Statement by Author

This dissertation has been submitted in partial fulfillment of requirements for an advanced degree at Homi Bhabha National Institute (HBNI) and is deposited in the Library to be made available to borrowers under rules of the HBNI.

Brief quotations from this dissertation are allowable without special permission, provided that accurate acknowledgement of source is made. Requests for permission for extended quotation from or reproduction of this manuscript in whole or in part may be granted by the Competent Authority of HBNI when in his or her judgment the proposed use of the material is in the interests of scholarship. In all other instances, however, permission must be obtained from the author.

Sanjib Banik

# Declaration

I, hereby declare that the investigation presented in the thesis has been carried out by me. The work is original and has not been submitted earlier as a whole or in part for a degree / diploma at this or any other Institution / University.

Sanjib Banik

## List of Publications (included in this thesis)

# Journal

1. "Size-induced modification of magneto-transport properties in nanocrystalline $Sm_{0.5}Ca_{0.5}MnO_3$ compound."

   ***Sanjib Banik***, *Kalipada Das and I. Das*

   **Journal of Magnetism and Magnetic Materials 403, 36 (2016)**.

2. "Enhancement of the magnetoresistive property by introducing disorder in the $(La_{1-x}Y_x)_{0.7}Ca_{0.3}MnO_3$ compound."

   ***Sanjib Banik***, *Kalipada Das and I. Das*

   **RSC Advances 7, 16575 (2017)**.

3. "Large magnetoresistance and relative cooling power in polycrystalline $Pr_{0.775}Sr_{0.225}MnO_3$ compound."

   ***Sanjib Banik*** *and I. Das*

   **Journal of Magnetism and Magnetic Materials 460, 234 (2018)**.

4. "Effect of A-site ionic disorder on magnetocaloric properties in large band width manganite systems."

   ***Sanjib Banik*** *and I. Das*

   **Journal of Alloys and Compounds 742, 248 (2018)**.

5. "Evolution from non-Griffiths phase to Griffiths phase: Giant enhancement of magnetoresistance in nanocrystalline $(La_{0.4}Y_{0.6})_{0.7}Ca_{0.3}MnO_3$ compound."

   ***Sanjib Banik***, *Nasrin Banu and I. Das*

   **Journal of Alloys and Compounds 745, 753 (2018)**.

6. "Huge magnetoresistance and ultra-sharp metamagnetic transition in polycrystalline $Sm_{0.5}Ca_{0.25}Sr_{0.25}MnO_3$."

   ***Sanjib Banik***, *Kalipada Das, Tapas Paramanik, N. P. Lalla, Biswarup Sat-*

*pati, Kalpataru Pradhan, and I. Das*

[arXiv:1710.03007v2 [cond-mat]]. **Accepted in NPG Asia Materials**

7. "Evolution from Griffiths like phase to non-Griffiths like phase with Y doping in $(La_{1-x}Y_x)_{0.7}Ca_{0.3}MnO_3$."

   ***Sanjib Banik*** *and I. Das*

   **Accepted in Journal of Magnetism and Magnetic Materials on 12th August 2018**.

8. "Instability of insulator state towards nanocrystallinity in $(La_{0.5}Y_{0.5})_{0.7}Ca_{0.3}MnO_3$ compound: Enhancement of low field magnetoresistance."

   ***Sanjib Banik***, *Pintu Sen and I. Das*

   **Accepted in Journal of Magnetism and Magnetic Materials on 13th August 2018**.

9. "Effect of A-site ionic radius on metamagnetic transition in charge ordered $Sm_{0.5}(Ca_{0.5-x}Sr_x)MnO_3$ compounds."

   ***Sanjib Banik*** *and I. Das*

   **Communicated**.

## Chapters in books and lectures notes : N. A.

## Other Publications:

a. Conference/Symposium

1. **Participation** at International workshop on Electron Microscopy and XXXIV Annual Meeting of the Electron Microscope Society of India (EMSI), Kolkata, India **2013**.
2. **Poster Presentation** at 59th DAE Solid State Physics Symposium, VIT University, Vellore, Tamil Nadu, India with the topic entitled "*Large Magnetocaloric Effect Near Room Temperature in Polycrystalline* $(La_{0.7}Ca_{0.3})_{0.7}Sr_{0.3}MnO_3$

*Compound". **2014***

3. **Poster Presentation** at International conference on Emerging Materials : Characterization & Application (EMCA), CSIR-Central Glass & Ceramic Research Institute, Kolkata, India with the topic entitled "*Study of memory effect and Magnetocaloric Properties in Polycrystalline* $(La_{0.7}Y_{0.3})_{0.7}Ca_{0.3}MnO_3$ *Compound".**2015***

4. **Poster Presentation** at 60th DAE Solid State Physics Symposium, Amity University, Noida, Uttar Pradesh, India with the topic entitled "*Study of Magnetic and Magnetocaloric Properties of* $(La_{1-x}Y_x)_{0.7}Ca_{0.3}MnO_3$ *Compounds". **2015***

4. **Paper Presentation** at 61st DAE Solid State Physics Symposium, KIIT University, Bhubaneswar, Odisha, India with the topic entitled "*Study of Transport and Magneto-transport Properties in Nanocrystalline* $Y_{0.7}Ca_{0.3}MnO_3$ *Compounds."*

   **Sanjib Banik** and I. Das

   *AIP Conf. Proc.* 1832, 050073 **(2016)**.

5. **Poster Presentation** at National conference on Recent Trends in Condensed Matter Physics, Bose Institute, Kolkata, India with the topic entitled "*Enhancement of Magnetoresistance and Magnetocaloric Effect at Room Temperature in Polycrystalline* $Pr_{1-x}La_xSr_{0.2}MnO_3(x = 0.2)$ *Compound." **2017***

## List of Publications (not included in this thesis)

# Journal

1. "Large magnetocaloric effect near room temperature in polycrystalline $(La_{0.7}Y_{0.3})_{0.7}Sr_{0.3}MnO_3$ compound."

*Kalipada Das,* ***Sanjib Banik*** *and I. Das*

**Materials Research Bulletin 73, 256 (2016)**.

2. "Large magnetocaloric effect in geometrically frustrated polycrystalline $ErMnO_3$ compound at cryogenic temperature."

   *Kalipada Das,* ***Sanjib Banik*** *and I. Das*

   **Physica B: Condensed Matter 533, 46 (2018)**.

3. "Multibit memory state in $Sm_{0.5}(Ca_{0.5}Sr_{0.5})_{0.5}MnO_3$ compound."

   ***Sanjib Banik****, Kalipada Das, kalpataru Pradhan and I. Das*

   **Manuscript under preparation**.

4. "Superconductivity of Cobalt in Thin Films."

   *Nasrin Banu, M. Aslam, Arpita Paul,* ***Sanjib Banik****, S. Das, S. Datta, A. Roy, I. Das, G. Sheet, U. V. Waghmare, B. N. Dev*

   [arXiv:1710.06114 [cond-mat]].

Sanjib Banik

# Dedications

*Dedicated to my family, teachers and friends*

# Acknowledgments

First of all, I would like to express my deepest gratitude to my supervisor Prof. Indranil Das who has introduced me to the amazing world of manganites. I greatly appreciate him for his tireless support, constant encouragement and extraordinary mentorship throughout my PhD tenure. Our both academic and non-academic discussions over the years have been of great value to me.

I would like to sincerely thank my collaborators, Dr. Kalpataru Pradhan, Prof. Biswarup Satpati, Dr. Pintu Sen, Dr. Kalipada Das who have contributed in many different ways to the progress of this work. I am very grateful to them for their immense help and extremely valuable advices.

I am also indebted to the members of my doctoral committee, Prof. Chandan Mazumdar , Prof. Bilwadal Bandhyopadhyay, Prof. Arti Garg and Dr. Gayathri N. Banerjeefor their encouraging words and thoughtful criticism.

I would like to specially thank to Dr. Kalipada Das. You have been a great senior, a great motivator and above all a wonderful friend. I am fortunate to come across seniors like Papri di, Rima di and Sudipta di. They have been more like elder sisters, than seniors. I am thankful to Tapas da for the stimulating discussions we had. I feel very lucky to have Suvayan, Snehal, Apurba, Dipak, Tanmay, Pooja as my juniors and Santanu, Shovan as my friends. You guys are like my family in SINP.

Many thanks to Anis da, Arun da for their tremendous support to carry out experimental work.

Thanks to Kamalenu, Alam, Tapas, Achyut, Arpan, Gouranga, Satyajit, Kuntal, Suvankar, Sayani, Sruti, Pankaj, Debu, Sabuj, Aritra, Tirtha, Chiru, Kumar, Sudip, Sanjukta, Amrita, Mily, Bini, Barnamala for their great friendship which i will cherish throughout my life. I treasure every minute I have spent with them. I will

miss our gossips in Room no:450 and pandal hopping during pujas.

I am also thankful to the canteen staff Suresh da, Shakti da, Kartik da and Hemanta da for providing us wonderful lunch and dinner.

I wish to thank my parents and siblings who has always encouraged me to continue my studies. They have always taught me to dream big yet stay grounded. Last but definitely not the least, my heartiest thanks goes to **someone special** of nickname ***didimoni*** for encouragements, love, patience and mental support to overcome my personal and professional wears and tears.

Let me once again thank all the people for their support. I would remain grateful to all of them.

# Contents

# Synopsis

The strong correlation between spin, charge and lattice degrees of freedom makes the manganites a unique system [1–4]. In contrast to the uncorrelated system where substantial disorder comparable to the fermi energy is needed for nontrivial effects to emerge, in manganites disorder only needs to be comparable to the polaronic bandwidth. Another important features of manganites is that the cooperative ordering between different order parameter shows phase transition and these phases being of small energy difference it is easy to transform from one phase to another via perturbations like magnetic field, electric field, chemical pressure, disorder etc [5–14]. This thesis studies the features of closer interplay between the correlation effect and disorder near the phase boundary in the context of manganites.

One of such correlated system is the half doped manganites which involve strong electron phonon interactions. In manganites electronic bandwidth is determined by the average A-site ionic radius of $R_{1-x}A_xMnO_3$ [15, 16]. For larger bandwidth system, the electron phonon interaction is not crucial and system is the ferromagnetic metal. While at lower bandwidth, electron phonon interaction localize the electrons and creates checkboard type charge ordered pattern. Besides the bandwidth, the stability of these phases also depends on the cationic disorder. Our idea is to modify the strong electron phonon interactions by modifying A-site ionic radius and by introducing disorder. Besides A-site doping, the impact of B-site dopants also affects the underlying magnetic ground state. Through modification of the magnetic ground state by A-site as well as B-site doping reveal phase separation which some-

times leads to large magnetoresistance. The aim is to exploit the disorder as a tool to have electronic phase separation which would give rise to magnetoresistance.

Among the manganite families, $Sm_{0.5}Ca_{0.5}MnO_3$ (SCMO) was reported [2] to have highly stable COAFM ground state with critical magnetic field ($H_C$) to destabilize the CO state as high as 500 kOe at T = 4 K. For weakening the robust charge ordering by increasing the FM phase fraction, in half-doped $Sm_{0.5}Ca_{0.5}MnO_3$, we have substituted systematically the $Ca^{2+}$-ions by $Sr^{2+}$ ions which have larger cationic size than both $Sm^{3+}$ and $Ca^{2+}$ ions. In this work, we present the observation of ultra-sharp jump in the isothermal magnetization in polycrystalline $Sm_{0.5}(Ca_{0.5-x}Sr_x)MnO_3$ ($x = 0, 0.1, 0.2, 0.25, 0.3, 0.5$) compounds. These jumps are also seen in the field dependent resistivity data. The critical field ($H_{Cr}$), required for the ultra-sharp jump in magnetization, decreases with increase of 'Sr' concentration or in other words with increase of A-site ionic radius $\langle r_A \rangle$. The dependence of $H_{Cr}$ with magnetic field sweep rate has also been observed from the comparison of the observed jump in isothermal resistivity and magnetization. The magnetotransport data indicates the increase phase separation with increase of $\langle r_A \rangle$. The presence of exchange bias at low temperature also signifies the presence of inhomogeneous phase separated states. The study reveals that, AFM to FM transition is of martensitic like and is at the origin of the magnetization jump. A phenomenological picture has also been presented here to understand the decrease of $H_{Cr}$ with $\langle r_A \rangle$.

Another intriguing property achieved in one of the polycrystalline $Sm_{0.5}(Ca_{0.5-x}Sr_x)MnO_3$ ($x = 0, 0.1, 0.2, 0.25, 0.3, 0.5$) compounds, $x = 0.25$ is the extraordinarily large value of magnetoresistance. For most of the magnetic materials the change in electrical resistance in the presence of external magnetic field namely magnetoresistance (MR) is limited to only few percentages. The materials and device structure having larger value of MR is of tremendous importance for

magnetic field sensor which is having applications in every spheres of life. Colossal magnetoresistance, for which resistivity changes several order of magnitude ($\sim 10^4$) in an external magnetic field, occurs mainly in phase separated oxide materials, namely manganites, due to the phase competition between the ferromagnetic metallic and the antiferromagnetic insulating region. The large MR value has become the basis of the application in magnetic sensors, magnetic memory devices, magnetic switches [16] etc. The rarity of large MR value with potentially low-cost stable materials motivates the worldwide activity of researcher to study magnetoresistive properties in materials from both fundamental and application point of view [17]. Here, we report the observation of ultrasharp metamagnetic transition and extremely large value of negative magnetoresistance, i.e. Supreme magnetoresistance (SMR) in $Sm_{0.5}(Ca_{0.5}Sr_{0.5})_{0.5}MnO_3$ compound. The obtained MR value is $\sim 10^{15}\%$ at 10 K on application of 90 kOe magnetic field and this value is certainly several orders of magnitude higher than any other so far reported MR value. Our model hamiltonian calculations show that the inhomogeneous disorder, deduced from the tunneling electron microscopy, suppress the CE-type phase and seeds the ferromagnetic metal in an external magnetic field.

The observed large magnetoresistive response in $Sm_{0.5}(Ca_{0.5}Sr_{0.5})_{0.5}MnO_3$ compound gives a hope to exploit it for memory applications. The current upsurge in research on the development of high density non volatile resistive memory devices leads to the search of materials of multiple resistance states [18]. Here we have found that the $Sm_{0.5}(Ca_{0.5}Sr_{0.5})_{0.5}MnO_3$ compound serves the purpose of multiple resistance states. Here we have shown that the different resistance states in manganites can be achieved not only by electric or magnetic field, as observed previously, but by heat pulse also. For the presently studied compound heat pulse converts the ferromagnetic (FM) metallic fraction to charge ordered antiferromagnetic (CO AFM) insulating fraction and different resistance states is achieved. The observed multiple resistance states has been explained on the basis of a theoretical model.

Together with the large magnetoresistance, another requirement for sensor application is to have large field coefficient of resistance (FCR) and temperature coefficient of resistance (TCR). By controlling the intrinsic electronic phase separation in polycrystalline $Sm_{1-x}(Ca_{0.5}Sr_{0.5})_xMnO_3(x = 0.45)$ compound a large FCR of 7500% at 20 K and TCR of 200% at 30 kOe magnetic field has been achieved.

Besides A-site doping, the effect of B-site doping in charge ordered $Sm_{0.5}Ca_{0.5}MnO_3$ compound in transport and magnetotransport properties has also been studied in the the thesis. Mn site of the compound has been doped with nonmagnetic $Ga^{3+}$ as well as magnetic $Cr^{3+}, Fe^{3+}, Co^{3+}$ ions. Compare to the parent SCMO compound an enhancement of magnetization is observed at low temperature in the partially Mn site doped compound. Interestingly, a huge enhancement of magnetization is observed in the $Cr^{3+}$ doped compound. It is also associated with an metal-insulator transition. Large exchange bias is achieved in 3% $Ga^{3+}$ doped compound compared with magnetic 3% $Cr^{3+}$ doped compound. As $Cr^{3+}$ coupled antiferromagnetically with Mn lattice, it creates small ferromagnetic clusters. On the other hand, $Ga^{3+}$ by creating disorder it creates also small ferromagnetic clusters. As, exchange bias depends on the FM-AFM interface, the large exchange bias in $Ga^{3+}$ doped compound implies that cluster size is small in $Ga^{3+}$ doped compound compared with $Cr^{3+}$ doped one.

Another interesting features in manganites is that near 30% hole doping in manganites the ferromagnetic double exchange interactions predominates over electron-phonon interactions(e-p) [19]. The relative strength of DE and e-p interaction modifies according to the A-site ionic radius. With changing ionic radius the disorder also comes into play. For large A-site disorder the resulted state is the cluster glass state. On the other hand for low bandwidth manganites the large disorder promotes the formation of polaron and strongly enhances the resistivity [20]. The aim here is to modify the ground state of 30% doped compound by deceasing the ionic ra-

dius so that e-p interaction increases and study the transport and magnetotransport properties of these modified compounds by external magnetic field or by enhancing surface pressure by creating nanoparticles.

One of such well known DE dominated system is $La_{0.7}Ca_{0.3}MnO_3$ compound. An extraordinarily large magnetoresistance (MR) has been obtained by optimal substitution of $Y^{3+}$ ion in $La^{3+}$ sites. To explore the origin of that giant enhancement of MR, we have carried out magnetic and magnetotransport measurments of $(La_{1-x}Y_x)_{0.7}Ca_{0.3}MnO_3$ $(x = 0, 0.4, 0.5, 0.6, 1)$ compounds in detail. Our analysis indicates that the disorder introduced by yttrium substitution plays the crucial role in magnetoresistive properties in this series. Large MR has been observed in the optimally doped $(La_{0.5}Y_{0.5})_{0.7}Ca_{0.3}MnO_3$ $(x = 0.5)$ compound. In this compound the MR value as high as $1.5 \times 10^7\%$ at 50 K temperature and $3.6 \times 10^4\%$ at 80 K temperature has been achieved for 90 kOe external magnetic field. Moreover at 80 K for $x = 0.5$ compound the MR is reversible in nature. The extraordinarily enhanced large MR value has been described by a phenomenological model of percolation via ferromagnetic clusters.

Another interesting features observed in the $(La_{1-x}Y_x)_{0.7}Ca_{0.3}MnO_3$ compounds is the evolution from the Griffiths like phase to non-Griffiths like phase with $Y^{3+}$ doping. The existence of Griffiths phase is identified from the downturn of the inverse susceptibility versus temperature plot from the curie weiss behavior for the compounds with $x = 0.3, 0.4$. Whereas the existence of non-Griffiths phase is revealed from the upward deviation of $1/\chi$ versus T plot from the Curie weiss line in the compounds with $x \geq 0.5$. The increased lattice distortion with increase value of $x$) (obtained from the XRD analysis), responsible for the enhancement of the antiferromagnetic effective superexchange (SE) interactions, has been attributed to the conversions from non-GP to GP phase. The magnetocaloric study has also been performed which also support the increased AF interaction with $x$.

We have also discussed the particle size driven modification of the non-Griffiths phase to Griffiths phase in $(La_{0.4}Y_{0.6})_{0.7}Ca_{0.3}MnO_3$ (LYCMO) compound with the help of x-ray diffraction, electrical transport, magnetotransport, magnetization and heat capacity measurements. The signature of the Griffiths phase in nanocrystalline LYCMO compound ($\sim 120nm$) is clearly observed from the anomalies in the heat capacity data as well as from the magnetic susceptibility data. The temperature dependent x-ray diffraction data reveals the decrease of lattice distortion in the nanocrystalline compound compared with its bulk counterpart. The decrease in lattice distortion helps to increase the ferromagnetic double exchange interactions (DE) between $Mn^{3+}$ and $Mn^{4+}$ ions compared with antiferromagnetic superexchange interactions (SE) between $Mn^{3+}/Mn^{3+}$ and $Mn^{4+}/Mn^{4+}$ ions. In nanocrystal, the decreased lattice distortions together with the quenched disorder arising from the ionic size mismatch of the different A-site ions are the possible reason for the occurrence of Griffiths phase. On the other hand, though in the bulk compound there is the presence of quenched disorder but the higher distortions enhances the SE interactions and may be the probable reason for the non-Griffiths phase which is identified by the upturn of the inverse susceptibility versus temperature plot from the Curie-Weiss line. The detailed low-temperature magnetization, nonequilibrium dynamical behavior and frequency dependent ac susceptibility data reveals that bulk LYCMO is a mixture of short-range FM correlated regions with canonical spin glass phase while nano LYCMO is the mixture of cluster glass phase with the FM correlated regions at low temperatures ($T < 50K$). Colossal magnetoresistance (CMR) is observed in bulk as well as nanocrystals. Moreover, an enhancement of CMR in the minimal surface disorder nanoparticle ($\sim 120nm$) has been observed. The study shows that for LYCMO compound, the enhancement of CMR in 120 nm nanoparticle is due to the conversion from non-Griffiths phase to Griffiths phase.

On the other hand, although the study of the influence of A-site disorder in transport and magnetotransport properties in larger bandwidth systems has been ex-

tensively studied previously, but a very less attentions has been paid to the investigation on magnetocaloric properties [21–24]. Here, we explore the influence of A-site ionic disorder ($\sigma^2$) on magnetocaloric properties in relatively larger bandwidth manganite systems like, well known $La_{0.7}Sr_{0.3}MnO_3$ compound. For the study, three isoelectronic manganites with same A-site ionic radius ($\langle r_A \rangle$ =1.24$\mathring{A}$) i.e. $La_{0.7}Sr_{0.3}MnO_3(\sigma^2 = 1.85 \times 10^{-3})$, $Pr_{0.7}Sr_{0.14}Ba_{0.16}MnO_3(\sigma^2 = 1.17 \times 10^{-2})$ and $Nd_{0.7}Sr_{0.07}Ba_{0.23}MnO_3(\sigma^2 = 1.66 \times 10^{-2})$ samples have been prepared. Magnetic measurements reveal that, upon increasing $\sigma^2$ from $1.85 \times 10^{-3}$ to $1.66 \times 10^{-2}$, ferromagnetic double exchange interaction diminishes and as a result, ferromagnetic ordering temperature ($T_C$) decreases from 360 K to 100 K. Accordingly, the magnetic entropy change ($-\Delta S_M$) has also been found to decrease from 4.6 J/kg-K to 4.1 J/kg-K on the application of 70 kOe magnetic field. However, for $\sigma^2$ =$1.66 \times 10^{-2}$, the value of $-\Delta S_M = 5.7 J/kg$ is relatively larger compared to the other two values of $-\Delta S_M$. Additionally, increased $\sigma^2$ ($1.85 \times 10^{-3}$ to $1.66 \times 10^{-2}$) broadens the peak of $-\Delta S_M$ which results in the increase in relative cooling power (RCP) from 80 J/kg to 121 J/kg on application of 20 kOe magnetic field.

Another, interesting system is the ferromagnetic insulator which appears near 20% hole doping in the manganites [25]. A strong electron-phonon coupling is believed to play the crucial role for the formation of FMI state. The modification of this e-p coupling by creating chemical pressure is another part of the present thesis. One of such FMI system is $Pr_{0.8}Sr_{0.2}MnO_3$. To study the effect of chemical pressure, partial substitution of $Pr^{3+}$ has been made by relatively higher ionic radii $La^{3+}$ and lower ionic radii $Y^{3+}$. The results shows the modification of the FMI ground state to the ferromagnetic metal in the $La^{3+}$ doped compound. While on the other hand FMI state become more insulator in the $Y^{3+}$ doped compound. Another interesting features has been observed in the higher chemical pressure compound is the formation of ferromagnetic clusters at higher temperature compared with its parent compound. The result is the increase in magnetoresistance and magnetocaloric

effect at the room temperature.

In summary, the results and conclusion presented in this thesis indicates the modification of ground state by different types of perturbation which leads to a large magnetoresistance. The results and discussions also lead a better way to understand the magnetoresistive properties in various strongly electron phonon coupled systems. The effect of A-site ionic disorder on magnetocaloric properties in large band width manganite systems has also been studied which shows a possible way to increase the RCP. Moreover, the usefulness of MCE as a tool to understand the kind of magnetic interactions present in the system has also been highlighted.

# List of Figures

# List of Tables

# CHAPTER 1

# Introduction

The investigation of the strongly correlated electron systems is one of the most demanding branches of solid state physics. Amongst various correlated systems, perovskite manganites have attracted considerable research attention from fundamental as well as technological perspectives because of its strong correlation between lattice, spin and charge degrees of freedom. The strong interplay between different degrees of freedom makes the manganite systems extremely sensitive to different external perturbations like chemical doping, temperature, pressure, magnetic field etc. Among the various functional properties, colossal magnetoresistance (CMR) and magnetocaloric effect (MCE) are the intriguing properties because of its application in magnetic field sensor and magnetic refrigeration technology (MRT). A tremendous effort had been paid in this research direction right from the pioneering experimental work of Wollan and Koehlar [26] with the theoretical study of Goodenough [27].

Usually, perovskite manganites exhibits large magnetoresistance and magnetocaloric effect at relatively larger magnetic field, but for practical utility of the manganite materials large MR and MCE should achieve at lower magnetic field. Keeping this context in mind, this thesis is organized and this chapter serves as an introduction

to the physics of manganite and to the overall thesis. This chapter begin with a discussion of the physical ingredients, required to explain basic feature of manganite. We then highlighted the issue of the phase competition and then discussed about the agencies which drives the phase transitions. We end our discussion by providing an outline of the problem addressed in the thesis.

## 1.1 Introduction to the manganites

The rare earth based manganites belongs to the perovskite family with the general formula $ABO_3$, where 'A' is trivalent rare earth (RE) element (La, Pr, Nd, Sm, etc.), 'B' is manganese (Mn) ion and 'O' is oxygen. The research in the field of manganites was initiated more than five decades back with the pioneering experimental works by Jonker and Van Santen in 1950 [28] on mixed valent manganites $RE_{1-x}AE_xMnO_3$ where alkaline rare earth element AE controls the hole doping. They observed a striking correlation between ferromagnetic ordering temperature ($T_C$) and electrical resistivity of the materials [28]. They also found the material to be antiferromagnetic insulator at the both ends of hole doping i.e. for $x = 0$ and $x = 1$ and at the intermediate hole doping around $x = 0.3$ the material becomes ferromagnetic which is associated with sharp decrease in resistivity. At the very next year, a double exchange model was proposed by zener to explain the relation between ferromagnetic ordering and resistivity in $RE_{1-x}AE_xMnO_3$. In an another study, Jonker indicated the connection of lattice with the magnetic and transport properties of the materials. In 1955 a theoretical model was constructed by Goodenough, which provide an excellent explanation of different magnetic structures of the manganites.

Although there was gradual theoretical and experimental development in the field of manganites during 1950's and 1980's but a burst activity has been stimulated in 1994 after the discovery of colossal magnetoresistance [29] in $La_{1-x}Ca_xMnO_3$

at $x = 0.33$ by Jin et al. This observation of such a large change in resistivity on application of magnetic field triggered an intense experimental and theoretical effort in hope that these compounds might be of practical applicability. Regardless of the practical applications, these compounds provide an excellent stage to study the cooperative ordering between different degrees of freedom.

### 1.1.1 Crystal structure

The basic perovskite manganites ($ABO_3$) process cubic crystallographic symmetry where 'Mn' ion is placed at an octahedral coordination of the oxygen ions. The schematic of the structure has been shown in Fig. 1.1. The basis comprise of one A ion at (0,0,0), Mn ion at (1/2,1/2,1/2), and three O ions at (0,1/2,1/2), (1/2,0,1/2), and (1/2,1/2,0). The structure is stabilized by the 12-fold and 6-fold oxygen coordination of the A ions and Mn ions respectively [30]. In 1958, Ruddlesden and Popper gave a general formula of a series of layered oxides as $A_{n+1}B_nO_{3n+1}$ in which n sheets of B-O layer form an isolated building block [31]. The manganites belong to that series as the end member with $n = \propto$. Although the ideal perovskite manganite is cubic in structure, but it is hardly realized except at very high temperature. Due to the buckling and distortion of the $MnO_6$ octahedra, the cubic structure is distorted and give rise to orthorhombic, rhombohedral structure etc.

The ionic size mismatch of trivalent rare earth element and bivalent alkaline divalent element, which jointly occupy the A-site of perovskite structure, produce internal stress in $Mn - O - Mn$ bonds and results in the alternate buckling of $MnO_6$ octahedra. Such distortion can be parameterized by Goldsmith tolerance factor which is given by

$$t = \frac{r_A + r_O}{\sqrt{2}(r_M n + r_O)} \tag{1.1}$$

where $r_A$, $r_{Mn}$ and $r_O$ are average radii of A-site cation, Mn ion and oxygen ion

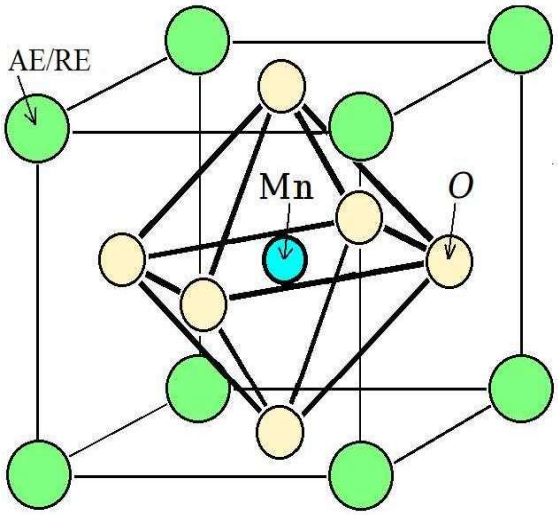


**Figure 1.1:** The perovskite structure of $AMnO_3$ where A are RE ions.

respectively. For ideal cubic symmetry $t \sim 1$ but the structure is stable for $0.89 < t < 1.02$. Large deviations from unity result in completely different crystal structures like hexagonal structure.

### 1.1.2 Electronic structure

The electronic properties of the manganites are mainly governed by the Mn ion which is placed at the center of the oxygen octahedral surroundings. The different Mn orbitals have different shapes, and thus interact with the surrounding oxygen ions differently. The five fold degeneracy of the Mn 3d orbitals are lifted partially by the crystalline electric field produced by the oxygen octahedra surroundings and splits into two sets. The level with lower energy includes the $d_{xy}$, $d_{yz}$, and $d_{zx}$ orbitals, whereas the higher one includes the $d_{x^2-y^2}$ and $d_{3z^2-r^2}$ orbitals. The doublet is referred as $e_g$ and triplet as $t_{2g}$. The energy difference between $t_{2g}$ and $e_g$ orbitals are about 1 eV. The schematic in Fig. 1.2 shows the different electronic energy state of the $Mn^{3+}$ ion in the crystalline environment.

The degeneracy of the energy levels $t_{2g}$ and $e_g$ are further lifted due to the Jahn-Teller (JT) distortion which arises due to the movement of the oxygen ions from

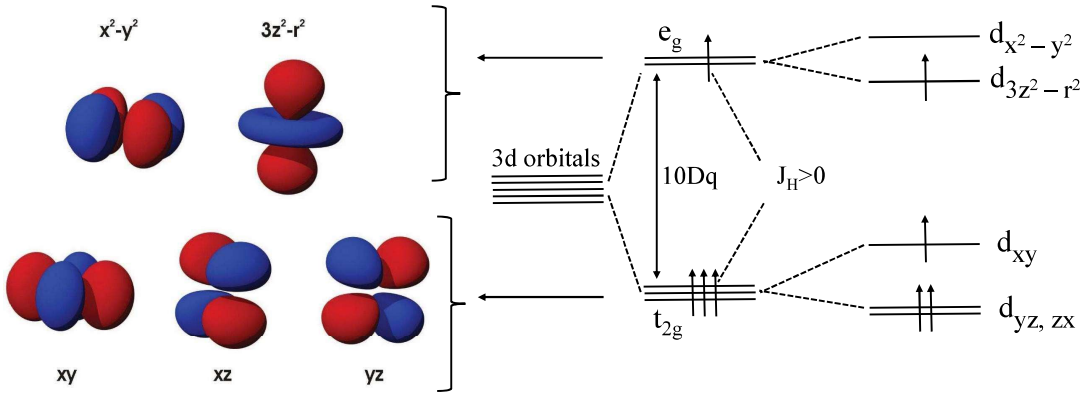


**Figure 1.2:** On the left shapes of different $e_g$ and $t_{2g}$ orbitals is shown. On the right different energy states of $Mn^{3+}$ ions in octahedral surroundings is presented.

their original position. There are two basic Jahn-Teller modes of vibrations, $Q_2$ and $Q_3$ (Fig. 1.3). $Q_3$ mode involve the stretching of $Mn - O$ bonds along Z direction and the compression in the $X - Y$ plane which favors the occupancy of $d_{3z^2-r^2}$ orbital. Whereas $Q_2$ mode is the basal plane collective distortion and it arises due to the superposition of $d_{3z^2-r^2}$ and $d_{x^2-y^2}$. The JT distortion reduces with increasing bivalent substitution. The triplet $t_{2g}$ state also splits into two levels due to the distortion. However, as long as the crystal field splitting is large, the degeneracy lifting in $t_{2g}$ is not important.

#### 1.1.2.1 Hunds coupling

All the Mn 3d electrons are strongly affected by the Coulomb repulsion and Hunds coupling. The $e_g$ electrons are strongly hybridized with the oxygen 2p states. On the contrary, the $t_{2g}$ electrons hybridized less with the oxygen orbitals and can be treated as localized. The ferromagnetic Hunds coupling causes the spins of $t_{2g}$ electrons in an Mn ion to align parallel to each other. Hunds coupling ($J_H$) is $\sim$ 2 - 3 eV and being $J_H \gg t$, where t is the hopping scale of the $e_g$ electrons, the $e_g$ electrons are bound to align with the local $t_{2g}$ spins. It implies that the hopping of the $e_g$ electrons will not take place if the $t_{2g}$ electrons are align antiparallel and in

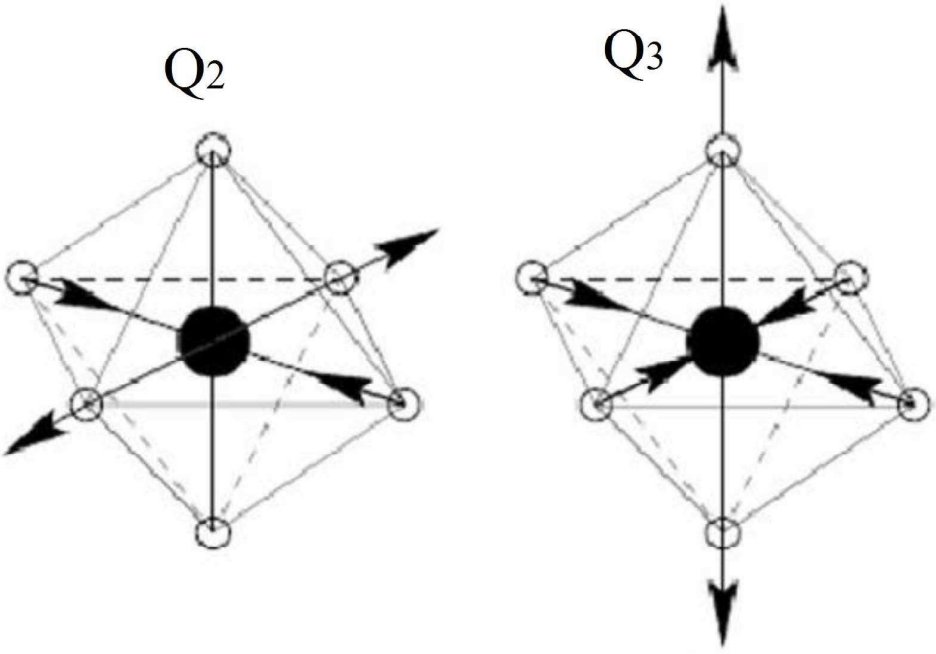


**Figure 1.3:** Different Jahn-Teller modes ($Q_2$ and $Q_3$) responsible for the splitting of the degenerate $e_g$ orbitals.

this way core spin affects the bandwidth and kinetic energy of the $e_g$ electrons. This is the origin of the coupling between charge and spin degrees of freedom.

#### 1.1.2.2 Double exchange interaction

The interdependence of electrical and magnetic properties in mixed valent manganites was first proposed by Zener using a Double exchange (DE) model. According to Zener model, a cluster is formed from one $Mn^{3+}$ ion and one $Mn^{4+}$ ion separated $O^{2-}$ ion. There is a possibility that the electrons in $Mn^{3+}$ ions can hops to the vacant $e_g$ level in the neighboring $Mn^{4+}$ ion via oxygen ion as the configurations $Mn^{3+} - O - Mn^{4+}$ and $Mn^{4+} - O - Mn^{3+}$ are degenerate. However because of the strong Hunds coupling between $e_g$ and $t_{2g}$ electrons, the probability of hopping of $e_g$ electrons from $Mn^{3+}$ ion to $Mn^{4+}$ ion depends on the relative angle between the core spins of those two sites. This hopping probability is maximum when core spins are parallel i.e, ferromagnetically ordered. Thus ferromagnetic state is stabilized by maximizing the kinetic energy of the $e_g$ electrons. The schematics of the explicit

movement of electrons is shown in Fig. 1.4.

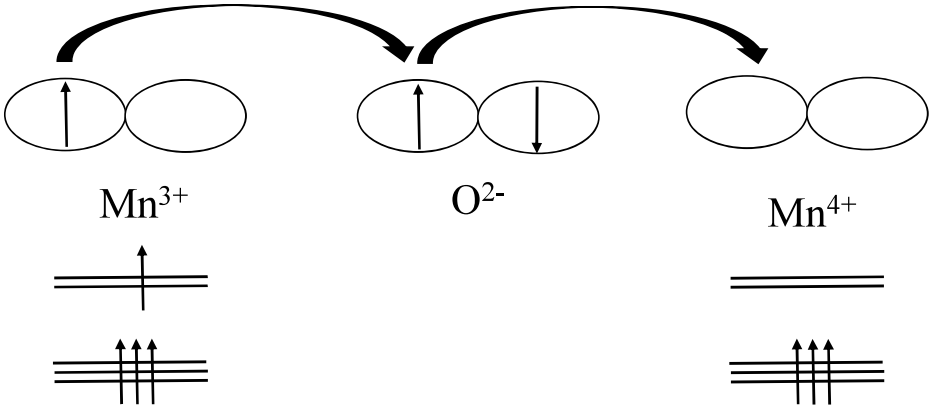


**Figure 1.4:** A schematic of the double exchange mechanism

Further work was performed by Anderson and Hasegawa [32] to visualize the double exchange processes. According to them, the hopping process is second order rather than simultaneous and the effective hopping for the $e_g$ electron to move from $Mn^{3+}$ site to the next $Mn^{4+}$ site is proportional to the square of the hopping from the p-oxygen orbitals to d-manganese orbitals. The effective hopping amplitude between two neighboring sites i and j is proportional to the relative angle between the core spins, Si and Sj. Considering electrons as classical object if they are indexed by their polar and azimuthal angles $\theta_i$ and $\phi_i$, the hopping probability in the strong coupling limit $J_H/t_{ij} \rightarrow \propto$ can be written as [32]

$$t_{ij} = t^0_{ij}[Cos(\theta_i/2)Cos(\theta_j/2) + e^(\phi_i - \phi_j)Sin(\theta_i/2)Sin(\theta_j/2)] \tag{1.2}$$

where $t^0_{ij}$ is the bare hopping amplitude and $J_H$ is the Hunds coupling energy. Neglecting Berry phase effects, the probability can be written as

$$t_{ij} = t^0_{ij}Cos(\theta_{ij}/2) \tag{1.3}$$

According to the above equation it is clear that the distortion of the crystal structure directly influence the hopping probability of the $e_g$ electrons and thus the bandwidth.

With increasing distortion, $\theta_{ij}$ deviates from $180^0$ which causes reduction of hopping probability.

De Gennes further developed the theory [33] of double exchange and predicted the formation of a canted spin structure for low hole doping levels in mixed-valent manganites. The essential feature of the model is the competition of the ferromagnetic double exchange with the antiferromagnetic interaction. If $\theta_0$ is the possible canting angle between adjacent ferromagnetic planes at zero temperature, then according to this model [33]

$$Coc(\frac{\theta_0}{2}) = \frac{bx}{4|J|S^2} \tag{1.4}$$

Where J is the inter-layer antiferromagnetic coupling and b is the double exchange mediated out of plane overlap integral.

#### 1.1.2.3 Super exchange interaction

Another important interaction in some doping regimes in manganites is the antiferromagnetic superexchange (SE) interaction. The superexchange (SE) interaction between Mn ions is also mediated by an intermediate $O^{2-}$ ion. One electron of the full filled 2p orbital of O ion virtually hops to the neighboring Mn ion where it spend some time and again come back to the oxygen 2p orbital. The schematics has been presented in Fig. 1.5. Superexchange interaction between the Mn spins are essential to explain the antiferromagnetic phase. Competition between the antiferromagnetic SE interaction and the ferromagnetic DE interaction decides the magnetic phase of the mixed-valent manganites.

#### 1.1.2.4 Electron-phonon coupling

The double exchange model alone cannot explain all the electrical, magnetic and CMR properties of the mixed valent manganites and is the main reason to investi-

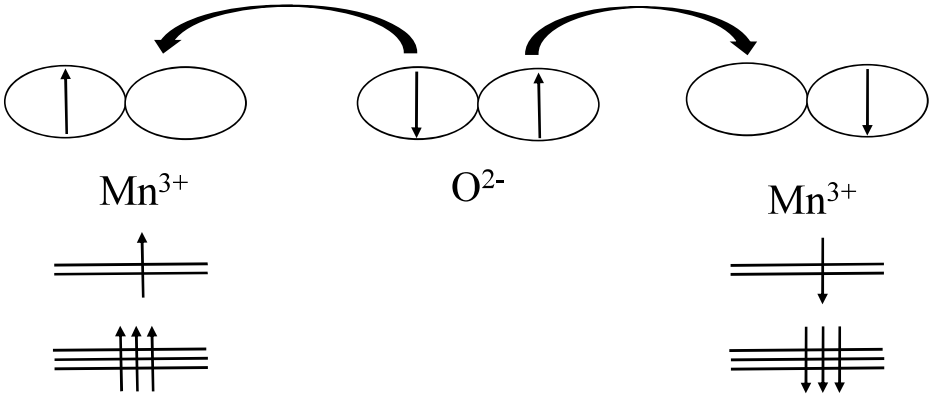


**Figure 1.5:** A schematic diagram of the superexchange mechanism showing the virtual transfer of electrons between the adjacent Mn ions in presence of oxygen ion

gate the importance of electron-phonon coupling in the manganites. In 1995, Millis et al. [34] suggested that Jahn-Teller(JT) splitting of the d-orbitals of $Mn^{3+}$ ions plays a crucial role in determining the electrical and magnetic properties of manganites. Jahn-Teller distortions reduce the energy of the system by lowering its crystal symmetry. The deformation of the $MnO_6$ octahedra caused by the Jahn-Teller (JT) effect splits the $e_g$ band. Greater the distortion, more localized the charge carriers are in the $e_g$ band. In a hole-doped manganite, when an $e_g$ electron of $Mn^{3+}$ ion hops to the neighboring $Mn^{4+}$ site it drags the lattice distortion along with it. Such an electron with its accompanying local lattice distortion is known as a polaron. Lattice polaron effects due to a strong electron-phonon interaction is a necessary ingredient of manganites physics [34]. Formation of static nanoscale lattice polarons above transition temperature was also experimentally shown in the prototype $La_{0.7}Ca_{0.3}MnO_3$ (LCMO) system [35]. It is also important to note that $MnO_6$ octahedra are connected to each other via corner shared oxygen. The distortion of octahedron creates a strain field that affects other octahedra or in other word the distortion of the $MnO_6$ octahedron is cooperative in nature. The distortion of the $MnO_6$ octahedron is largest at $x = 0$, but is visible as a structural distortion almost upto $x = 0.20$ [36].

### 1.1.3 Complex ordered phases

#### 1.1.3.1 Doping dependence

Depending upon the doping concentration, manganites can exhibit different magnetic structures, as the strength of double exchange interaction depends upon the $Mn^{4+}/Mn^{3+}$ ratio. Several magnetic configurations that occur in the manganites are shown in Fig. 1.6. Here we will show the $x - T$ phase diagram for $La_{1-x}Ca_xMnO_3$ (Fig. 1.7) which exhibits various phases that arises due to the change in the carrier concentration. System shows some features at commensurate fillings $p/8, p = 1, 3, 4, 5, 7$ which we will also discuss here.

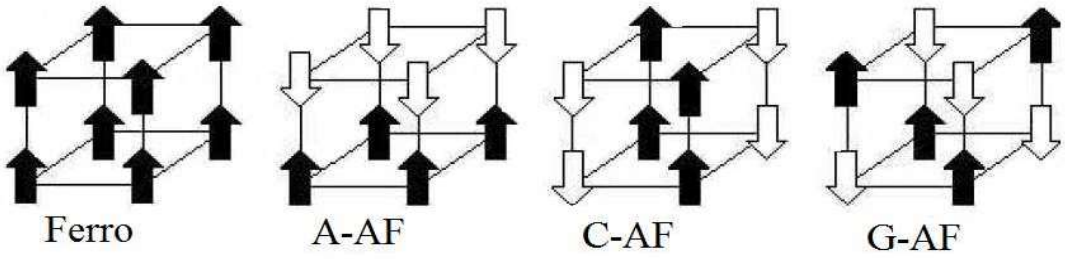


**Figure 1.6:** Different spin arrangement in the manganites. Another important arrangement is CE-type antiferromagnetic ordering which is introduced later.

***Undoped region*** $x = 0$: The undoped compound $LaMnO_3$ is an A-type antiferromagnetic insulator. As all the Mn ions are JT active, the collective cooperative Jahn-Teller distortion leads to orbital ordering on the $a - b$ plane with alternate $d_{3x^2-r^2}$ and $d_{3y^2-r^2}$ orbitals. Here, the x and y axes has been taken along the orthogonal $Mn - O$ bond directions on the $a - b$ plane. The system undergoes orbital ordering at $T_{OO} \sim 780$ K and A-type antiferromagnetic ordering at $T_N = 120$ K. The schematic of the charge and orbital pattern in the a - b plane, has been shown in Fig. 1.8(a).

***Light to intermediate doping region*** $0 < x < 0.5$***:*** The hole doping canted the ordered spins as it allows the hopping to take advantages of the empty sites. With

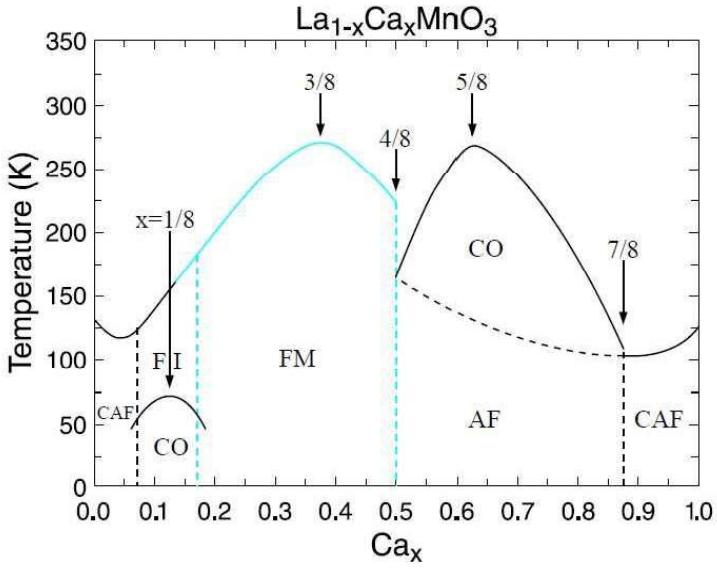


**Figure 1.7:** Phase diagram of $La_{1-x}Ca_xMnO_3$ compound where FM: ferromagnetic metal, FI: ferromagnetic insulator, AF: antiferromagnetism, CAF: canted antiferromagnet, CO: charge/orbital order. (*This figure has been taken from S-W Cheong et. al., Colossal Magnetoresistive Oxides, edited by Y. Tokura, Gordon and Breach, Amsterdam (2000)*) [37].

increase in hole doping (above $x \sim 0.07$) the system becomes ferromagnetic due to the local excursion of the $e_g$ electrons although the system remain in the orbital ordered insulating state up to doping $x \leq 0.17$. In the region $0.07 < x < 0.17$ the orders of the doped holes leads to the AF-CO state. This state is most stable at $x = 1/8$. With increasing temperature this AF-CO state becomes ferromagnetic insulator state. This low doped insulating state appears to be a mixture of hole rich FM regions and hole poor antiferromagnetic regions. The state beyond $x = 0.17$ becomes ferromagnetic metal (FM-M) which is also associated with the decrease in the Jahn-Teller distortions. The paramagnetic to ferromagnetic transition temperature ($T_C$) increases with increase of $x$ up to 3/8 and then decreases. This decrease in $T_C$ is because of the presence of some competing magnetic phase arises due to the electron-lattice coupling.

***Half doped region*** $x = 0.5$ : At half filling system changes from FM-M to a spin, charge and orbital ordered insulator (CE-CO-OO-I) phase. This CE phase appears

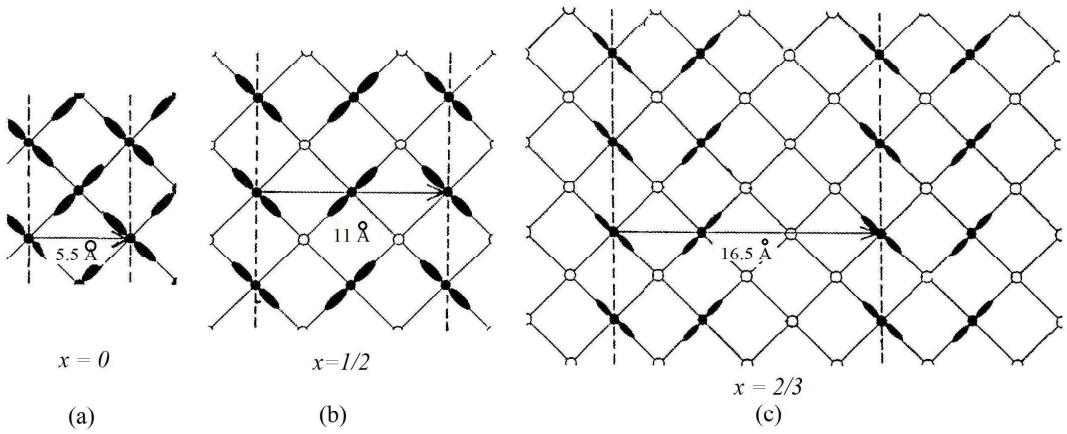


**Figure 1.8:** The charge and orbital ordering in $La_{1-x}Ca_xMnO_3$ compound in the orthorhombic basal plane at the hole densities *x=0, 1/2* and *2/3*. Open circles represent the $Mn^{4+}$ ion and lobes indicate the populated $e_g$ orbital of $Mn^{3+}$ ion. The charge modulation waves lengths are 5.5 $\AA$, 11 $\AA$ and 16.5 $\AA$ for (a) *x=0*, (b) *1/2* and (c) *2/3* respectively. (*This figure has been taken from Nanoscale Phase Separation and Colossal Magnetoresistance: The Physics of Manganites and Related Compounds, edited by E. Dagotto (Springer 2003)) [38].*

in all manganites. In the CE type phase, ferromagnetic zig-zag chains are coupled antiferromagnetically in the $a-b$ plane. This pattern also repeats in the c direction such that zig-zag chains are coupled antiferromagnetically. Because of the absence of any $e_g$ electron, the orbital degree is inactive in $Mn^{4+}$ ion. Orbitals of $Mn^{3+}$ are directed toward Mn4+ when the two ions are ferromagnetically coupled, and they are directed away from $Mn^{4+}$ when the two ions are antiferromagnetically coupled. The schematic of the in plane $(a-b)$ charge and orbital pattern has been shown in Fig. 1.8(b). Although the electrons can delocalize on the zigzag chains but the overall system is insulating. Beyond $x > 0.5$, the doped carrier localize and stripelike charge ordering occurs which is most robust at $x = 5/8$. This CO is also associated with antiferromagnetic ordering. Above $x > 5/8$, this CO-AF phase weaken.

***Overdoped regime*** $7/8 \leq x \leq 1$***:*** In this hole doped region system is in canted antiferromagnetic (CAF) state. The state at $x = 1$ is a G-type insulator.

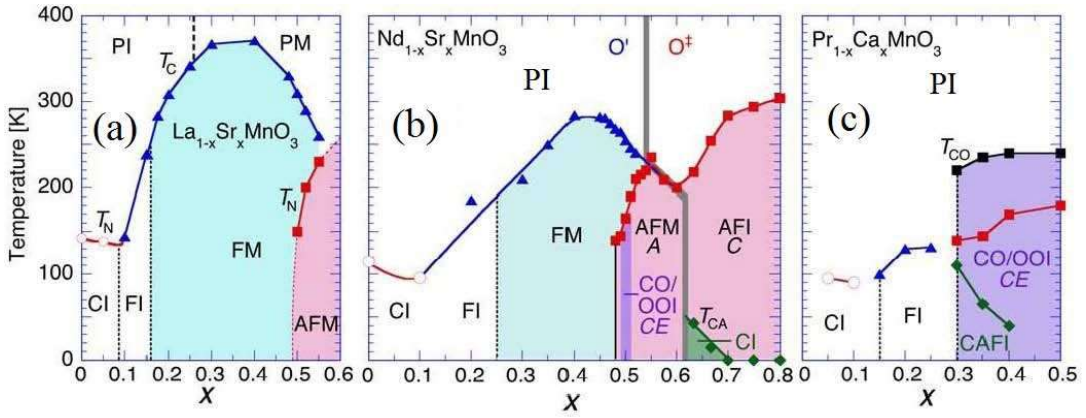


**Figure 1.9:** The magnetic and electronic phase diagrams of (a) $La_{1-x}Sr_xMnO_3$, (b) $Nd_{1-x}Sr_xMnO_3$ and (c) $Pr_{1-x}Ca_xMnO_3$. Here PI, PM and CI stand for the paramagnetic insulating, paramagnetic metallic and spin-canted insulating states, respectively. FI, FM and AFM denote the ferromagnetic insulating, ferromagnetic metallic and antiferromagnetic (A-type) metallic states, respectively. (*From Tokura et. al., J. Magn. Magn. Mater.* ***200****, 1, (1999) [39].*)

#### 1.1.3.2 Bandwidth dependence

The expression of bandwidth (BW) is given as

$$BW \propto \frac{Cos[\frac{1}{2}(\pi - \beta)]}{d_{Mn-O}} \tag{1.5}$$

where $\beta$ is the $Mn - O - Mn$ bond angle and it is smaller when $\langle r_A \rangle$ is larger. It implies that larger the $\langle r_A \rangle$ means larger the BW. The phase diagram of three manganites $La_{1-x}Sr_xMnO_3$, $Nd_{1-x}Sr_xMnO_3$ and $Pr_{1-x}Ca_xMnO_3$ with successively smaller mean cation radius $\langle r_A \rangle$ has been shown from (a) to (c) in Fig. 1.9. It implies that reducing BW changes the windows for the various phases, and sometimes brings in new phases. Larger BW promotes ferromagnetism through the double exchange mechanism. On the other hand, with reduction of BW the JT coupling becomes relevant and charge or orbital ordered phase appears. In manganites generally AE elements like Ca, Sr, and Ba changes the average A site ionic radius $\langle r_A \rangle$. Therefore $La_{0.5}Ca_{0.5}MnO_3$ (LCMO) is a CE type antiferromagnetic charge ordered material, which changes to A-type antiferromagnetic material without any

charge ordering in $La_{0.5}Sr_{0.5}MnO_3$ (LSMO) [40] and finally change to ferromagnetic metal in $La_{0.5}Ba_{0.5}MnO_3$ (LBMO) [2]. Experiments with the variation of BW has also been done with different combinations of Ca, Sr and Ba ions. For example in $La_{0.5}Ca_{0.5-y}Sr_yMnO_3$, CE type antiferromagnetic CO state appears for $y \sim 0-0.3$[] while it changes to A-AFM state for $y > 0.3$. The ground state phase diagram in terms of hole doping and BW variation has been presented in Fig. 1.10 which shows a clear evolution of the ground state with BW for a fixed hole doping.

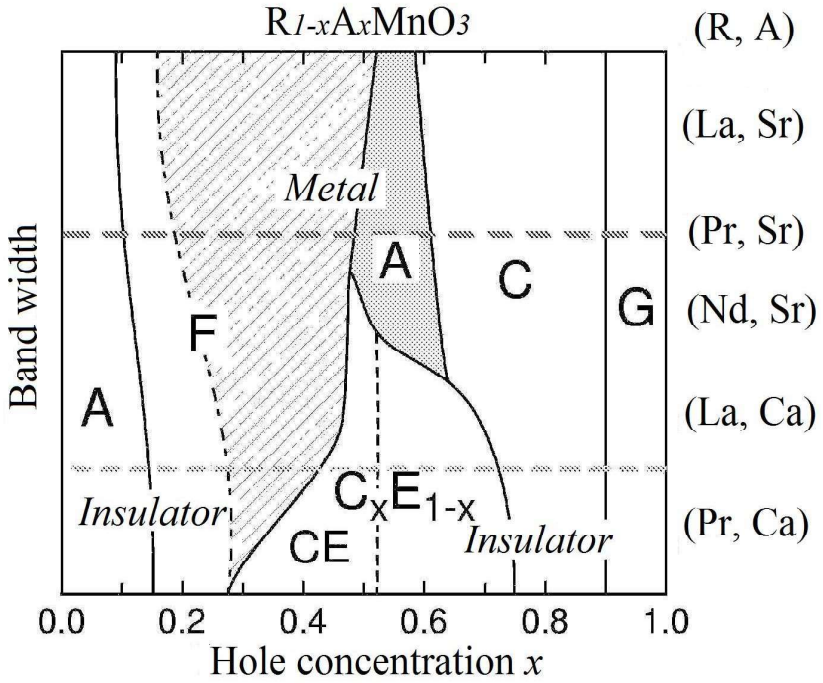


**Figure 1.10:** Schematic phase diagram of $R_{1-x}A_xMnO_3$ where F denotes FM state. A, CE, C, G and $C_xE_{1-x}$ denote A-type, CE-type, C-type, G-type and incommensurate charge/orbital ordered AFM states respectively. *(From R. Kajimoto, et al., Phys. Rev. B 66, 180402 (2002). [40])*

#### 1.1.3.3 Effect of disorder

The ionic radius of AE and RE ions being different, the substitution of RE with AE ions adjust the oxygen octahedra to a tilted situation (Fig. 1.11). It suppresses the hopping amplitude as $\propto Cos^2\theta$, where $\theta$ is the $Mn-O-Mn$ bond angle. This reduces the overall BW. Apart from ionic size mismatch, there is the difference in the

ionic charge of AE and RE ions also. The different local environment of different Mn ions leads to a random potential on the Mn ions. The hopping modulation and scattering potential are the two main sources of A-site disorder. Usually the quenched disorder suppresses ordering tendencies which leads to an inhomogeneous phase. In manganites, the average A-site ionic radius $\langle r_A \rangle$ controls the bandwidth and the variance $\sigma$ of the A-site radii control the magnitude of the disorder. A site disorder is unavoidable except in few cases of special doping concentration $x$ and special growth technique [2].

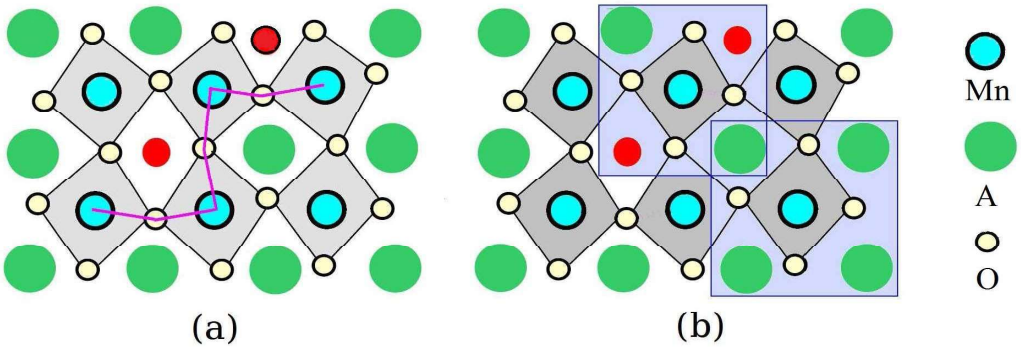


**Figure 1.11:** Schematic of the A-site disorder (a) shows a system where few A sites have been substituted with A' of different radii and (b) disorder arising due to the local charge environment of the Mn sites in the two squares when valence state of the A' is different from that of A, which is typically the case.

### 1.1.4 Phase separation

Tuning the doping level or bandwidth near a phase boundary leads to drastic change in the physical properties. Phase competition across a first order phase boundary in presence of disorder leads to the phase separation. Here we will discuss the effect of disorder on the ordered state and their response on application of external magnetic field.

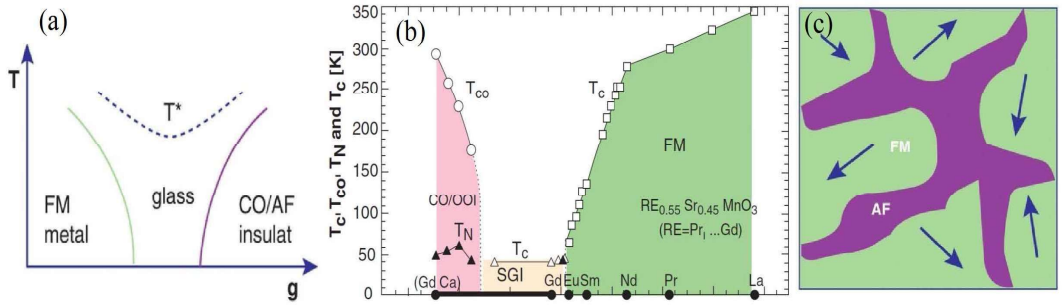


**Figure 1.12:** (a) Generic phase diagram of two competing states ( FM-M and an AF-CO-I) in the presence of quenched disorder [4,38]. Here $\boldsymbol{g}$ is a generic variable to move from one phase to the other (e.g., electronic density or bandwidth). (b) Experimental phase diagram of manganites with disorder [41, 42] which shows the disorder-induced suppression of the ordering temperatures and the appearance of a glass state, as predicted by the schematic shown in (a). (c) Typical sketch of the CMR state for the manganites containing FM clusters with randomly oriented moments separated by CO/AF regions [38, 42, 43].

#### 1.1.4.1 Phase coexistence and CMR

The effect of disorder on the ordered state has been studied rigorously by experimentally as well as theoretically. A schematic view emerged from theoretical study on the effect of the disorder on the ordered state has been presented in Fig. 1.12(a). It shows that over a narrow window of coupling $g$ neither of the FM-M or the AF-CO-I phase occurs globally which is on the contrary to the clean system where phases are separated by first order boundary at low temperature. In the presence of disorder the long range ordering breaks and both the phases coexist with short range order. Experimental results also supports this possibility and transport study indicates the glassy nature of the phase separated state (Fig. 1.12(b)). A schematic view of the cluster glass state has been shown in Fig. 1.12(c) which indicates that the ferromagnetic clusters are oriented randomly. On application of the magnetic field these clusters orient in the direction of the field as well as grow in size and if sufficient percolation path appears then CMR occurs. It has also been observed that in $Nd_{0.5}Ba_{0.5}MnO_3$ the CMR occurs in the disordered state, while it is absent in the ordered state. This clearly shows the importance of the disorder on CMR.

In real systems disorder is always present. This thesis is primarily concerned with such disorder effects, especially in half doped manganites.

#### 1.1.4.2 Effect of disorder near half doping

It is well known that decreasing $\langle r_A \rangle$ reduces the BW and accordingly the material like $La_{0.5}Sr_{0.5}MnO_3$ (LSMO) with larger $\langle r_A \rangle$ has a FM-M ground state at half doping while smaller BW material like $Nd_{0.5}Sr_{0.5}MnO_3$ (NSMO) has a CE-CO-I ground state. Now, let us look at the effect of the disorder on the CE-CO-I state. In the Fig. 1.13 the superimposed phase diagram of ordered and disordered perovskite manganites at half doping of the $Ln_{0.5}Ba_{0.5}MnO_3$ family has been described. In the ordered case (black line), with increasing BW increase in $T_C$ is observed as increase in BW stabilized the double exchange driven FM phase. On the other hand, with decreasing BW there is enhancement of the carrier localization tendencies which causes stable charge ordered state and leading to the increase in $T_{CO}$. Moreover, $T_{CE}$ decreases with decrease in BW. As kinetic energy gain by the electrons by local hopping is suppressed due to the localization, and the delicate balance between kinetic energy and antiferromagnetic superexchange interaction, which stabilized the CE phase, is destroyed by weakening. On the other hand, the CE-CO-I phase is completely destroyed in presence of disordered (red line). The disorder transforms the long range CE-CO-I state in spin glass state with short range charge and orbital correlations. While, large disorder (like Ba-family) converts the CE-CO-I state into glassy state, it is natural to ask about the fate of the CE-CO-I state in the presence of small disorder. In this thesis we will highlight this issue.

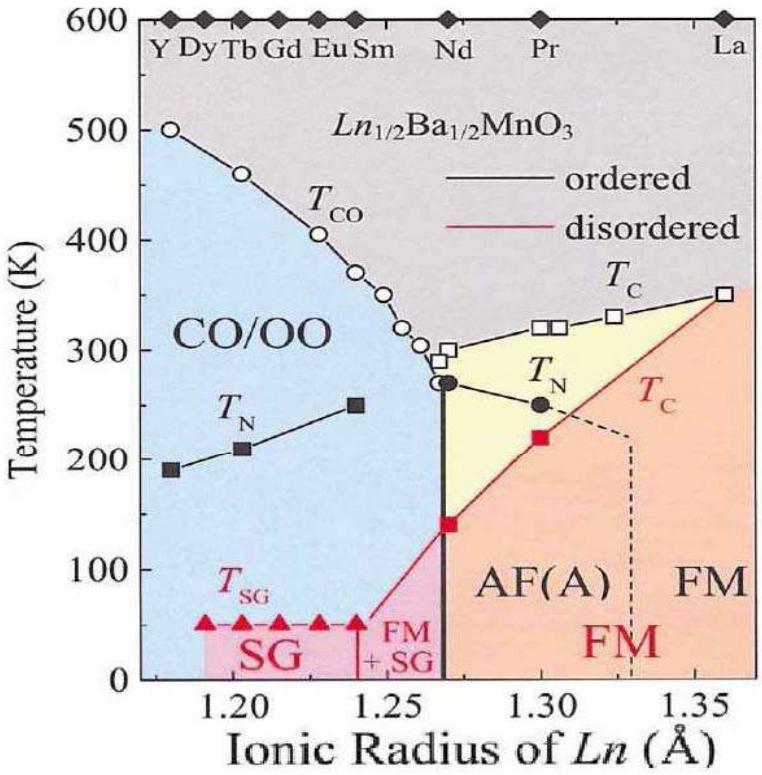


**Figure 1.13:** Electronic phase diagrams for the A-site ordered (black line and symbols) and disordered (red line and symbols and the red shaded region) perovskites at half doping in $Ln_{0.5}Ba_{0.5}MnO_3$, as a function of the ionic radius of Lanthanides. Here CO/OO, FM, and SG stand for the charge/orbital ordered, ferromagnetic, and spin-glass states, respectively.(This figure has been taken from (*D. Akahoshi, et al., Phys. Rev. Lett.* ***90****, 177203 (2003)) [42].*

### 1.1.5 Electronic transport

Manganites being strongly correlated system its magnetic and transport properties are strongly coupled. Generally, in the hole doping range $x \sim 0.2 - 0.3$, the metal to insulator transition takes place which is also associated with the paramagnetic to ferromagnetic ordering. Whereas near the doping $x \sim 0.5$, the system is an insulator at low temperature due to the charge ordering. In the paramagnetic state, the temperature dependence of resistivity in the manganites has been explained by different models. According to Jonker and Van Santen, in $La_{1-x}Sr_xMnO_3$ above

the $T_C$ [28] the resistivity is governed by the activation process

$$\rho(T) \propto exp(\frac{E_0}{k_B T}) \tag{1.6}$$

where $E_0$ is the activation energy. Similar activated behavior in the paramagnetic state has also been observed in other systems [44, 45]. Many authors also believe that the polaron hopping is the main mechanism to determine the resistivity in the paramagnetic region [46–48]. Polarons can be of two type:large or small. The large polaron case corresponds to a situation in which the lattice distortion induced around a charge carrier extend over distances larger than the lattice constant. Whereas for the small polaron case, the lattice distortion extends over a distance comparable with the lattice constant. According to the small polaron hopping (SPH) the resistivity is expressed as

$$\rho(T) = \rho_0 T^n exp(\frac{E_0}{k_B T}) \tag{1.7}$$

where $n \sim 1$ for adiabatic case, when polaron hopping rapidly between two sites without changing the configuration. On the other hand, in the non-adiabatic case $n$ varies from '1' and it is $\sim$ 1.6 for $La_{0.67}Ca_{0.33}MnO_3$ above $T_C$ [49]. Another frequently used model to describe the resistivity in the paramagnetic region is the Mott's Variable range hopping (VRH) model [50]. According to VRH model the resistivity is expressed by the following equation

$$\rho(T) = \rho_0 exp(\frac{T_0}{T})^{\frac{1}{4}} \tag{1.8}$$

where $T_0$ is constant which depends upon the density of states at the Fermi level of the system. Further modification of the VRH model has been done by Viret et al. [51] By considering the localization of the the $e_g$ electrons by the random spin dependent potentials above $T_C$ and $\rho$ being a function of magnetization as well, the

expression of resistivity has been put forwarded by them as

$$\rho(T) = \rho_0 exp[T_0(1-(M/M_s)^2)/T]^{1/4} \tag{1.9}$$

However, for some systems both the small polaron hopping model and VRH model is applicable in the paramagnetic region. Although, the SPH is valid for $T > \theta_D/2$ and VRH is valid for $T < \theta_D/2$, where $\theta_D$ is the Debye temperature [52].

A huge effort has also been paid to explain the electron transport in the ferromagnetic state. Initially, double exchange model proposed by Zener was used to explain the transport properties in the ferromagnetic region. Subsequently, it has been found that electron-electron interaction, electron-phonon interaction also plays a major role in the resistivity. Synder et al. shows that in the ferromagnetic state resistivity can be expressed as [53]

$$\rho(T) = \rho_0 + AT^2 + BT^{4.5} \tag{1.10}$$

Here, $T^{4.5}$ term arises to incorporate the two magnon process [54]. Resistivity in conventional ferromagnetic system for single magnon scattering process varies as $\rho \sim T^2$. Although, according to the double exchange model, single magnon scattering process in the manganites is absent. In spite of this fact the $T^2$ contribution in resistivity is universally observed in the ferromagnetic state of the manganites and has been attributed to the electron-electron interaction. An alternative picture of electronic transport in the ferromagnetic state has also been suggested by the Alexandrov et al. Their model predicts that the polaron is the dominating charge carrier even in the paramagnetic state and transport is dominated by the polaron tunneling mechanism [55] and the temperature dependent resistivity can be expressed as

$$\rho(T) = \rho_0 + E\omega_S/Sinh^2(\hbar/2k_BT) \tag{1.11}$$

where E is a constant, $\omega_S$ is the softest optical mode. The expression gives a $T^2$ contribution to $\rho(T)$ above $T = \hbar/k_B$.

### 1.1.6 Heat capacity

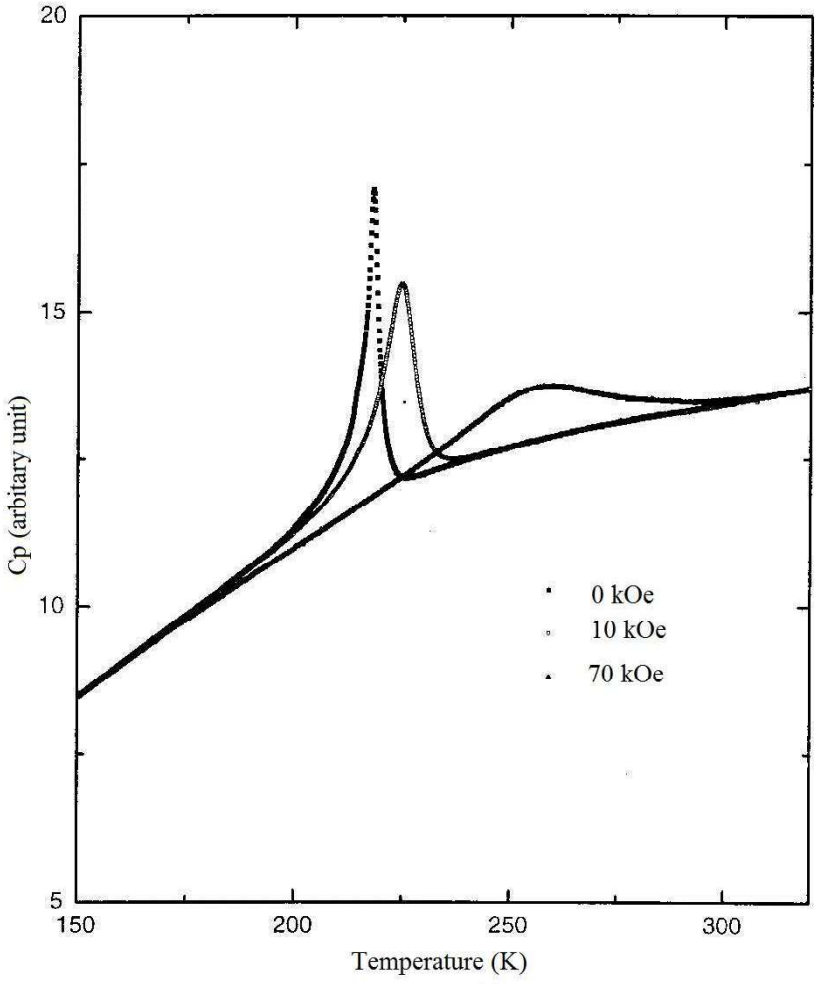


**Figure 1.14:** C vs. T curve for $La_{0.7}Sr_{0.3}MnO_3$ compound in absence and in presence of different magnetic fields (10 kOe and 70 kOe). The sharp peak indicates the paramagnetic to ferromagnetic transition temperature and becomes broad in application of the external magnetic field. (*From Lin et al. J. Appl. Phys.*, ***87***, *5825 (2000) [56].*)

The temperature dependent heat capacity gives valuable information about the different magnetic ordering in the manganites. The ferromagnetic as well as antiferromagnetic ordering is manifested by the observed anomaly in the $C(T)$ data. As a

representative figure, $C(T)$ data of $La_{0.7}Sr_{0.3}MnO_3$ [56] has been presented in Fig. 1.14 which shows a clear signature of the ferromagnetic ordering by a maxima in $C(T)$. The low temperature heat capacity data can be expressed by

$$C(T) = C_e + C_l + C_m \tag{1.12}$$

where $C_e$ is the electronic contribution, $C_l$ is the lattice contribution and $C_m$ is the magnetic contribution to the heat capacity. The temperature dependence of the following terms are

$$C_e = \gamma T \tag{1.13}$$

$$C_l = \beta T^3 + \alpha T^5 \tag{1.14}$$

$$C_m = \begin{cases} \delta T^{3/2} \quad For \quad ferromagnetic \quad system \\ \delta T^2 \quad For \quad antiferromagnetic \quad system \end{cases} \tag{1.15}$$

In some cases hyperfine term ($\sim T^{-2}$) is also included to take into account the hyperfine splitting of the nuclear magnetic levels of Mn and Ln ions [57]. The coefficient of the linear term ($\gamma$) is related to the density of states [$N(E_F)$] at the Fermi level by the following relation

$$N(E_F) = 3\gamma/(\pi k_B)^2 \tag{1.16}$$

Besides this, the Debye temperature ($\theta_D$) can be calculated by determining $\beta$ and using the following expression

$$\theta_D = (\frac{12\pi^4 nR}{5\beta})^{1/3} \tag{1.17}$$

Some manganites exhibit Schottky anomaly in $C(T)$ at the low temperature. The

study of Gordon et al. shows that the presence of Schottky anomaly in $Nd_{0.67}Sr_{0.33}MnO_3$ [58] arises due to the presence of intrinsic magnetic moment of $Nd$. Such anomaly is absent in $Pr_{0.67}Ca_{0.33}MnO_3$ [59]. This direct contradiction can be explained by Kramers theorem [58]. According to this theorem, an ion possessing an odd number of electrons must have a doubly degenerate ground state. This degeneracy leads to thermal depopulation which originates the Schottky anomaly in the Heat capacity. It has also been found that heat capacity at low temperature for antiferromagnetic charge ordered sample ($R_{0.5}Ca_{0.5}MnO_3$) is 100 times larger than that the ferromagnetic system $La_{0.67}Ba_{0.33}MnO_3$ [58]. This high value is due to the increase in the effective mass of the electrons caused by the localization.

### 1.1.7 Magnetocaloric effect

The magnetocaloric effect (MCE) has recently drawn several attentions due to the possible application in magnetic refrigeration technique which is energy efficient as well as environment-friendly and can be the alternative of the conventional gas-compressor based refrigeration [21–24, 60–64]. The magnetocaloric effect (MCE) is defined as the adiabatic temperature change of magnetic materials due to the application of external magnetic field. The adiabatic temperature change ($\Delta T_{ad}$) and the isothermal magnetic entropy change ($\Delta S_M$) are the two parameters which describe the MCE. A remarkable advancement in this field is the discovery of the giant MCE around room temperature in $Gd_2Si_2Ge_2$ by Pecharsky and Gschneidner in 1997 [65] and the reported value of MCE in $Gd_2Si_2Ge_2$ is twice than the well known magnetic refrigerant Gadolinium. A lot of interest have been drawn on finding new efficient magnetic refrigerant materials, which can be applicable in different temperature regions from room temperature or higher to liquid helium temperature. Apart from its technological importance, the study of MCE can provide us various valuable information about the magnetic materials as well.

The magnetic entropy change can be determined by using one of the Maxwell's thermodynamic equations

$$[\frac{\partial S(T,H)}{\partial H}]_T = [\frac{\partial M(T,H)}{\partial T}]_H \tag{1.18}$$

where, S and M are correspondingly the entropy and magnetization of a system at temperature T and magnetic field H.

Integrating the above equation gives the isothermal entropy change ($\Delta S_M$) for the magnetic field change 0 to $H_F$ as

$$\Delta S_M(H,T) = \int_0^{H_F} (\frac{\partial M}{\partial T})_H dH \tag{1.19}$$

The total differential of the total entropy of the system $S(T,H)$ can be written as

$$dS = (\frac{\partial S}{\partial T})_H dT + (\frac{\partial S}{\partial H})_T dH \tag{1.20}$$

Under adiabatic condition the total entropy of the system remains constant (i.e. dS = 0) and the above equation gives

$$dT = [(\frac{\partial S}{\partial H})_T / (\frac{\partial S}{\partial T})_H] dH \tag{1.21}$$

Again, according to the second law of thermodynamics,

$$\frac{C_H(T,H)}{T} = (\frac{\partial S}{\partial T})_H \tag{1.22}$$

where, $C_H(T,H)$ is the heat capacity of the system under constant magnetic field.

Now, integrating equation 1.x with respect to the field and taking into account

equation 1.x, the adiabatic temperature change ($\Delta T_{ad}$) can be obtained as

$$\Delta T_{ad}(T,H) = -\int_0^{H_F} \frac{T}{C_H(T,H)}(\frac{\partial M}{\partial T})_H dH \tag{1.23}$$

If the value of $T/C_H(T,H)$ varies much slower with H than that of $(\frac{\partial M}{\partial T})_H$, which generally occurs near the magnetic phase transition, then the adiabatic temperature change can be calculated as

$$\Delta T_{ad}(T,H) = -(\frac{T}{C_H(T,H)})\Delta S_M(T,H) \tag{1.24}$$

Together with the isothermal magnetic entropy change ($\Delta S_M$) and adiabatic temperature change $\Delta T_{ad}$, another important parameter for magnetic refrigerants is the relative cooling power (RCP). In an ideal refrigeration cycle, the amount of heat transfer between hot and cold end is determined by RCP and it is defined as the twice the area under the $\Delta S_M$ versus T curve.

#### 1.1.7.1 Measurement techniques

The magnetocaloric effect of a material can be measured directly or it can be calculated indirectly from the measured magnetization or heat capacity data. Utilizing direct measurement, one can get only $\Delta T_{ad}$ and the magnetization measurement can provide only $\Delta S_M$, whereas the infield heat capacity measurement can give simultaneously both $\Delta T_{ad}$ and $\Delta S_M$.

***Direct measurement***

In this technique, the change of sample temperature with the application of magnetic field is measured directly. If the sample temperature changes from $T_i$ to $T_f$ due to change of magnetic field $H_i$ to $H_f$, then the measured adiabatic temperature change of the sample is $\Delta T_{ad} = T_f - T_i$. During the direct measurement, a rapid

change of magnetic field is required to maintain the adiabatic condition and it can be performed by using electromagnet or pulse magnets. On the other hand for superconducting magnet the field sweep rate being not too rapid, sample movement is required to provide the varying magnetic field environment. The accuracy in the direct MCE measurement techniques is limited to $5-10\%$ due to the error bars in thermometry, error in setting the field and on the quality of thermal insulation of the sample. In addition this technique can not provide any any information about isothermal entropy change $\Delta S_M$, which is essential for complete characterization of MCE of a given magnetic materials.

***Indirect measurement***

The isothermal magnetic entropy change $\Delta S_M$ can be determined from the magnetic field dependence of magnetization measurement at constant temperatures using equation 1.x. The concept to calculate $\Delta S_M$ from isothermal magnetization measurements has been illustrated in Fig. 1.15(a). Although, the magnetization measurement only gives the value of $\Delta S_M$ but it is possible to calculate $\Delta T_{ad}$ also using the knowledge of zero field heat capacity value by employing equation 1.x.

On the other hand, the magnetocaloric parameters both $\Delta T_{ad}$ and $\Delta S_M$ can be determined from the temperature dependent heat capacity data measured under various constant magnetic fields. The total entropy (S) of a material as a function of temperature is calculated from the temperature dependent heat capacity (C) using the relation

$$S = \int_0^T \frac{C}{T} dT \tag{1.25}$$

From the calculated total entropy as a function of temperature in zero magnetic field $S(T,0)$ and in final magnetic field $S(T,H)$, the isothermal entropy change $\Delta S(T,H)$

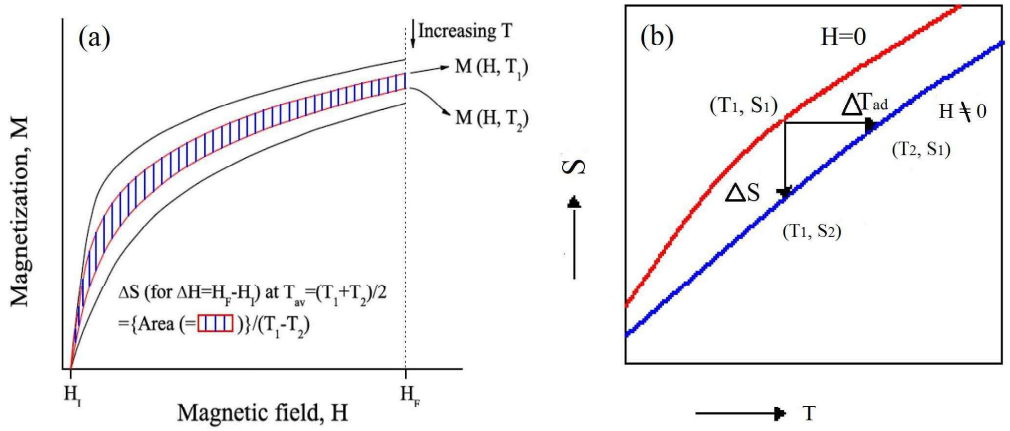


**Figure 1.15:** (a) Typical isothermal magnetization curves of a ferromagnetic material. The area enclosed between two magnetization isotherms $M(H,T_1)$ and $M(H,T_2)$ (shown by patterned line) divided by the temperature difference i.e. $(T_1 - T_2)$ gives the isothermal magnetic entropy change at the average temperature $T_{av} = (T_1 + T_2)/2$ for the magnetic field change $\Delta H = H_F - H_I$. (b) Schematic diagram of total entropy (S) as a function of temperature (T) in absence and in presence of magnetic field. In the figure $\Delta S$ and $\Delta T$ has also been indicated.

can be determined at any temperature as

$$\Delta S(T,H) = S(T,H) - S(T,0) \tag{1.26}$$

and the adiabatic temperature change $\Delta T_{ad}$ is obtained as

$$\Delta T_{ad} = T(S,H) - T(S,0) \tag{1.27}$$

where $T(S,H)$ and $T(S,0)$ are the temperatures in the field H and at zero field at a constant entropy S. The method in determining the $\Delta S(T,H)$ and $\Delta T_{ad}$ from $S(T,H)$ curves has been illustrated in Fig. 1.15(b).

Among the different magnetic refrigerants, the doped perovskite manganites have attracted increasing attentions because of several advantages such as relatively large magnetic entropy change [66,67], tunable $T_C$ [68], chemical stability, low production cost and relatively large resistivity [69] which favors the reduction of loss due to the eddy current heating [70]. The magnetocaloric properties of some selected manganite

compounds are listed in the Table. 6.2.

**Table 1.1:** Comparison the values of $-\Delta S_M(J/kg-K)$ and $RCP(J/kg)$ of some manganites around their ferromagnetic transition temperature $T_C$

| *Sample* | $T_C(K)$ | $\Delta H(kOe)$ | $-\Delta S_M(J/kg-K)$ | $RCP(J/kg)$ | Reference |
|---|---|---|---|---|---|
| $La_{0.8}Ag_{0.2}MnO_3$ | 300 | 10 | 2.40 | 32 | [71] |
| $La_{0.7}Ca_{0.3}MnO_3$ | 256 | 10 | 1.38 | 41 | [72] |
| $La_{0.7}Ba_{0.3}MnO_3$ | 336 | 10 | 1.60 | 36 | [73] |
| $Nd_{0.5}Sr_{0.5}MnO_3$ | 155 | 10 | 2.80 | 17 | [74] |
| $La_{0.8}Ca_{0.2}MnO_3$ | 230 | 15 | 5.5 | 72 | [67] |
| $La_{0.55}Ca_{0.45}MnO_3$ | 238 | 15 | 1.9 | 68 | [67] |
| $La_{0.75}Sr_{0.25}MnO_3$ | 340 | 15 | 1.5 | 65 | [75] |
| $La_{0.87}Sr_{0.13}MnO_3$ | 197 | 50 | 5.8 | 232 | [76] |
| $La_{0.67}Ca_{0.33}MnO_3$ | 257 | 50 | 2.06 | 175 | [77] |
| $La_{0.87}Sr_{0.13}MnO_3$ | 197 | 50 | 5.80 | 232 | [76] |
| $La_{0.84}Sr_{0.16}MnO_3$ | 244 | 50 | 5.85 | 240 | [76] |
| $La_{0.67}Sr_{0.33}MnO_3$ | 348 | 50 | 1.69 | 211 | [77] |
| $La_{0.67}Ba_{0.33}MnO_3$ | 292 | 50 | 1.48 | 161 | [77] |

## 1.2 Plan of the thesis

Among the various phenomena exhibited by the manganites, observation of colossal magnetoresistance and sizeable magnetocaloric response has attracted considerable attentions from fundamental as well as technological perspectives. A significant effort had been paid to study the magnetoresistive properties of manganites, as large magnetoresistive materials are of immense interest for a number of spintronic applications by developing high density magnetic memory devices, magnetic sensors and magnetic switches. An effort had also been paid to investigate the novel routes to achieve huge enhancement of magnetoresistance. With this motivation we have carried out the systematic magnetic and magnetotransport study of charge ordered $Sm_{0.5}(Ca_{0.5-x}Sr_x)MnO_3$ compounds and disordered ferromagnetic $(La_{1-x}Y_x)_{0.7}Ca_{0.3}MnO_3$ compounds. The whole thesis is organised as follows:

• In the Chapter 3, we present the observation of ultra-sharp jump in the isothermal

magnetization in polycrystalline $Sm_{0.5}(Ca_{0.5-x}Sr_x)MnO_3$ ($x = 0, 0.1, 0.2, 0.25, 0.3, 0.5$) compounds. These jumps are also seen in the resistivity data. The critical field ($H_{Cr}$), required for the ultra-sharp jump in magnetization, decreases with increase of 'Sr' concentration or in other words with increase of A-site ionic radius $\langle r_A \rangle$. The dependence of $H_{Cr}$ with magnetic field sweep rate has also been observed from the comparison of the observed jump in isothermal resistivity and magnetization. The magnetotransport data indicates the increase phase separation with increase of $\langle r_A \rangle$. The presence of exchange bias at low temperature also signifies the presence of inhomogeneous phase separated states. The study reveals that, AFM to FM transition is of martensitic like and is at the origin of the magnetization jump. A phenomenological picture has also been presented here to understand the decrease of $H_{Cr}$.

As we know that, large magnetoresistive materials are of interest for a number of spintronic applications by developing high density magnetic memory devices, magnetic sensors and magnetic switches. Colossal magnetoresistance, for which resistivity changes several order of magnitude ($\sim 10^4\%$) in an external magnetic field, occurs mainly in phase separated oxide materials, namely manganites, due to the phase competition between the ferromagnetic metallic and the antiferromagnetic insulating regions. Can one further enhance the magnetoresistance by tuning the volume fraction of the two phases? In this chapter, we also report an extreme colossal magnetoresistance along with the ultra-sharp metamagnetic transition in half doped $Sm_{0.5}Ca_{0.25}Sr_{0.25}MnO_3$ manganite compound by suitably tuning the volume fraction of the competing phases. The obtained magnetoresistance value is as large as $\sim 10^{15}\%$ at 10 K in 90 kOe external magnetic field and is several orders of magnitude higher than any other observed magnetoresistance value reported so far. Our model Hamiltonian calculations show that the inhomogeneous disorder, deduced from tunneling electron microscopy, suppresses the CE-type phase and seeds the ferromagnetic metal in an external magnetic field.

• In the Chapter 4, we present the extraordinarily large magnetoresistance (MR) in $La_{0.7}Ca_{0.3}MnO_3$ compound by optimal substitution. To explore the origin of that giant enhancement of MR, we have carried out magnetic and magnetotransport measurements of $(La_{1-x}Y_x)_{0.7}Ca_{0.3}MnO_3$ $(x = 0, 0.4, 0.5, 0.6, 1)$ compounds in detail. Our analysis indicates that the disorder introduced by yttrium substitution plays the crucial role in magnetoresistive properties in this series. Large MR has been observed in the optimally doped $(La_{0.5}Y_{0.5})_{0.7}Ca_{0.3}MnO_3$ $(x = 0.5)$ compound. In this compound, the MR value as high as $1.5 \times 10^7\%$ at 50 K temperature and $3.6 \times 10^4\%$ at 80 K temperature has been achieved for 90 kOe external magnetic field. Moreover at 80 K for $x = 0.5$ compound the MR is reversible in nature. The extraordinarily enhanced large MR value has been described by a phenomenological model of percolation via ferromagnetic clusters.

Detail analysis of the temperature dependent dc susceptibility data shows the modification from the Griffiths (GP) like phase to non-Griffiths (non-GP) like phase in $(La_{1-x}Y_x)_{0.7}Ca_{0.3}MnO_3$ $(x = 0, 0.3, 0.4, 0.5, 0.6)$ compounds with $x$. The existence of non-Griffiths phase is revealed from the upward deviation of the inverse susceptibility $(\chi)$ versus temperature plot from the curie weiss behavior for the compounds with $x \geq 0.5$. Whereas Griffiths phase is identified from the downturn of $1/\chi$ versus T plot from the Curie weiss line in the compounds with $x = 0.3, 0.4$. The increased lattice distortion (with $x$) decreases the $M - O - Mn$ bond angle and at the same time increase the electron phonon coupling which in turn decreases the ferromagnetic double exchange (DE) interactions and enhances the effective short range antiferromagnetic superexchange interactions between $Mn^{3+}/Mn^{3+}$ and $Mn^{4+}/Mn^{4+}$ ions above the curie temperature $(T_C)$. The enhancement of this short range antiferromagnetic (SR-AFM) interactions has been attributed to the conversions from GP to non-GP phase. The increased SR-AFM interactions with Y doping has also been substantiate from the magnetocaloric study.

We have also seen the modification of the insulator state to metallic state with reduction of particle size in $(La_{0.5}Y_{0.5})_{0.7}Ca_{0.3}MnO_3$ compound by magnetotransport measurements. The decrease in the activation energy as well as increase in the effective density of states near fermi level is observed with particle size reduction. This modification leads to the decrease in the resistivity in the nanoparticle in the low temperature regime ($T < 150K$). On the other hand, the temperature dependent dc susceptibility data shows the evolution of the non-Griffiths phase to Griffths phase with reduction of particle size in the temperature range $100K < T \leq 200K$. This evolution from non-Griffiths phase to Griffths phase leads to the formation of large ferromagnetic clusters in expense of antiferromagnetic interactions which is responsible for the non-Griffiths phase. The presence of the large ferromagnetic clusters helps to create percolation path for electronic transport and is the probable reason for the enhancement of magnetoresistance in this temperature range. On the otherhand, enhancement of low field magnetoresistance (LFMR) observed below 100 K has been attributed to the increased spin polarized tunneling (SPT) component due to the increase in size of the ferromagnetic clusters in the nanoparticle compare with that of bulk.

• In the Chapter 5, the particle size driven modification of the non-Griffiths phase to Griffiths phase in $(La_{0.4}Y_{0.6})_{0.7}Ca_{0.3}MnO_3$ (LYCMO) compound have been presented. In the nanocrystal, the decreased lattice distortions together with the quenched disorder arising from the ionic size mismatch of the different A-site ions are the possible reason for the occurrence of Griffiths phase. On the other hand, though in the bulk compound quenched disorder is present but the higher distortions enhances the effective antiferromagneic superexchange interactions and may be the probable reason for the non-Griffiths phase which is identified by the upturn of the inverse susceptibility versus temperature plot from the Curie-Weiss line. An enhancement of Colossal magnetoresistance (CMR) in the minimal surface disorder nanoparticle ($\sim 120nm$) has been observed. The study shows that for LYCMO com-

pound, the enhancement of CMR in 120 nm nanoparticle is due to the conversion from non-Griffiths phase to Griffiths phase.

On the other hand, the study of magnetocaloric effect (MCE) is another promising field of research due to its environment friendly energy efficient magnetic cooling technology. A lot of studies has been carried out to find out new efficient refrigerant materials applicable in different temperature regimes. Besides the technological importance of MCE, it is also important from fundamental aspects. With this motivation we have investigated the MCE properties of some manganite compounds which are described below.

• In the Chapter 6, we explore the influence of A-site ionic disorder ($\sigma^2$) on magnetocaloric properties in relatively larger bandwidth manganite systems like, well known $La_{0.7}Sr_{0.3}MnO_3$ compound. For the study, three isoelectronic manganites with same A-site ionic radius ($\langle r_A \rangle$ =1.24$\mathring{A}$) i.e. $La_{0.7}Sr_{0.3}MnO_3(\sigma^2 = 1.85 \times 10^{-3})$, $Pr_{0.7}Sr_{0.14}Ba_{0.16}MnO_3(\sigma^2 = 1.17 \times 10^{-2})$ and $Nd_{0.7}Sr_{0.07}Ba_{0.23}MnO_3(\sigma^2 = 1.66 \times 10^{-2})$ samples have been prepared. Magnetic measurements reveal that, upon increasing $\sigma^2$ from $1.85 \times 10^{-3}$ to $1.66 \times 10^{-2}$, ferromagnetic double exchange interaction diminishes and as a result, ferromagnetic ordering temperature ($T_C$) decreases from 360 K to 100 K. Accordingly, the magnetic entropy change ($-\Delta S_M$) has also been found to decrease from 4.6 J/kg-K to 4.1 J/kg-K on the application of 70 kOe magnetic field. However, for $\sigma^2$ =$1.66 \times 10^{-2}$, the value of $-\Delta S_M = 5.7 J/kg$ is relatively larger compared to the other two values of $-\Delta S_M$. Additionally, increased $\sigma^2$ ($1.85 \times 10^{-3}$ to $1.66 \times 10^{-2}$) broadens the peak of $-\Delta S_M$ which results in the increase in relative cooling power (RCP) from 80 J/kg to 121 J/kg on application of 20 kOe magnetic field. Critical analysis has been performed to explain the enhancement in RCP with $\sigma^2$ and the anomaly in $-\Delta S_M$ for $Pr_{0.7}Sr_{0.14}Ba_{0.16}MnO_3(\sigma^2 = 1.17 \times 10^{-2})$ compound.

We have also described the effect of the phase boundary of ferromagnetic metallic

and ferromagnetic insulator state (FMM-FMI) on magnetotransport and magnetocaloric properties in the $Pr_{0.775}Sr_{0.225}MnO_3$ compound has been described in this study. An enhancement of magnetoresistance (MR) has been observed in the $Pr_{0.775}Sr_{0.225}MnO_3$ compound compared to the compounds, reside on both sides of the phase boundary (i.e. FMI and FMM phases for Sr doping 0.2 and 0.3 respectively in $Pr_{1-x}Sr_xMnO_3$). Moreover, a large relative cooling power (RCP), an important parameter for utilization of magnetocaloric materials, has also been achieved in this compound. The large value of RCP has been attributed to the formation of ferromagnetic clusters, formed above the ferromagnetic ordering temperature ($T > T_C$). On the other hand, enhancement of MR is achieved because of the suppression of enhanced phase fluctuations, arises due to the closeness of FMM-FMI phases.

# CHAPTER 2

# Methodology

## 2.1 Introduction

In this chapter, the methods used to carry out this thesis work has been described. The nanocrystalline and most of the bulk samples were prepared by the well known sol-gel method. To prepare some bulk samples, solid state reaction route was used. The prepared samples were characterized by x-ray diffraction and electron microscopy. Electronic transport and magnetotransport measurements were performed by four probe method in longitudinal geometry by utilizing variable temperature cryostat and magnet systems (Cryogenic). For heat capacity and ac susceptibility measurements physical property measurements system was utilized. The magnetization measurements were performed by employing VSM-SQUID of quantum design. To explain some of the experimental results, model hamiltonian calculations has been performed.

## 2.2 Sample preparation

### 2.2.1 Sol-gel method

The polycrystalline bulk and nanoparticles of the perovskite manganites has been prepared by the sol-gel method. This is a liquid state reaction route which ensures a better mixture of the starting ingredients. Initially, all the ingredients were converted to their respective nitrates by using concentrated nitric acid and millipore water. After preparing the clear solution of the individual elements, all solutions were mixed up and stirred continuously with a magnetic stirrer. Then citric acid was added to the mixture to convert into citrates of the metal ions present in the mixture. The amount of citric acid was sufficiently high such that all the metal ions can get convert into their citrates form. This enables us to obtain a mixture which is homogeneous on the atomic level.

The solution was the heated at 80-90$^0C$ to slowly evaporate the water until gel is formed. Then gel was decomposed at 250$^0C$ and it gives black porous powder. This powder was ground and pelletized and subsequently heated at different temperature for different span of time to obtain sample of different particle sizes. Since the mixture of the ingredients are nearly homogeneous at the atomic scale in the gel, the samples forms at relatively lower temperature compared to other routes to synthesize the manganite compounds. To get the nanocrystalline samples, annealing of the samples were carried out at 700-1000$^0C$ for 3-6 hours depending on the compositions of the samples. However to prepare bulk samples, annealing temperature was maintained at 1300$^0C$ for longer period of heat treatment (24-36 hours). The samples $Sm_{0.5}(Ca_{0.5-x}Sr_x)MnO_3$, $(La_{1-x}Y_x)_{0.7}Ca_{0.3}MnO_3$ were prepared in this method.

### 2.2.2 Solid state reaction

This is most frequently used method in the solid state synthesis. In this method, diffusion of the constituent ions take place across the solid interfaces of the ingredients. For this reason, reaction occurs at slow rate and it needs typically from few days to few weeks time with heat treatment at high temperatures. In this method, the ingredients of high purity were mixed in stoichiometric ration and ground together and after that calcined at $900^0C$ for 12 hours to start the calcination of the constituents. The temperature was increased to the final reaction temperature with heating at several intermittent temperatures. Since the reaction occurs in the solid state, with proceeding the reaction the diffusion path becomes longer due to the diffusion of the constituents through the product phase and it reduces the reaction rate. Therefore, several intermediate grindings in between heat treatments were performed. After calcination of all the constituents, final heat treatment of the sample was performed in pellet form at the highest possible temperature without the changing the composition. In this method, polycrystalline $Sm_{0.5}Ca_{0.5}Mn_{0-y}M_yO_3$ $(M = Fe, Co, Cr, Gaetc)$ samples were prepared.

## 2.3 Characterizations

### 2.3.1 X-ray diffraction

The crystallographic phase purity of all the samples were characterized by powder x-ray diffraction technique using Rigaku-TTRAX-III diffractometer with $Cu - K\alpha$ radiations. In this technique, a beam of x-rays is bombarded on the specimen from various angles. The x-rays are scattered elastically from the electron clouds of the atoms in the specimen and yields a diffraction pattern due to the periodic arrangement of the atoms in the space. According to the Bragg's law of diffraction

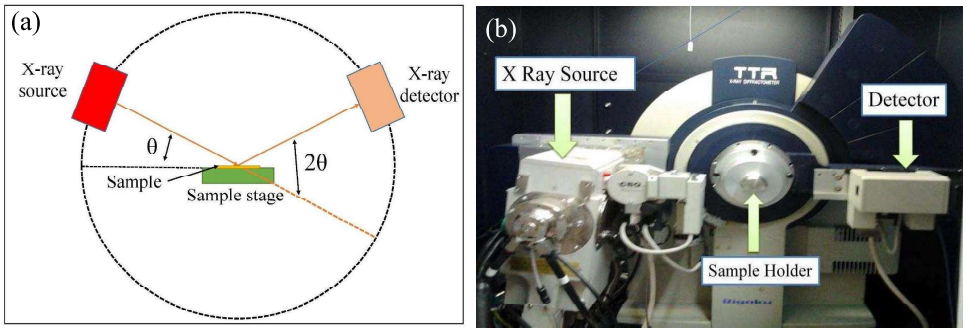


**Figure 2.1:** Figure represents (a) schematic diagram of x-ray diffraction for powder sample, (b) Rigaku-TTRAX-III diffractometer.

$$2d_{hkl}Sin\theta = n\lambda \tag{2.1}$$

Where $\theta$ is the Bragg angle, $d_{hkl}$ is the distance between two parallel planes for a given $(hkl)$ and $\lambda$ is the wavelength of the $Cu - K\alpha$ radiations. By varying the angle of incidence, a diffraction pattern is obtained which is the characteristic of the sample. In most cases scanning speed has been maintained at $4^0/min$. The Rietveld profile fitting of the x-ray diffraction (XRD) gives the crystallographic lattice parameters of the samples. From the XRD data, the nanoparticle's size can also be determined using the Scherrer's formulae [79]

$$d = K\lambda/\beta Cos\theta \tag{2.2}$$

where $K \sim 0.9$, $\lambda$ is the wavelength of the $Cu - K\alpha$ radiation (1.54 Å) and $\beta$ is the full width at half maxima (FWHM) of a diffraction peak corresponding to the diffraction angle $\theta$. For nanoparticles this FWHM is masked with the instrumental broadening. To take into account the instrumental broadening $\beta$ is replaced by the relation [80]

$$\beta = B - b^2/B \tag{2.3}$$

where 'B' and 'b' are the FWHM's of a peak of the nanocrystalline and its corresponding bulk counter part at a particular diffraction angle measured in the same

instrument.

### 2.3.2 Scanning electron microscopy

The scanning electron microscopy is an essential characterization tool to extract valuable information about the chemical composition, crystal structure as well as external morphology of the materials. A schematic diagram of SEM along with its essential components has been shown in Fig. 2.2.

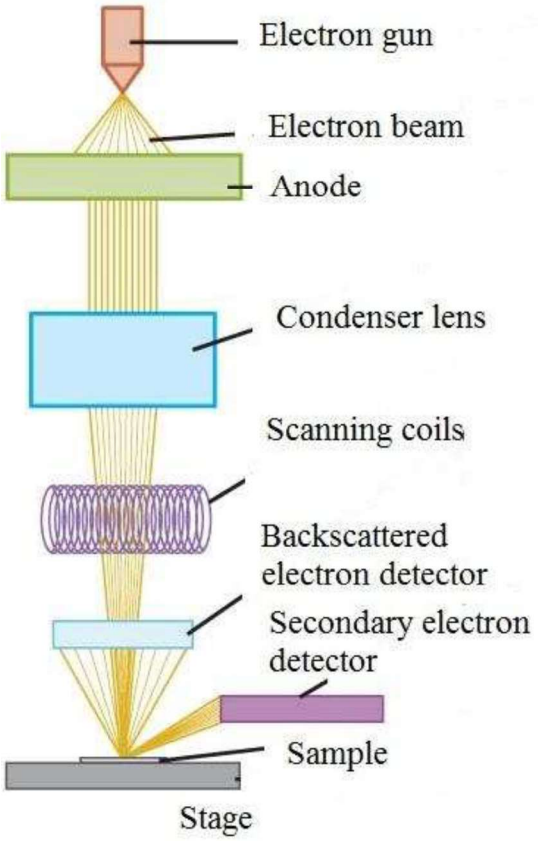


**Figure 2.2:** A schematic diagram of Scanning Electron Microscopy

In SEM, a beam of electrons are generated in vacuum from a field emission gun which accelerates the electrons to energy range $0.1 - 30$ keV. This electron beam is collimated by the electromagnetic condenser lenses and then focused by an objective lens. Subsequently, the beam scan the surface of the sample using electromagnetic deflection coil. When electron beam hit the sample, the energy is dissipated as a

variety of signals produced by electron-sample interaction. These signals includes x-rays, backscattered electrons, diffracted backscattered electrons and secondary electrons. Secondary electrons are used for imaging purpose, backscattered electrons gives the contrast in composition, diffracted backscattered electrons gives the crystal structure and x-rays is used for chemical analysis of the sample. In case of insulator material to avoid any charge pile up on the sample surface, a conducting coating of thin layer of gold is made by glow discharge sputtering. For imaging, detection of secondary electrons is carried out which after amplification gives a three dimensional micrograph of the samples.

In this study, model INSPECT F50 of FEI has been used to examine the morphology of the samples.

### 2.3.3 Transmission electron microscopy

Transmission electron microscopy (TEM) is an another versatile and indispensable material characterization tool due to its high spatial resolution. Although, TEM system is comprised with a set of electromagnetic lens like SEM but there are the following differences:

- SEM is based on scattered electrons but TEM is based on transmission electrons
- Resolution of TEM is higher than SEM
- SEM provides 3-dimensional images, whereas TEM provides 2-dimensional images of the materials
- Large amount of samples can be analyzed in SEM at a time, whereas in TEM only very small amount of samples can be analyzed at at time

A schematic block diagram of TEM has been shown in Fig. 2.3. Here a beam of monochromatic electrons, produced by the electron gun, is focused by the electro-

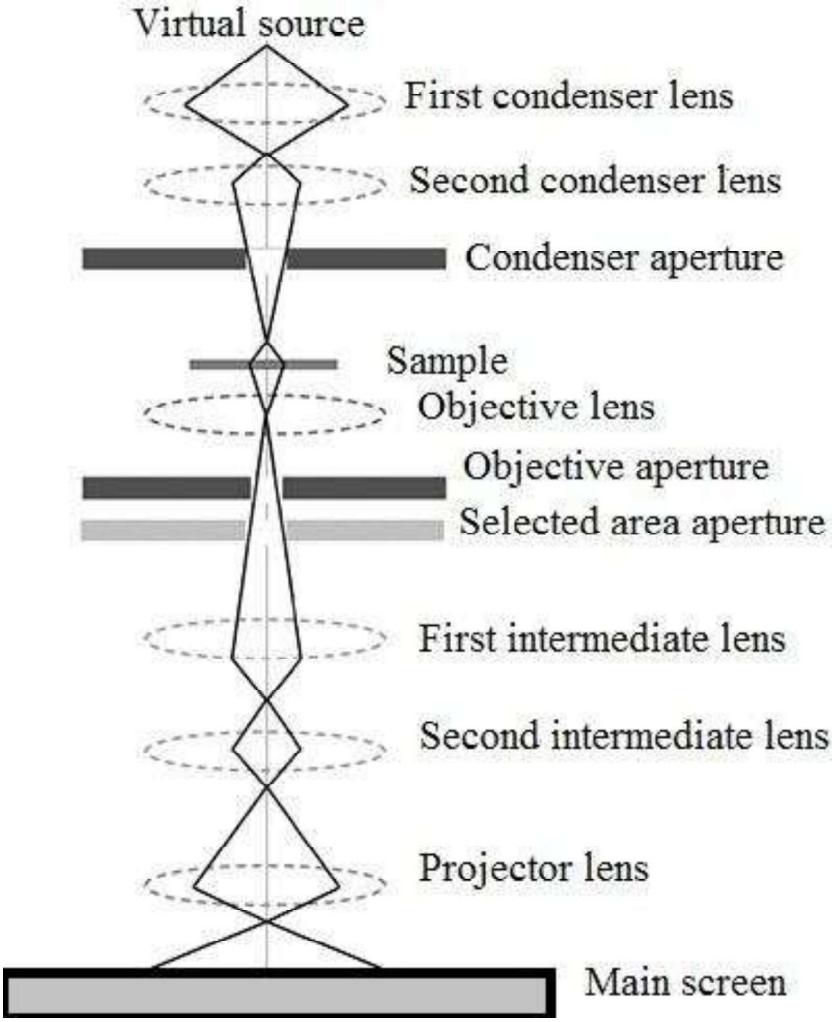


**Figure 2.3:** A schematic diagram of Transmission Electron Microscope.

magnetic condenser lens on the sample and transmit partially after interaction with the specimen. The image is formed by focusing the transmitted beam through the objective lens. There are two mode of operation in TEM, namely diffraction mode and imaging mode. The backfocal plane of the objective lens contains both diffraction pattern and image. Using intermediate and projector lens one can focused the transmitted beam on either image plane for imaging or in the back focal plane for producing diffraction pattern (schematic is shown in Fig. 2.4). To obtain contrast in image, an objective aperture is introduced in the back focal plane and depending upon the positioning of the aperture one can have dark field (DF) image or bright field (BF) image. In the dark field image the direct beam is blocked by the aperture

whereas in the bright field image direct beam pass through the aperture. Schematics of DF and BF images has been presented in Fig. 2.5. As opposed to conventional microscopy, high resolution transmission electron microscopy (HRTEM) does not use amplitude for image formation, instead it arises due to the interference of the electron's wave.

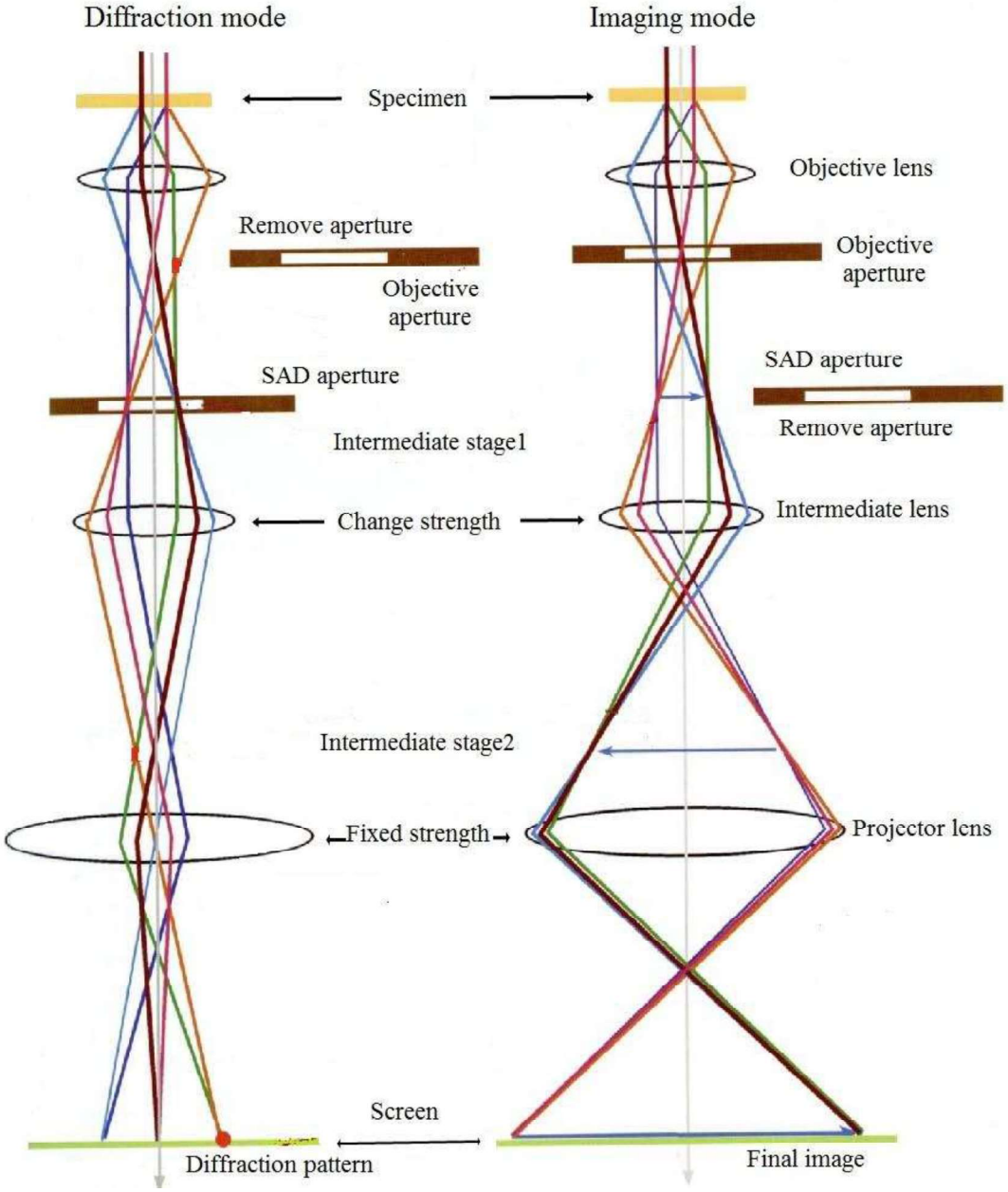


**Figure 2.4:** Different imaging mode in Transmission Electron Microscopy.

In our study, high resolution TEM of FEI, TECNAI $G^2$ $F30$, S-TWIN microscope operating at 300 kV equipped with a GATAN Oricus CCD camera has been used.

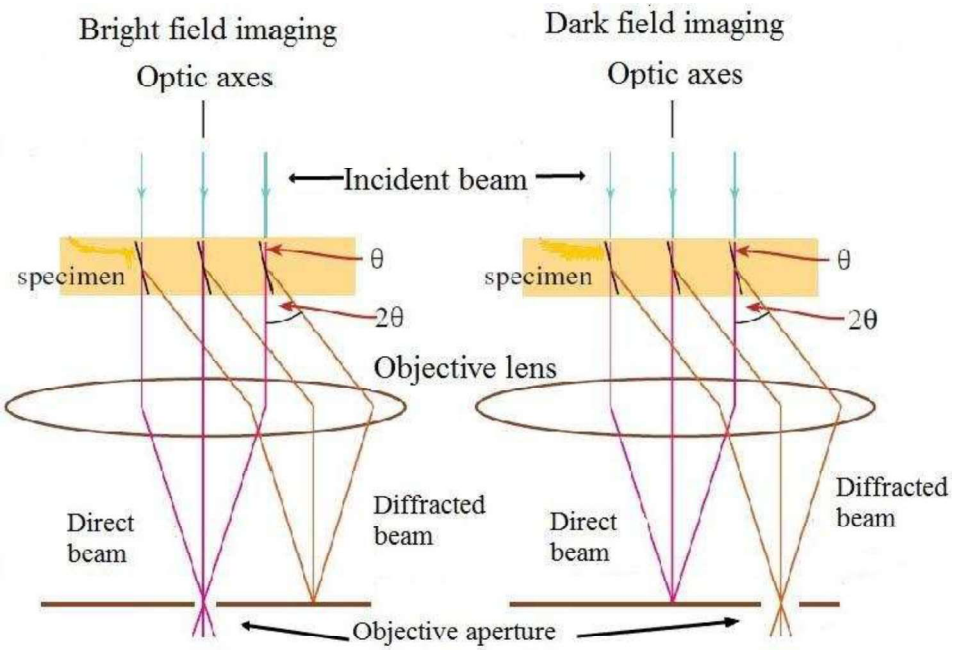


**Figure 2.5:** Schematic diagram of Dark Field (DF) and Bright Field (BF) imaging.

High angle annular dark field scanning transmission electron microscopy (STEM-HAADF) measurement has been done using the same microscope equipped with a scanning unit and HAADF detector.

### 2.3.4 Energy dispersive analysis of x-rays

In order to study the elemental composition in $Sm_{0.5}Ca_{0.25}Sr_{0.25}MnO_3$ compound, energy dispersive x-ray spectroscopy (EDS) has been performed using an attachment with the high resolution TEM of FEI, TECNAI $G^2$ $F30$, S-TWIN microscope. The measurements has been performed on large as well as small areas in order to acquire global composition and the compositions at the small regions in various parts of the sample. The compositions obtained in the measurement has been found as expected according to the chemical compositions within an error bar of about 1%.

## 2.4 Measurements

### 2.4.1 Electronic transport and magnetotransport measurement

Electronic transport and magnetotransport measurements has been carried out in a home made set up using cryogenic magnet and variable temperature cryostat. The working temperature in the system can vary from 1.7 K to 320 K and magnetic field can reach up to 9 T. The measurements has been performed on bar shaped samples by four probe method.

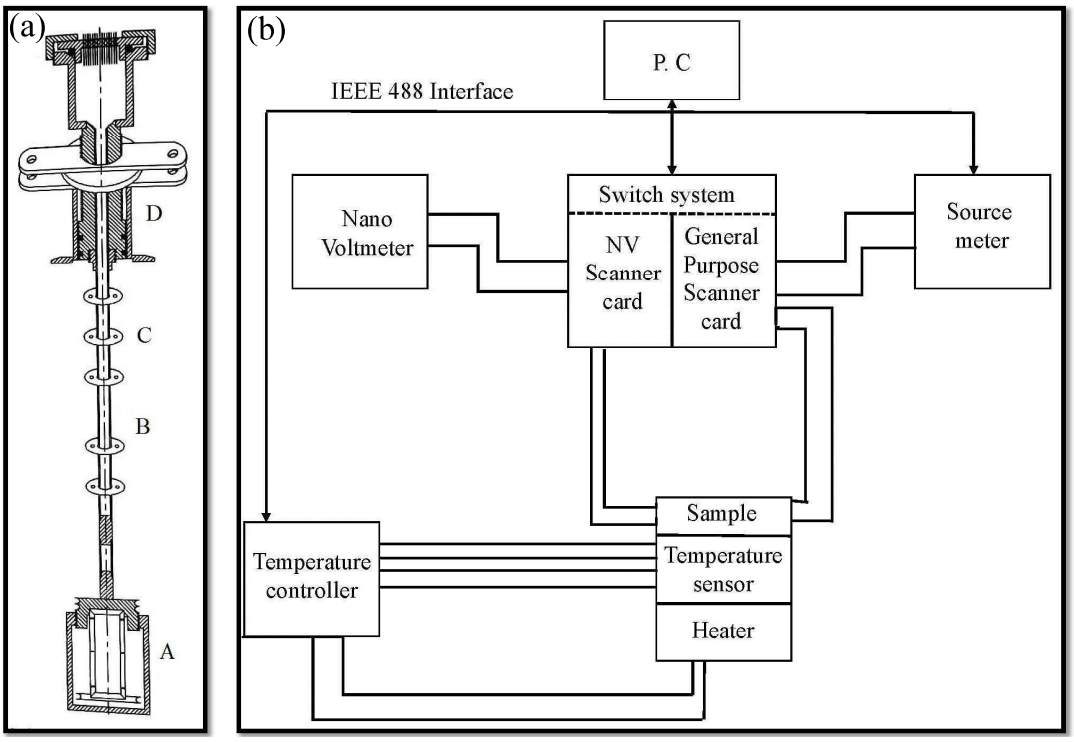


**Figure 2.6:** Figure represents (a)schematic diagram of the insert for the electrical transport measurements, (b) block diagram of the experimental set-up for the transport measurements.

The schematic diagram of the insert used for the measurements is shown in Fig. 2.6(a). The square shaped sample holder is made of oxygen free high purity copper (OFHC). The samples were mounted on the face of the holder with the help of

GE-varnish to make proper electrical isolation from the copper sample holder. The temperature of the holder was measured by calibrated cernox sensor placed at the fourth face of the holder. To uniform heat the sample holder, a pair wise twisted manganin wire was wounded at the both ends of the sample holder. A stainless steel rod is connected with the sample holder and in the rod at uniform distances some copper baffles are brazed which are acting as the radiation shield. Copper wire of SWG44 were used for electrical connection between the samples and sensor to the end of the insert. Voltage and current leads were separately pair wise twisted.

The electrical connections between various electrical instruments and the insert have been shown schematically in Fig. 2.6(b).

### 2.4.2 Magnetization measurement

A commercial Superconducting Quantum Interference Device Vibrating Sample Magnetometer (SQUID-VSM) was employed for the temperature and magnetic field dependence of the magnetization related to this thesis work. It can operate in the temperature range from 1.8 K to 380 K with a maximum magnetic field of $\pm$ 7 T. The magnetometer consists of several superconducting components such as a superconducting magnet, a superconducting detection coil, a SQUID connected to the detection coil and a superconducting magnetic shield surrounding the SQUID. A schematic block diagram of a SQUID-VSM magnetometer has been shown in Fig. 2.8.

A SQUID device in essence consists of two superconductors separated by thin insulating layers to form two parallel Josephson junction. It can resolve change of magnetic field $\sim 10^{-15}T$. It is basically a flux to voltage converter. There is a voltage drop across the Josephson junction when there is a coupling of external magnetic flux with SQUID. As the external flux increases or decreases, the voltage changes

**Figure 2.7:** Electrical and magnetotransport measurement system.

in a periodic manner with the period of the flux quantum $\Phi_0$. Fig. 2.9 shows the change in voltage due to the magnetic flux change which is coupled with the SQUID loop. By measuring this voltage, magnetization of the sample can be determined. Although SQUID is a very sensitive device for measuring magnetic field, but it can not detect magnetization of the sample directly. In a SQUID magnetometer, sample

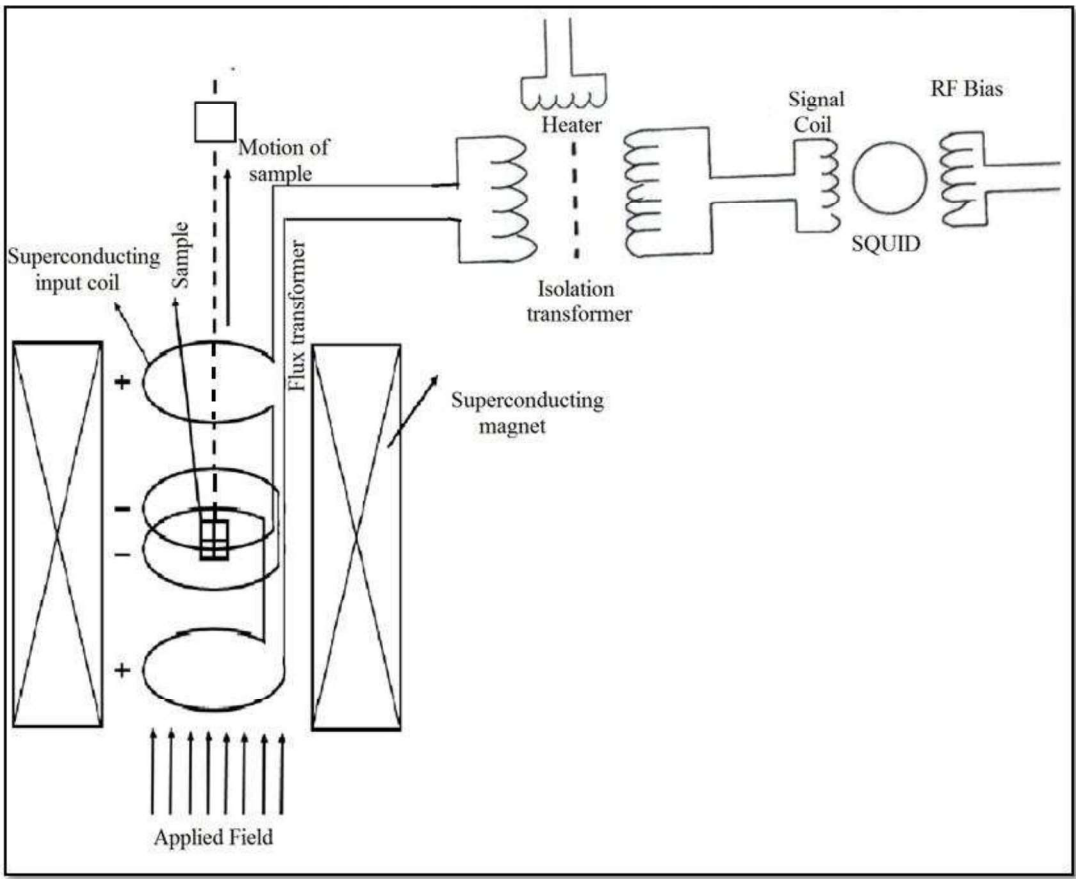


**Figure 2.8:** Schematic diagram of SQUID-VSM magnetometer

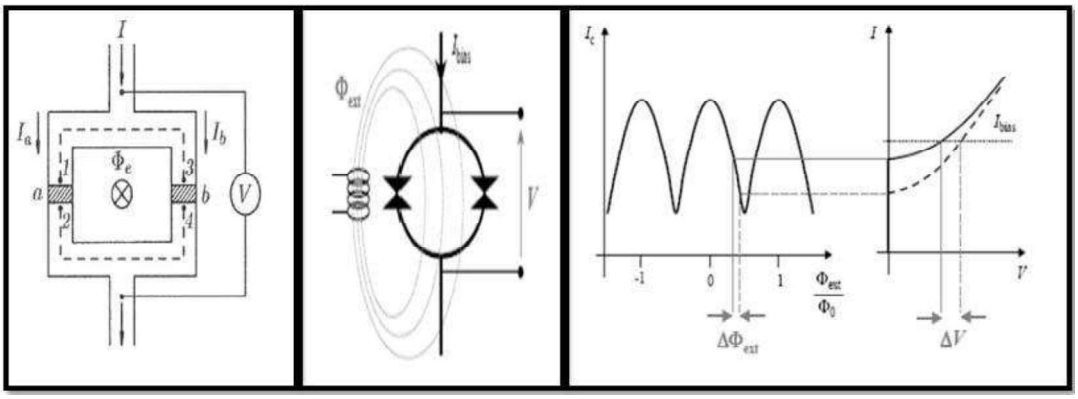

**Figure 2.9:** Schematic of the magnetic signal detection technique in SQUID.

is allowed to move through the superconducting detection coils placed at the center of the magnet. As the sample moves through the coils, the magnetic moment of the sample induces an electric field in the coils which in turn produces a change in the persistent current in the detection circuit. This change in current is proportional to the change in the magnetic flux. The variation of the current in the detection

coils results in the variation in the output voltage in the SQUID, which in turn is proportional to the magnetic moment of the sample.

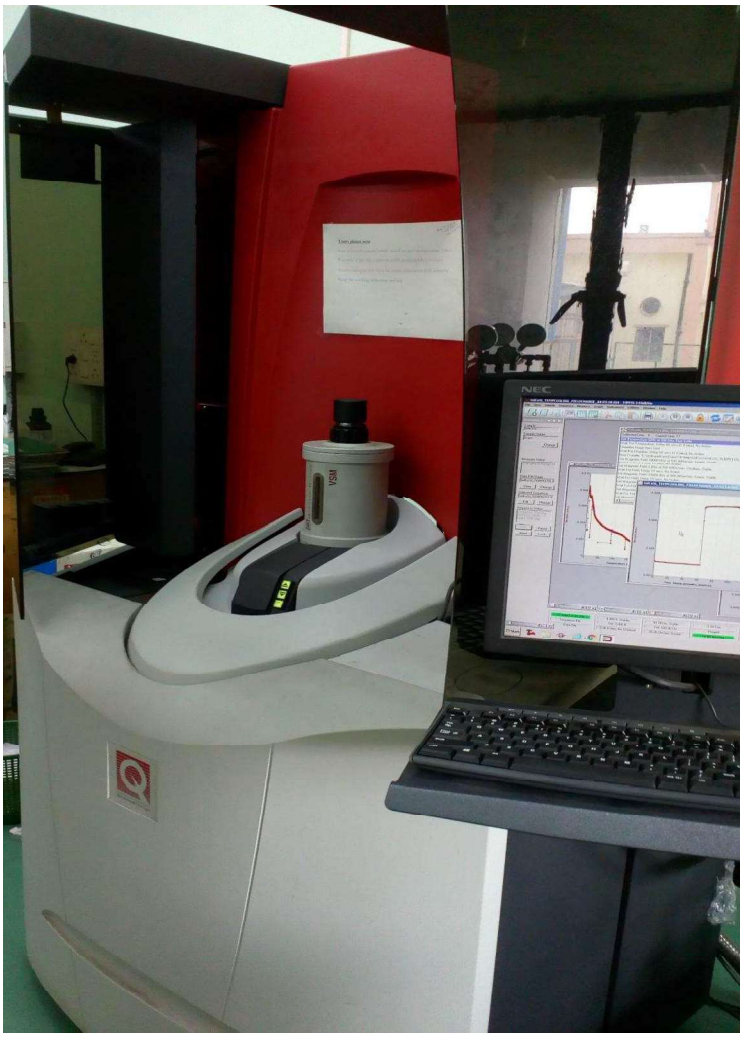

**Figure 2.10:** Image of a SQUID-VSM magnetometer (Quantum Design).

In the SQUID-VSM system, the VSM linear motor system vibrates the sample at frequency $\omega$ about the centre of the detection coils where the signal is picked up as a function of sample position z. It produces a SQUID signal V as a function of time t:

$$V(t) = AB^2Sin^2(\omega t) \tag{2.4}$$

as $V(z) = Az^2$ for small vibration amplitudes and $z(t) = BSin(\omega t)$. Here A is the scaling factor relating to the magnetic moment of the sample and B is the amplitude of the sample vibration. Since $Sin^2(\omega t) = 1/2[1-Cos(2\omega t)]$, the technique of a lock-

in amplifier is applied to isolate and quantify the signal occurring at frequency $2\omega$ and it is achieved by using a phase corrected reference signal at $2\omega$. The detection coils are configured as a second order gradiometer to reduce noise in the detection circuit due to the fluctuations in the large magnetic field. This configuration can also minimize the background drift in the detection system due to the relaxation in the magnetic field of the superconducting magnet. Because of high sensitivity of SQUID, the sensor is shielded properly from the fluctuations of the ambient magnetic field as well as from the magnetic field produced by the superconducting magnet. The picture of SQUID-VSM magnetometer used for the magnetization study has been shown in Fig. 2.10.

### 2.4.3 Heat capacity measurement

The heat capacity measurements of some compounds related with the thesis work has been performed by utilizing commercially available physical property measurement system (PPMS) of Quantum Design. A schematic diagram of the attachment of the heat capacity has been shown in Fig. 2.11. The system measures the heat capacity at constant pressure

$$C_P = (dQ/dT)_P \tag{2.5}$$

To measure the heat capacity, a known amount of heat pulse is applied for a fixed duration of time to heat the sample and is followed by cooling of same duration. For applying the heat energy, a platform heater is attached at the bottom of the sample platform where a thermometer is also attached to note the temperature change. A small flat sample piece is mounted on the platform by using epiezon grease for making the good thermal contact with the platform. To calculate the heat capacity, relaxation technique is used where the entire temperature response data is fitted

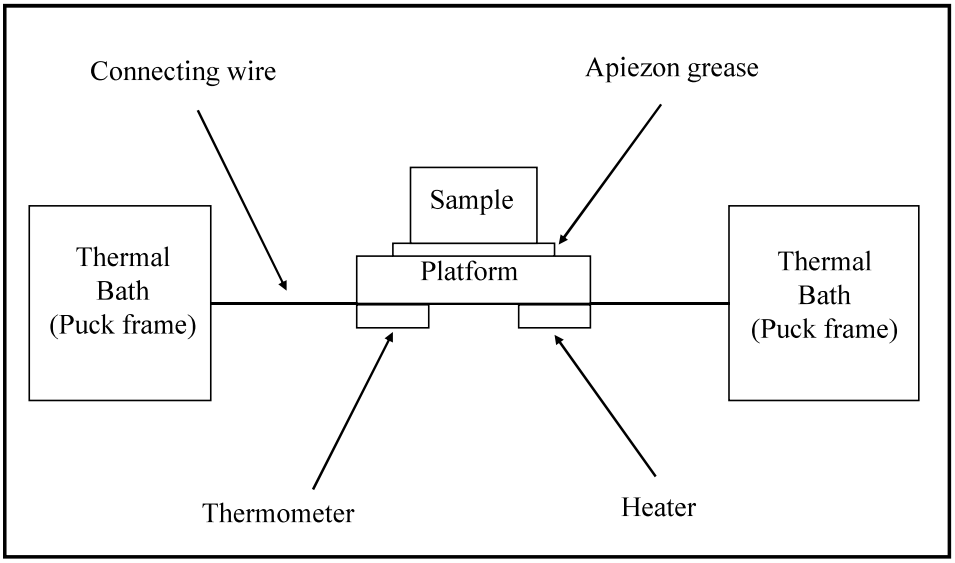


**Figure 2.11:** Thermal connections to the sample and sample platform in the Heat capacity option of Physical property measurement system (PPMS).

**Figure 2.12:** Physical property measurement system (PPMS) (Quantum Design).

with the model. Generally two models are used to calculate the heat capacity of the sample.

### (i) Simple model

This model estimates the total heat capacity of the sample and the platform when the sample is in good thermal contact with the platform. According to this model,

variation of temperature T of the platform with time t is given by

$$C_{total}\frac{dT}{dt} = -K_w(T - T_b) + P(t) \tag{2.6}$$

where $C_{total}$ is the total heat capacity of the sample and the platform, $K_w$ is the thermal conductance of the supporting wires, $T_b$ is the temperature of the thermal bath and $P(t)$ is the power supplied by the heater which is equal to $P_0$ during heating and zero during cooling. The solution of this equation is an exponential function with characteristic time constant $C_{total}/K_w$.

**(ii) Two-tau model**

In the case of poor thermal contact between sample and the platform an another sophisticated two-tau model is used to measure the heat capacity of the sample. Here temperature difference between sample and the platform is taken into account. According to this model

$$C_p\frac{dT_p}{dt} = P(t) - K_w[T_p(t) - T_b] + K_g[T_s(t) - T_p(t)] \tag{2.7}$$

$$C_s\frac{dT_s}{dt} = -K_g[T_s(t) - T_p(t)] \tag{2.8}$$

where $C_p$ and $C_s$ are the heat capacity of the platform and the sample respectively. $K_g$ is the thermal conductance of the grease and $T_p(t)$ and $T_s(t)$ are the temperature of the platform and the sample respectively. By fitting the recorded platform temperature with the two-tau model two time constants are extracted as below:

$$\tau_1 = \frac{1}{\alpha + \beta}; \quad \tau_2 = \frac{1}{\alpha - \beta}, \tag{2.9}$$

$$\alpha = \frac{K_w}{2C_p} + \frac{K_g}{2C_p} + \frac{K_g}{2C_s}, \tag{2.10}$$

$$\beta = \frac{\sqrt{(K_g C_s)^2 + 2K_g^2 C_p C_s + (K_g C_p)^2 + (K_w C_s)^2 + 2K_s K_w C_s^2 - K_g K_w C_p C_s}}{2C_p C_s} \tag{2.11}$$

The heat capacity of the samples can then be extracted using the obtained two tau values by subtracting the heat capacity of the addenda.

### 2.4.4 ac susceptibility measurement

To measure ac-susceptibility, the ac-susceptibility option available for use with MPMS was utilized. While dc-susceptibility record the equilibrium value of the magnetization, ac-measurements provide information about the magnetization dynamics in a material. A small ac driving field $H_{ac}$ of frequency $\omega$ is applied to the sample in addition to the applied dc field. It induces a time dependent moment. The quantity measured $M_{ac} = (dM/dH)H_{ac}Sin(\omega t)$ is sensitive to the susceptibility $\chi = dM/dH$. Thus the features will be observed in the data when there are changes in the slope of the magnetization. When the sample response lags behind the driving field, a phase shift is introduced into the above equation. Thus the ac-susceptibility has two components, the real ($\chi'$) and imaginary ($\chi''$) parts which probe dM/dH and dissipative energy loss in the samples.

# CHAPTER 3

# Ultrasharp metamagnetism and extremely large magnetoresistance

## 3.1 Introduction

Recently, materials exhibiting field induced metamagnetic phase transition between two energetically competing phases have attracted a lot of attention because of its presence in a wide range of complex magnetic systems [81–85]. The occurrence of metamagnetic transition is perceptible by the sharp jump in isothermal magnetization. It is well established, that this transition is independent to the microstructure and actually related to the intrinsic nature of the materials [86]. An extensive studies on this field induced metamagnetic transition has been carried out over the last decades [87–90]. Examples are certain phase separated manganites, intermetallic alloys such as $Nd_5Ge_3$, $Gd_5Ge_4$, $CeF_2$ etc. and some phase separated well known multiferroic $Eu_{1-x}Y_xMnO_3$ systems. The appearance of the magnetization steps has been found to be sensitive to the cooling magnetic field as well as on the magnetic field sweep rate [81, 84]. Hardy et al [91]. have shown that in $Pr_{0.5}Ca_{0.5}Mn_{1-x}Ga_xO_3$, the occurrence of the spontaneous magnetization jump in

the time evolution of magnetization for a fixed temperature and magnetic field. Wu et al [92]. has also observed the same phenomenon in manganites thin films. The observation of resistivity and magnetization steps in $(La_{0.5}Nd_{0.5})_{1.2}Sr_{1.8}Mn_2O_7$ has also been reported by Liao et al [93]. The origin of these metamagnetic transition is still a matter of controversy. Very different kind of mechanisms have been proposed, such as field dependent orbital ordering in $Pr_{0.5}Ca_{0.5}Mn_{0.95}Co_{0.05}O_3$ [81], spin quantum transition in $Pr_{5/8}Ca_{3/8}MnO_3$ [94], spin reorientation in $FeRh$ thin films [95], geometrical frustration in garnets [96], spin flop transition in $Ca_3CoMnO_6$ [97] and burst like growth of the ferromagnetic fraction in the phase separation picture. Although, according to the most of the authors the origin of the magnetization steps is because of martensitic like transition [84, 91, 98]. In spite of having lot of study on metamagnetism in various systems, the investigation the origin through detailed analysis has been rarely addressed.

In manganites, metamagnetic transition is usually observed in low bandwidth charge ordered systems. Therefore, as a part of our investigation the origin of metamagnetism, we have chosen $Sm_{0.5}Ca_{0.5}MnO_3$ as parent compound which is one of the lowest bandwidth and robust charge ordered system. It needs 500 kOe magnetic field at 4 K for the metamagnetic transition to occur [2]. Again, electronic bandwidth depends on the average A-site ionic radius $\langle r_A \rangle$ [14, 99]. Thus the study on the effect of A-site ionic radius on metamagnetism will give the origin of the metamagnetic transition. To obtain material with different electronic bandwidth, 'Ca' in $Sm_{0.5}Ca_{0.5}MnO_3$ compound has been systematically replaced with 'Sr'. This 'Sr' doping undoubtedly increases the $e_g$ electronic bandwidth as 'Sr' being higher ionic radii compared with 'Ca'. In this study, a set of samples with different $\langle r_A \rangle$ has been prepared and subjected them for a detailed structural, magnetic and electrical transport measurements. The decrease of critical field with increase of $\langle r_A \rangle$ and $\sigma^2$ has been observed and explained on the basis of ferromagnetic clusters formation which are acting as the nucleation center for the metamagnetism.

On the other hand, for the last two decades search for materials with large magnetoresistance (MR) and the studies on related phenomena [17, 43, 104–107] are at the forefront of the worldwide research activity due to its widespread application in the field of the magnetic sensor, magnetic memory devices, magnetic switches etc. The highest value of MR in principle can be achieved if the resistivity value of the material can be transformed from an extreme insulating material (like mica) to a very good metallic one (like Copper) by applying a magnetic field. In perovskite manganite, insulating state is observed in charge ordered antiferromagnetic (CO-AFM) sample which generally appears near the half doping. Critical magnetic field, that is required to melt the charge-ordered antiferromagnetic state, increases with decreasing the bandwidth [108, 109]. This CO-AFM state can be weakened, that requires comparatively smaller critical magnetic field, by introducing ferromagnetic proximity: (i) by effectively increasing the bandwidth of the $e_g$ electrons via substituting larger cations at the A-sites [110–113], (ii) by B-site doping (e.g, Cr, Ru doping on Mn sites) [114, 115], (iii) by making FM-AFM core-shell nanostructures (or nanoparticles) [116–118].

CO-AFM state in low bandwidth $Sm_{0.5}Ca_{0.5}MnO_3$ (SCMO) is very stable and $\sim$ 500 kOe (at T = 4.2 K) critical magnetic field ($H_{CR}$) is required to destabilize the CO state [108]. On the other hand CO-AFM and FM metallic phases coexist in $Sm_{0.5}Sr_{0.5}MnO_3$ (SSMO) and is metallic at low temperature [119]. Keeping this in mind we prepare $Sm_{0.5}Ca_{0.25}Sr_{0.25}MnO_3$ [SCSMO] by replacing half of the $Ca^{2+}$ ions by $Sr^{2+}$ ions. This substitution reduces the charge-ordering temperature ($T_{CO}$) and Neel temperature ($T_N$) by $\sim$50 K from its parent compound SCMO [120]. Although SCSMO remains a strong insulator, the critical field decreases to 48 kOe from 500 kOe (for SCMO).

For the prepared polycrystalline SCSMO, surprisingly, we obtain an unprecedented magnetoresistance of $\sim 10^{15}\%$ at 10 K in 90 kOe external magnetic field. We

also find ultra-sharp metamagnetic transition [81, 121–123] below 10 K. We explain the metamagnetic as well as ultra-sharp metamagnetic transition using martensitic scenario. Our Monte Carlo simulations using a two-band double-exchange model show that A-site disorder suppresses the CE-type phase, but the system remains insulating without any external magnetic field. In an external magnetic field the inhomogeneous disorder seeds the ferromagnetic-metallic clusters into the system and as a result resistivity decreases at low temperatures which gives rise to large magnetoresistance.

## 3.2 Effect of A-site ionic radius on metamagnetic transition in chargeordered $Sm_{0.5}(Ca_{0.5-x}Sr_x)MnO_3$ compounds

### 3.2.1 Sample Preparation and Characterization

All the bulk polycrystalline compounds $Sm_{0.5}(Ca_{0.5-x}Sr_x)MnO_3$ $(x = 0 - 0.5)$ has been prepared by the well sol gel method with $Sm_2O_3$, $CaCO_3$, $Sr(NO_3)_2$ and $MnO_2$ as the starting chemicals of purity 99.9%. To prepare bulk samples, decomposed gel has been pelletized and heated at $1300^0C$ for 36 hours.

### 3.2.2 Experimental Results and Discussion

The single phase nature of the samples has been characterized from room temperature x-ray diffraction (XRD) measurements by using Rigaku-TTRAX-III with 9 kW rotating anode copper source of wavelength $\lambda = 1.54\mathring{A}$. Magnetic measurements has been performed using quantum design SQUID-VSM. The transport and magneto-transport measurements has been carried out on bar shaped samples in longitudinal

geometry by four probe method using Cryogenic setup.

The room temperature XRD study (Fig. 6.1) display the single phase nature of all the bulk polycrystalline compounds. The crystal structure information has been obtained from Rietveld refinement of the XRD data using FULLPROF software which shows that all the samples crystallize in orthorhombic structure with 'Pnma' space group. The extracted lattice parameters and the average A-site ionic radius $\langle r_A \rangle$ calculated from shanon effective ionic radii has been presented in Table. 6.1. The gradual increase of $\langle r_A \rangle$ has been observed with increase of 'Sr' concentrations because of larger ionic radius compared with 'Ca'.

**Table 3.1:** The lattice parameters and average A-site ionic radii for the samples $Sm_{0.5}(Ca_{0.5-x}Sr_x)MnO_3$ $(x = 0, 0.1, 0.2, 0.25, 0.3, 0.5)$

| $x$ | a $(\AA)$ | b $(\AA)$ | c $(\AA)$ | $\langle r_A \rangle$ $(\AA)$ |
|---|---|---|---|---|
| 0 | 5.423 | 5.370 | 7.582 | 1.156 |
| 0.1 | 5.415 | 5.381 | 7.593 | 1.169 |
| 0.2 | 5.410 | 5.401 | 7.626 | 1.182 |
| 0.25 | 5.404 | 5.413 | 7.629 | 1.188 |
| 0.3 | 5.410 | 5.416 | 7.634 | 1.195 |
| 0.5 | 5.441 | 5.425 | 7.660 | 1.221 |

From the lattice parameters orthorhombic distortion, defined as $\Delta = \frac{a+b-c/\sqrt{2}}{a+b+c/\sqrt{2}}$, has been estimated which shows (Fig. 3.2) that with initial increase of $\langle r_A \rangle$ distortion decreases rapidly up to $x = 0.2$ and with further increase of $\langle r_A \rangle$ there is a gradual increasing tendency of the distortion. On the other hand, unit cell volume increases steadily with increase of $\langle r_A \rangle$. The variation of $\Delta$ and unit cell volume with $\langle r_A \rangle$ has been presented in Fig. 3.2.

The increase of average A-site ionic radius and reduction of orthorhombic distortion greatly influences the transport and magnetotransport properties as band width of $e_g$ electrons in manganites is directly proportional to the $\langle r_A \rangle$. The temperature dependence of resistivity $[\rho(T)]$ in absence of any external magnetic field has been performed for the samples with $x = 0, 0.1, 0.2, 0.25, 0.3, 0.5$. The measurements were

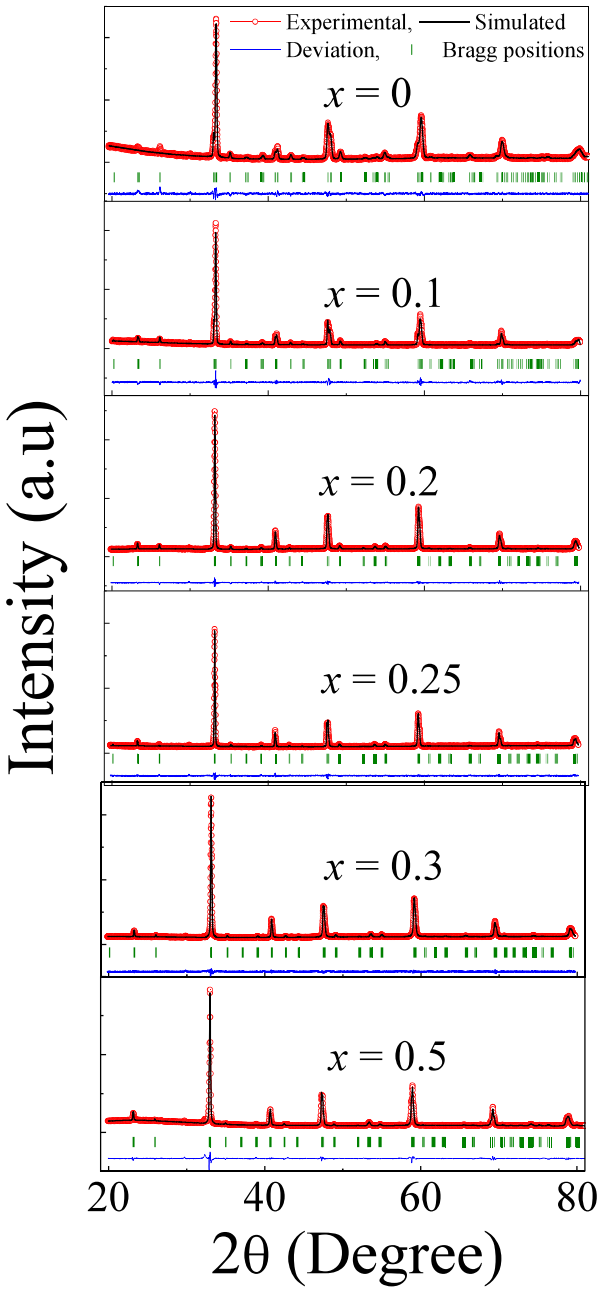


**Figure 3.1:** Room temperature XRD data with its corresponding profile fitted data for the compounds $Sm_{0.5}(Ca_{0.5-x}Sr_x)MnO_3$ ($x$=0, 0.1, 0.2, 0.25, 0.3, 0.5)

done during warming cycle after cooling the samples in zero magnetic field. The evolution of $\rho(T)$ with different 'Sr' concentration ($x$) has been presented in Fig. 3.3 which shows the insulating nature of the samples down to the measurable resistance limit. In spite of being insulating nature of the samples the relative suppression of resistivity is observed with increase of 'sr' concentrations. Moreover, the 'Sr' substi-

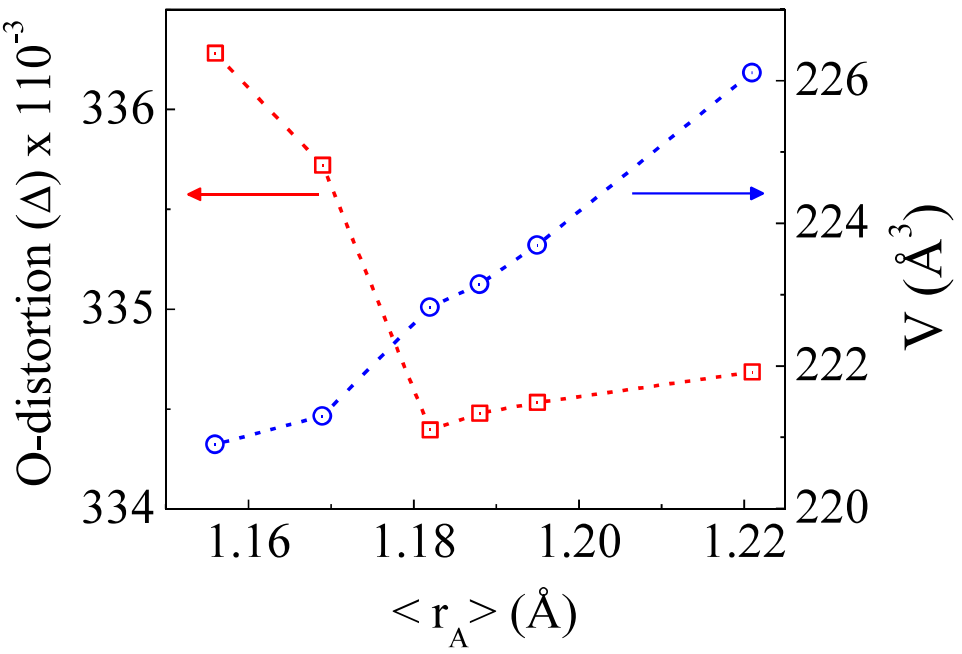


**Figure 3.2:** Evolution of orthorhombic distortion ($\Delta$) and Unit cell volume with $\langle r_A \rangle$.

tution also decreases the charge ordering temperature ($T_{CO}$) from 260 K for $x = 0$ to 210 K for $x = 0.5$ and at the same time makes the CO state fragile (inset of Fig. 3.3). The reduction of resistivity with '$x$' as well as softening of CO state is due to the increase of band width by increasing A-site ionic radius. For further investigation, the high temperature ($T > T_{CO}$) resistivity data has been analyzed with the help of small polaron hopping model (SPH) as in manganites the electrical resistivity in paramagnetic region is mainly governed by the polaronic activation. According to the SPH model [100] the expression of resistivity is $\rho = \rho_0 T exp(E_A/k_B T)$ where $E_A$ is the polaronic activation energy. From the fitting of the high temperature ($T > 260$) resistivity data, the activation energy for the different 'Sr' doped samples has been calculated and its evolution with '$x$' has been presented in the inset (B) of Fig. 3.3. From this figure, the reduction of $E_A$ with '$x$' is observed and it is also expected as increasing band width decreases the activation energy. Previously, x et al. has showed that increase of $\langle r_A \rangle$ makes the charge ordered state to the electronically phase-separated state which causes spontaneous metal insulator transition.

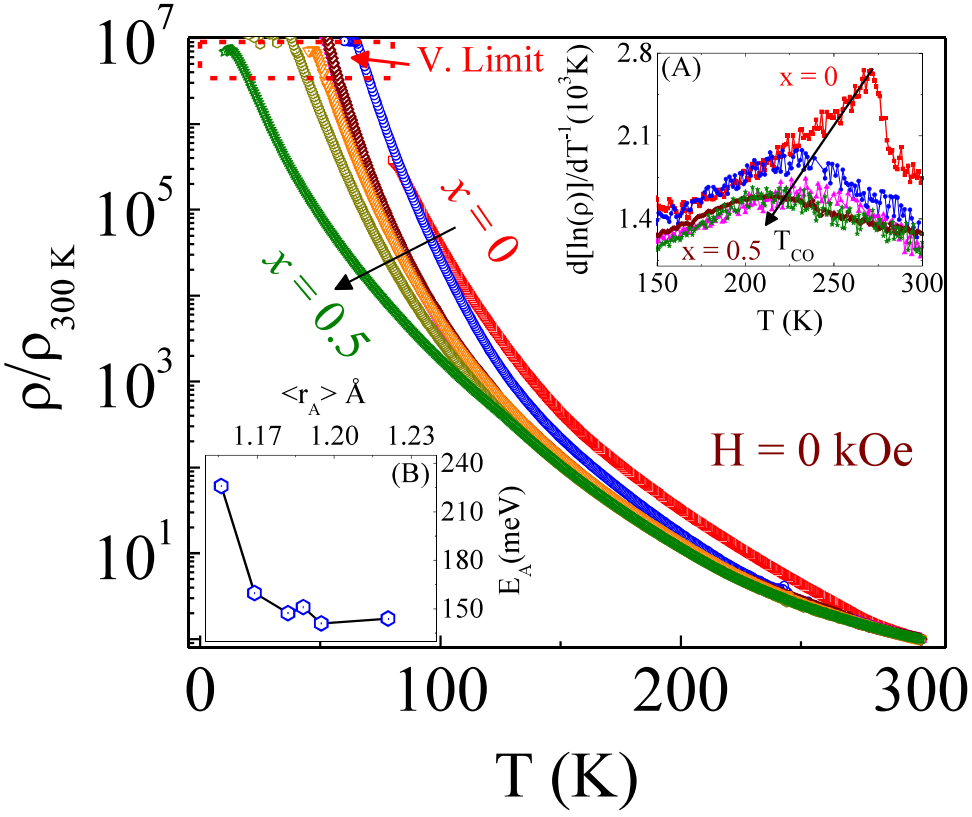


**Figure 3.3:** Temperature dependence of reduced resistivity of the samples $Sm_{0.5}(Ca_{0.5-x}Sr_x)MnO_3$ ($x$=0, 0.1, 0.2, 0.25, 0.5) in absence of external magnetic field. Insert (A) shows the $d[ln(\rho)]/dT^{-1}$ vs. T plot of the samples and (B) shows the variation of activation energy with $\langle r_A \rangle$.

Though in our case, spontaneous metal insulator transition does not take place but the reduction of resistivity and softening of CO state with '$x$' is a probable signature of phase coexistence.

To have a clear vision about this phase coexistence, the temperature variation of resistivity in presence of 90 kOe magnetic field has also been performed and it is presented in Fig. 3.4. There is almost no effect of 90 kOe field in the resistivity of $x = 0$ sample and it is also expected as $Sm_{0.5}Ca_{0.5}MnO_3$ is a robust charge ordered material which needs 500 kOe magnetic field to destabilize. On substitution of 'Sr' in place of 'Ca' the huge suppression of resistivity is observed on application of 90 kOe magnetic field and insulator to metal transition ($T_{MI}$) take place. Moreover, with increasing 'Sr' concentration $T_{MI}$ gets broaden which is the signature of

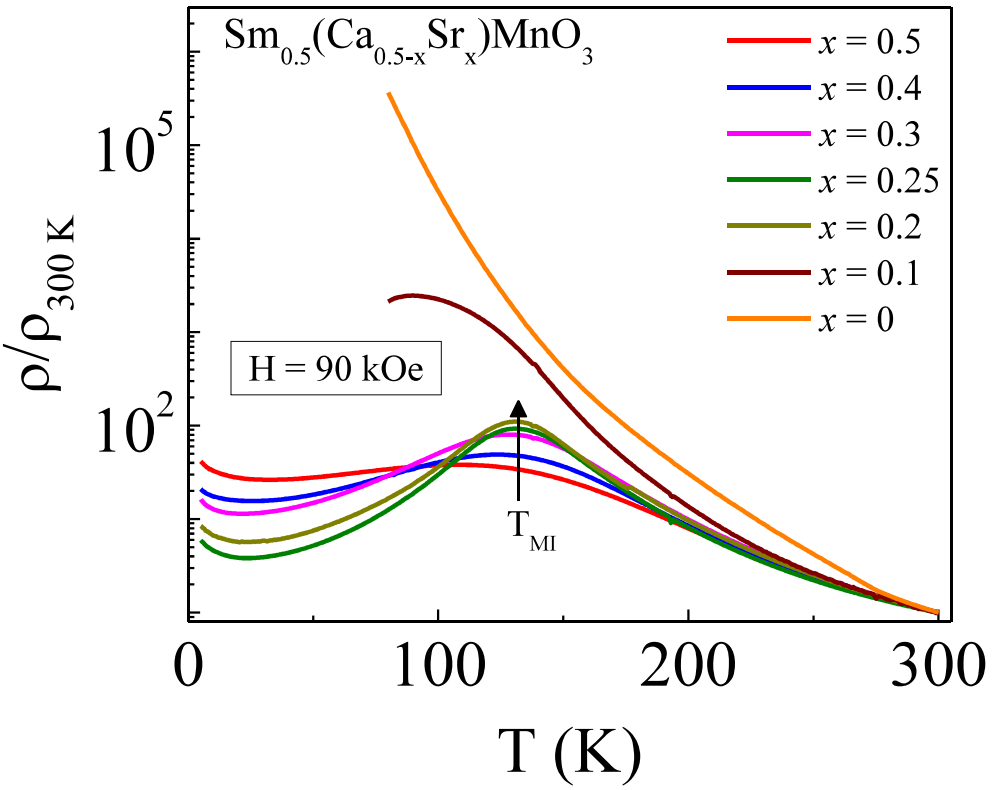


**Figure 3.4:** Temperature dependence of reduced resistivity of the samples $Sm_{0.5}(Ca_{0.5-x}Sr_x)MnO_3$ ($x$=0, 0.1, 0.2, 0.25, 0.5) in presence of 90 kOe external magnetic field.

enhancing phase coexistence. Thus it can be safely said that 'Sr' has fragiled the robustness of CO state and introduced the phase separation.

Manganite systems being strongly correlated in nature, the phenomena of phase separation should also be reflected in magnetization also. In this regard, magnetization as a function of temperature [M(T)] has been measured in the field cooled warming (FCW) protocol in presence of 100 Oe magnetic field for the samples with 'Sr' concentrations $x = 0, 0.1, 0.2, 0.25, 0.5$. The evolution of M(T) for the samples has been shown in Fig. 6.9. At low temperature ($T < 50K$) with 'Sr' doping, the increase of magnetization is observed. The value of magnetization increases from $0.004\mu_B$ to $0.303\mu_B$ at $25K$ with increasing 'Sr' concentration from $x = 0.25$ to $x = 0.5$. This result indicates the enhancement of ferromagnetic phase fraction with 'Sr' doping. At the same time 'Sr' substitution decreases the both charge ordering temperature

($T_{CO}$) as well as anti-ferromagnetic ordering temperature ($T_N$). In $x = 0.5$ composition no signature of $T_N$ is observed which is because of the existence of tri-critical point around $100K$ [101]. This enhancement of ferromagnetic interactions with 'Sr' doping is basically due to the increase of band width.

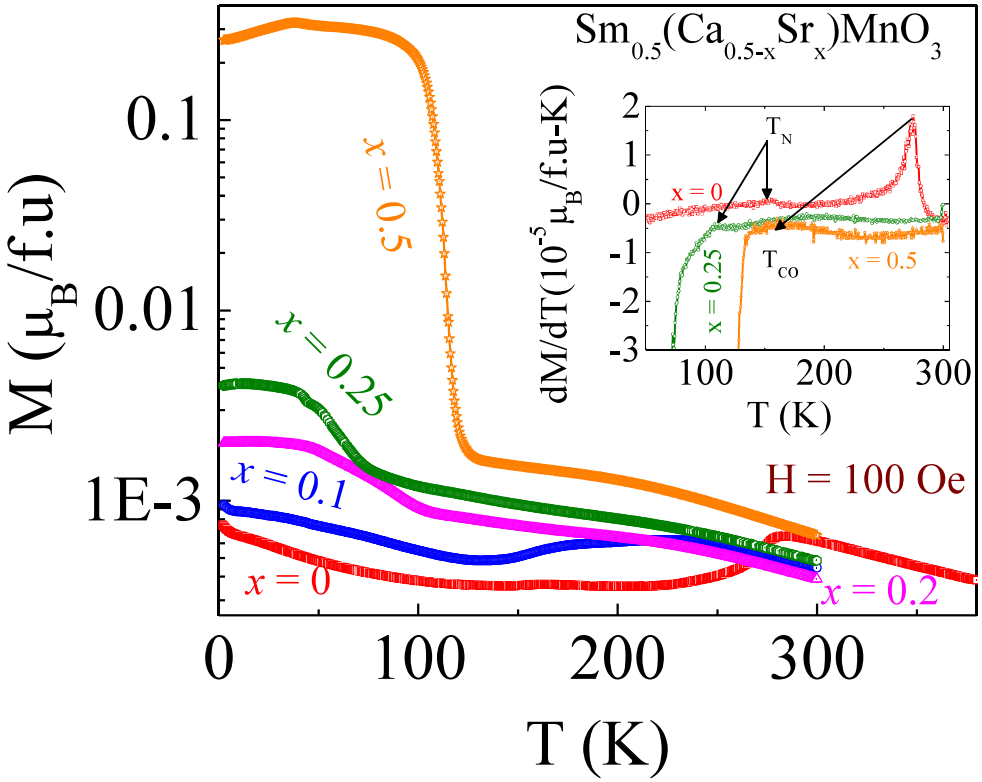


**Figure 3.5:** Evolution of magnetization with temperature, measured in FCW protocol in presence of 1 kOe magnetic field, for the samples $Sm_{0.5}(Ca_{0.5-x}Sr_x)MnO_3$ ($x$=0, 0.1, 0.2, 0.25, 0.5). Insert shows the temperature derivative of the corresponding magnetization of the samples.

For further investigation, high temperature ($T > 260K$) inverse dc susceptibility (H/M) versus temperature data at 100 Oe magnetic field has been analyzed with the Curie-Wiss law $\chi = C/(T - \theta_{CW})$ where $C = \mu_{eff}^2/3k_B$ and $\mu_{eff}$, $\theta_{CW}$ are the effective paramagnetic moment in Bohr magnetron and paramagnetic curie temperature respectively. The variation of dc susceptibility (H/M) with temperature for $x = 0.1, 0.25, 0.5$ samples and their corresponding Curie-Weiss fitted data is presented in Fig. 6.3. From the fitting, paramagnetic curie temperature comes out to be $110K, 122K$ and $145K$ for the samples with 'Sr' concentrations $x = 0.1, 0.25$

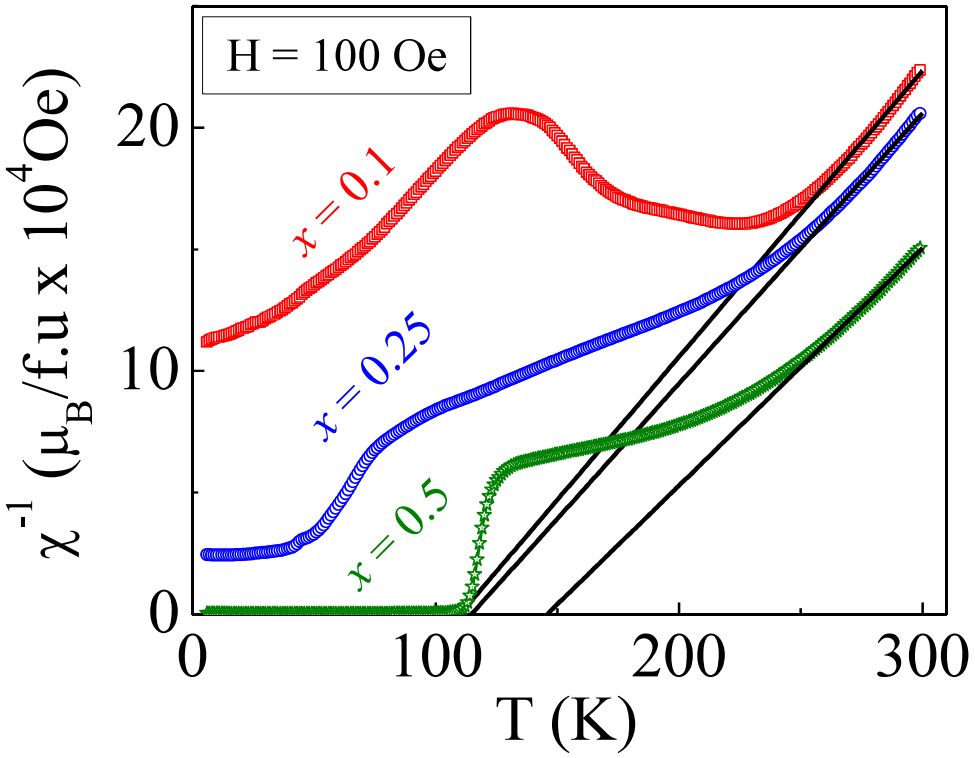


**Figure 3.6:** Temperature dependence of inverse dc susceptibility (H/M) data, measured in presence of 100 Oe magnetic field, for the samples $Sm_{0.5}(Ca_{0.5-x}Sr_x)MnO_3$ ($x$=0, 0.25, 5).

and 0.5 respectively. Furthermore, the enhancement of the effective paramagnetic moment ($\mu_{eff} = 6.16\mu_B$ for $x = 0.1$ to $\mu_{eff} = 6.76\mu_B$ for $x = 0.5$) has also been observed. This increase of $\theta_{CW}$ and $\mu_{eff}$ clearly indicates the enhancement of ferromagnetic interactions in the increased 'Sr' doped samples. Here another point needs to mention that the values of the effective moments are larger than the theoretical calculated value of $4.42\mu_B$. It indicates the presence of ferromagnetic clusters in the high temperature region ($T > 260K$) and these clusters behaves as an individual paramagnetic entity which contains more than one Mn ion [103]. Although for $x = 0$ sample its value is $4.32\mu_B$ which is close to the theoretical expected value. This result implies that with 'Sr' doping there is appearance of ferromagnetic clusters which grows in size with increased 'Sr' concentrations. Thus low temperature phase of the samples (except $x = 0$) consists of ferromagnetic clusters in the host antiferromagnetic phase.

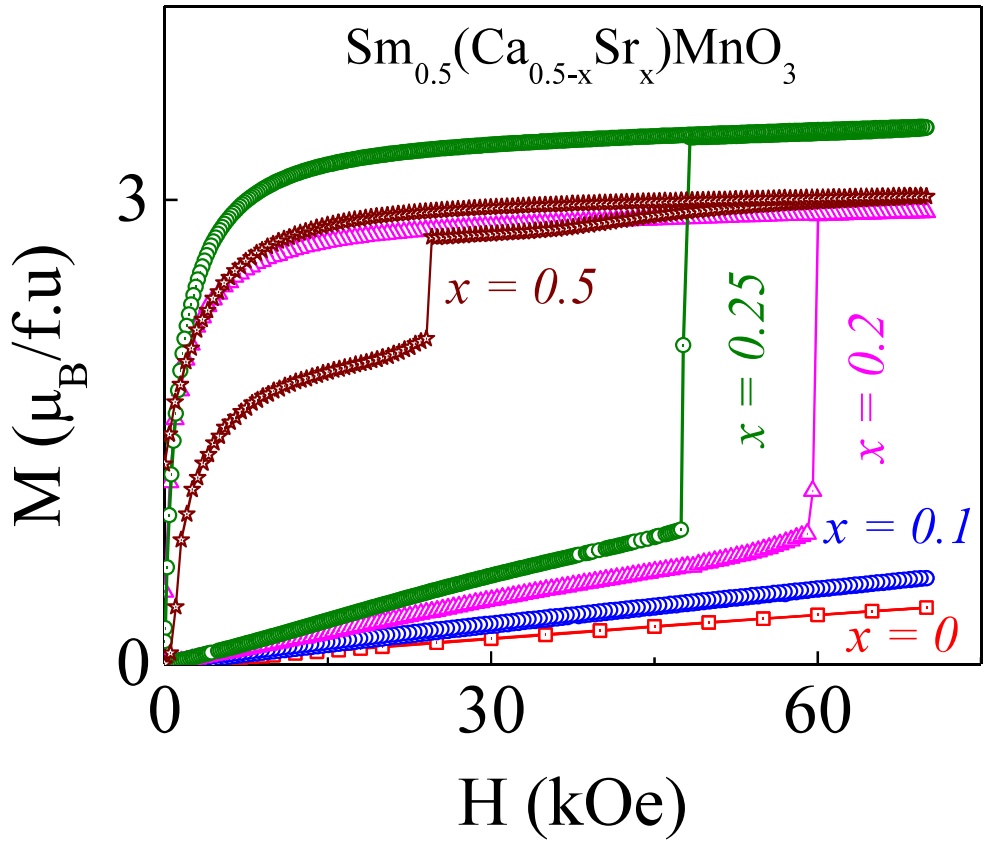


**Figure 3.7:** Isothermal magnetization of the samples $Sm_{0.5}(Ca_{0.5-x}Sr_x)MnO_3$ ($x$=0, 0.1, 0.2, 0.25, 5) at 2 K.

Finally, to see the effect of magnetic field in these phase separated state, the field dependence of magnetization at $2K$ for the samples has been performed and presented in Fig. 5.8. For the samples with 'Sr' concentrations $x = 0$ and $x = 0.1$ the linear increase of magnetization with magnetic field has been observed up to the 70 kOe field which implies the dominance of antiferromagnetic phase. With further increase of 'Sr' concentration i.e. to $x = 0.2$, a sharp metamagnetic transition is observed at 55 kOe and magnetization increases from $0.75\mu_B$ to $3\mu_B$ i.e. system converts completely from CO antiferromagnetic (COAFM) to ferromagnetic (FM) phase. The descending branch of the M-H curve remains almost flat down to 10 kOe field which indicates the irreversible nature of the field induced COAFM to FM transformation and for further decreasing the field rapidly decrease of magnetization is observed. On the other hand, with further increase of 'Sr' concentrations

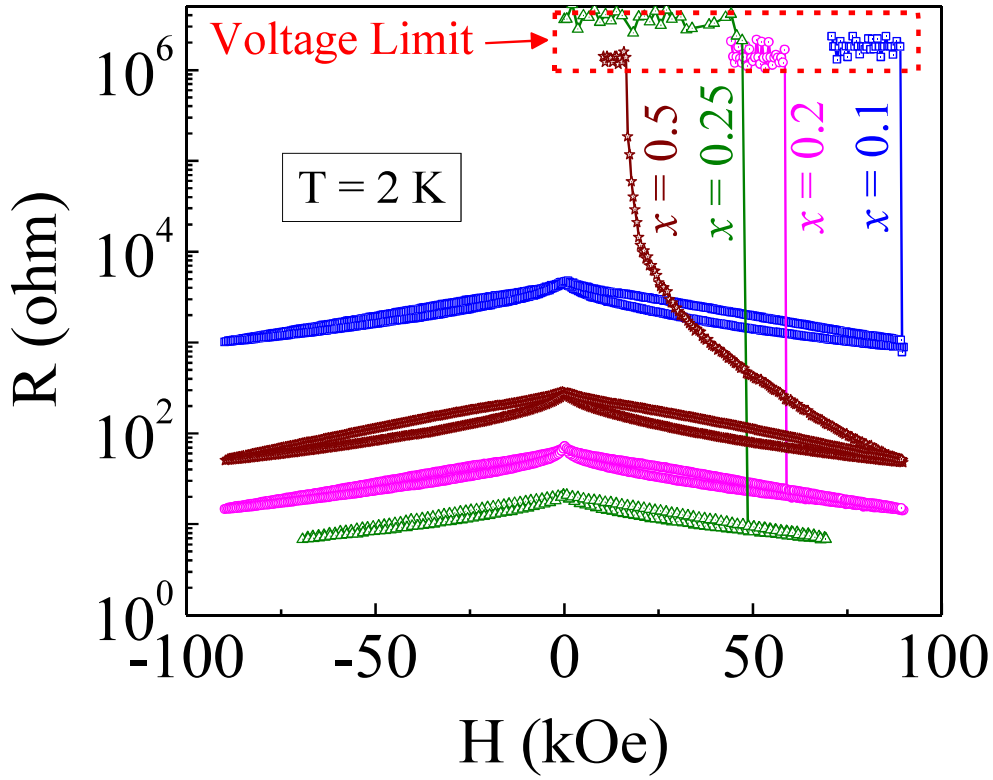


**Figure 3.8:** Magnetic field dependence of resistance of the $Sm_{0.5}(Ca_{0.5-x}Sr_x)MnO_3$ compounds at 2 K.

requirement of critical field for this metamagnetic transition decreases and it reaches to 47 kOe in $x = 0.25$ and 20 kOe in $x = 0.5$. Although in $x = 0.5$, the initial increase of magnetization was soft ferromagnetic like which tells the dominance of ferromagnetic phase with coexisting antiferromagnetic phase. Previously, this same kind of sharp metamagnetic transition has been observed in Mn site doped CO manganites, for instance for $Pr_{0.5}Ca_{0.5}Mn_{1-x}M_xO_3$. According to Raveau et al. [102] the occurrence of this step like behavior in Mn site doped manganites is because of the presence of the short range ordered ferromagnetic region in the COAFM region. Here, the existence of ferromagnetic clusters and its growth with 'Sr' doping has been observed from the analysis of dc susceptibility data. This ferromagnetic clusters play the role of nucleation centers for the COAFM to FM metamagnetic transitions and sharpness of steps indicates the jerky growth of these FM clusters and martensiticlike transformation occurs. The observed downward shifting of the

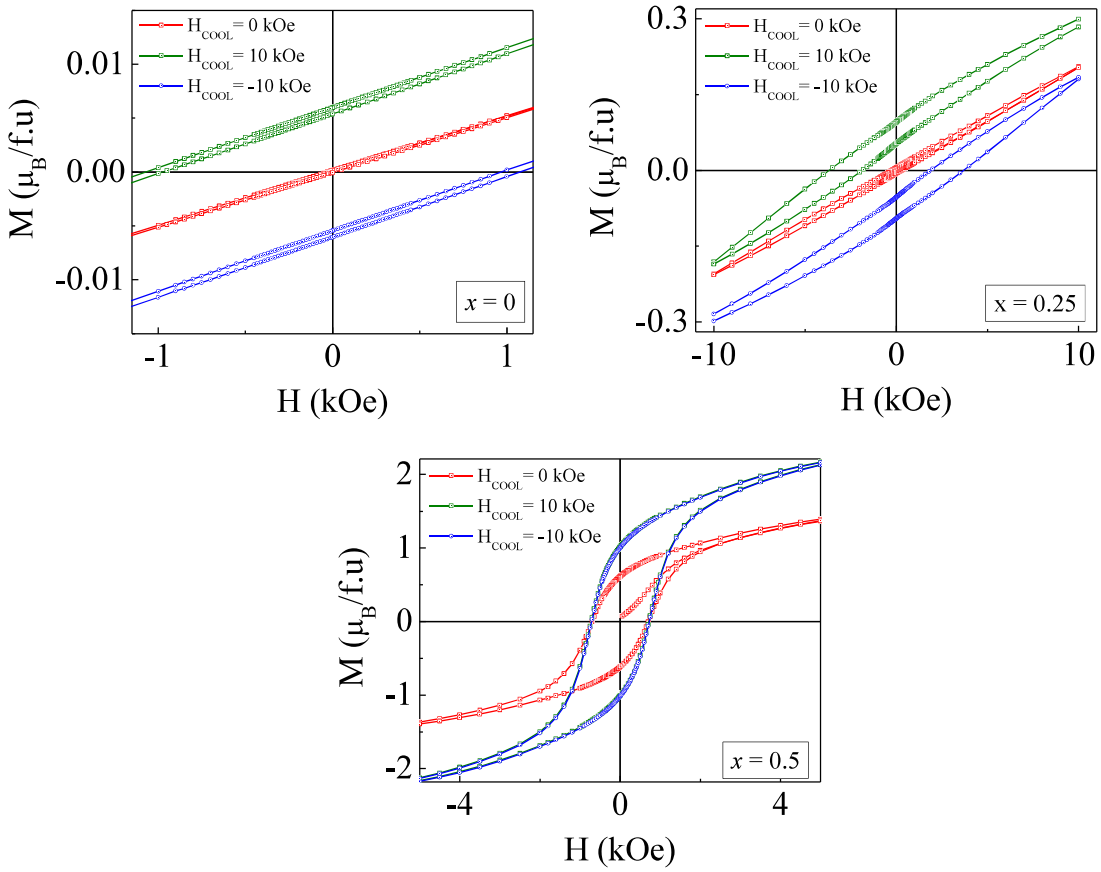


**Figure 3.9:** Isothermal magnetization at 2 K temperature with different cooling fields (0 kOe, 10 kOe and -10 kOe) for the samples with $x$ =0, 0.25, 0.5

critical fields with increasing 'Sr' concentrations is possibly because of the enhanced ferromagnetic clusters, responsible for the nucleation center of this jerky growth.

To correlate this phenomena of shifting the critical field for the metamagnetic transition, measurements of resistance with variation of magnetic fields at 2 K temperature has been performed in the samples. Here in the sample $x = 0.1$, metamagnetic transition is observed at 89.7 kOe which was not visible in magnetization because of the instrumental limitation and in $x = 0$ sample there was almost no effect of magnetic field (not shown in the figure). In the subsequent 'Sr' doped samples i.e in $x = 0.2$ metamagnetic transition occurs at 58.8 kOe and in $x = 0.25$ it occurs at 48.5 kOe. The slight higher values of the critical field determined from R-H compared with M-H is possibly due to different average sweep rate of the field. For example for $x = 0.25$ sample, in M-H sweep rate was 100 Oe/sec and in R-H it was 24 Oe/Sec.

The dependence of critical field on sweep rate is also an signature of martensitic like transition as smaller sweep rate assist the progressive accommodation of the martensitic strain which push the instability towards higher magnetic field.

The existence of these ferromagnetic clusters, responsible for the metamagnetism can also be perceptible from the exchange bias measurements as exchange bias originates from the pinned interfacial spins between adjacent FM and AFM domains. In this regard we have performed exchange bias measurements at 5 K for the samples with 'Sr' doping $x = 0, 0.25$ and 0.5. The samples has been cooled to 5 K with $H_{COOL} = 10kOe$) and M(H) measurements has been performed over the field range $\pm 10kOe$. The M(H) loops has been found to be asymmetric about the both magnetization as well as field axis which indicates the presence of exchange bias. The exchange bias field (defined as $H_E = (H_{C1} - H_{C2})/2$, where $H_{C1}$ and $H_{C2}$ are the left and right coercive field) obtained for the samples are $1.02kOe, 2.79kOe$ and $5Oe$ respectively. The presence of this exchange anisotropy undoubtedly gives the proof of the existence of the FM clusters in the COAFM background. The possibility of any artifact in the exchange bias measurements has been discarded from the shift of the M(H) loop in the positive field direction from the M(H) measurement at 5 K but cooling at $-10kOe$ field.

This whole scenario can be explained by a simple phenomenological picture. According to this picture at low temperatures, there is a development of ferromagnetic clusters with increase of band width by doping 'Sr' in place of 'Ca'. These ferromagnetic cluster phase increases gradually with 'Sr' doping and at $x = 0.5$ these ferromagnetic cluster phase is maximum. These clusters act as the nucleation center in the COAFM phase and after martensitic like transformation this COAFM phase converts to FM phase. With increasing band width this phase septation increases as a result of which strength as well as number of these nucleation center increases which results in the decrease of the critical field for the COAFM to ferromagnetic

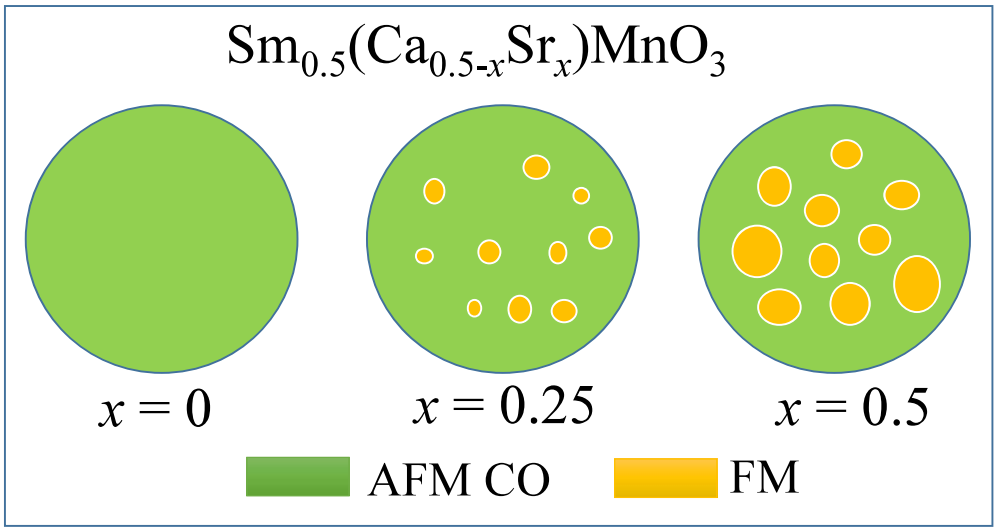


**Figure 3.10:** A schematic picture to describe the reduction of critical magnetic field for the metamagnetic transition in the samples $Sm_{0.5}(Ca_{0.5-x}Sr_x)MnO_3$.

transition.

## 3.3 Extreme colossal magnetoresistance in the $Sm_{0.5}Ca_{0.25}Sr_{0.25}MnO_3$ (SCSMO) compound

### 3.3.1 Synthesis and structural characterization.

High quality polycrystalline SCSMO was prepared by the well-known sol-gel technique (see methods for details). The crystalline structure and single phase nature of the sample was studied using room temperature x-ray diffraction (XRD) and transmission electron microscopy (TEM).

The room temperature XRD data has been profile fitted using Pnma space group and shows the single phase nature of the sample with orthorhombic structure. The low temperature data has also been tried to fit with single Pnma space group but

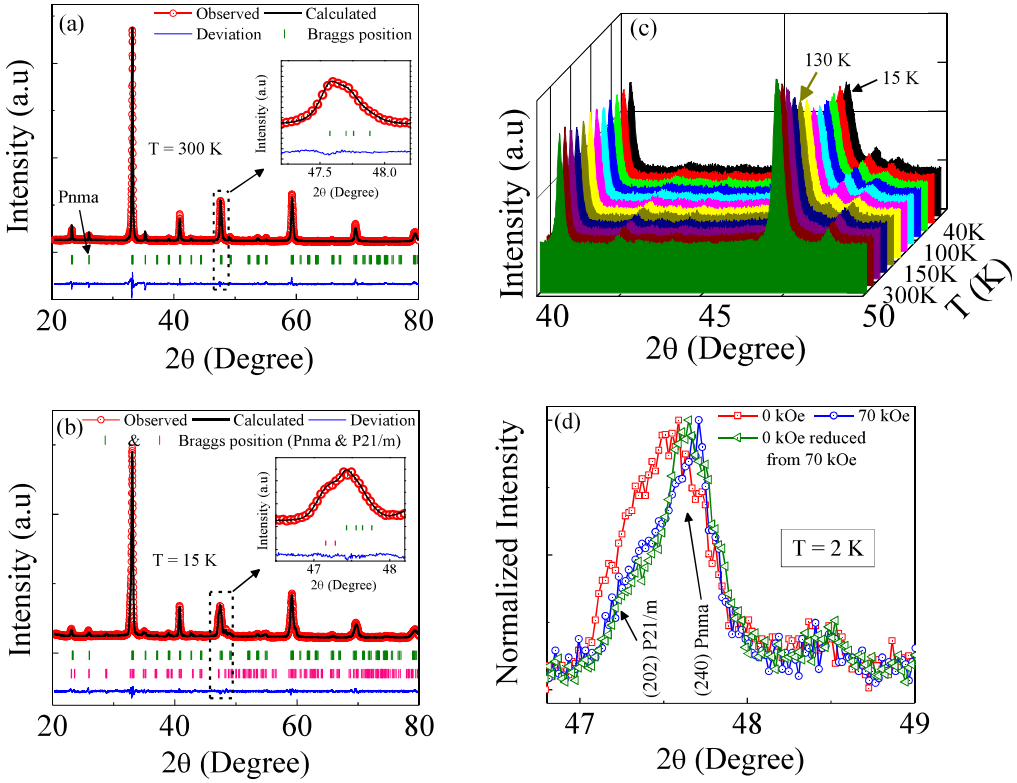


**Figure 3.11:** Profile fitting of the (a) room temperature XRD data using Pnma space group and (b) low temperature XRD data using Pnma and P21/m space group. Inset of (a) and (b) shows the fitting of the peaks at $2\theta = 47.5^0$ where new monoclinic phase (P21/m) appears at low temperature. (c) Evolution of the appearance of the new peak of P21/m space group with temperatures. (d) XRD line width modification in the presence of zero magnetic field, 70 kOe field as well as after removing the field.

does not give satisfactory fitting. The new peak appeared at low temperature (15 K)also does not fit with the single Pnma space group. Previously it was reported that $Sm_{0.5}Sr_{0.5}MnO_3$ sample undergoes crystallographic phase coexistence at low temperature with monoclinic P21/m symmetry [124]. Since the present sample is in between $Sm_{0.5}Ca_{0.5}MnO_3$ and $Sm_{0.5}Sr_{0.5}MnO_3$, we had tried to fit the low temperature (15 K) XRD data with P21/m but it also does not give any satisfactory fitting. Finally, fitting with Pnma+P21/m gives the best fit and has been plotted in Fig. 3.11(b). We present extracted lattice parameters in Table. 6.1. The temperature dependence of the XRD measurements has also been performed and the evolution of the appeared new peak corresponding to the P21/m monoclinic space group has been presented in Fig. 3.11(c). It indicates that below 120 K the new

peak appears at $2\theta = 47.5^0$ and its intensity remains almost constant below 100 K. It implies that below 100 K, P21/m phase gets trapped within host Pnma phase. The modification of x-ray line width at 2 K has also been studied by applying external magnetic field and is presented in Fig. 3.11(d). On application of 70 kOe magnetic field the full width at half maxima of the peak at $2\theta = 47.5^0$ decreases from $0.58^0$ to $0.46^0$ and stay at that value even after removal of the magnetic field. This shows that strain decreases in an external magnetic field and stays as it is even after removing the field. TEM diffraction pattern (see Fig. 3.12) also shows the orthorhombic crystallographic symmetry (Pnma) of the sample. With lowering of temperature another crystallographic phase with monoclinic symmetry P21/m along with the room temperature symmetry Pnma i.e. combinations of Pnma and P21/m appears below $T \leq 120K$ and creates lattice strain in the host Pnma phase. Strain is also evident from the TEM analysis [see Fig. 3.12(e)] at 100K.

**Table 3.2:** The lattice parameters and unit cell volumes of $Sm_{0.5}Ca_{0.25}Sr_{0.25}MnO_3$

| Temperature (K) | Space group | a ($\AA$) | b ($\AA$) | c ($\AA$) | V ($\AA^3$) | |
|---|---|---|---|---|---|---|
| 300 | Pnma | 5.395 | 7.611 | 5.408 | 222.049 | |
| 15 | Pnma + P21/m | 5.456 | 7.618 | 5.384 | 223.804 | Pnma |
| 15 | Pnma + P21/m | 5.380 | 10.849 | 7.569 | 441.802 | P21/m |

**Table 3.3:** The EDS analysis of the sample $Sm_{0.5}Ca_{0.25}Sr_{0.25}MnO_3$

| Element | Atomic % |
|---|---|
| O (K) | 59.39 |
| Ca (K) | 4.94 |
| Mn (K) | 20.43 |
| Sr (K) | 5.71 |
| Sm (L) | 9.50 |

The EDS analysis in scanning transmission electron microscopy high angle annular dark field (STEM-HAADF) mode was carried out with a $\sim$ 2 nm probe. It shows that the crystal is highly homogeneous distribution of elements [Fig. 3.13]. The chemical analysis (presented in Table. 3.3) confirms the stoichiometric nature of the compound.

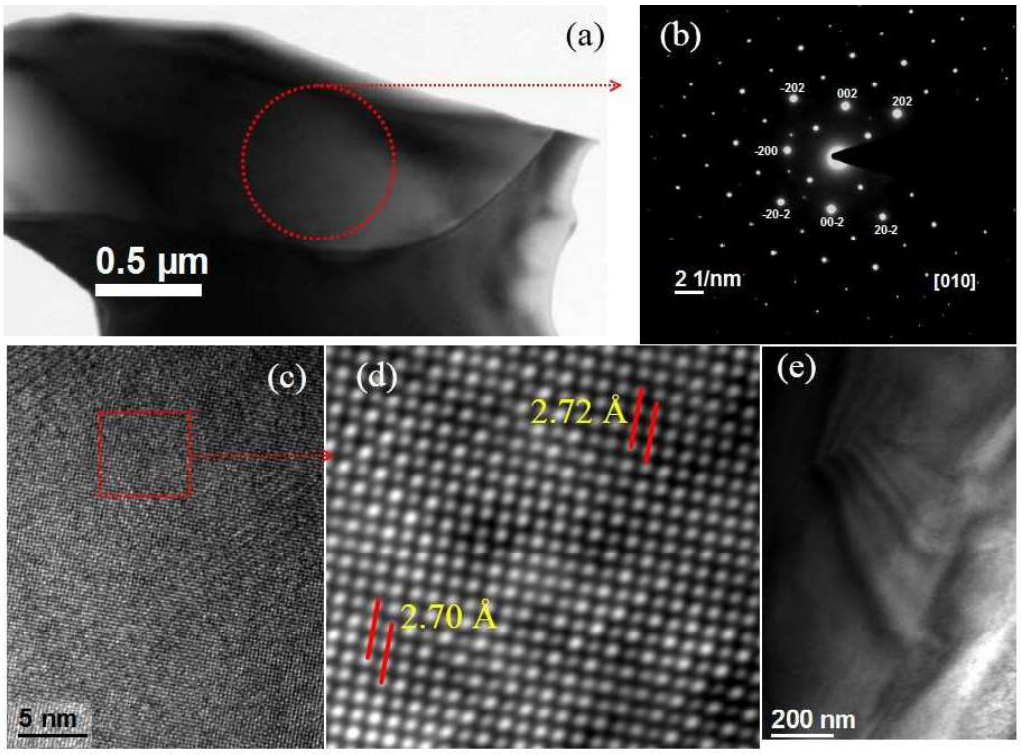


**Figure 3.12:** Panel (a) gives a typical TEM overview of one crystallite where two grains are visible. Panel (b) displays a typical [010] zone axis ED patterns at room temperature (RT). The pattern was indexed using orthorhombic structure (Pnma). Panel (c) gives a typical HRTEM overview of one crystallite. Panel (d) shows a magnified view of tiny domains in (c) displays an example of atomic scale variation of the contrast and panel (e) demonstrates [001] bright-field image recorded at 100 K.

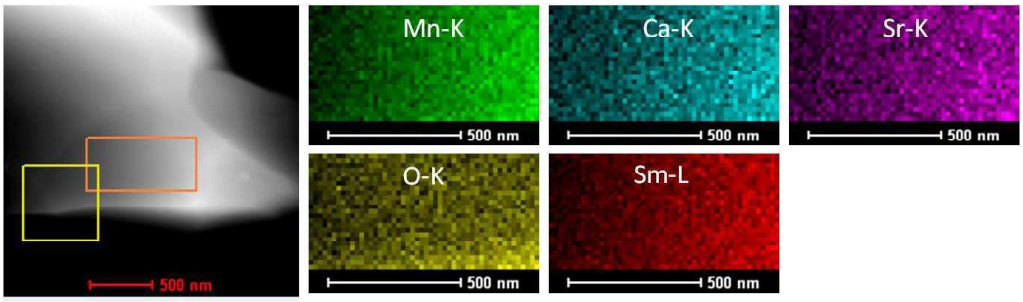


**Figure 3.13:** STEM-HAADF image and corresponding drift corrected chemical maps from the area marked by the orange box in the left panel.

### 3.3.2 Magnetic and Magnetotransport Measurements

The temperature dependent magnetization and resistivity for different applied magnetic fields are shown in Figs. 3.14(a) and (b). Interestingly below 60 K magnetization increases, but the ferromagnetic fraction is very small and this fact is

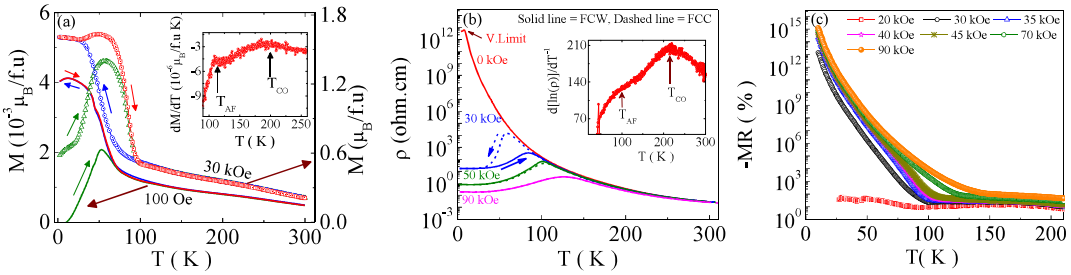


**Figure 3.14:** Magnetotransport properties: (a) Variation of magnetization with temperature in 100 Oe and 30 kOe external magnetic field. The inset shows the signature of CO and AFM ordering, indicated by arrows, from the temperature derivative of M(T) data taken in FCW protocol in the presence of 100 Oe magnetic field. (b) Temperature dependent resistivity without (red), with [30 kOe (blue), 50 kOe (olive), 90 kOe (violet)] external magnetic fields. The dotted lines represent the resistivity data taken during field cooling cycle and the solid lines are for the FCW cycle. The inset shows variation of activation energy ($E_A \propto d[ln(\rho)]/dT^{-1}$) with temperature, calculated from the temperature dependence of zero field resistivity data and ordering temperatures are indicated by arrows. (c) Magnetic field dependence of MR with temperature for different magnetic fields.

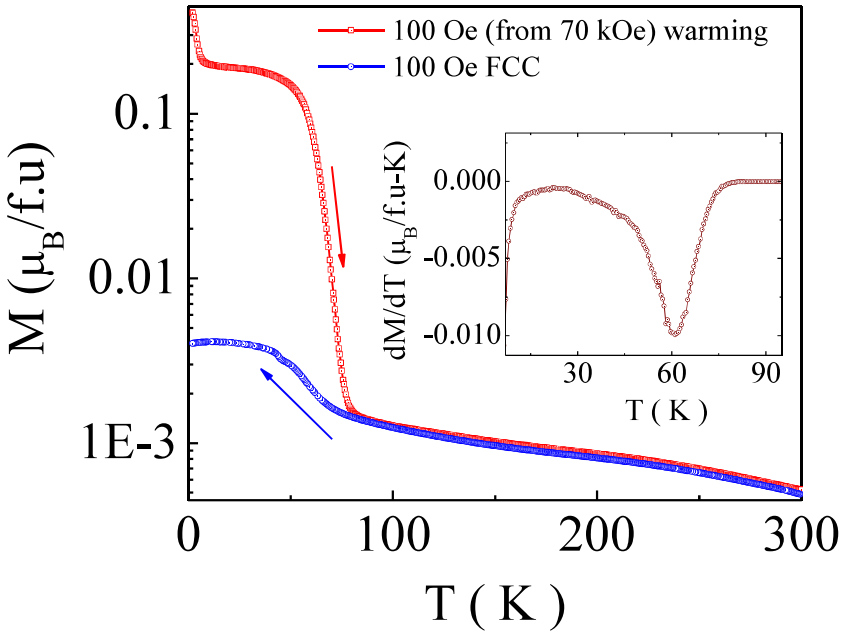


**Figure 3.15:** Magnetization as a function of temperature at H = 100 Oe external magnetic field. The blue curve is the magnetization during cooling of the sample (at H = 100 Oe). The red curve is magnetization during warming in the presence of H = 100 Oe external magnetic field (before starting measurements (at T = 2 K) the field cycled from 100 Oe to 70 kOe to 100 Oe). Inset indicates the temperature derivative of the warming magnetization data taken at 100 Oe field after reducing the field from 70 kOe.

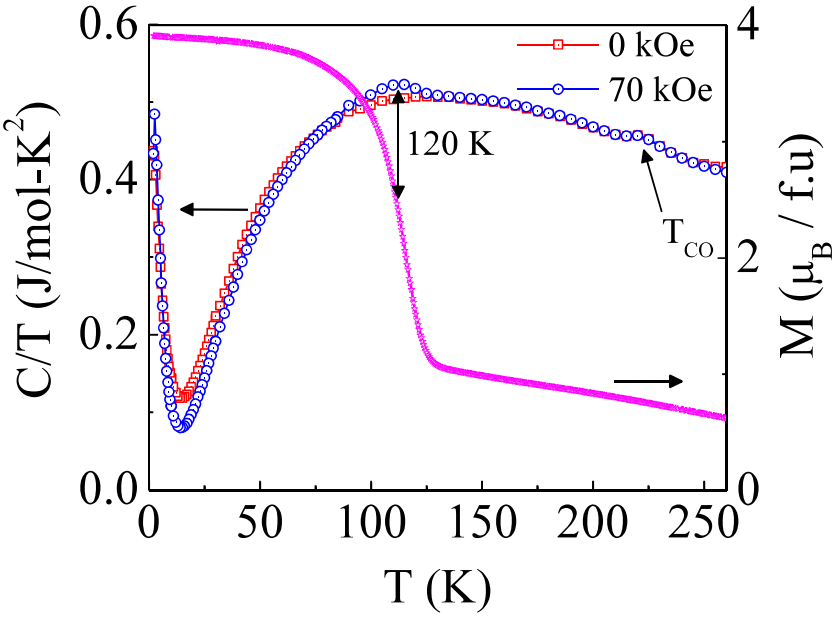


**Figure 3.16:** Left axes: C/T as a function of temperature (C is heat capacity) in the absence and in the presence of 70 kOe external magnetic field. Right axes: Temperature dependence of the magnetization measured in presence of 70 kOe magnetic field.

reconfirmed from the thermoremanent magnetization measurements. Thermoremanent magnetization measurements were carried out by the following protocol: the sample was cooled down from the room temperature in the presence of 100 Oe external magnetic field and the magnetization data was recorded (denoted by 100 Oe FCC in Fig. 3). The 100 Oe FCC data indicates the presence of a very small fraction of ferromagnetic phase. After reaching the specified temperature (T = 2 K), magnetic field increases from 100 Oe to 70 kOe and stayed for some time (approximately 5 mins). After that magnetic field was reduced to 100 Oe and magnetization data recorded during warming. From the experimental data it is clear that due to the expose of the 70 kOe external magnetic field, system gets converted to the long-range ferromagnetic phase which results in the larger value of the magnetization below T = 60 K (shown in Fig. 3.15). The inset also indicate the presence of the ferromagnetic transition at T = 60 K (derived from the minima of the temperature derivative of M(T) curve, measured during warming cycle in the presence of 100 Oe magnetic field after reducing the field from 70 kOe.). Because of the presence of very

small ferromagnetic clusters in the virgin sample, the system without any magnetic field remains insulating at low temperature as seen in Fig. 3.14(b). Below a certain temperature ($T < 10K$) the value of resistance is $R \sim 10^{13} ohm$, which is limiting value of our measuring instruments (see method section for details). The ordering temperatures ($T_{CO}$ and $T_N$) are indicated in the inset of Figs. 3.14 (a) and (b) and similar $T_{CO}$ is also obtained from the heat capacity measurement. Around 120 K, magnetization data measured at 70 kOe field also shows a sharp increase like paramagnetic to ferromagnetic transition. Thus the kink at 120 K in the heat capacity is associated with the paramagnetic to ferromagnetic transition. Though in the virgin sample around 120 K there is an antiferromagnetic transition as observed from the derivative of M(T) data in 100 Oe field. Therefore, it can be concluded that 70 kOe field converts the AFM fraction to FM phase which results in the rise in the peak in C/T versus T data at 120 K (see Fig. 3.16). Another peak observed at 220 K is the signature of the onset of charge ordering. Additionally, the sharper increasing nature of C/T below 15 K is observed which is due to the magnetic ordering of $Sm^{3+}$ ions [125, 126].

A 30 kOe magnetic field induces larger ferromagnetic fraction and as a result resistivity decreases considerably (from $10^{12}$ Ohm-cm to $\rho \sim 17.5$ Ohm-cm at T = 2.5 K) at low temperatures [see Figs. 2(a) and (b)]. This shows that not only $T_{CO}$ decreases, but the robustness of CO-AFM state is reduced in SCSMO. A huge hysteresis is observed between field cooling and heating cycle for 30 kOe in the temperature range $50K < T < 100K$, in both magnetization and resistivity curves, which is the signature of field induced electronic phase separation [127]. With further increase of applied magnetic field this phase coexistence is suppressed and low temperature resistivity goes to $10^{-2}$ Ohm-cm (for 90 kOe).

To quantify the field induced change in resistivity, we plot the MR $= \frac{\rho(H)-\rho(0)}{\rho(H)} \times 100$ with temperature at different magnetic field in Fig. 3.14(c). MR is ~10% for 20

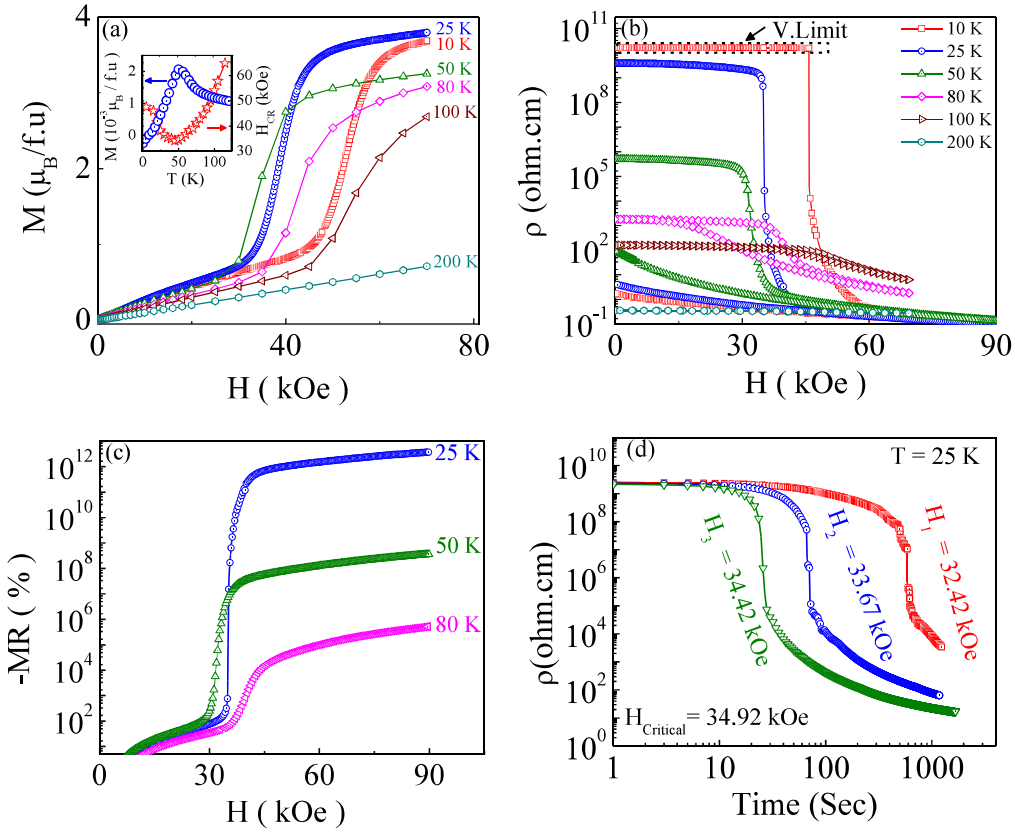


**Figure 3.17:** Metamagnetic transition: (a) Magnetization vs. magnetic field and (b) resistivity vs. magnetic field at different temperatures. Inset in (a) shows the temperature dependence of $H_{CR}$ and ZFC magnetization in 100 Oe magnetic field. (c) Magnetic field dependent magnetoresistance at different temperatures. (d) Evolution of resistivity with time at 25 K for different applied magnetic fields ($H_1, H_2, H_3$) such that $H_1 < H_2 < H_3 < H_{CR}$.

kOe, but astonishingly increases to $10^{13}$% for 30 kOe external magnetic field and as large as $\sim 10^{15}$% at 10 K for 90 kOe magnetic field. The magnetoresistance value as high as $10^{15}$% in polycrystalline stable SCSMO compound is a unique observation.

### 3.3.3 Metamagnetic Transition

Isothermal magnetization measured in ZFC protocol at different temperatures [presented in Fig. 3.17(a)] shows the field induced metamagnetic transitions. Experimentally obtained saturation magnetic moment ($3.82\mu_B$) at 30 K is close to the estimated magnetic moment for the full saturation of the $Mn^{3+}/Mn^{4+}$ and $Sm^{3+}$

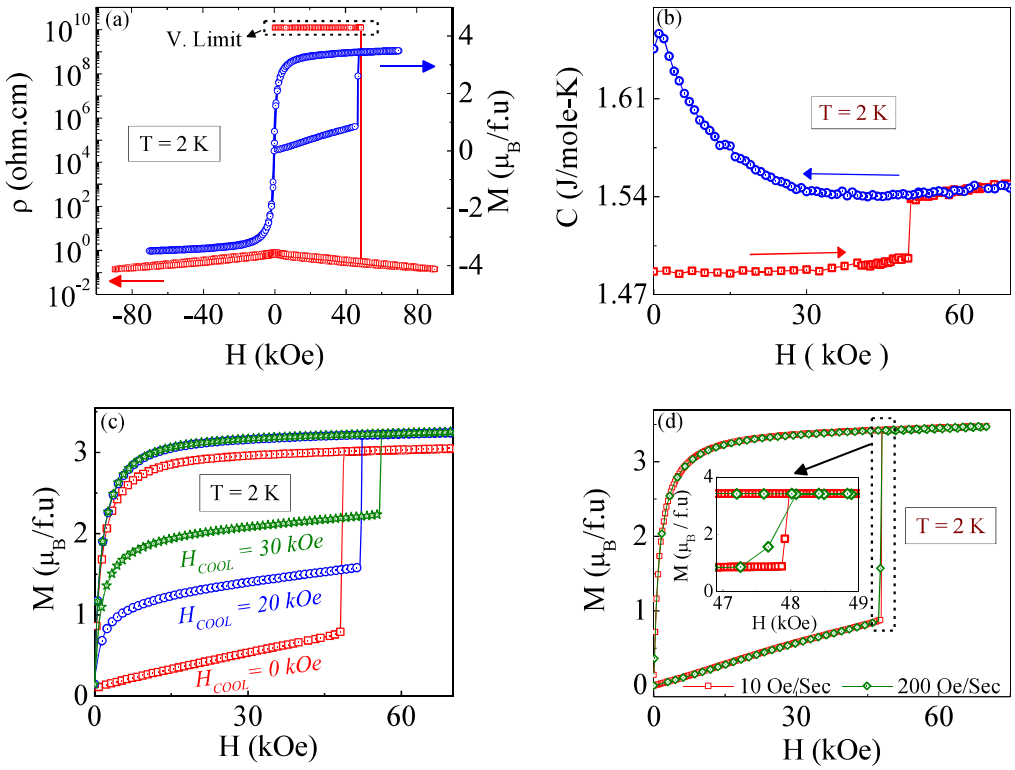


**Figure 3.18:** Ultra-Sharp metamagnetic transition: (a) Magnetization (and resistivity) vs magnetic field at 2 K; (b) variation of heat capacity with external magnetic field at 2 K. Here red and blue symbols are for the C(H)data taken during increasing and decreasing field respectively (c) Effect on isothermal magnetization with different cooling fields at 2 K. (d) Isothermal magnetization as a function of external magnetic field at 2 K temperature for different field sweep rate 10 Oe/sec and 200 Oe/sec.

ions ($3.85\mu_B$). It clearly indicates that the CO-AFM state melts completely on application of the magnetic field via metamagnetic transition near critical magnetic field $H_{CR}$. Temperature variation of $H_{CR}$ measured from M(H) isotherms is opposite to that of ZFC magnetization as shown in the inset of Fig. 3.17(a). The FM components present in the ZFC sample act as the nucleation center and grows at the expense of AFM components in an external magnetic field resulting in a metamagnetic transition at $H_{CR}$. The ZFC magnetization increases from 2 K to 50 K (due to increase of the thermal energy) and as a result $H_{CR}$ decreases from 47.8 kOe at 2 K to 34.5 kOe at 50 K. For $T > 60K$ the $H_{CR}$ increases due to reduction of ZFC magnetization. In the absence of AFM components, above $T_N$ (say 200 K), the field induced metamagnetic transition vanishes.

Fig. 3.17(b) shows the resistivity vs. magnetic-field isotherms measured at different temperatures. Interestingly, the isotherms measured at lower temperature (10 K) show sharp metamagnetic jump. With increasing temperature, the loop area reduces between increasing and decreasing field sweeps and at 100 K it almost disappears. Thus, we believe that field induced phase coexistence sustains up to $T_N$ ( 120 K). Another point to note here is that the system remains in the low resistive state even after removing the field for $T < 50K$. Also it is important to note is that our resistivity measurement is limited to $10^{10}$ ohm-cm in an external magnetic field. Due to resistivity measurement limitation we only able to measure the MR for temperature above 25 K. The MR is equal to $10^{12}$% ($10^{4}$%) at 25 K (80 K) for 45 kOe magnetic field as shown in Fig. 3.17(c) and will be even larger at lower temperatures.

To investigate the dynamics of the resistivity jumps we performed resistivity relaxation measurement at T= 25 K (sample was cooled in a zero field from room temperature down to 25 K) by applying three different magnetic fields ($H_1, H_2, H_3$) smaller than the $H_{CR}$ as shown in Fig. 3.17(d). The resistivity of the sample as a function of time shows that the resistivity jumps at different incubation time. The *incubation time*, time spent before the jumps, increases from 20 Sec to 1000 Sec with decrease in the applied magnetic field. For the fixed temperature (25 K) the elastic barrier height (arises due to the lattice strain at low temperature) increases with decrease in the applied magnetic field and for this reason the system needs more *incubation time* to overcome the elastic barrier for burst-like growth of the ferromagnetic fractions at the expense of the antiferromagnetic components. This type of relaxation behavior is generally the characteristics of standard martensitic transformations [92, 128–131].

### 3.3.4 Ultra-Sharp Metamagnetic Transition

Interestingly, the resistivity (and magnetization) vs. magnetic-field isotherms, [see Fig. 3.18(a)], at 2 K show exceptionally ultra-sharp steps with a width of 10 Oe (the smallest step kept during the measurement is 3 Oe). To explore the origin of this ultra-sharp metamagnetic transition we turn now to measure the heat capacity (C) with magnetic field. During the field increasing cycle the heat capacity show a step-like behavior around 48 kOe, as shown in Fig. 3.18(b), shows one-to-one correspondence with the step-like behavior observed in the magnetization and resistivity isotherms. This is opposite to the case observed in earlier studies where C decreases sharply with H at the transition point and was associated with the rise in temperature of the system due to release of energy that assists the abrupt field-induced transition [121, 128]. The sharp increase in the heat capacity at 48 kOe magnetic field rules out the possibility of exothermic temperature driven avalanche metamagnetic transition observed in our system and we believe that the system changes martenisitically as discussed in Fig. 3.17(d).

To ascertain the martensitic nature we also study the isothermal magnetization (at 2 K) for different cooling fields $H_{COOL}$ [see Fig. 3.18(c)]. The FM fraction increases with the cooling field and as a result interfacial elastic energy increases. Due to this the critical field increases with increasing the cooling field. At the same time the critical field decreases slightly when we increase the sweep rate from 10 Oe/sec to 200 Oe/sec for ZFC sample [see Fig. 3.18(d)]. This is because the lattice do not have adequate time to accommodate the induced interfacial strain between AF and FM domains for larger sweep rate (e.g., 200 Oe/sec) and a smaller magnetic field is required to break the energy barrier. Both these scenario indicates a ultra-sharp martensitic transition unlike at higher temperatures [see Fig. 3.17(a) and (b)].

### 3.3.5 Theoretical Simulation

In this section we discuss the physical origin of the extreme magnetoresistance using a two-band double exchange model including super-exchange ($J$) and electron-phonon coupling ($\lambda$). We consider following two-band double-exchange model [132] for $e_g$ electrons, Hund's coupled to $t_{2g}$ (Mn core spins) in a square lattice:

$$\begin{aligned} H &= -\sum_{\langle ij\rangle\sigma}^{\alpha\beta} t_{\alpha\beta}^{ij} c_{i\alpha\sigma}^{\dagger} c_{j\beta\sigma} - J_H \sum_i \mathbf{S}_i.\boldsymbol{\sigma}_i \\ &\quad + J_{AF} \sum_{\langle ij\rangle} \mathbf{S}_i.\mathbf{S}_j - \lambda \sum_i \mathbf{Q}_i.\boldsymbol{\tau}_i + \frac{K}{2} \sum_i \mathbf{Q}_i^2 + \sum_i \epsilon_i n_i. \end{aligned} \tag{3.1}$$

Here, $c$ ($c^{\dagger}$) is the annihilation (creation) operator for $e_g$ electrons and $\alpha$, $\beta$ are the two Mn-$e_g$ orbitals $d_{x^2-y^2}$ and $d_{3z^2-r^2}$. $t_{\alpha\beta}^{ij}$ are hopping amplitudes between nearest-neighbor sites in $x$ and $y$ directions: $t_{aa}^{x} = t_{aa}^{y} \equiv t$, $t_{bb}^{x} = t_{bb}^{y} \equiv t/3$, $t_{ab}^{x} = t_{ba}^{x} \equiv -t/\sqrt{3}$, $t_{ab}^{y} = t_{ba}^{y} \equiv t/\sqrt{3}$. $J_{\mathrm{H}}$ is the Hund's coupling between $e_{\mathrm{g}}$ electron spin $\sigma_i$ and $t_{2\mathrm{g}}$ spin $\mathbf{S}_{\mathrm{i}}$ at site $i$. The $e_{\mathrm{g}}$ electrons are also coupled to Jahn-Teller phonons $\mathbf{Q}_{\mathrm{i}}$ by $\lambda$. $J$ is antiferromagnetic super-exchange coupling between the $t_{2\mathrm{g}}$ spins. We treat $\mathbf{S}_{\mathrm{i}}$ and $\mathbf{Q}_{\mathrm{i}}$ as classical variables [133, 134] and adopt the double-exchange limit [132] , i.e. $J_H \to \infty$. We set K (stiffness of Jahn-Teller modes) and $|\mathbf{S}_{\mathrm{i}}|$ to be 1. This well studied model Hamiltonian qualitatively reproduces the phase diagram of manganites. We include the effect of the disorder by adding $\sum_i \epsilon_i n_i$ term to the Hamiltonian, where $\epsilon_i$ is the quenched disorder potential.

We applied Monte-Carlo simulation to the classical variables $\mathbf{S}_{\mathrm{i}}$ and $\mathbf{Q}_{\mathrm{i}}$, and an exact diagonalization scheme is employed to the fermionic sector ($e_g$ electrons). We used travelling cluster approximation (TCA) [135] based Monte-Carlo to handle large system size ($24 \times 24$ lattice). We annealed the randomized classical spins $\mathbf{S}_i$ and lattice distortions $\mathbf{Q}_i$ in an arbitrary quenched disorder configuration, and anneal

down from temperature $T = 0.1t$ ($t$ is the hopping parameter). The resistivity, in units of $\hbar a/\pi e^2$ ($a$: lattice constant) is obtained by calculating the $dc$ limit of the conductivity using the Kubo-Greenwood formalism [136, 137]. The magnetic structure factor at wave vector $\mathbf{q} = (0, 0)$ is calculated from $S(\mathbf{q}) = \frac{1}{N^2} \sum_{ij} \mathbf{S_i} \cdot \mathbf{S_j}\ e^{i\mathbf{q}\cdot(\mathbf{r_i}-\mathbf{r_j})}$. Physical quantities (resistivity and ferromagnetic structure factor) are averaged over ten different disorder configurations in addition to the thermal averages taken during the Monte Carlo simulations.

Our model Hamiltonian [138–141], effectively a lattice of Mn ions, qualitatively reproduces the phase diagram of manganites. For SCMO (and SSMO) like materials, involving two A-type elements [108], one generally add $\sum_i \epsilon_i n_i$ such that $\overline{\epsilon}_j = 0$ (e.g., $\pm\Delta_{\mathrm{A}}$) to model the A-site cationic disorder [138, 141]. Considering the fact that the $Sr^{2+}$ ions occupy randomly in the A-site in the polycrystalline SCSMO compound and being larger in size compared with both $Sm^{3+}$ and $Ca^{2+}$ creates chemical disorder. This is also evident from the HRTEM images at room temperature shown in Figs. 1(c) and (d). So in order to model SCSMO, we add $\sum_i \epsilon_i n_i$ at each Mn site picked from the distribution $P(\epsilon_i) = \frac{1}{4}\delta(\epsilon_i - \Delta) + \frac{3}{4}\delta(\epsilon_i + \Delta)$, where $\Delta$ is the quenched disorder potential. We add a Zeeman coupling term $-\sum_i \mathbf{h} \cdot \mathbf{S}_i$ to the Hamiltonian in an external magnetic field, where $\mathbf{S_i}$ are Mn $t_{2g}$ spins to analyze the magnetoresistance. We measure $J$, $\lambda$, $\Delta$, $h$ and temperature ($T$) in units of kinetic hopping parameter $t$. The estimated value of $t$ in manganites is 0.2 eV [138].

A spin-fermion Monte Carlo (MC) technique based on the travelling cluster approximation [135] (TCA) is used on a two dimensional 24×24 lattice (see supplementary section II for details). We use $J/t = 0.1$ and $\lambda/t = 1.65$ that reproduces the CE-CO-OO-I phase [140] at electron density $n = 1 - x = 0.5$. The electron density is the number of itinerant $e_g$ electrons per Mn site in our calculations. The system, as shown in Figs. 3.19(a) and (b), remains insulating at low temperatures for $\Delta = 0.3$ and $h = 0$ and the ferromagnetic structure factor S(0,0) is ∼0.001 (for an

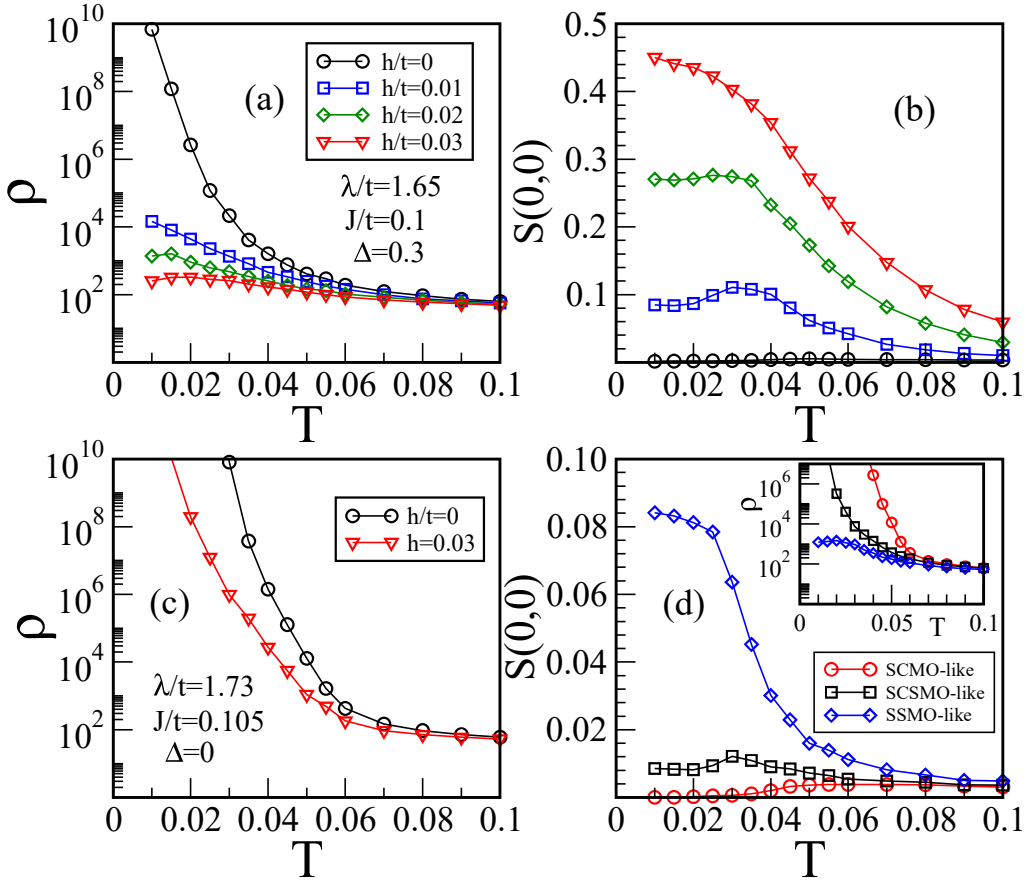


**Figure 3.19:** Temperature dependence of (a) the resistivity $\rho$ in units of $\hbar a/\pi e^2$ and (b) the FM structure factor S(0,0) in different external magnetic field $h/t$ values for $\lambda/t$= 1.65, $J/t$ = 0.1 and $\Delta$ = 0.3 (SCSMO-like materials). Legends in (a) and (b) are the same. Electron density is fixed at $n$ = 0.5 in all figures. (c) Temperature dependence of $\rho$ for $\lambda/t$= 1.73, $J/t$ = 0.105 and $\Delta$ = 0 (SCMO-like materials). (d) Temperature dependence of FM structure factor S(0,0)[inset: resistivity] for three sets of parameter in a very small magnetic field $h$=0.002 (parameters for SSMO-like materials: $\lambda/t$= 1.57, $J/t$ = 0.095 and $\Delta$ = 0.3). See the text for details.

outline of the resistivity and the magnetic structure factor calculations please see Supplementary Section II).

The resistivity at low temperatures decreases with magnetic field $h$ [Fig. 3.19(a)] similar to our experimental results. This is due to the increase of the FM correlations at low temperatures [Fig. 3.19(b)]. On the other hand, SCMO-like materials [Fig. 3.19(c)] remains insulating at all temperatures even for $h$ = 0.03. Recall that SCMO (SSMO) has smaller (larger) bandwidth than SCSMO. In our model calculations larger $\lambda/t$ (and $J/t$) corresponds to smaller bandwidth or vice versa. For

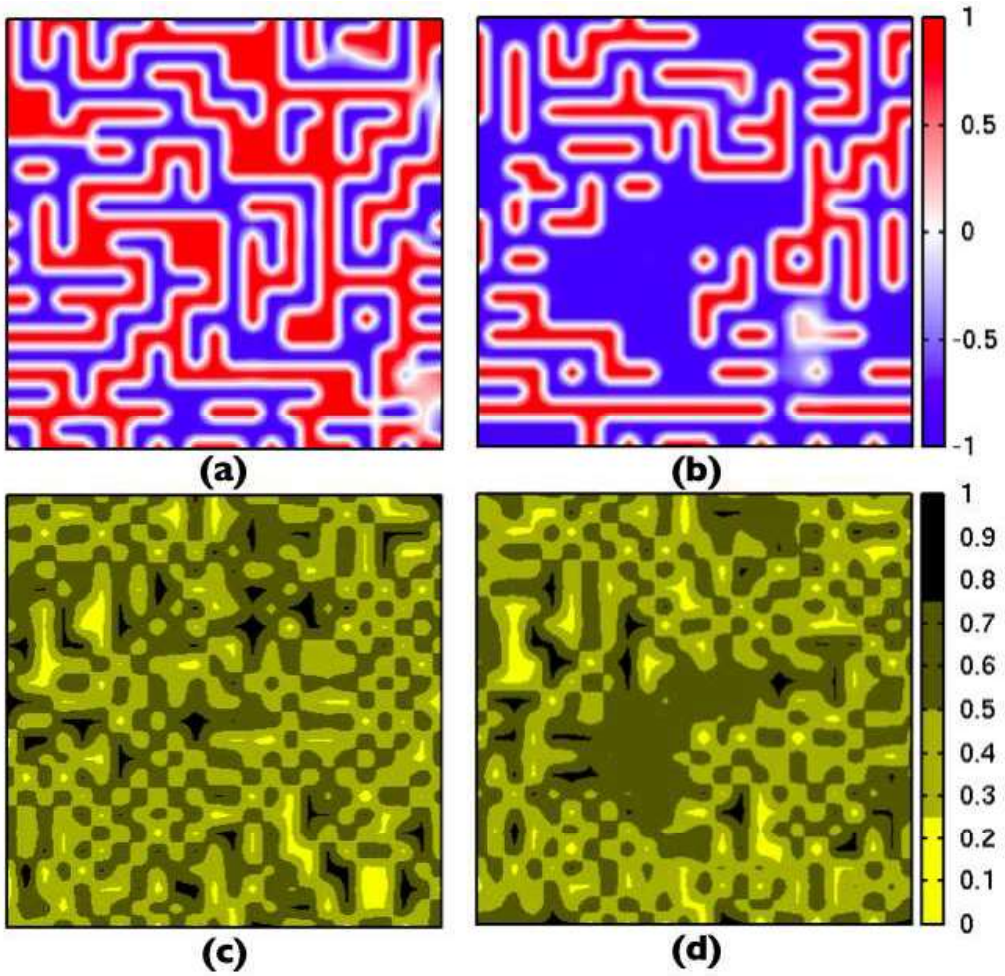


**Figure 3.20:** (a) and (b) The $z$ components of simulated Mn ($t_{2g}$) spins; (c) and (d) electron density for each site on a 24×24 lattice at $T = 0.01$ using $\lambda/t$= 1.65, $J/t$ = 0.1 and $\Delta = 0.3$. In (a) and (c) $h/t = 0$, and in (b) and (d) $h/t = 0.01$.

clarity we use $\Delta = 0$ (due to the small mismatch between Sm and Ca ionic radii) and set $\lambda/t$= 1.73, $J/t = 0.105$ for SCMO-like materials. For SSMO-like materials we set $\Delta_A = 0.3$ and use $\lambda/t$= 1.57, $J/t = 0.095$. The FM correlations at low temperatures increases and the resistivity decreases from SCMO-like to SCSMO-like to SSMO-like like materials [Fig. 3.19(d)] similar to the experimental results qualitatively [108, 119].

We turn now to understand the magnetoresistance in SCSMO by plotting Monte Carlo snapshots obtained at $T = 0.01$. For $h = 0$ the system remains insulating due to the CE-type correlations without any significant homogeneous charge disordered

regions [see Figs. 3.20 (a) and (b)] in the system. For $h = 0.01$, ferromagnetic clusters coexist with zig-zag ferromagnetic chains and the electron density is roughly homogeneous ($\sim$0.65) within the ferromagnetic clusters [see Figs. 3.20 (c) and (d)]. Eventually, the ferromagnetic clusters get connected with each other at reasonable large magnetic fields unlike SCMO-like materials for which resistivity decreases at lower temperatures. So, overall the disorder due to Sr ions present in SCSMO weakens the CE-type state of SCMO and seeds the ferromagnetic charge-disordered clusters and result in a large magnetoresistance in SCSMO samples.

## 3.4 Summary

In summary, we have investigated the metamagnetic properties of the polycrystalline $Sm_{0.5}(Ca_{0.5-x}Sr_x)MnO_3$ compounds through isothermal magnetization and resistivity measurements. The presence of ultra-sharp jump at low temperature ($T < 5K$) in both isothermal resistivity and magnetization suggest the strong spin and electronic coupling in the systems. The sweep rate dependence of the critical field ($H_{Cr}$) is consistent with the martensitic scenario. The increased phase separation with increase of the average A-site ionic radius $\langle r_A \rangle$ is perceived from the magnetotransport and magnetization data. The existence of this phase separation is also clear from the exchange bias measurement. The presence of this ferromagnetic component act as the nucleation center in the COAFM background for the burst like growth of the COAFM fraction to FM fraction. The increased FM fraction with increase of $\langle r_A \rangle$ is responsible for the decease of the $H_{Cr}$. This whole scenario has been explained by a phenomenological picture.

In the second part of the chapter, we have seen that by controlling electronic phase separation in narrow bandwidth CO-AFM material a record value of magnetoresistance ($\sim 10^{15}$% at 10 K in a 90 kOe external magnetic field) till date is obtained

in SCSMO polycrystalline compound. We also observed magnetic field induced ultra-sharp meta-magnetic transition at low temperatures. The many order of magnitudes higher MR than any other magnetoresistive materials reported so far will be of great to importance improve the functional spintronic materials such as magnetic field sensors, magnetic switches and magnetic memory devices.

# CHAPTER 4

# Disorder induced modification of magnetic and magnetotransport properties in $(La_{1-x}Y_x)_{0.7}Ca_{0.3}MnO_3$ compounds

## 4.1 Introduction

Usually, CMR occurs near the first order magnetic transitions. In 1994 Jin et al. [142] have observed huge MR of about 1400% around 200 K for 60 kOe magnetic field in $La_{0.67}Ca_{0.33}MnO_3$ thin film near paramagnetic to the ferromagnetic transition temperature. In a review article Ramirez [143] has also discussed the CMR near the paramagnetic to ferromagnetic transition. Recently Das et al. have shown the enhancement of MR, in charge ordered nanoparticles because of the appearance of surface ferromagnetism [144] and in core-shell nanostructure because of the influence of ferromagnetism on antiferromagnetic charge ordered clusters [145].

The motivation of the present study is to find out whether MR can be enhanced by introducing disorder in a system, in contrast to generally observed facts. According

to Rodrigues-Martinez and Attfield [146] disorder can be quantified by the variance of the A-site ionic radii distribution, $\sigma^2 = \sum y_i r_i^2 - < r_i >^2$, where $< r_i >$ is the average A-site ionic radius, $y_i$ is the fractional occupancies of the $i^th$ ion in A-site . Dong et al. [147] have shown that A - site cation size disorder brings the ferromagnetic system into short- range cluster glass state. Rivas et al. [148] have also shown that quenched disorder arising from the A-site ionic disorder suppress the first order magnetic phase transition. In an another report Hwang et al. [19] described a universal behavior of $R_{0.7}A_{0.3}MnO_3$ compounds which show the transition of the ferromagnetic system to a spin glass state below a particular A-site ionic radius $< r_A >$. Reduction of $< r_A >$ leads to the decrease of $Mn - O - Mn$ bond angle which enhance lattice distortion. Following their work Teresa et al. [149] have also showed the evolution from long range ferromagnetic (FM) to spin glass (SG) insulator state in $(La_{1-x}Tb_x)_{2/3}A_{1/3}MnO_3$ compound. Thus tuning lattice distortion by changing A -site ionic radius together with quenched disorder one can change the transition from first order to second order. It enhances disorder resistivity because of the magnetic disorder. This enhanced magnetic disorder can be suppressed by applying external magnetic field and may lead to the enhancement of MR.

Among the different manganite families of materials one of the most well known CMR compounds is $La_{0.7}Ca_{0.3}MnO_3$ which has first order ferromagnetic transition [150] around curie temperature $T_C \sim 223K$. It is a strongly correlated system having strong electron-phonon coupling and shows strong Jahn-Teller (JT) distortion [151]. This correlation can be modified by introducing $Y^{3+}$ ion in place of $La^{3+}$. In spite of being CMR material, the $La_{0.7}Ca_{0.3}MnO_3$ material has only $3.7 \times 10^2\%$ MR at 233 K for the 60 kOe magnetic field [152]. To increase MR value we have prepared and studied in detail transport and magnetotransport properties in $(La_{1-x}Y_x)_{0.7}Ca_{0.3}MnO_3$ compounds with different Y concentrations.

Again the coupled interactions between different degrees of freedom produces nearly

degenerate ground states of competing phases i.e. phase inhomogeneity. Among the various forms of phase separation, preformation of ferromagnetic clusters well above the curie temperature seems to be particular important. This often leads to Griffiths singularity [158] which appears below a characteristic temperature $T_{GP}$. Originally, the Griffiths phase was proposed for a randomly diluted ising ferromagnet with nearest-neighbour exchange bonds of strength J and 0 with probability $p$ and $(1-p)$ respectively. Above the percolation threshold ($p_c$), long range ferromagnetic order sets in at $T_C(p)$ which is below the ordering temperature of undiluted system $T_C(p=1)$, recognized as $T_{GP}$. In the region $T_C(p) < T < T_{GP}$, the thermodynamic properties are analytic and the system shows spatially distributed small ferromagnetic (FM) clustering of different sizes. The Griffiths behavior has been observed in several systems including layered manganites [159], heavy fermions [160, 161], spin glass systems [162], hole doped manganites [163–165]. For formation of Griffiths phase one of the prerequisite component is the quenched disorder which intrinsically present in manganites because of the random distribution of valences and cations of different sizes at $R/A$ sites. Moreover, the size mismatch of $R/A$ ions also modifies the $Mn-O-Mn$ bond angles and length and therefore FM-DE and AFM-SE also modifies [166] although the strength of AFM interaction is about a factor of two smaller than the FM interaction [167]. Depending upon the hole doping ($Mn^{4+}$) and electron phonon coupling the relative strength of FM and AFM interactions changes [168] and sometimes even becomes comparable. Therefore, for such a system with competing FM and AFM interactions, T-p phase diagram proposed by Griffiths modifies and GP is confined in a restricted region where FM interaction dominates [163, 165]. On the other hand, in the AFM dominated region a non-Griffiths like phase appears as reported recently in different systems. Currently, a non-GP phase has been reported in several systems where competing FM-AFM interactions are present like cobaltites [169], double-perovskites [170], manganites [66, 171] etc. Jiang et al [165]. has described that depending upon the

AFM/FM phase fraction system evolve from GP to NGP phase. In another study, Zhou et al [172]. proposed that weakening of the antiferromagnetic interactions with reduction of particle size converts the system from non-Griffiths-like phase to Griffiths-like phase above the curie temperature.

Therefore competition between the FM and AFM interactions are playing the main role for conversion from non-GP to GP phase [163–165]. Although a systematic study regarding this phase transformation has been addressed rarely in the literature. Among the different manganite families, one of the most well known ferromagnetic double exchange (DE) dominated system is $La_{0.7}Ca_{0.3}MnO_3$ [150]. Here there is the dominance of DE interactions between $Mn^{3+}$ and $Mn^{4+}$ ions compared with antiferromagnetic superexchange interactions (SE) between $Mn^{3+}/Mn^{3+}$ and $Mn^{4+}/Mn^{4+}$ ions. So, here idea is to modify the strength of the DE and SE interactions by replacing $La^{3+}$ ions with $Y^{3+}$ ions of less ionic radii which will enhance the relative strength of SE interactions by increasing the electron phonon coupling. In this regard the series $(La_{1-x}Y_x)_{0.7}Ca_{0.3}MnO_3$ $(x = 0, 0.3, 0.4, 0.5, 0.6)$ has been prepared and a systematic study has been carried out.

Here the study reveals that with $Y^{3+}$ doping, A-site ionic radius decreases $\langle r_A \rangle$. It is also well known that $\langle r_A \rangle$ is proportional to the $Mn-O-Mn$ bond angle [99, 104]. Thus $Y^{3+}$ doping basically reduces the $Mn-O-Mn$ bond angle. Again with $Y^{3+}$ doping the distortion of $MnO_6$ octahedra increases which enhances the electron phonon coupling [99]. This increased electron phonon coupling as well as decreased $Mn-O-Mn$ bond angle enhances the effective SE interaction. The increase of the effective SE interactions drives the system gradually from GP to non-GP phase above the critical Y doping $x_C$=0.5.

Recently, LFMR effect have drawn several interests from both fundamental and application perspectives [173, 174]. In hole doped polycrystalline manganites, magnetoresistance originates from two different contributions. The first component is dom-

inating close to the ferromagnetic ordering temperature and arises due to the zener double exchange mechanism between two adjacent manganese ions [176]. Whereas the other component for which a rapid drop in resistance at low magnetic field occurs much below $T_C$, arises mainly due to the intergrain spin polarized tunneling mechanism (SPT). Therefore, to increase LFMR one needs a system with increased grain boundaries as well as high degree of spin polarization. Again, grain boundary brings with it different kind of disorders which decreases the degree of spin polarization. So, is there any other origin to increase the LFMR other than the presence of physical grain boundary?.

It has been reported that decrease lattice distortions favours the formation of ferromagnetic clusters [69]. These clusters being ferromagnetic, it will have high degree of spin polarization which may help to increase SPT. Although a lot of studies regarding the effect of particle sizes on LFMR has been carried out but the effect of decreasing the lattice distortions with reduction of particle size on LFMR has been addressed rarely. One of the prototype CMR system is $La_{0.7}Ca_{0.3}MnO_3$ which is a strongly correlated system with strong electron-phonon coupling [151]. Very recently it has been shown that this electron-phonon coupling can be enhanced via $Y^{3+}$ doping in place of $La^{3+}$ by increasing lattice distortions [69]. Moreover, the size mismatch of $R/B$ ions also changes the $Mn-O-Mn$ bond length and bond angle which modifies the strength of ferromagnetic double exchange and antiferromagnetic superexchange interactions. Depending upon the $Mn^{4+}$ doping and electron-phonon coupling the relative strength of ferromagnetic and antiferromagnetic interactions changes [177]. Zhou et al [172]. has proposed that the reduction of particle size weakens the antiferromagnetic interactions and changes the system from non-Griffiths phase to Griffiths phase. The weakening of AFM interaction in nanodimension also gives rise to the enhancement of magnetoresistance. It is also well known that due to the finite size effect in nanoregime the distortions can be easily modified and by decreasing lattice distortions one can also enhance the

magnetoresistance [178].

Thus motivation of the present study is to find a system where large lattice distortions is present. Our objective is to reduce this lattice distortions by making nanoparticles and study their magnetotransport properties. Thus, for the study we prepare $(La_{0.5}Y_{0.5})_{0.7}Ca_{0.3}MnO_3$ compound as this is a system where enhanced lattice distortions due to $Y^{3+}$ doping in place of $La^{3+}$ changes the ground state of $La_{0.7}Ca_{0.3}MnO_3$ from metallic to insulator [69]. Moreover, this insulator state is unstable towards magnetic field. However, the effect of particle size on the magnetotransport properties of $(La_{0.5}Y_{0.5})_{0.7}Ca_{0.3}MnO_3$ compound are overlooked. In this article, we present the low field enhancement of magnetoresistance with reduction of particle size of $(La_{0.5}Y_{0.5})_{0.7}Ca_{0.3}MnO_3$ compound. Our study shows that enhancement of ferromagnetic cluster size with reduction of particle size is responsible for this enhancement of magnetoresistance.

## 4.2 Enhancement of the magnetoresistive property by introducing disorder in the polycrystalline $(La_{1-x}Y_x)_{0.7}Ca_{0.3}MnO_3$ compound

### 4.2.1 Sample Preparation and Characterization

All the polycrystalline bulk samples $(La_{1-x}Y_x)_{0.7}Ca_{0.3}MnO_3$ $(x = 0, 0.4, 0.5, 0.6, 1)$ has been prepared by the well known sol- gel method. To prepare the samples high purity ($> 99.9\%$) $La_2O_3$, $Y_2O_3$ and $CaCO_3$ were used as raw materials. An appropriate amount of pre-heated oxides and carbonate were converted to their nitrates by adding nitric acid and an aqueous solution of them were prepared. After that, all the solutions were mixed together with required amount of citric acid and

was heated at 80 $^0$C - 90 $^0$C in a heat bath until the gel is formed. After decomposing the gel black porous powder was obtained which after preheating at 400 $^0$C were pelletized and heated finally at 1300 $^0$C for 36 hours to make bulk polycrystalline samples.

### 4.2.2 Experimental Results and Discussion

Phase purity of all the samples was verified by performing room temperature x-ray diffraction (radiation Cu-K$\alpha$ of wavelength $\lambda = 1.54$ $\mathring{A}$) measurements. Scanning electron microscopy (SEM) measurements were performed to see the morphology and grain size of the samples. Magnetic measurements were carried out using SQUID VSM. Electrical transport and magnetotransport measurements were performed using four probe technique in longitudinal geometry on the bar-shaped samples.

Room temperature x-ray diffraction study confirms the single phase nature of the polycrystalline compounds $(La_{1-x}Y_x)_{0.7}Ca_{0.3}MnO_3$ ($x = 0, 0.4, 0.5, 0.6, 1$). All these compounds belong to *'Pnma'* space group. Lattice parameters of the compounds were determined by Profile fitting the XRD data using FULLPROF software. For a representative X-ray diffraction pattern, XRD of $x = 0.5$ compound along with simulated data has been shown in Fig. 4.1 (A). From the lattice parameters, orthorhombic distortion defined by $\Delta = \frac{a+b-c/\sqrt{2}}{a+b+c/\sqrt{2}}$ and unit cell volume was calculated and their corresponding variation is indicated in Fig. 4.1 (B). Enhancement of lattice distortion and decrease of unit cell volume have been observed with the increase of $Y$ concentration. SEM images show the well-connected micron size grain of the compounds and a representative figure for $x = 0.5$ compound has been shown in the inset of Fig. 4.1 (A).

Electrical transport and magnetotransport properties in perovskite manganite materials are greatly influenced by the lattice distortion. Measurement of resistivity

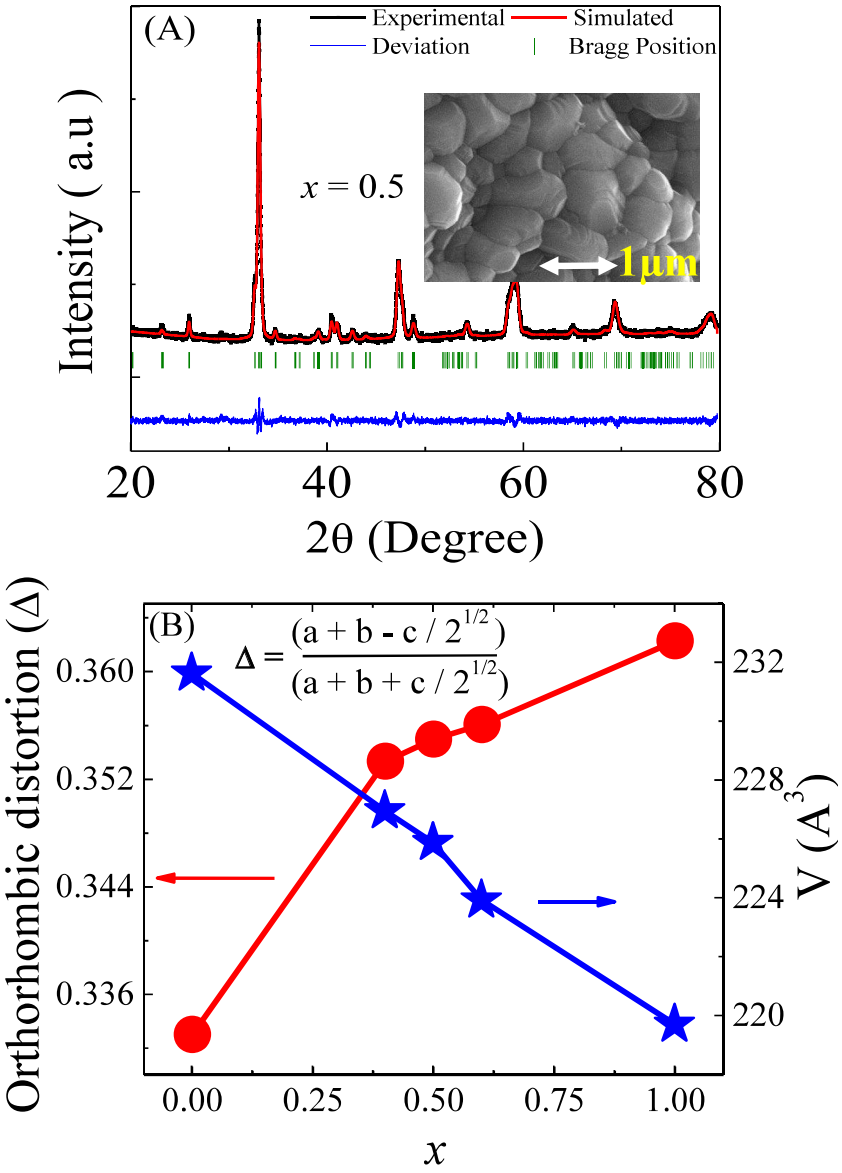


**Figure 4.1:** (A) X-ray diffraction pattern with profile fitted data of the $(La_{1-x}Y_x)_{0.7}Ca_{0.3}MnO_3$ ($x = 0.5$) compound and its SEM image in the inset (B). Orthorhombic distortion and unit cell volume with different different $Y$ concentrations

as a function of temperature $\rho(T)$ of all the polycrystalline bulk samples were performed in the absence of as well as in the presence of 90 kOe external magnetic field (Fig. 4.2). All these measurements were carried out during warming cycle from low temperature (2 K) to room temperature after cooling in zero field. From zero field data, it can be seen that with an increase of Y concentration from $x = 0$ to $x = 0.4$ metal to insulator transition temperature ($T_{MI}$) decreases from 220 K to 100 K. With further increase of $Y$ concentration, $x = 0.5$ and above metal-insulator transi-

tion vanishes. Such a modification from metallic to a an insulator state corresponds to the conversion of the system from ferromagnetic to glassy state [153]. As a result from $x = 0.5$ with increasing $x$ the length over which magnetic moments are correlated ferromagnetically decreases significantly which causes the insulating nature of the compounds. On application of 90 kOe external magnetic field $\rho$ values do not change significantly in the samples spontaneously melted sample. This field value has affected only $T_{MI}$ and changes it from 220 K to 250 K in $x = 0$ and 100 K to 150 K in $x = 0.4$ samples respectively. Surprisingly a huge suppression of resistivity of ($\sim 10^6$) order has been observed in $x = 0.5$ sample on the application of 90 kOe magnetic field at around 50 K. However, the magnetic field has a less impact on $\rho(T)$ for the sample $x = 0.6$.

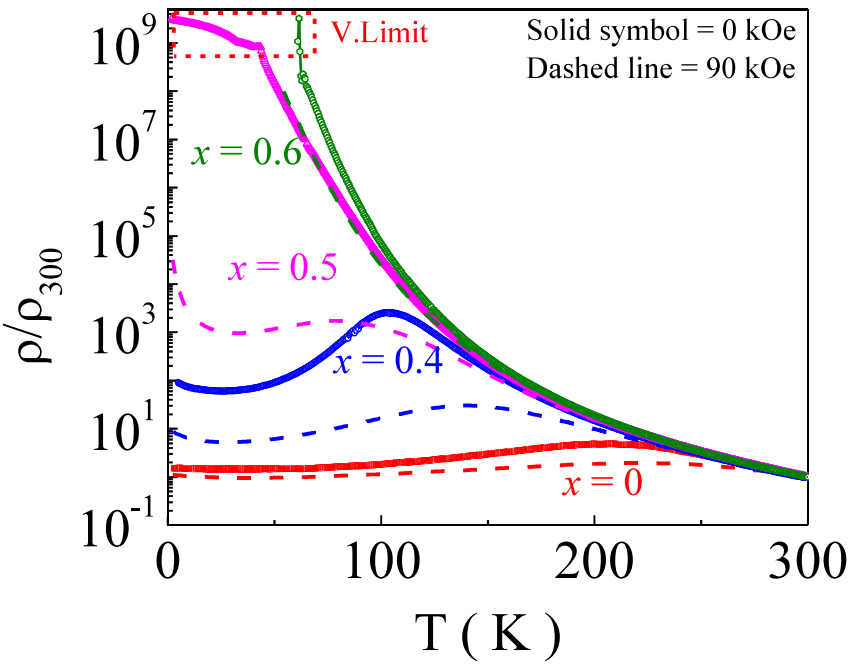


**Figure 4.2:** (A) Temperature variation of reduced resistivity of the polycrystalline $(La_{1-x}Y_x)_{0.7}Ca_{0.3}MnO_3$ compounds with $x = 0, 0.4, 0.5, 0.6$ in absence of magnetic field (solid symbol) and in presence of 90 kOe field (dotted line). Here resistivity data of $x = 1$ composition has not been shown since 90 kOe magnetic field has no significant modification in resistivity.

The magnetization measurement as a function of temperature [M(T)] and also as a function of field [M(H)] were performed in all the samples. Fig. 4.3(A) shows the zero field cooled warming (ZFCW) and field cooled warming (FCW) magnetization

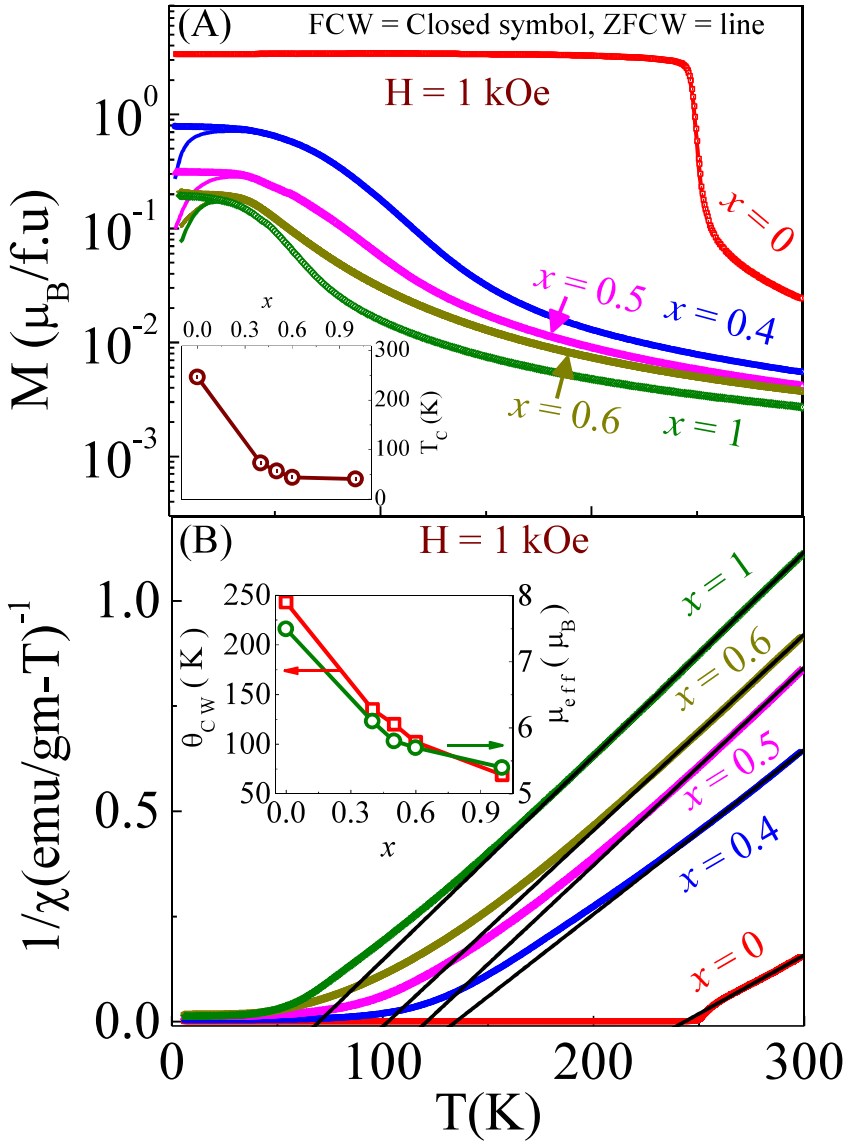


**Figure 4.3:** (A) Zero field cooled warming (ZFCW) and Field cooled warming (FCW) magnetisation data as a function of temperature of the $(La_{1-x}Y_x)_{0.7}Ca_{0.3}MnO_3$ $(x = 0, 0.4, 0.5, 0.6, 1)$ samples. Inset in the figure indicates the modification of $T_C$ with Y-concentration (B) Variation of inverse susceptibility with temperature of the samples and their corresponding Curie weiss fitted data. Black lines are the curie-weiss fitted curve. Variation of curie weiss temperature and effective paramagnetic moment with Y-concentration is shown in the inset.

as a function of temperature in the presence of 1kOe external magnetic field of the samples $x = 0, 0.4, 0.5, 0.6, 1$. Enhancement of bifurcation between ZFC and FCW with '$x$' has been observed which is one of the signatures of glassy behavior. Reduction of curie temperature ($T_C$) and suppression of magnetization is observed in FCW magnetization with increasing Y concentration. With the increase of '$x$',

A-site ionic radius decreases which result in the decreases of $Mn-O-Mn$ bond angle and an increase of $MnO_6$ octahedra distortion. This distortion diminishes the strength of double exchange (DE) interaction between Mn ions around the octahedra and hence favors antiferromagnetic insulator state to be a ground state rather than the ferromagnetic metallic state. At the same time with increase of $Y$ concentration $\sigma^2$ increases from $2.7 \times 10^{-4}$ for $x = 0$ to $3.7 \times 10^{-3}$ for $x = 0.5$. This enhanced $\sigma^2$ in $x = 0.5$ randomizes the distribution of $Mn-O-Mn$ bond angle which results in the decrease of the length over which ferromagnetic metallic correlation exists. These correlated regions are ferromagnetic clusters which interact with each other by dipolar interaction. The anisotropic nature of this dipolar interaction randomizes the clusters' orientations that suppress the magnetization and enhances the electrical resistivity.

To understand more clearly magnetic interaction between Mn moments, paramagnetic region of inverse *dc* susceptibility (H/M) with temperature data was fitted with Curie-Weiss law of the form $\chi = C/(T-\theta_{CW})$ and $C = \mu_{eff}^2/3k_B$ where $\mu_{eff}$ is effective magnetic moment in Bohr magnetron and $\theta_{CW}$ is paramagnetic curie temperature. Fig. 4.3 (B) shows the linear fitting of $1/\chi$ vs T data with Curie-Weiss law for all the samples. From the fitting, Curie-Weiss temperature ($\theta_{CW}$) and effective paramagnetic moment ($\mu_{eff}$) has been calculated which has been shown in the inset of Fig. 4.3(B). For the parent compound (x=0) $\theta_{CW} \sim T_C$ but for other concentrations larger values of $\theta_{CW}$ compared to their corresponds $T_C$ has been observed. The calculated $\mu_{eff}$ shows the gradual decreasing nature with x. Another point here is to be noted that the values of the $\mu_{eff}$ of the samples are higher than the theoretical value of $4.62\mu_B$ for an effective Mn ion. This result indicates that the high-temperature paramagnetism comes from the individual magnetic entities containing more than one Mn ions. These results imply that the samples consist of FM clusters which forms at higher temperature ($> T_C$) [155, 171].

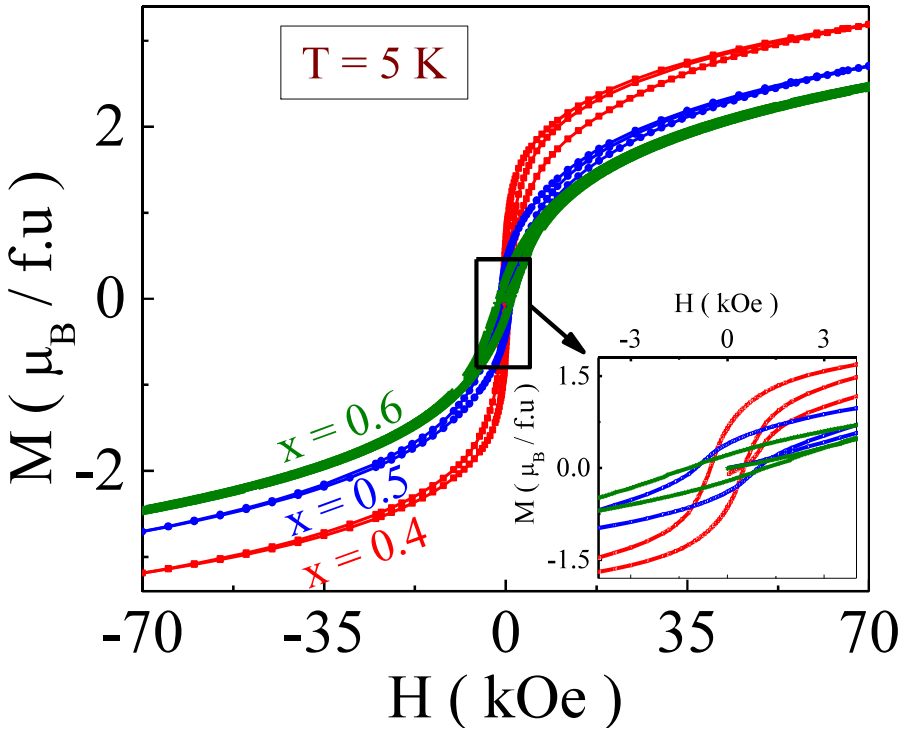


**Figure 4.4:** Magnetisation as a function of magnetic field at 5 K temperature of the samples x=0.4, 0.5 and 0.6. The inset shows the zoomed portion near the origin to show enhancement of coercivity with increase of $x$

To grasp the low-temperature ground state of the samples, isothermal magnetization measurements (Fig. 4.4) were performed at T = 5 K and the external magnetic field was up to 70 kOe. Nearly saturation tendency has been observed up to the composition $x = 0.4$ but at and above $x = 0.5$ there is a gradually increasing tendency in the magnetization even at 70 kOe field. Huge enhancement of coercivity and reduction of magnetisation value at H = 70 kOe with increasing '$x$' has been observed which are the signature of the enhanced magnetic disorder.

Finally, magnetotransport studies were carried out from where magnetoresistance $MR(\%)$ calculations were performed. Since in the present case conservative definition of magnetoresistance $MR(\%) = \frac{R(H)-R(0)}{R(0)} \times 100$ saturates at 100% in the low temperature and at high field region, here other useful definition [156], generally used for CMR materials has been considered i.e. $MR(\%) = \frac{R(H)-R(0)}{R(H)} \times 100$, where R(H) is resistance of magnetic field and R(0) is resistance in absence of magnetic

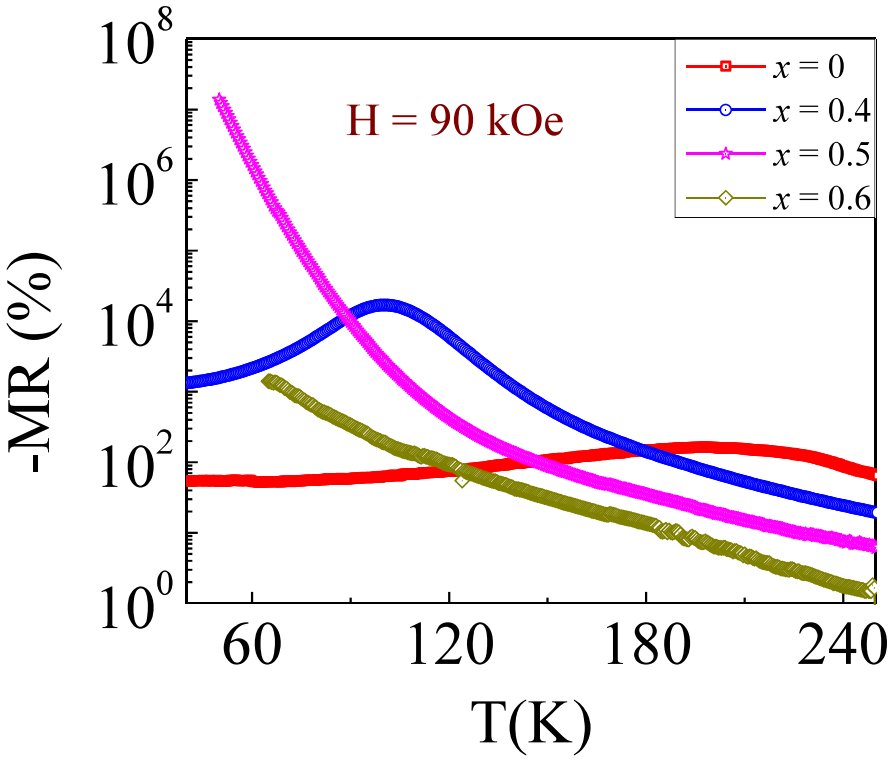


**Figure 4.5:** Variation of magnetoresistance with temperature of the samples with x=0, 0.4, 0.5, 0.6

field. Fig. 4.5 shows the temperature variation of MR, calculated from zero field and 90 kOe external field resistivity data, of the samples. Compare to $x = 0$ compound, enhancement of MR occurs for all other samples in the entire temperature range. At the low temperature (below 80 K), especially for $x = 0.5$ compound, the MR value supersedes the value of all the samples and it becomes gigantic $10^7\%$ at 50 K.

Field variation of MR at 80 K (Fig.4.6) has also been studied for the $x = 0.4, 0.5$ and 0.6 compounds. The MR value at 90 kOe magnetic field increases from $6 \times 10^3\%$ in $x = 0.4$ compound to $3.6 \times 10^4\%$ in $x = 0.5$ compound respectively, whereas it reduces in $x = 0.6$ to $7 \times 10^2\%$ . In the inset of Fig.4.6 resistance as well as magnetization at 80 K with the external magnetic field has been shown. The values of resistance and magnetization remain almost unchanged even after field cycling which shows the reversible nature of the compound.

To know the origin of this extraordinary enhancement of MR in $x = 0.5$ com-

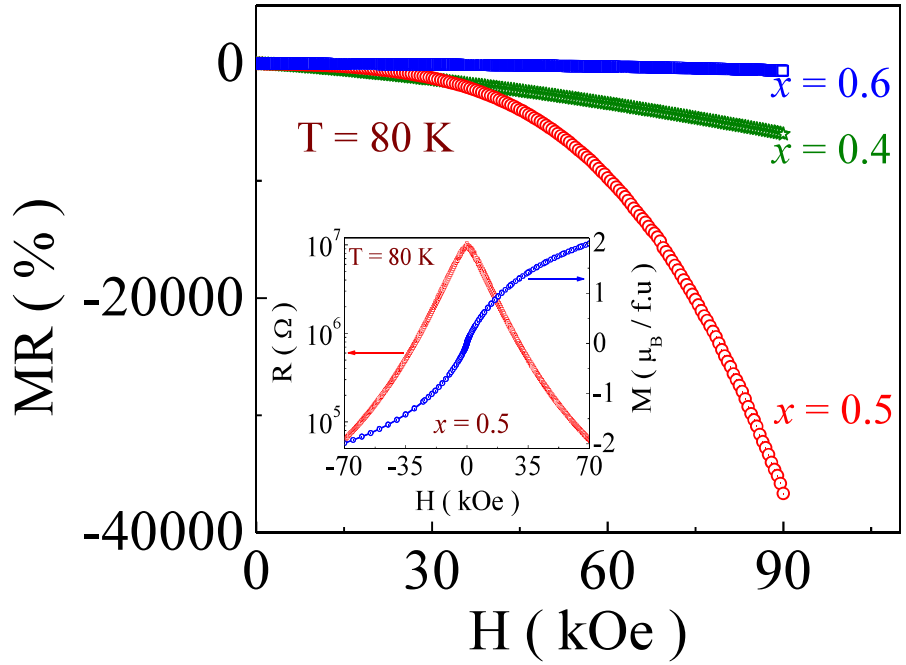


**Figure 4.6:** MR as a function of magnetic field at 80 K temperature for $x = 0.4, 0.5, 0.6$ compounds and in the inset, variation of resistance and magnetisation for $x = 0.5$ compound with magnetic field has been shown

pound compared with other samples, isothermal magnetization measurements of $x = 0.4, 0.5$ and 0.6 compounds were carried out. As discussed earlier from susceptibility data that all the samples consist of ferromagnetic clusters above $T_C$, M(H) at various temperatures above $T_C$ were measured. Considering these magnetic clusters to be nearly non-interacting much above the transition temperature M(H) data was fitted with modified Langevin function of the form $M(H) = N\mu L(\frac{\mu H}{k_B T}) + AH$, where "L(x)" is the Langevin function, "$\mu$" is the average magnetic moment of the clusters and "N" is the number density of the clusters. The magnetization data fitted well with this modified Langevin function. From the fitting of M(H) data average cluster moment $\mu$ and cluster density $N$ at different temperatures have been estimated which is shown in Fig. 4.7 (A) and as a representative plot here fitting with M(H) data at 150 K of $x = 0.4, 0.5$ and 0.6 samples has been shown in Fig. 4.7(B).

It is clear that cluster size depends on both temperatures as well as on composition i.e

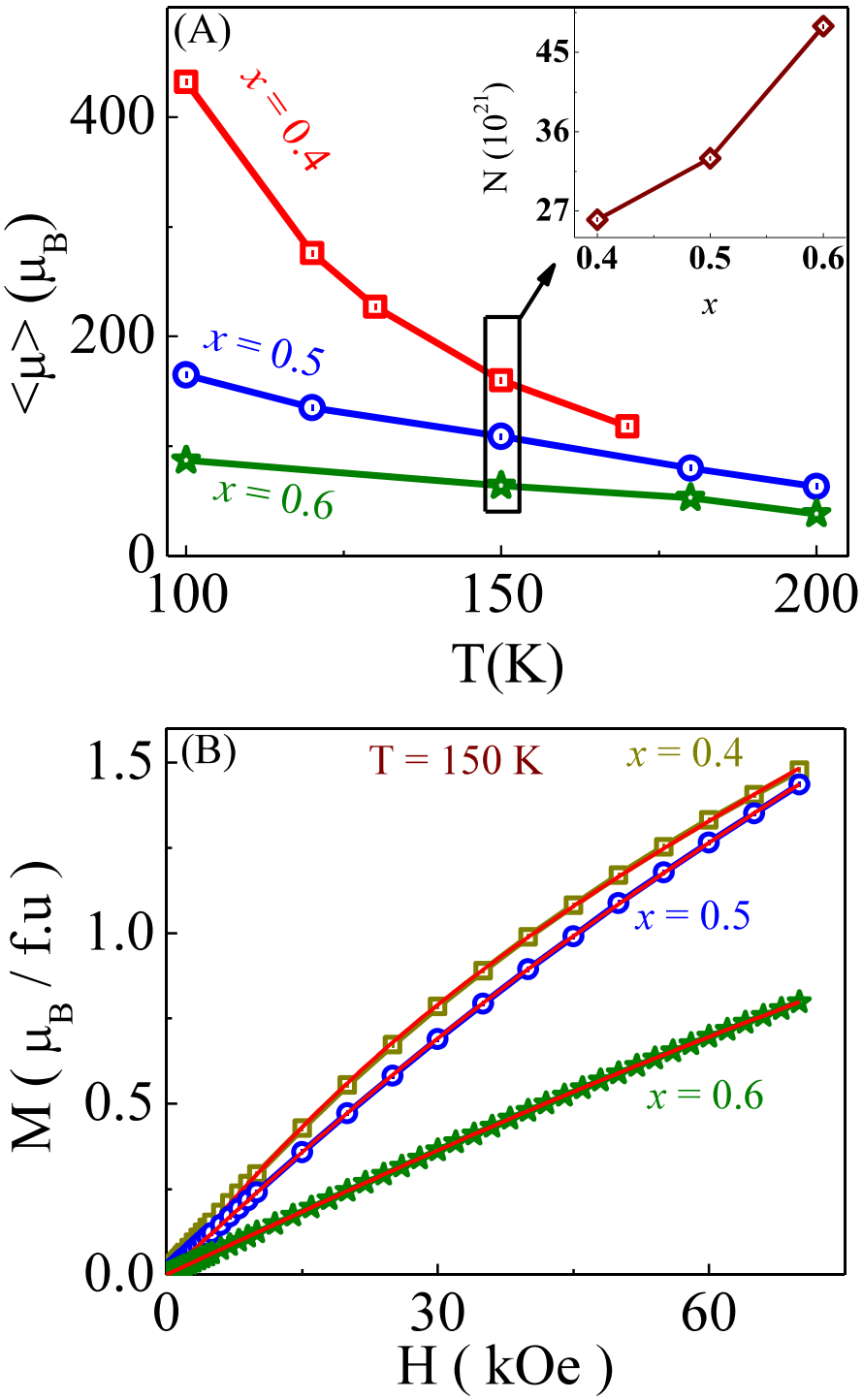


**Figure 4.7:** (A) Variation of magnetic cluster size with temperature of $x = 0.4, 0.5$ and 0.6 compound, and in the inset variation of cluster density at 150 K temperature of the $x = 0.4, 0.5$ and 0.6 compounds has been shown (B) Fitting of M(H) data with modified Langevin function at 150 K of $x = 0.4, 0.5$ and 0.6 samples where solid red lines are the fitted curves

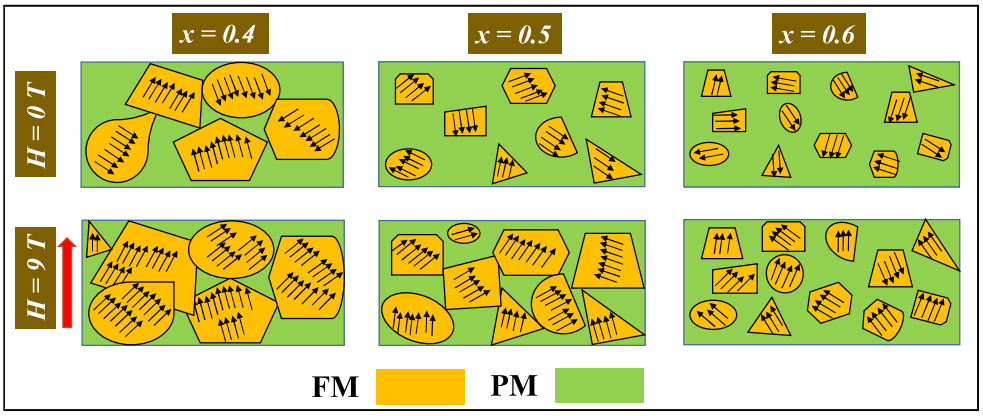


**Figure 4.8:** Schematic picture to describe the enhanced magnetoresistance in $x = 0.5$ compound

with an increase of temperature and '$x$' magnetic cluster size decreases. For $x = 0.4$ sample cluster size strongly depends on temperature but in other compounds, there is a less pronounced effect of temperature. It is also known that the calculated average moment of the clusters also depends on the magnetic field and grow in size with the increase of magnetic field which results in the increase of cluster moment [157]. These clusters at high temperatures (at 80 K and above) are nearly non-interacting which is responsible for the reversibility of MR at 80 K.

Based on these above results and discussions a phenomenological model for huge MR in $x = 0.5$ compound has been proposed. In $x = 0.4$ compound, cluster sizes are large in zero magnetic field and below $T_{MI}$ they gets connected and creates the percolation path for transport as a result of which resistivity decreases and applied magnetic field only increases this percolation path by increasing cluster size. On the other hand, in $x = 0.5$ compound in absence of any external magnetic field, these FM clusters were disconnected, as a result the sample was an insulator in nature. With the application of external magnetic field these clusters grow in size and create the percolation path and field induced metal-insulator transition occur which results in gigantic MR. However for $x = 0.6$ compound even 90 kOe magnetic field is not enough to create the percolation path by growing cluster size. Fig. 4.8 shows the pictorial view of the effect of external magnetic field on the cluster sizes

in the compositions $x = 0.4, 0.5$ and $0.6$.

## 4.3 Evolution from Griffiths like phase to non-Griffiths like phase with Y doping in the $(La_{1-x}Y_x)_{0.7}Ca_{0.3}MnO_3$ compounds

### 4.3.1 Sample Preparation and Characterization

All the bulk polycrystalline $(La_{1-x}Y_x)_{0.7}Ca_{0.3}MnO_3$ $(x = 0, 0.3, 0.4, 0.5, 0.6)$ compounds were prepared by the conventional sol-gel method with $La_2O_3$, $Y_2O_3$, $CaCO_3$ and $MnO_2$ as the starting materials of purity 99.9%. To prepare the bulk samples, decomposed gels were pelletized and subsequently heated at $1300^0C$ for 36 hours.

### 4.3.2 Experimental Results and Discussion

The phase purity of the samples were checked from room temperature x-ray diffraction measurements using Rigaku-TTRAX-III with 9 kW rotating anode Cu-source of wavelength $\lambda = 1.54\mathring{A}$. To perform the magnetic measurements quantum design SQUID-VSM was used.

The room temperature XRD study shows (Fig. 4.9(A) and (B)) the single phase nature of all the bulk polycrystalline samples with 'Pnma' space group. Using FULLPROF software, Rietveld refinement of all the XRD data has been performed which indicates the orthorhombic structure of the samples having 'Pnma' space group symmetry. The extracted lattice parameters is presented in Table. 4.1. A systematic reduction of unit cell volume with increase of Y concentrations has been observed which is because of the smaller ionic radius of Y compare with La and for the same

reason A-site ionic radius has also decreased with increased Y concentrations. Decrease of unit cell volume is also clear from the shifting of main intense peak (121) towards higher angle (Fig. 4.9(C)) with Y doping, as peak shifting towards higher angle suggest the decrease of interplanar spacing which in turn implies the decrease of unit cell volume. Another point here is to be noted that increased Y doping also enhance the angular separation between (200), (121) and (002) peaks which indicates the enhancement of lattice distortion. Using the expression of orthorhombic lattice distortion $\Delta = \frac{a+b-c/\sqrt{2}}{a+b+c/\sqrt{2}}$, the calculated orthorhombic distortion has comes out to be 0.333, 0.336 and 0.339 for Y doping $x = 0.3, 0.4$ and $x = 0.6$ respectively.

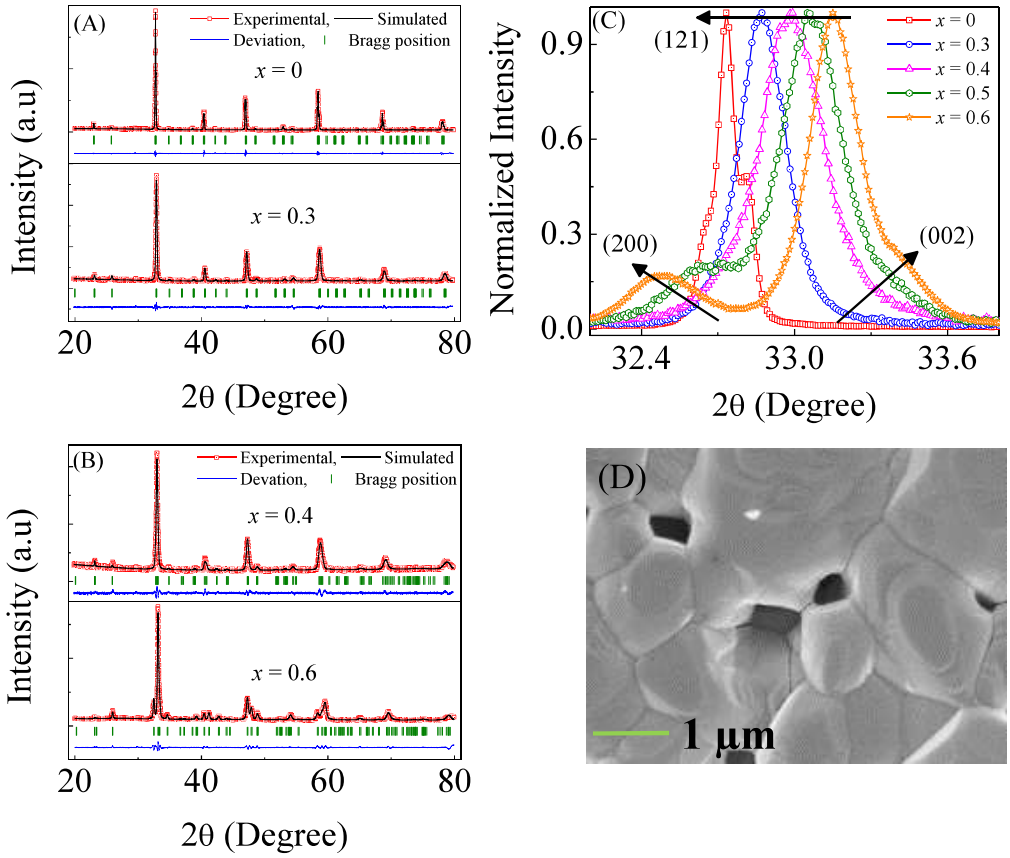


**Figure 4.9:** Room temperature XRD data with its profile fitted data for the samples with Y concentration (A) $x = 0$ and $x = 0.3$ (B) $x = 0.4$ and $x = 0.6$. (C) Evolution of of main intense peak (121) and its separation with (200) and (002) peaks with Y concentrations. (D) Scanning electron microscopy image of the $x = 0.5$ compound.

The enhanced lattice distortions with Y doping greatly influences on the magnetic properties of the systems. To understand the effect of this distortions, temperature

**Table 4.1:** The lattice parameters, unit cell volumes and average A-site ionic radii for the samples $(La_{1-x}Y_x)_{0.7}Ca_{0.3}MnO_3$ $(x = 0, 0.3, 0.4, 0.5, 0.6)$

| $x$ | a $(\AA)$ | b $(\AA)$ | c $(\AA)$ | V $(\AA^3)$ | $\langle r_A \rangle$ $(\AA)$ |
|---|---|---|---|---|---|
| 0 | 5.465 | 5.481 | 7.725 | 231.419 | 1.205 |
| 0.3 | 5.451 | 5.449 | 7.714 | 229.089 | 1.176 |
| 0.4 | 5.463 | 5.409 | 7.680 | 226.939 | 1.166 |
| 0.5 | 5.489 | 5.386 | 7.638 | 225.808 | 1.158 |
| 0.6 | 5.511 | 5.366 | 7.597 | 224.659 | 1.146 |

dependence of magnetization [M(T)] of all the samples has been performed in presence of 100 Oe external magnetic field in field cooled warming (FCW) protocol and the corresponding plot has been presented in Fig. 4.10. The suppression of magnetization with increase of Y concentrations is perceived at low temperature. Moreover, there is also reduction of curie temperature ($T_C$, determined from the temperature derivative of magnetization data) with increase of Y doping (inset of Fig. 4.10) and it reduces from 260 K for $x = 0$ to 40 K for $x = 0.6$. Usually the value of curie temperature indicates the strength of ferromagnetic interactions which has been found to suppressed for Y doping. As, Y doping decrease the A-site ionic radius which in turn decrease the $Mn - O - Mn$ bond angle and therefore ferromagnetic double exchange interactions is weakened. Another important observation here is that, for $x = 0$ the transition from paramagnetic (PM) to ferromagnetic (FM) is sharp in nature but with increase of Y this PM-FM transition became broader which possibly due to the increase of the distribution of exchange interactions in the samples.

For further investigating the broadening of the PM-FM phase transition, the inverse dc susceptibility (H/M) versus temperature data measured in presence of 100 Oe and 1 kOe external magnetic field for $x = 0.3, 0.4, 0.5$ and 0.6 samples has been investigated in details and is presented in Fig. 4.11. All these measurements has been performed in FCW protocol. For these samples ($x = 0.3, 0.4, 0.5$ and 0.6), the high temperature $(T > 200K)$ inverse susceptibility data has been analyzed with Curie-Weiss law of the form $\chi = C/(T - \theta_{CW})$ where $C = \mu_{eff}^2/3k_B$ and $\mu_{eff}$,

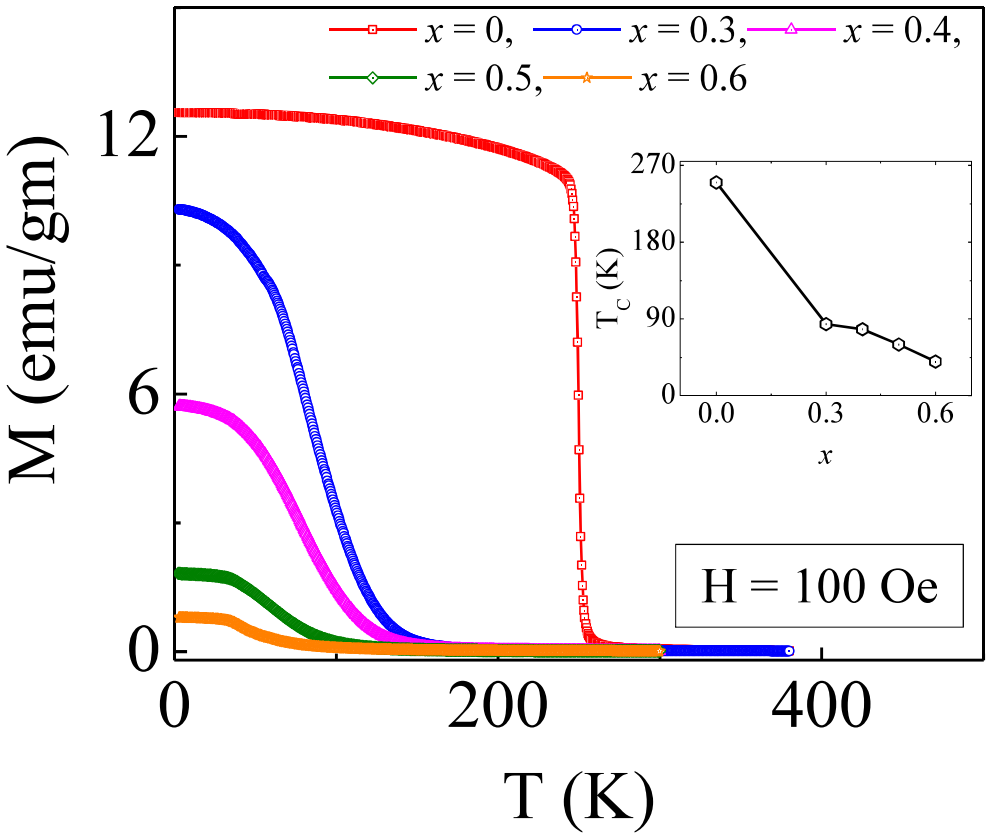


**Figure 4.10:** Variation of magnetization with temperature for different Y doped samples ($x = 0, 0.3, 0.4, 0.5, 0.6$). Inset represents the evolution of curie temperature with Y doping.

$\theta_{CW}$ are the effective paramagnetic moment and paramagnetic curie temperature respectively. The reduction of paramagnetic curie temperature with Y doping is observed and it takes value 135 K for $x = 0.3$ to 102 K for $x = 0.6$. Here it is to be noted that for $x = 0.3$ and $x = 0.4$ samples, susceptibility data measured at 100 Oe field deviates downward from Curie-Weiss fitted line (Fig. 4.11(A) and (B)) near 200 K. This downturn is possible if there is short range ferromagnetic ordering in the paramagnetic region. Moreover, from Arrot plot [180] ($M^2$ versus H/M plot shown in in the inset of Fig. 4.11(A) and (B)) no presence of spontaneous magnetization is observed in this deviated region ($150K \leq T \leq 200K$). The onset of this downturn is represented as $T^*$. With application of higher magnetic field (1 kOe) this downward deviation vanishes which is probably because of the enhancement of the background paramagnetic signal [163]. This downward deviation, as previously

observed in other doped manganites, is a typical signature of Griffiths like phase. Microscopically in $(La_{1-x}Y_x)_{0.7}Ca_{0.3}MnO_3$ sample the $Mn-O-Mn$ bond angle in the 'La' rich site is more compared with 'Y' rich site because of smaller ionic radii and as a result ferromagnetic double exchange interactions in 'La' rich site is more compared with 'Y' rich site and 'La' site act as a nucleation center for the developing short range ferromagnetic clusters. Surprisingly, with further Y-doping i.e. from $x = 0.5$, this downturn in H/M versus temperature data measured at 100 Oe magnetic field ceases and rather shows upward deviation and it almost superimposes with the H/M versus temperature data taken at 1 kOe magnetic field. This upward deviation from Curie-Weiss behavior indicates the reduction of susceptibility even from paramagnetic signal and it is possible when there is antiferromagnetic interaction between ferromagnetic clusters [66] or there is a ferromagnetic and antiferromagnetic phase coexistance [169–171] or competing FM and AFM interactions. Previously, Banerjee et al [181]. in $La_{0.5}Ba_{0.5}CoO_3$ compound has observed the same kind of upward deviation of inverse susceptibility which they explained on the basis of antiferromagnetic correlation between ferromagnetic clusters developed in the paramagnetic phase. Jiang et al [165]. has shown from neutron diffraction data that in $(La_{1-y}Pr_y)_{0.7}Ca_{0.3}MnO_3$ compound with Pr substitution in La site antiferromagnetic phase fraction exceeds the ferromagnetic phase fraction which results in the upward deviation of inverse susceptibility from CW behavior. Recently, Sun et al [182]. has shown from electron spin resonance measurements that there is short range antiferromagnetic correlations in the paramagnetic regime which is responsible for the susceptibility upturn in antiperovskite $Cu_{1-x}NMn_{3+x}$ $(0.1 \leq x \leq 0.4)$. Though in the present case no phase coexistence (FM and AFM) is observed from M(T) data.

Basically, with increasing Y doping magnitude of DE interactions through $Mn-O-Mn$ bond gets suppressed because of smaller $Mn-O-Mn$ bond angle than La site. Another point is that local $MnO_6$ octahedral distortion being more in Y site it

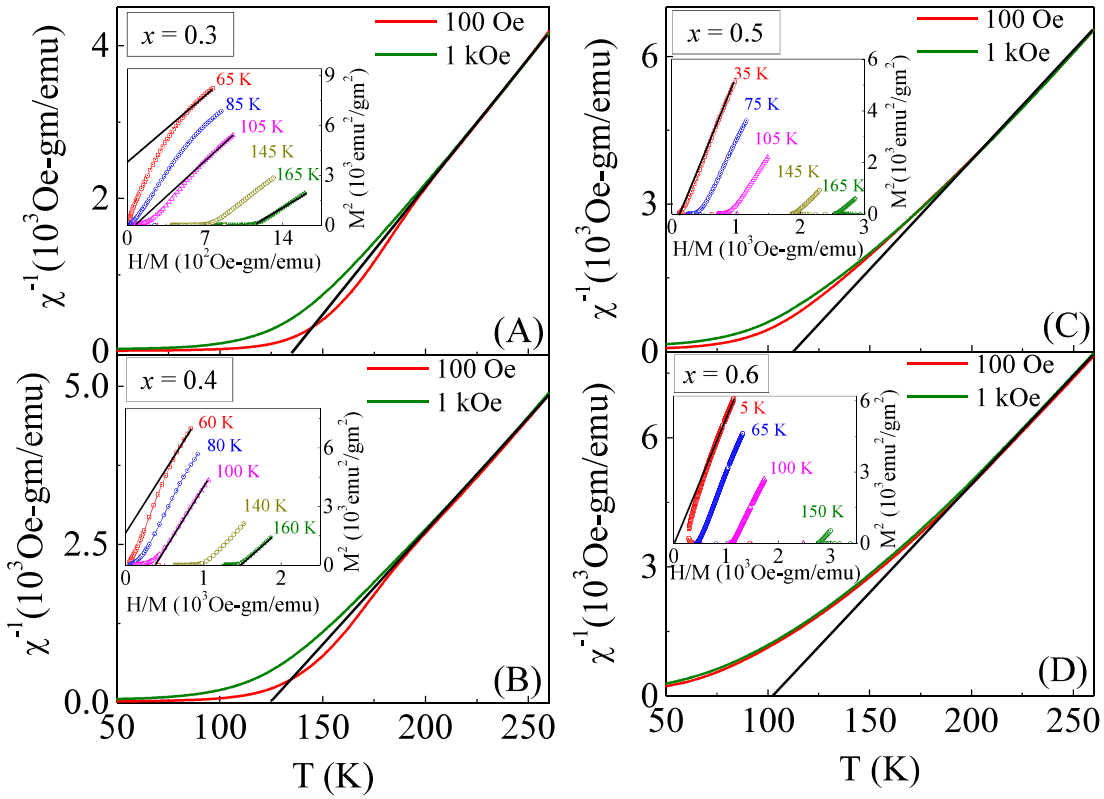


**Figure 4.11:** Variation of inverse dc susceptibility (H/M) with temperature in presence of 100 Oe and 1 kOe external magnetic field for the samples with Y doping (A) $x = 0.3$ (B) $x = 0.4$ (C) $x = 0.5$ and (D) $x = 0.6$. The Curie-Weiss fitted line in the high temperature paramagnetic region of all the samples ($T > 200K$) has been presented by the black solid line in the corresponding figures. The Arrot plot ($M^2$ versus H/M) at different temperatures is shown in the inset of the corresponding figures.

creates strong electron phonon coupling. The increase of electron phonon coupling localize the carrier which enhances the resistivity and the signature of the enhancement of the electron phonon coupling with Y doping is also clear from our recent studies of the Y doped series $(La_{1-x}Y_x)_{0.7}Ca_{0.3}MnO_3$ [183]. The increase of this electron phonon coupling increases the effective antiferromagnetic superexchange interactions between $Mn^{3+} - Mn^{3+}$ and $Mn^{4+} - Mn^{4+}$ ions compare with DE between $Mn^{3+}/Mn^{3+}$ ions. Thus there is the competing FM and AFM interaction which is probably related with the evolution from downward deviation to upward deviation in susceptibility from CW law.

For further investigating, the magnetization data (M verses H data) in the CW deviated region (180 K) for all the samples has been analyzed with the Modified

Langevin function [183] of the form $M(H) = N\mu L(\frac{\mu H}{k_B T}) + AH$, where "L(x)" is the Langevin function, "N" is the number density of the clusters and "$\mu$" is the average magnetic moment of the clusters. The experimental data (M versus H) fitted well with the modified Langevin function and has been presented in Fig. 4.12(A). From the fitting, calculated average magnetic moment of the clusters $\mu$ and cluster number density N for various Y doped samples is shown in Fig. 4.12(B). With increasing of Y doping a systematic reduction of cluster moments has been observed and it is also associated with increase in the cluster density. This is also correlated, as with increasing Y doping ferromagnetic DE interactions decreases and for this reason cluster size reduces. Thus, the analysis indicates the presence of the ferromagnetic clusters in the susceptibility deviated region irrespective of the Y concentrations but does not elucidate the crossover of the susceptibility from downturn to the upturn from CW law with increasing Y concentrations from $x = 0.4$ to $x = 0.5$.

Finally, to probe the anomaly in the magnetic susceptibility with changing Y concentrations, magnetocaloric study has been performed for the samples with Y concentrations $x = 0.3, 0.4$ and 0.5. Usually, the magnetocaloric entropy change $(\Delta S_M)$ is determined from the Maxwell's thermodynamic relation $\Delta S_M = \int_0^H (\frac{\partial M}{\partial T}) dH$. The magnetocaloric entropy change for the samples $(x = 0.3, 0.4, 0.5)$ has been calculated from the isothermal magnetization [M(H)] data. All the M(H) isotherms has been measured in zero field cooled (ZFC) protocol and before each successive isotherms, sample has been heated at 300 K to destroy magnetic history. In the paramagnetic region according to mean field theory [184, 185] $-\Delta S_M \propto H^2$. In this regard, variation of $-\Delta S_M$ with magnetic field at 150 K for the samples has been tried to fit (Fig. 4.13(B)) with the power law $-\Delta S_M \propto H^m$ and the power has comes out to be 1.4, 1.49 and 1.73 respectively for the samples $x = 0.3, 0.4$ and 0.5. The deviation of the power from the ideal value of 2 implies the existence of short range ferromagnetic interactions above the curie temperature of the samples (150K). It also clear the fact that the effect of this short range interactions at 150 K in $x = 0.5$ sample is

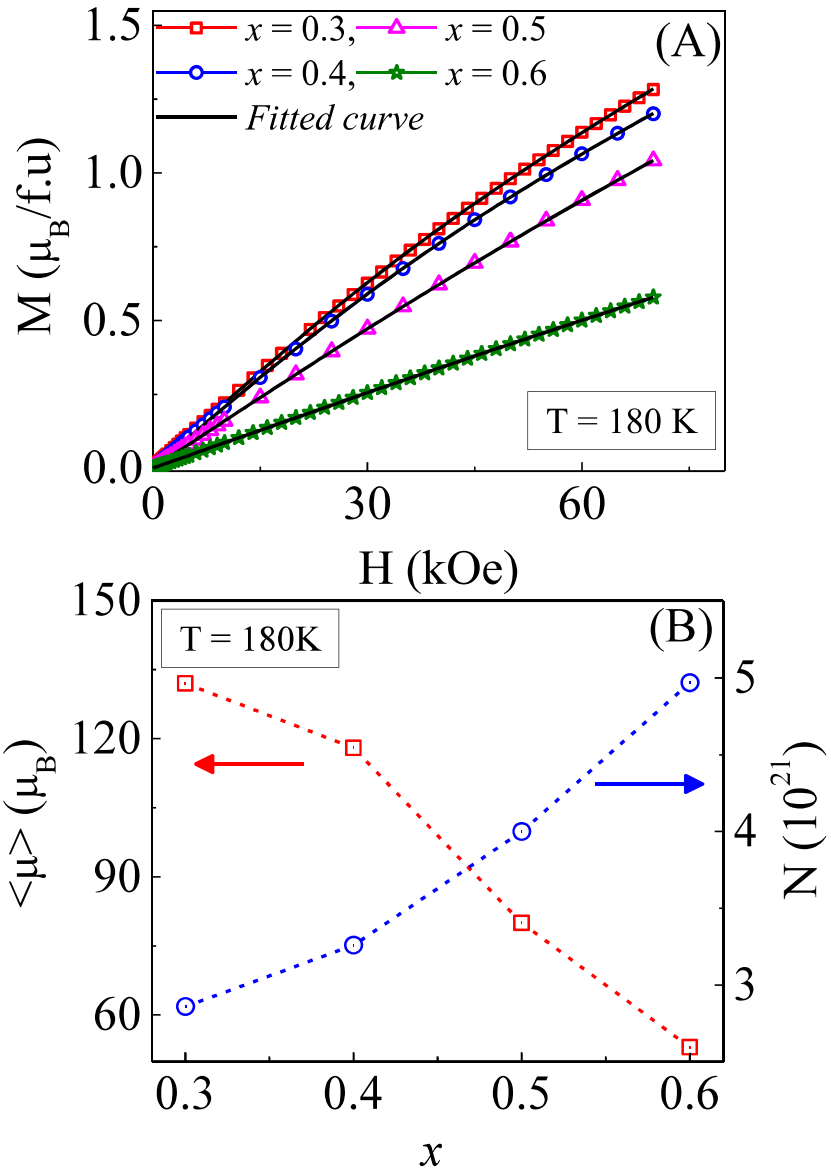


**Figure 4.12:** (A) Fitting of the M versus H data with the modified Langevin function for the samples having Y concentrations $x = 0.3, 0.4, 0.5$ and 0.6. (B) Evolution of average cluster moment and cluster density with Y concentrations.

less compared $x = 0.3$ and it also agrees with the previous calculation of reduction of clusters moment with increase of Y concentrations. Theoretically, $-\Delta S_{max}$ near paramagnetic to ferromagnetic transition ($T_C$) follows the $H^{2/3}$ dependence. The field dependence of $-\Delta S_{max}$ and its corresponding fitted data with the power law $-\Delta S_{max} \propto H^n$ for the samples has been presented in Fig. 4.13(C). Though there is a good fitting of the $-\Delta S_{max}$ versus field data with the power law, the obtained power deviates for all the samples and its values are 0.96, 1.07 and 1.19 for the

samples $x = 0.3, 0.4$ and 0.5. More importantly this discrepancy is more for $x = 0.5$ sample compared with lower Y concentrations, though reduction of ferromagnetic interaction in $x = 0.5$ is observed compared with other Y concentrations. The increase of this anomaly is probably because of the presence of some other kind of interactions.

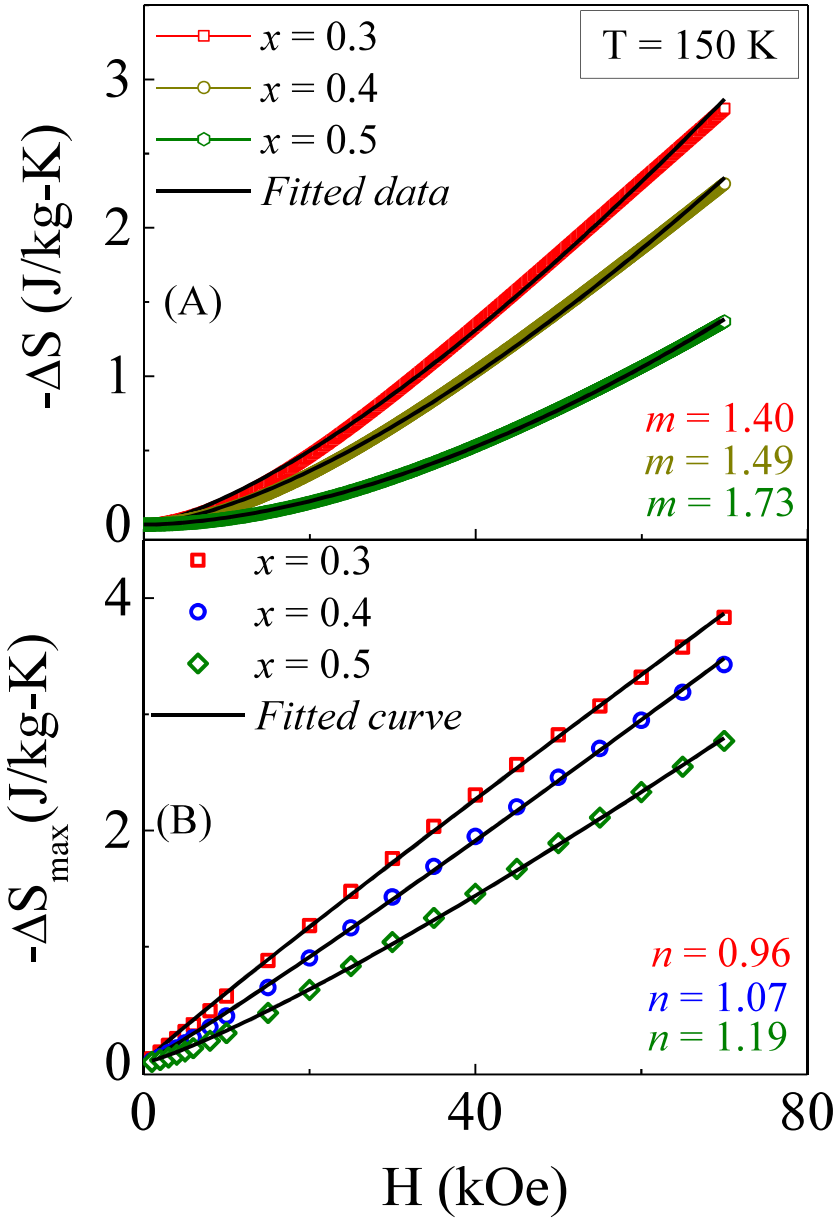


**Figure 4.13:** (A) Magnetic field dependence of $-\Delta S_M$ at 150 K temperature for $x = 0.3, 0.4$ and 0.5 samples and their corresponding power law fitted curves. (B) $-\Delta S_{max}$ versus H and its fitted data for $x = 0.3, 0.4, 0.5$ compounds.

To get signature of the kind of interactions present in the systems, measurements

of $-\Delta S_M$ with temperature for the samples has been performed. The temperature variation of magnetocaloric entropy change for 30 kOe applied magnetic field for the samples has been shown in Fig. 4.14(A). The suppression of MCE is observed with increase of Y substitution ($1.75 J/kg.K$ for $x = 0.3$ to $1.03 J/kg.K$ for $x = 0.5$). Moreover, there is a shifting of MCE peak from 90 K for $x = 0.3$ to 70 K for $x = 0.5$. It indicates the gradual suppression of ferromagnetic DE interactions with Y substitution [19, 186]. Another point here is to be noted that the temperature evolution of magnetic entropy change $\Delta S_M$ is asymmetric about the maximum. Normally, for systems having long range ordering $\Delta S_M$ is symmetrically distributed about the maximum which is close to the ordering temperature of the system. The presence of this asymmetry implies the presence of short range ordering above the transition temperature as observed previously for many other manganites systems [21, 188]. Usually, in manganites for a fixed $Mn^{3+}/Mn^{4+}$ concentration with increasing magnetic disorder MCE gets distributed over a wide temperature range. Recently Lee. et al [187]. reported that in $La_{0.7-x}Y_xCa_{0.3}MnO_3$ with increasing Y doping from $x = 0$ to $x = 0.08$ the full-width-at-half maximum of $-\Delta S_M$ gets enhanced from 17 K to 50 K and simultaneously the maximum value of $-\Delta S_M$ decreases from 8.9 J/kg.K to 4.3 J/kg.K for 30 kOe magnetic field value. The reduction of MCE is due to the suppression of DE ferromagnetic interactions for decreasing $Mn - O - Mn$ bond angle by Y doping and increase of effective temperature span is because of the formation of ferromagnetic clusters above the curie temperature. Similarly, in the present case with Y substitution from $x = 0.3$ to $x = 0.5$ the maximum value of $-\Delta S_M$ also decreases as expected because of weakening the DE interaction. On contrary to the increase of full-width-at-half maximum of $-\Delta S_M$ for Y concentrations $x = 0 - 0.08$, the effective $\Delta T_{FWHM}$ seems to decreases for $x = 0.3 - 0.5$, though presence of ferromagnetic clusters has also been observed here. Recently, Das et al [188]. has shown in charge ordered antiferromagnetic $La_{0.48}Ca_{0.52}MnO_3$ compound that with decreasing particle sizes from 150 nm to 45 nm, $\Delta T_{FWHM}$ of the MCE increases because of

the appearance of ferromagnetic correlations in the 45 nm sample. Therefore, the reduction of the temperature span in $(La_{1-x}Y_x)_{0.7}Ca_{0.3}MnO_3$ with 'x' is likely due to the enhancement of the effective short range antiferromagnetic interactions compared with DE interactions and due to the proximity effect of the SR-AFM fraction, the FM magnetic coupling decay with distance which results in the decrease in the FM cluster size with increased Y doping.

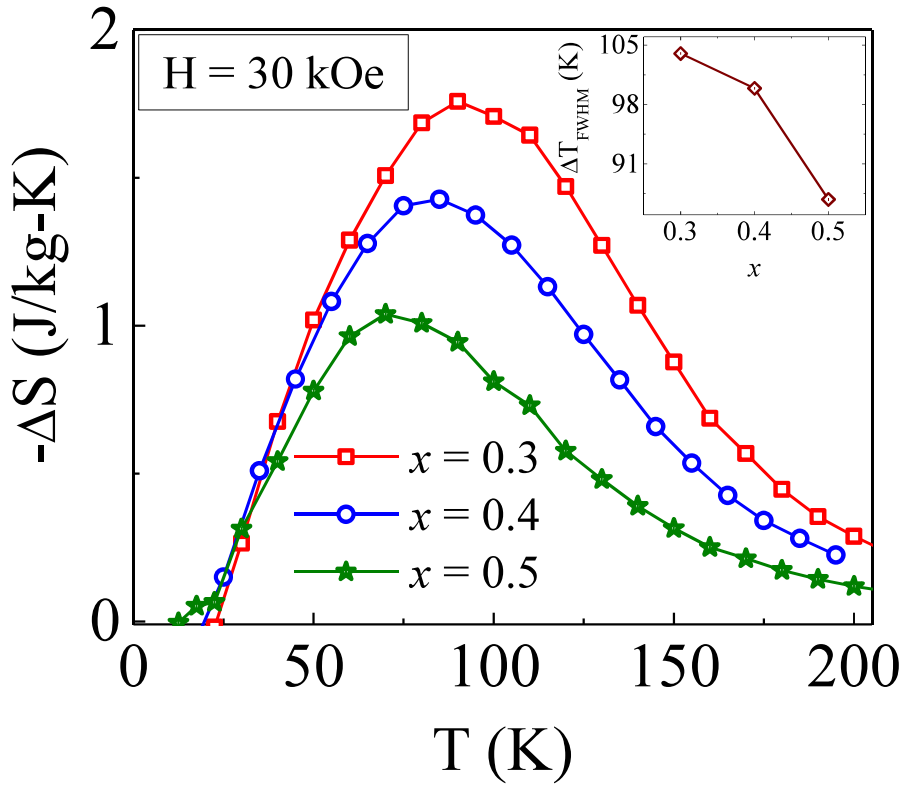


**Figure 4.14:** Plot of Magnetocaloric entropy change $(-\Delta S)$ with temperature in application of 30 kOe magnetic field for $x = 0.3, 0.4, 0.5$. In the inset variation of FWHM of the MCE versus temperature curves with 'x' is shown.

## 4.4 Instability of insulator state towards nanocrystallinity in the $(La_{0.5}Y_{0.5})_{0.7}Ca_{0.3}MnO_3$ compound and enhancement of low field magnetoresistance

### 4.4.1 Sample Preparation and Characterization

The polycrystalline bulk and nanocrystalline $(La_{0.5}Y_{0.5})_{0.7}Ca_{0.3}MnO_3$ compounds has been prepared by the well known sol gel route with $La_2O_3$, $Y_2O_3$, $MnO_2$ and $CaCO_3$ of purity 99.9% as the starting materials. For preparation of bulk sample decomposed gel was pelletized and heated at $1300^0C$ for 36 hours whereas to prepare its nanocounterpart it was heated at $1000^0C$ for 3 hours.

### 4.4.2 Experimental Results and Discussion

The phase purity of the samples was characterized from x-ray diffraction (XRD) measurements using Rigaku-TTRAX-III with 9 kW rotating anode source (Cu-K$\alpha$ of wavelength $\lambda = 1.54\mathring{A}$). Scanning electron microscopy (SEM) measurements were performed to determine the size of the particles. The magnetic measurements were carried out using quantum design SQUID-VSM. The transport and magnetotransport measurements were performed on bar shaped sample by four probe method using longitudinal geometry.

The room temperature x-ray diffraction study reveals the single phase nature of the bulk and nanocrystalline samples. To get information about the crystal structure, Rietveld refinement of the XRD data has been carried out with FULLPROF programme and it has been observed that both the samples crystallize in orthorhombic

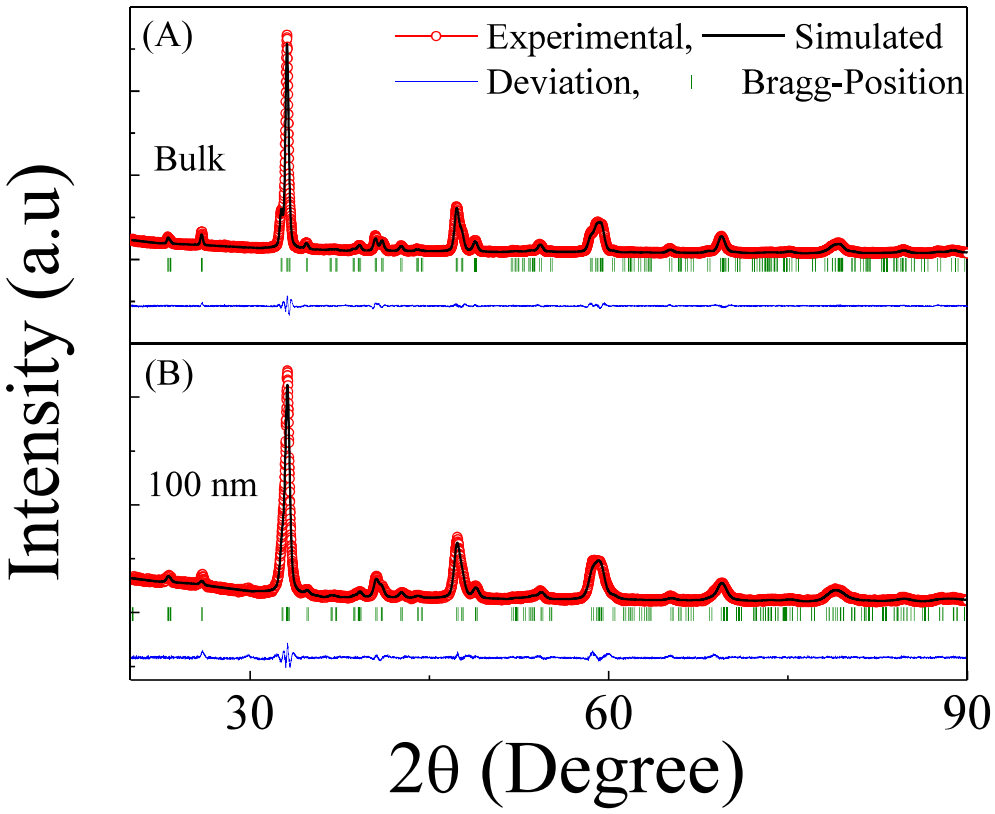


**Figure 4.15:** Room temperature XRD data with profile fitting for (A) Bulk and (B) Nanocrystalline samples.

structure having 'Pnma' space group symmetry. The obtained structural parameters are summarized in Table. 4.2. The unit cell volume and reduction of orthorhombic distortion has been observed in nanocrystalline sample compared with bulk sample.

The scanning electron microscopy (SEM) image of the bulk (Fig. 4.16(A)) and nanocrystalline (Fig. 4.16(B)) samples shows the average grain sizes to be $\sim 1\mu m$ and 100 $nm$ respectively.

The reduction of particle sizes greatly influences the electrical transport and magnetotransport properties. The dependence of resistivity with temperature $[\rho(T)]$ in zero field as well as in presence of different external magnetic fields has been performed in both the samples (Fig. 4.17). All these measurements were done during warming cycle after cooling in zero external magnetic field. The zero field resistivity data of the bulk sample shows the insulating nature down to measurable resistance

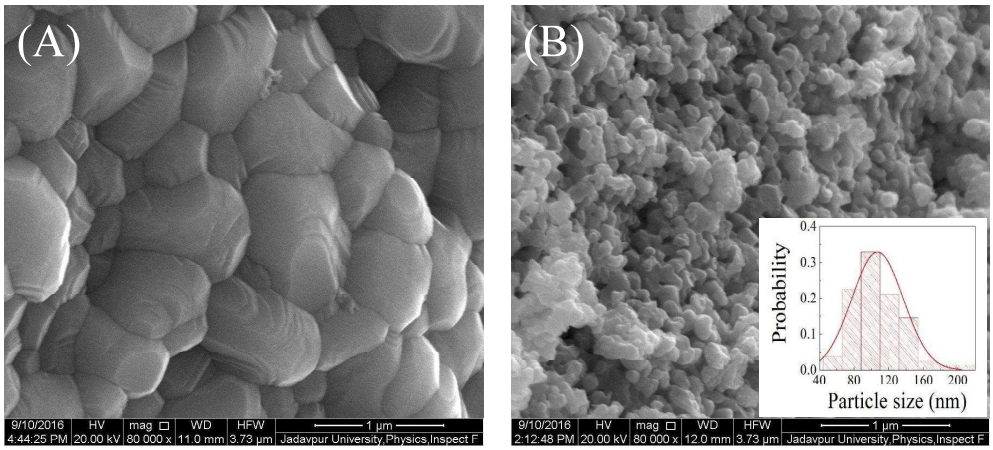


**Figure 4.16:** SEM images for (A) Bulk and (B) Nanocrystalline samples. Inset of Fig. 4.16(B) is the histogram for the size distribution of nanoparticles.

**Table 4.2:** The lattice parameters, unit cell volume and orthorhombic distortion and their corresponding error bars.

| Sample | a ($\mathring{A}$) | b ($\mathring{A}$) | c ($\mathring{A}$) | V ($\mathring{A}^3$) | $\Delta(\|\|)$ |
|---|---|---|---|---|---|
| Bulk | 5.491±0.0002 | 7.625±0.0003 | 5.384±0.0002 | 225.426 | 0.23 |
| Nano | 5.480±0.0003 | 7.622±0.0002 | 5.391±0.0004 | 225.178 | 0.35 |

range. On application of external magnetic field suppression of resistivity occurs at low temperature. The system undergoes metal-insulator like transition around 80 K for 30 kOe magnetic field and 100 K for 70 kOe magnetic field. In contrast to bulk sample, in nanoparticle spontaneous metal insulator transition take place and shows huge reduction of resistivity of $\sim 10^5$ order near 50 K. The effect of magnetic field in this case also shows the suppression of resistivity but the effect is less prominent compared with bulk sample. Here another point has to be remembered that, even after insulator to metallic transition resistivity is high enough compared with normal metallic resistivity (for example $\rho_{Cu} = 1.7\ \mu\Omega cm$). It implies that the systems has not been converted completely in metallic state, rather consists of metal and insulator state together.

In order to acquire knowledge of this huge modification of resistivity on particle size reduction as well as on application of external magnetic field, detail analysis of the high temperature resistivity data has been performed employing different models.

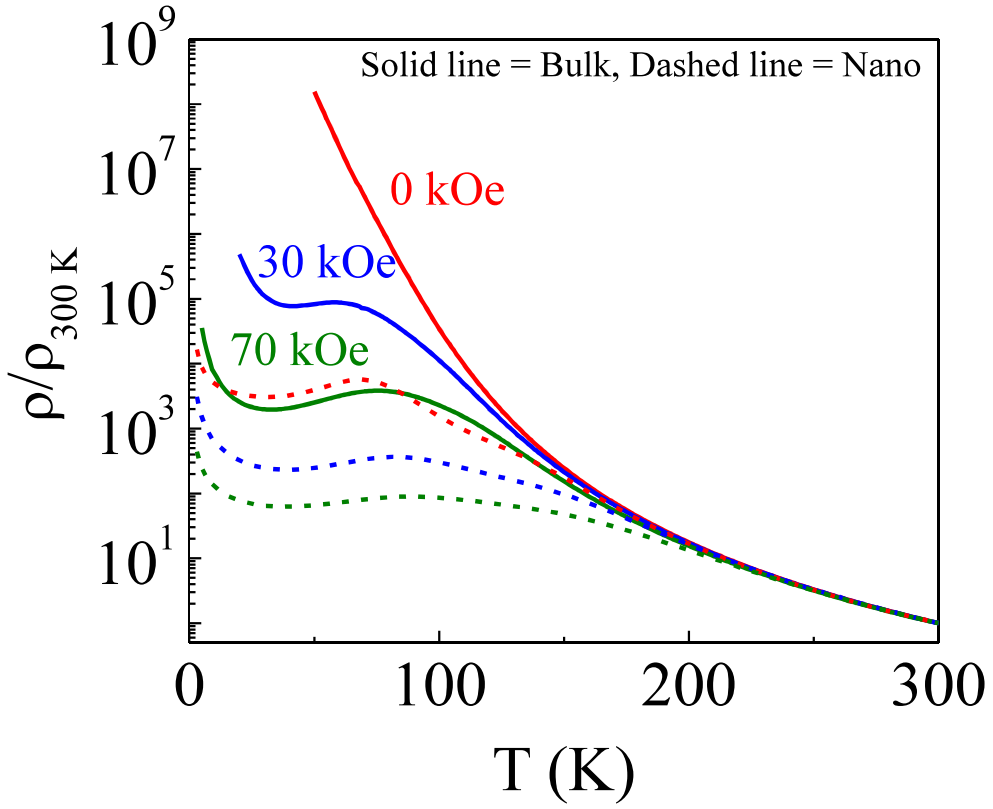


**Figure 4.17:** Temperature dependence of reduced resistivity of bulk and nanocrystalline compounds in absence and in presence of applied external magnetic field (30 kOe and 70 kOe). Here dashed lines and solid lines are the reduced resistivity data corresponds to the nanocrystalline and bulk samples and color codes bear the different field values.

For manganites the high temperature resistivity in paramagnetic region is mainly governed by the formation of polaron [53]. The polaronic radius ($r_P$), governed by the equation [189] $r_P = (1/2)[\pi/6N]^{1/3}$ where 'N' is the number of transition metal ions per unit volume, has comes out around 2.25$\mathring{A}$ for both the samples. This polarons being much smaller than the unit cell volume, small polaron hopping (SPH) model has been utilized to describe the electrical transport data at high temperature regime ($T \geq 250K$). According to the SPH model [190, 191] resistivity is expressed as $\rho = \rho_0 T exp(E_A/k_B T)$ where $E_A$ is the polaronic activation energy. From the fitting $E_A$ has been estimated and its variation with magnetic field for both bulk and nanocrystallite samples has been shown in Fig. 4.18. Interestingly, decrease in activation energy is observed in nanocrystallite sample compared to bulk and this

reduction is more prominent at higher magnetic field. An effort has also been paid to describe the resistivity data in the paramagnetic insulating region by an another frequently used Mott's variable range hopping (VRH) model. The expression of resistivity according to the VRH model [190] is given by $\rho = \rho_{\propto} exp[(T_0/T)^{1/4}]$ where $T_0$ is the characteristic temperature related to the density of states by the relation $T_0 = 16\alpha^3/k_B N(E_F)$. This model also fit satisfactorily with the resistivity data ($T \geq 250K$) and density of states has been estimated (using $\alpha = 2.22nm^{-1}$) [189]. Enhancement of density of states near fermi level with application of magnetic field is observed for both bulk and nanocrystallite samples (Fig. 4.18). The typical fitting of the resistivity data with VRH model is represented in Fig. 4.18(B). From this analysis it can be said safely that in $\sim 100nm$ particle compared with bulk, there is some intrinsic modification which causes the increase of density of states near fermi level and results in huge suppression of resistivity in nanoparticle.

To get further insight into the systems, measurements of isothermal resistivity as a function of magnetic field has been performed from where magnetoresistance (MR) calculations has been done by using the definition $MR(\%) = \frac{\rho(H)-\rho(0)}{\rho(0)} \times 100$ where $\rho(H)$ and $\rho(0)$ are the resistivity in presence and in absence of external magnetic field. The field variation of MR at different temperature has been presented in Fig. 4.19. Low field enhancement of MR is observed in $\sim 100nm$ particle compared to the bulk sample. For instance at 80 K temperature in presence of 5 kOe magnetic field, MR increases from 18% to 38%. Another point here is to be noted that there is a clear cross-over in MR with magnetic field between bulk and nanoparticle. This cross-over point shift to higher magnetic field with increase of temperature and vanishes above 100 K. At 150 K, MR data shows that the enhancement of MR occurs in nanoparticle in the both low field as well as high magnetic field regime.

To understand this low field enhancement of magnetoresistance in nanocrystalline sample, MR data has been analyzed with the help of spin polarized tunneling (SPT)

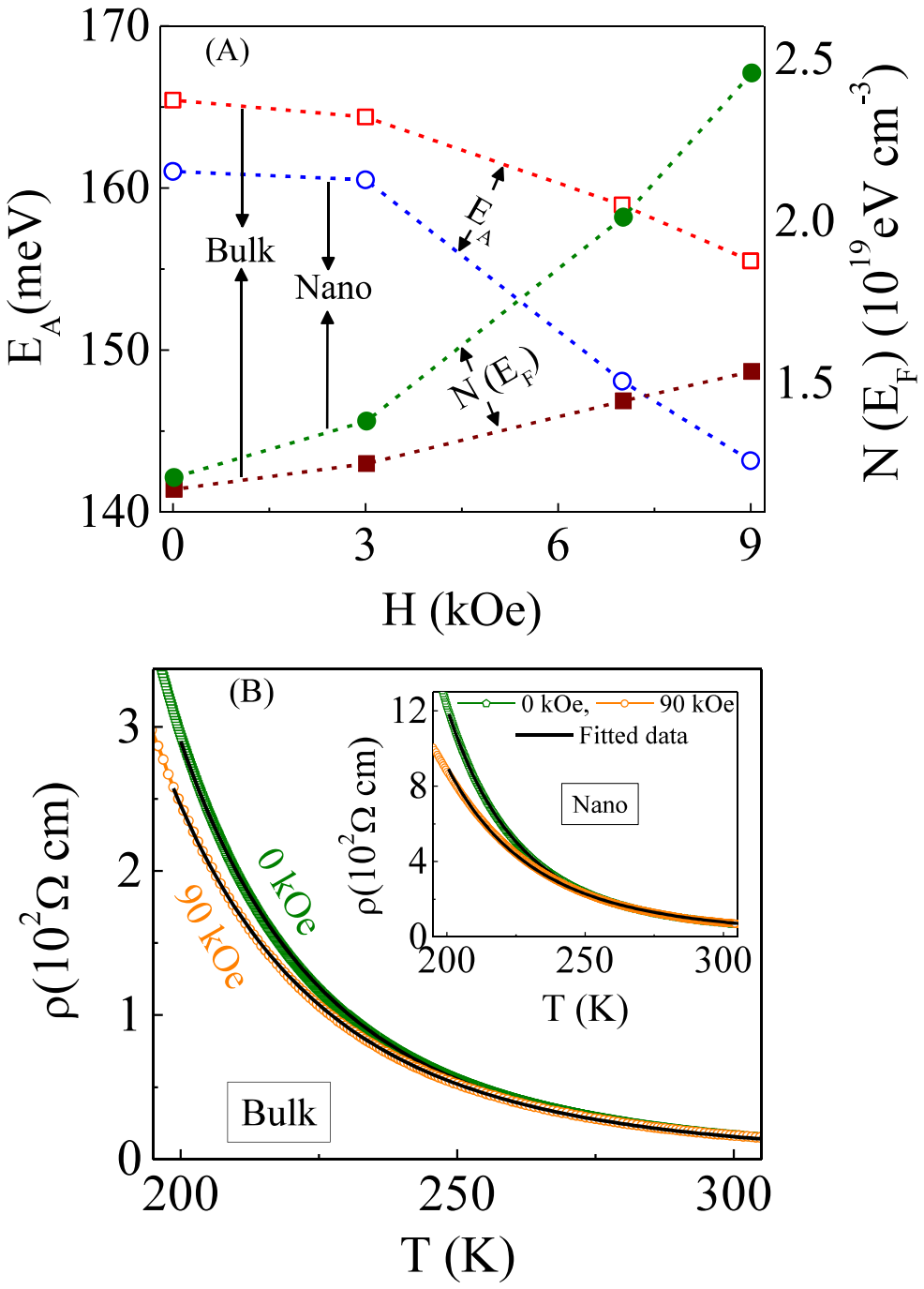


**Figure 4.18:** (A) Variation of activation energy $E_A$ (open symbols) and effective density of states $N(E_F)$ (closed symbols) with external magnetic fields for bulk and nanocrystalline compounds. (B) A typical fitting of the resistivity data (200-300K) with VRH model for 0 kOe and 90 kOe magnetic fields in both the samples and here black lines are the fitted data.

model. According to SPT model, expression of MR is of the form

$$MR = -A' \int_0^H f(k)dk - JH - KH^3 \tag{4.1}$$

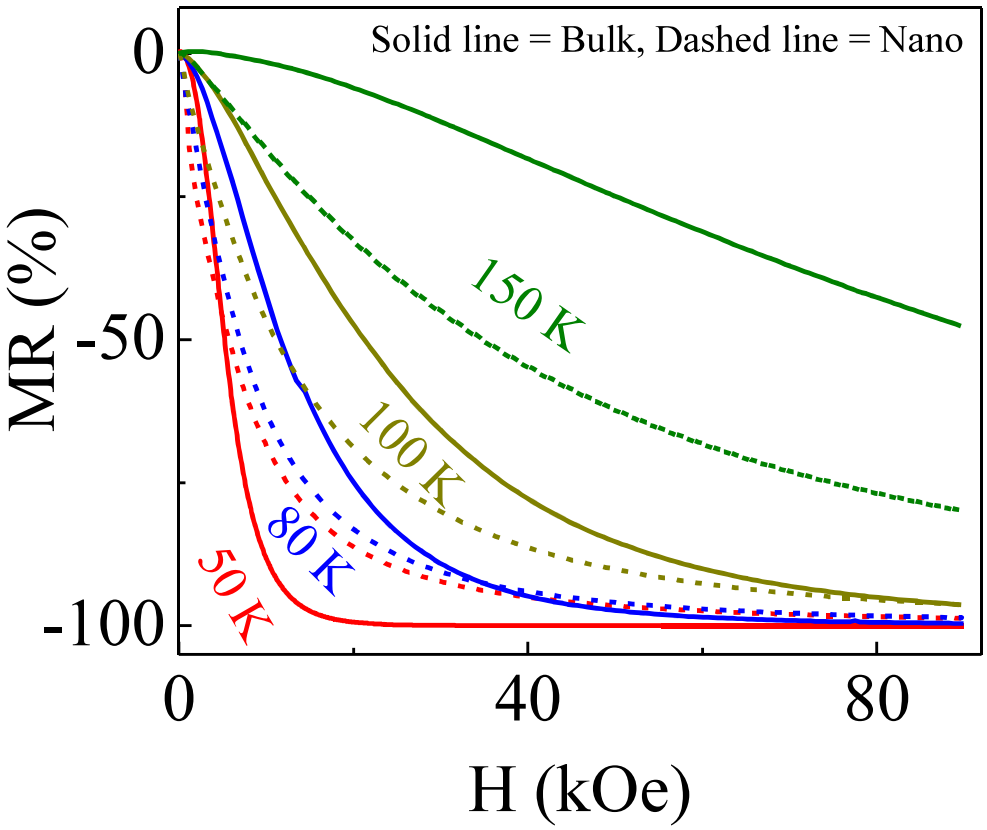


**Figure 4.19:** Evolution of magnetoresistance at different fixed temperatures (50K, 80K, 100K and 150K) with magnetic field, where dashed lines are for nanocrystalline sample and solid lines for bulk sample.

where first term arises due to the spin polarized tunneling mechanism and the other two terms gives the intrinsic contributions described by zener double exchange mechanism. The term $f(k)$ gives the distribution of pinning strength and is expressed as $f(k) = Aexp(-Bk^2) + Cexp(-Dk^2)$. A typical fitting of MR data (80 K) with SPT model is presented in Fig. 4.20 which shows reasonably good fitting of the MR data with the SPT model. From the fitting, SPT part of MR has been extracted and its variation with magnetic field in bulk and nanopartcles has been presented in Fig. 4.20. Here it is clearly seen that in nanoparticle SPT part is dominating which is causing the low field enhancement of magnetoresistance. Another point here is to be noted that, above a certain field (40 kOe) SPT component of bulk exceeds the value of nanoparticle and this particular field is the same where cross-over of MR occurs between bulk and nanosample. Thus the cross-over is associated with enhancement

of SPT component in Bulk with magnetic field ($H \geq 40kOe$).

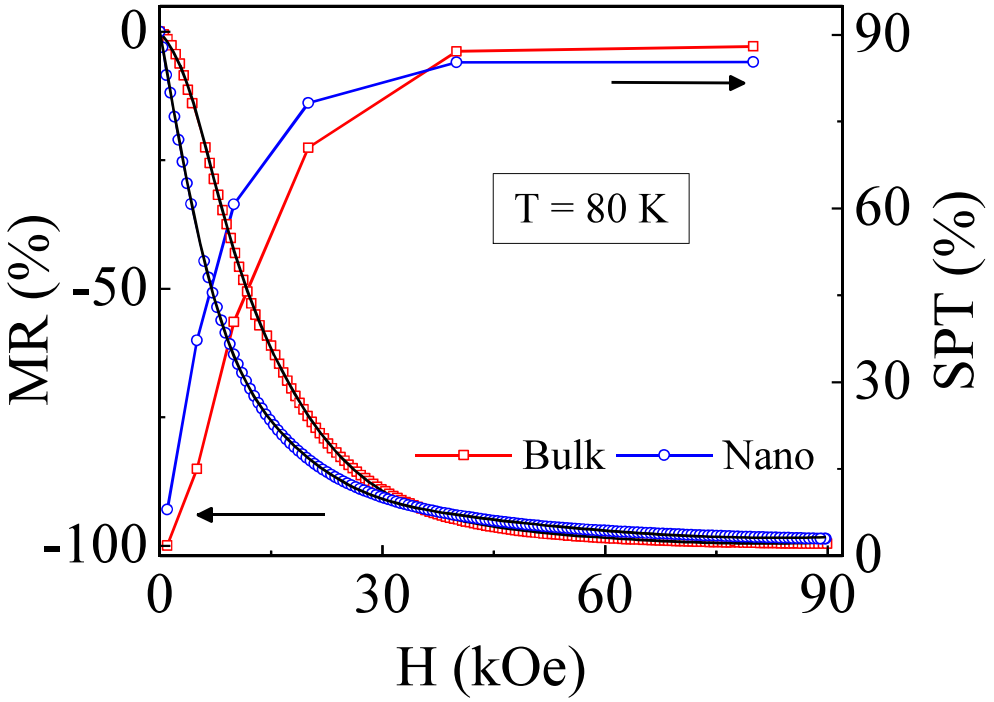


**Figure 4.20:** A typical fitting of MR versus H data with SPT model at 80 K and variation of SPT component with different magnetic field value in the samples.

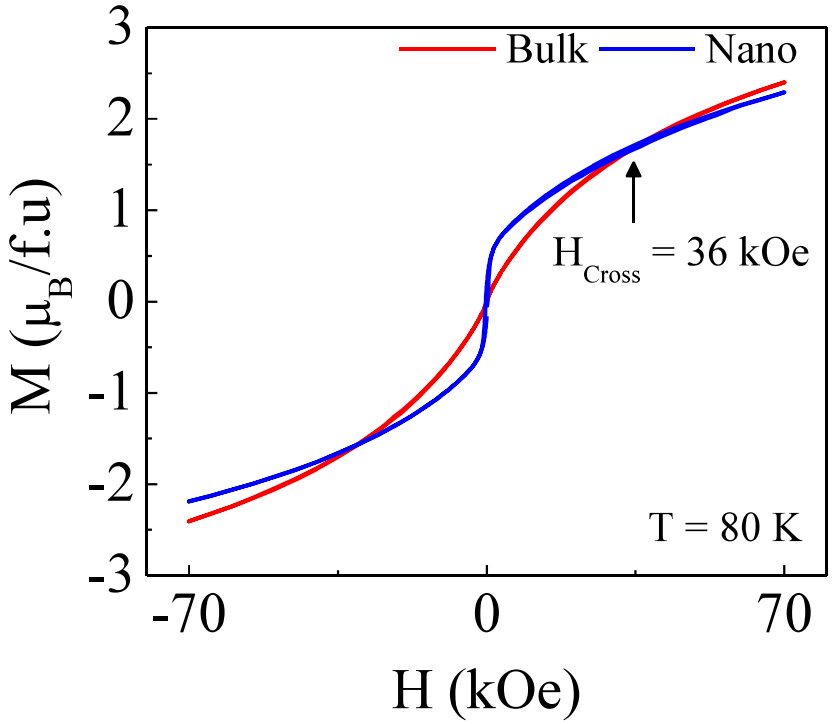


**Figure 4.21:** Isothermal magnetization at 80 K for Bulk and nanocrystalline samples.

It is well known that magnetic properties are correlated with transport properties in

manganites. So to understand this enhancement of LFMR for $T < 100K$, magnetic field dependence of magnetization at 80 K has been performed (see Fig. 4.21). For low magnetic field ($H < 36kOe$), an increase in magnetization for Nano sample is observed. This enhancement of magnetization is undoubtedly related with the enhancement of SPT component in nanoparticle as around the same magnetic field there is also crossover of the SPT components of Bulk and Nano samples as shown in Fig. 4.20. Whereas for higher field value ($H > 36kOe$) magnetization for Nano sample is lower than that Bulk sample and this low magnetization value is due to the presence of the surface disorder. Thus M(H) data tells that surface contribution comes into play above $H_{Cross} = 36kOe$ at 80 K.

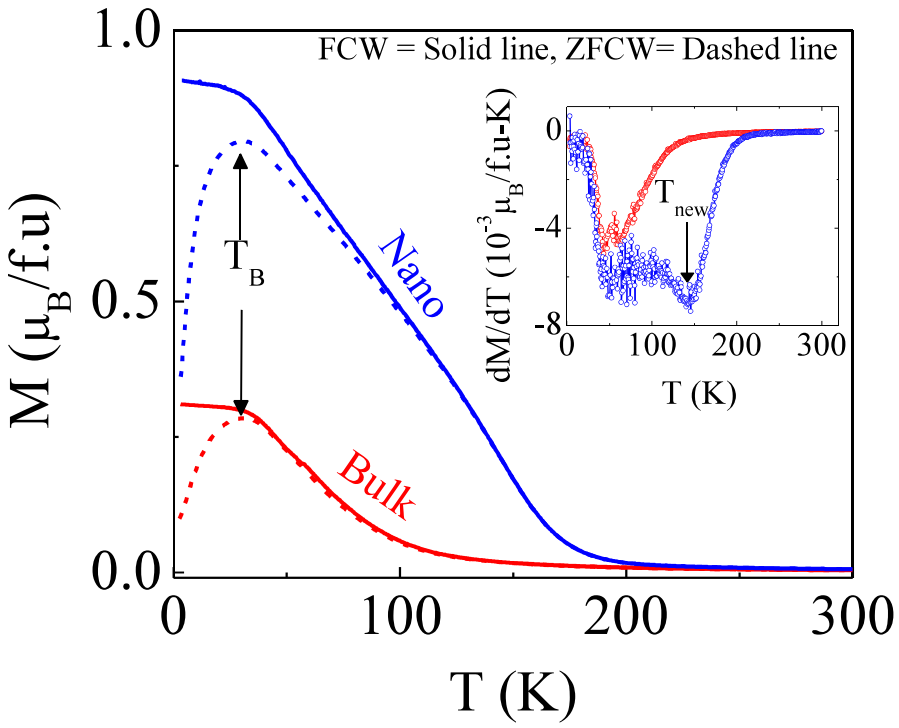


**Figure 4.22:** Evolution of magnetization measured in ZFC and FCW protocol with temperature in 1 kOe magnetic field value.

Again, for $T > 100K$ there is an enhancement of MR in nanoparticles in the whole magnetic field range. Thus magnetization measurement as a function of temperature in presence of 1 kOe external magnetic field has been performed (Fig. 4.22) for both zero field cooled warming (ZFC) and field cooled warming (FCW) protocol. In

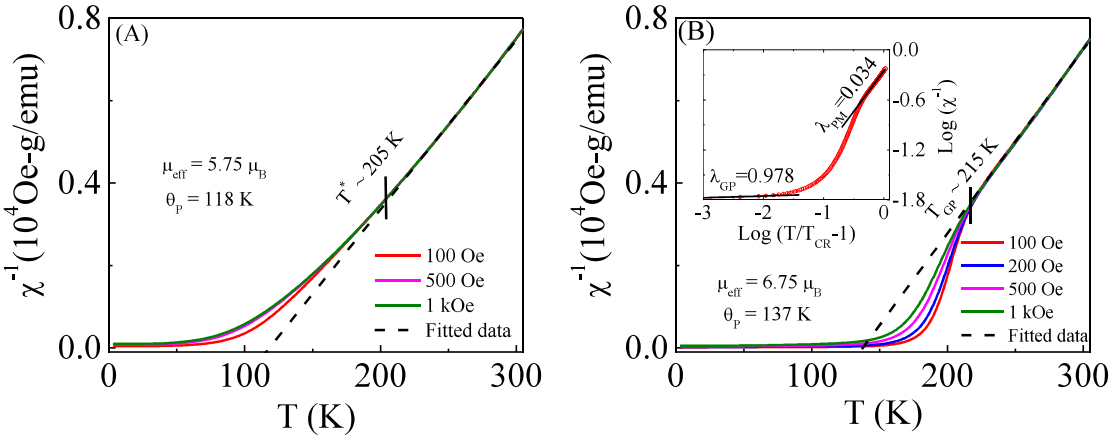


**Figure 4.23:** (A) Temperature variation of inverse dc susceptibility (H/M) data in presence of 100 Oe, 500 Oe and 1 kOe magnetic field for bulk sample. Dashed line is the Curie-Weiss fitting of the high temperature data. (B) Variation of (H/M) with temperature in 100 Oe, 200 Oe, 500 Oe and 1 kOe magnetic field for nanoparticle and dashed line is the Curie-Weiss fitted data.

both the samples a huge bifurcation is observed between ZFC and FCW curves below 30K, though in nanoparticle bifurcation started from higher temperature (near 100 K). The observed bifurcation is one of the signature of glassy behavior of the systems [193, 194]. The maxima of ZFC curves, known as the blocking temperature ($T_B$) remains almost unchanged (30 K) in both the samples. Enhancement of magnetization has been observed in 100 nm particle and this enhancement starts from 200 K. Though in bulk sample around 200 K nothing is visible from M(T) curve as well as from its temperature derivative curve (inset of Fig. 4.22).

For this reason, temperature dependence of inverse dc susceptibility (H/M) data in presence of 100 Oe, 500 Oe and 1 kOe magnetic field for bulk sample has been investigated and is presented in Fig. 4.23. The data was taken in FCW protocol. Here it can be seen that all the curves almost superimposes. To clarify the high temperature paramagnetic state ($T \geq 250K$), (H/M) data has been fitted with Curie-Weiss law $\chi = C/(T - \theta_{CW})$ where $C = \mu_{eff}^2/3k_B$ and $\mu_{eff}$, $\theta_{CW}$ are effective magnetic moment in Bohr magnetron and paramagnetic curie temperature respectively. From the fitting, effective magnetic moment comes out to be $5.75\mu_B$ which is greater than the theoretically expected value of $4.62\mu_B$ and it indicates that the paramagnetic

state consists of ferromagnetic clusters containing more than one Mn ions [195, 196]. Also, the positive value of $\theta_{CW} \sim 118K$ implies the dominance of ferromagnetic interactions in the system. Here another important observation is that (H/M) deviates upward from Curie-Weiss fitted curve and this upward deviation implies the less susceptibility value than the paramagnetic value. Previously, this kind of upward deviation from curie-weiss law has been observed in different manganites [171], double perovskites [170], cobaltites [169] and in antiperovskites [198] systems. In all the cases the presence of antiferromagnetic interactions has been claimed to be the reason behind this upward deviation. Thus it indicates the presence of some kind of short range antiferromagnetic interactions in the paramagnetic region. More importantly, this upward deviation starts near 205 K, where in nanoparticle enhancement of magnetization appears.

For further clarification, (H/M) data of nanoparticle has also been analyzed and in this case downward deviation from Curie-Weiss fitting is observed (Fig. 4.23(B)). Most interestingly, here the downward deviation arises almost around the same temperature (215 K) where there was upward deviation in bulk sample. This downward deviation is a signature of Griffiths phase [205–208]. Usually Griffiths singularity is characterized by the exponent of magnetic susceptibility ($\lambda$) which is obtained from the power law [160] $\chi^{-1} \propto (T - T_{CR})^{1-\lambda}$, where $0 < \lambda < 1$ and $T_{CR}$ is the critical temperature of ferromagnetic clusters where susceptibility diverges. Here, after determining $T_{CR}$ accurately by the method followed by Jiang et al. [165] the exponent comes out to be $\lambda_{PM} = 0.034$ in the paramagnetic region which is close to ideal value of '0' and in Griffiths region it is $\lambda_{GP} = 0.978$ which is comparable with other manganite samples. The fitting has been shown in the inset of Fig. 4.23(B). Thus, it can be safely said that due to the reduction of particle size antiferromagnetic interactions, responsible for upward deviation from Curie-Weiss behavior has been diluted and is replaced with ferromagnetic one which results in Griffiths phase. And it can also be seen from the enhanced $\mu_{eff} = 6.75\mu_B$ in the nanoparticle sample than

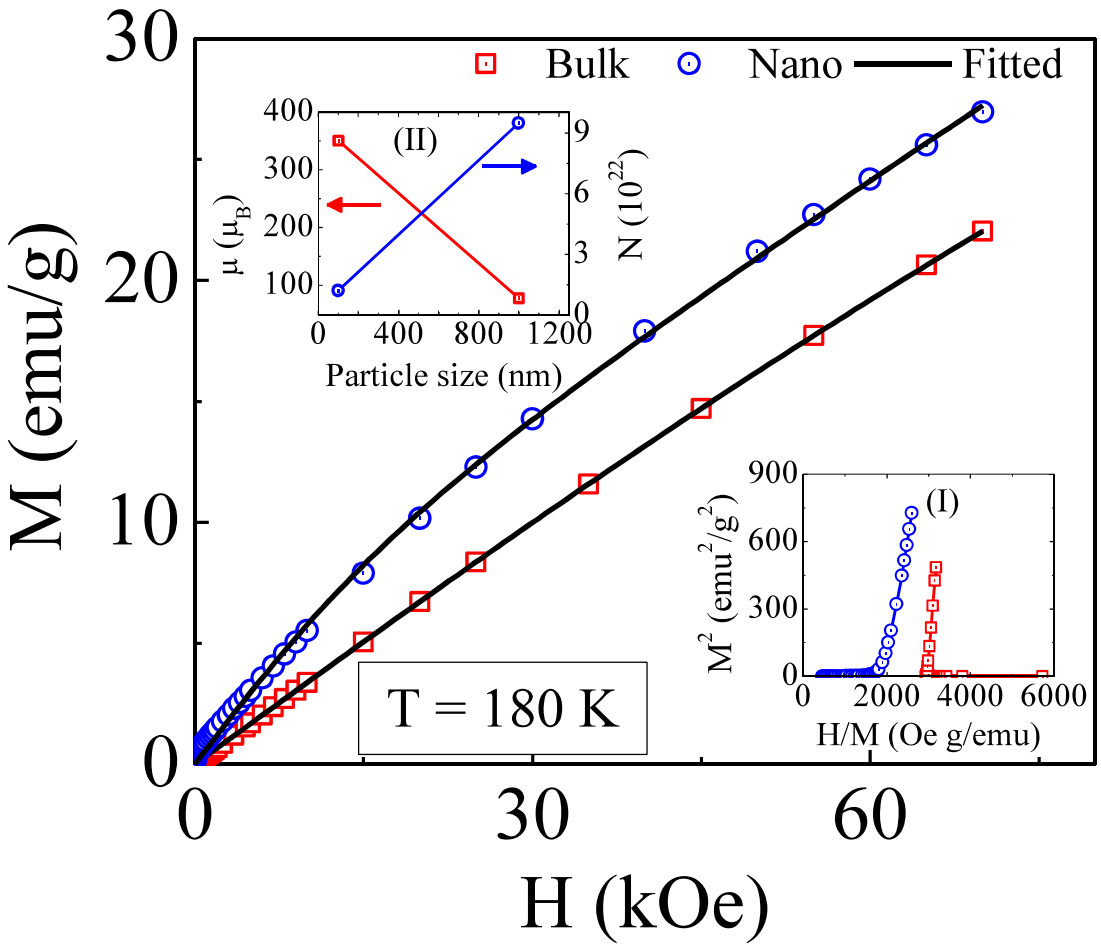


**Figure 4.24:** Fittings of the M vs H data for the bulk and nanocrystalline samples with Wohlfarths model where black lines are the corresponding fitted lines. Inset (I) shows the Arrott plots ($M^2$ vs H/M) of the samples and (II) presents the evolution of the average cluster size and density for the bulk and nanocrystalline samples.

that of bulk $\mu_{eff} = 5.75\mu_B$ value. Therefore, the enhancement of magnetoresistance at high temperature ($T \geq 100K$) in nanoparticles is because of the modification of non-Griffiths phase to Griffiths phase.

To understand the appearance of the new magnetic phase with particle size reduction as well as to further investigate the evolution from non-Griffiths phase to Griffths phase (around 200 K), isothermal magnetization measurement for the samples has been performed at 180 K. The Arrott plot [180] ($M^2$ vs $H/M$) at 180 K presented in the inset (I) of Fig. 4.24 does not show any spontaneous magnetization which ruled out any signature of long range ordering. Again, presence of the ferromagnetic

clusters is observed from the analysis of $1/\chi$ vs T data. To get a qualitative idea about these clusters and considering these clusters to be nearly noninteracting, M(H) data has been fitted with the Wohlfarths model [204] $M(H) = N\langle\mu\rangle L(\langle\mu\rangle H/k_BT)$ where '$N'$ is the density of the ferromagnetic clusters, '$\langle\mu\rangle'$ is the average clusters moment and $L(x)$ is the Langevin function. The variation of '$\langle\mu\rangle'$ and '$N'$ extracted from the fitting has been shown in the inset (II) of Fig. 4.24 which indicates the increase in the size of the ferromagnetic clusters and decrease in the cluster density with particle size reduction.

Based on the above discussions a phenomenological picture can be proposed. According to this picture both bulk and nanoparticles samples consists of ferromagnetic clusters which are sensitive to external magnetic field as well as temperature. The sizes of these clusters at low temperatures ($T < 100K$) being larger in nanopartcles ($\sim 100nm$), spin polarized tunneling increases which results in the enhancement of low field magnetoresistance in nanoparticle. For bulk sample with application of magnetic field these clusters grows in size and creates percolation path for electronic transport and this is the reason for suppression of resistivity in bulk sample in presence of magnetic field ($\sim 30kOe$). On the other hand, in nanosample because of relatively larger clusters sizes than that of the clusters in bulk sample, with lowering temperature even in absence of field there is the spontaneous creation of percolation path between clusters which results in the spontaneous insulator to metal transition. With application of magnetic field these percolation path further increases and resistivity simultaneously decreases.

## 4.5 Summary

In summary, the enormous MR has been achieved in $(La_{0.5}Y_{0.5})_{0.7}Ca_{0.3}MnO_3$ compound by controlling magnetic disorder via tuning lattice distortion together with

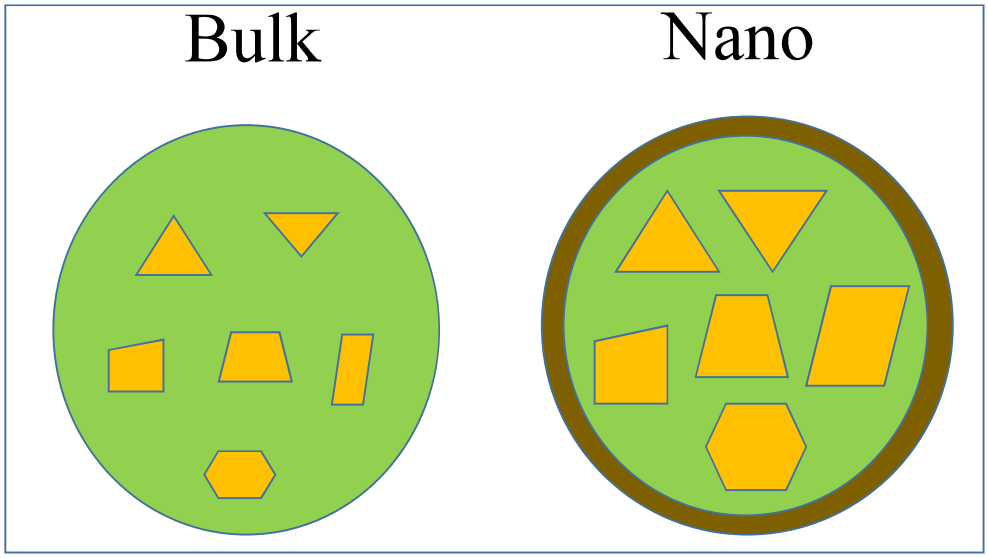


**Figure 4.25:** A schematic picture of the bulk and nanocrystalline samples for phenomenological model.

quenched disorder. Reversibility of magnetoresistance is due to the presence of non-interacting ferromagnetic clusters. The study reveals that massive enhancement of MR can be achieved by introducing disorder and shows the way to find out promising magnetoresistive material. The enhanced magnetoresistance in $x = 0.5$ compound is described by a phenomenological model of percolation path created by ferromagnetic clusters.

In the second part of the chapter, the systematic analysis of the dc susceptibility data of the series $(La_{1-x}Y_x)_{0.7}Ca_{0.3}MnO_3$ $(x = 0, 0.3, 0.4, 0.5, 0.6)$ indicates a critical point $x_C = 0.5$, above which GP like phase does not occur. The appearance of short range antiferromagnetic interactions above curie temperature prohibits the formation of ferromagnetic interactions due to the proximity effect. Due to this randomly distribution of SR-AFM interactions, it is difficult for FM coupling develop globally and for this reason size of the ferromagnetic cluster decreases gradually with increasing Y concentrations. The development of this SR-AFM interactions is responsible for the appearance of non-GP like phase which gets suppressed with decreasing Y concentrations. Decrease of $Y^{3+}$ concentrations, increase the $Mn - O - Mn$ bond angle which prohibits the formation of SR-AFM interactions and favors GP like

phase.

In the last part of the chapter, the study shows the reduction of orthorhombic distortion in the $(La_{0.5}Y_{0.5})_{0.7}Ca_{0.3}MnO_3$ compound with decrease in particle size and is also associated with an enhancement of the effective density of states. Moreover, the reduction of particle size also leads to the evolution from non-Griffiths phase to Griffiths phase which helps to increase the size of the ferromagnetic clusters. This large ferromagnetic clusters helps to create percolation path for electronic transport and as a result enhancement of magnetoresistance occurs in the nanoparticle at higher temperature ($T > 100K$). At lower temperature ($T < 100K$) these ferromagnetic clusters further grow in size in nanoparticle compare with bulk which results in the increase in spin polarized tunneling component in the nanoparticle and is the possible reason for low field enhancement of magnetoresistance.

# CHAPTER 5

# Evolution from non-Griffiths phase to Griffiths phase and giant enhancement of magnetoresistance in the nanocrystalline $(La_{0.4}Y_{0.6})_{0.7}Ca_{0.3}MnO_3$ compound

## 5.1 Introduction

The observation of Griffiths singularities [158] in materials exhibiting complex magnetic interactions has drawn notable scientific interest [205–208]. Griffiths pointed out that, for a magnetic system, the quenched random distribution makes the thermodynamic function unanalytic in the temperature range $T_C < T < T_G$, where $T_G$ represents the characteristic temperature below which ferromagnetic clusters start to nucleate and $T_C$ is the ferromagnetic ordering temperature. This temperature regime $T_C < T < T_G$ is the Griffiths phase (GP) which is microscopically characterized by a short-range ferromagnetic cluster like system induced by quenched disorder. The

signature of GP is visualized experimentally from the anomalies in magnetic susceptibility and heat capacity data [160,161,209]. The GP behavior has been observed in various systems including spin glass systems [162], heavy fermi materials [160,161], layer manganites [210] and hole-doped manganites [163,164,211,212]. Burgy [213] has pointed out that the coexistence of competing ferromagnetic (FM) and antiferromagnetic (AFM) phases can also exhibit GP phase. Thus the main ingredients for GP observation are the competition between magnetic interactions and the intrinsic disorder. However, depending upon the dominance of AFM interactions system can also exhibit a non-Griffiths like phase which is identified by an upturn from the Curie-Weiss law $\chi^{-1} \propto (T - \theta_P)$ behavior in $\chi^{-1}(T)$ data above the Curie temperature. Currently, a non-Grifiths like phase has been observed in various systems with competing FM-AFM interactions such as cobaltites [169], manganites [66,171], double perovskites [214] etc. Therefore, depending upon the relative strength of FM and AFM interactions system may behave non-Griffiths phase or Griffiths phase. Recently, there is an ongoing debate [164,210] on the concurrence of GP and CMR. However, the effect of the modification of non-Griffiths phase to Griffiths phase and its effect on CMR property has rarely been addressed. Very recently, a non-Griffiths like phase has been observed in bulk polycrystalline $(La_{1-x}Y_x)_{0.7}Ca_{0.3}MnO_3$ compounds with 'Y' doping, where field induced modification is observed up to the doping range $x < 0.6$ [183]. However, investigations on the reduction of particle sizes in the $(La_{1-x}Y_x)_{0.7}Ca_{0.3}MnO_3$ compounds are ignored.

In this article, we report the observation of Griffiths phase in nanocrystalline $(La_{0.4}Y_{0.6})_{0.7}Ca_{0.3}MnO_3$ compound via magnetization, electrical transport and heat capacity measurements. Our study implies that the origin of Griffiths phase is associated with the release of lattice distortions. The study reveals that occurrence of Griffiths phase is also associated with the enhancement of colossal magnetoresistance (CMR) in the nanocrystalline samples.

## 5.2 Sample Preparation and Characterization

The polycrystalline bulk and nanoparticles of $(La_{0.4}Y_{0.6})_{0.7}Ca_{0.3}MnO_3$ compound have been prepared by the conventional sol-gel method with $La_2O_3$, $Y_2O_3$, $MnO_2$ and $CaCO_3$ as starting materials of purity 99.9%. For the preparation of nanoparticles, the decomposing gel was pelletized and subsequently heated for 3 hours at $1000^0$C, $900^0$C and $800^0$C respectively. Whereas to prepare the bulk counterpart it was heated for 36 hours at $1300^0$C.

## 5.3 Experimental Results and Discussion

Phase purity of all the samples was confirmed by room temperature x-ray diffraction. From x-ray line width broadening using Debye-Scherrer's formulae average nanocrystallite size was determined which are 112, 71 and 50 nm for samples sintered at $1000^0$C, $900^0$C and $800^0$C respectively. Scanning electron microscopy (SEM) measurements were also performed to determine the average particle sizes of the samples and it comes out to be 120, 80 and 65 nm respectively and these values are close to the sizes calculated from x-ray linewidth broadening. The average particle size of the bulk sample from SEM measurements comes out to be $\sim 1000nm$. For convenience, hereafter bulk sample will be referred as 'Bulk' whereas nanocrystallite samples will be referred as 'Nano1' (average particle size 120 nm), 'Nano2' (average particle size 80 nm) and 'Nano3' (average particle size 65 nm) respectively. Magnetic measurements such as magnetic field and temperature dependency of macroscopic magnetization were carried out using quantum design SQUID VSM. The temperature and magnetic field dependence of specific heat was measured by employing PPMS of quantum design. The ac magnetic measurements were performed by utilizing commercial SQUID magnetometer. The x-ray diffraction (XRD) measurements

of the samples over the temperature range 20 - 300 K were carried out utilizing Rigaku-TTRAX-III with 9 kW rotating anode source. The electrical transport and magnetotransport measurements were performed by four probe method using the longitudinal geometry of the bar-shaped samples.

### 5.3.1 Structural characterization

The room temperature XRD data (Fig. 5.1) of all the polycrystalline samples have been analyzed by Rietveld profile fitting using FULLPROF software. The Rietveld profile fitting of the XRD data shows the single phase nature of all the samples with 'Pnma' space group. The particle sizes determined from SEM and x-ray line width broadening gives almost the similar result. The average particle size of the bulk sample from SEM measurements comes out to be $\sim 1000nm$. For convenience, hereafter bulk sample will be referred as 'Bulk' whereas nanocrystallite samples will be referred as 'Nano1' (average particle size 120 nm), 'Nano2' (average particle size 80 nm) and 'Nano3' (average particle size 65 nm) respectively.

From the extracted lattice parameters a, b and c the modification of orthorhombic distortions, defined as $\Delta(\perp) = \frac{a+b-c/\sqrt{2}}{a+b+c/\sqrt{2}}$ and $\Delta(\parallel) = \frac{a-b}{a+b}$, has been compared for bulk and nanocrystallite samples. The distinct reduction of $\Delta(\perp)$ is observed with decreasing particle sizes and the same happens for $\Delta(\parallel)$ also (Fig. 5.2(b)), though there is a little increase when particle size decreases from 120 nm. The decrease of $\Delta(\perp)$ and $\Delta(\parallel)$ is also perceptible from the decrease of the angle between (200) and (121) planes with the decrease of particle size. As crystal lattice is susceptible to have higher symmetry with reduction of particle sizes [215], decrease in distortions in nanocrystallite samples is expected. The unit cell volume has also decreased with the reduction of particle size (Fig. 5.2(a)) which may be due to the enhanced surface pressure.

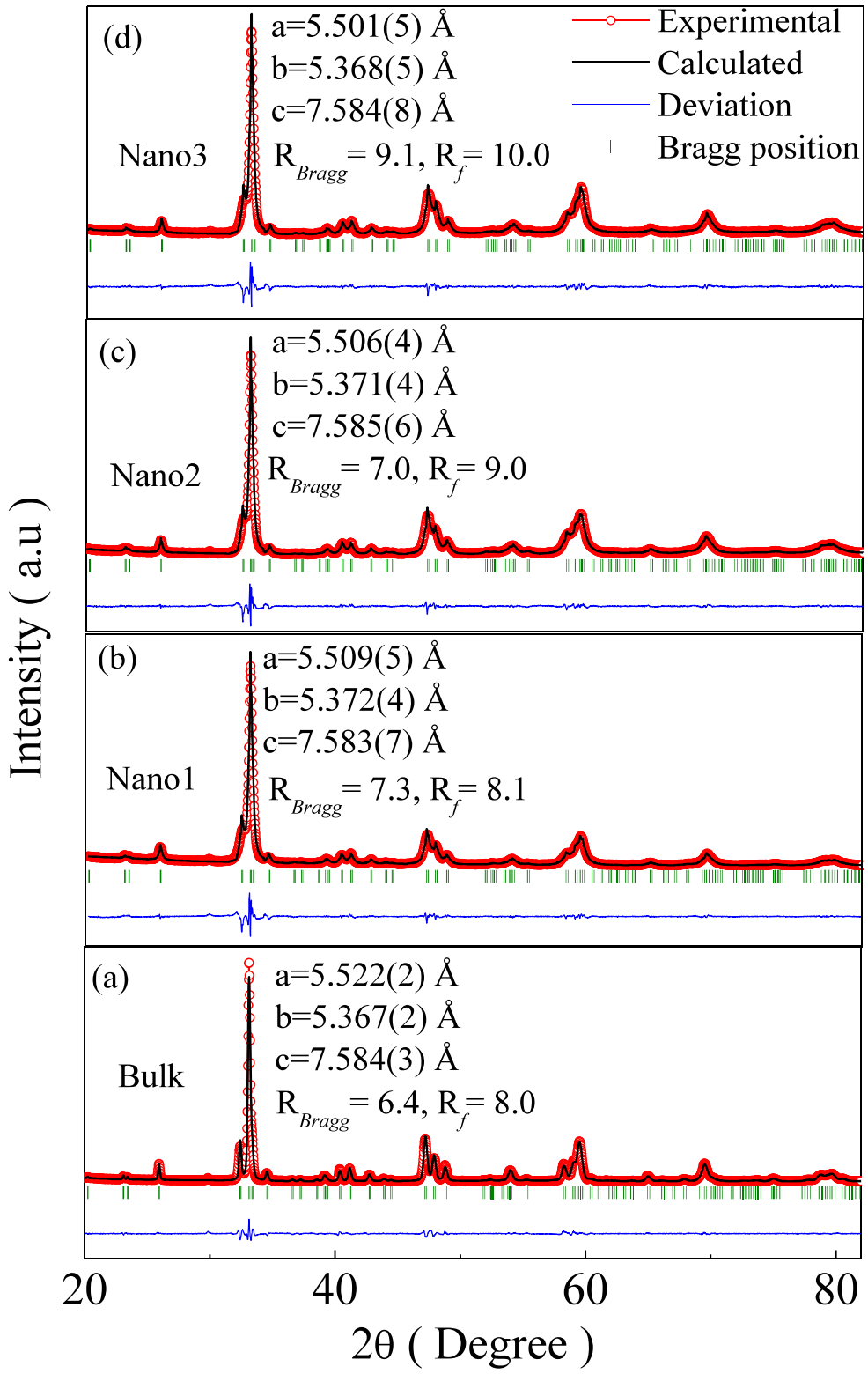


**Figure 5.1:** Room temperature XRD data along with profile fitted data for (a) Bulk (b) Nano1 (c) Nano2 and (d) Nano3 sample.

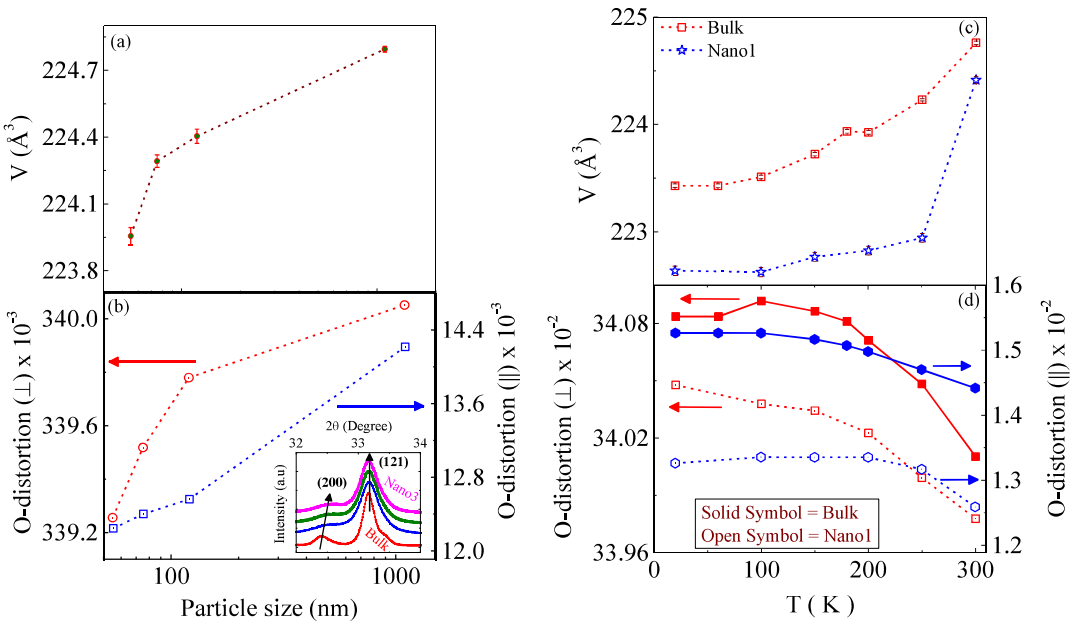


**Figure 5.2:** (a) Variation of unit cell volume with particle sizes. (b) The evolution of orthorhombic distortions [$\Delta(\perp)$ and $\Delta(\|)$] with particle size variation. Inset shows the relative shift of (200) and (121) peaks in Bulk and nanoparticles. (c) Temperature dependence of unit cell volume for 'Bulk' and 'Nano1' sample. (d) The evolution of orthorhombic distortions [$\Delta(\perp)$ and $\Delta(\|)$] as a function of temperature for 'Bulk' and 'Nano1' sample.

The temperature dependence of XRD measurements of 'Bulk' and 'Nano1' has also been performed. The unit cell volume of 'Bulk' decreases with decreasing temperature and it is expected because of the reduction of lattice vibrations. On the other hand in case of 'Nano1' there is a sudden decrease of unit cell volume around 250 K, below which there is a gradual decrease of the unit cell volume. Although there is no structural phase transition around 250 K. The calculated distortions $\Delta(\perp)$ and $\Delta(\|)$ has been compared for 'Bulk' and 'Nano1' samples in the temperature ranges 20 - 300 K. With decreasing temperature, enhancement of $\Delta(\perp)$ and $\Delta(\|)$ is observed. Though in 'Nano1' these distortions are small in the whole temperature range compared with the bulk sample.

### 5.3.2 Electrical transport and Magnetotransport study

The evolution of distortions from bulk to nanocrystallite greatly influence the electrical transport and magnetotransport properties. The temperature dependence of resistivity [$\rho(T)$] of all the polycrystalline samples has been carried out in the absence and in the presence of 90 kOe external magnetic field. The measurements were performed during warming cycle from 2 - 300 K after cooling the samples in zero magnetic field. The temperature dependence of zero field resistivity data shows the insulating nature of all the samples down to measurable temperature limit as shown in Fig. 5.3. Compared to the 'Bulk' sample resistivity value decreases for the 'Nano1' sample. However, for the consecutive nanoparticles the value of resistivity increases from the 'Nano1' sample. Usually, with the reduction of particle sizes, the decrease of resistivity is observed in charge-ordered compound due to the growth of surface ferromagnetism [144] and enhancement of resistivity occurs in case of ferromagnetic compound due to the enhanced surface disorder [216]. In the present case, initial size reduction (from $\sim \mu$m to 120 nm) suppress the resistivity and further reduction enhances it. This feature indicates that there are two competing features, one is surface disorder and other is related to the change in the structural parameter from bulk to 'Nano1'. In 'Nano1' sample reduction of distortions is observed which is one of the competing features playing the role in huge reduction of resistivity with initial particle size reduction. On application of 90 kOe external magnetic field suppression of resistivity is observed in all the nanoparticles but a huge change of $\sim 10^5$ order near 50 K temperature is observed in 'Nano1' sample. The field induced metal-insulator transition is observed in 'Nano1' particle around 75 K and in 'Nano2' it is around 60 K but no signature of metallic transition is visible in 'Nano3'. This decrease of $T_{MI}$ with the reduction of particle sizes is due to the lowering phase fraction responsible for conduction. In 'Nano1' at low temperature ($< 25K$) there is an upturn in resistivity and this upturn increases with lowering particle sizes. It

implies the dominating feature of surface contribution from 'Nano2' particle.

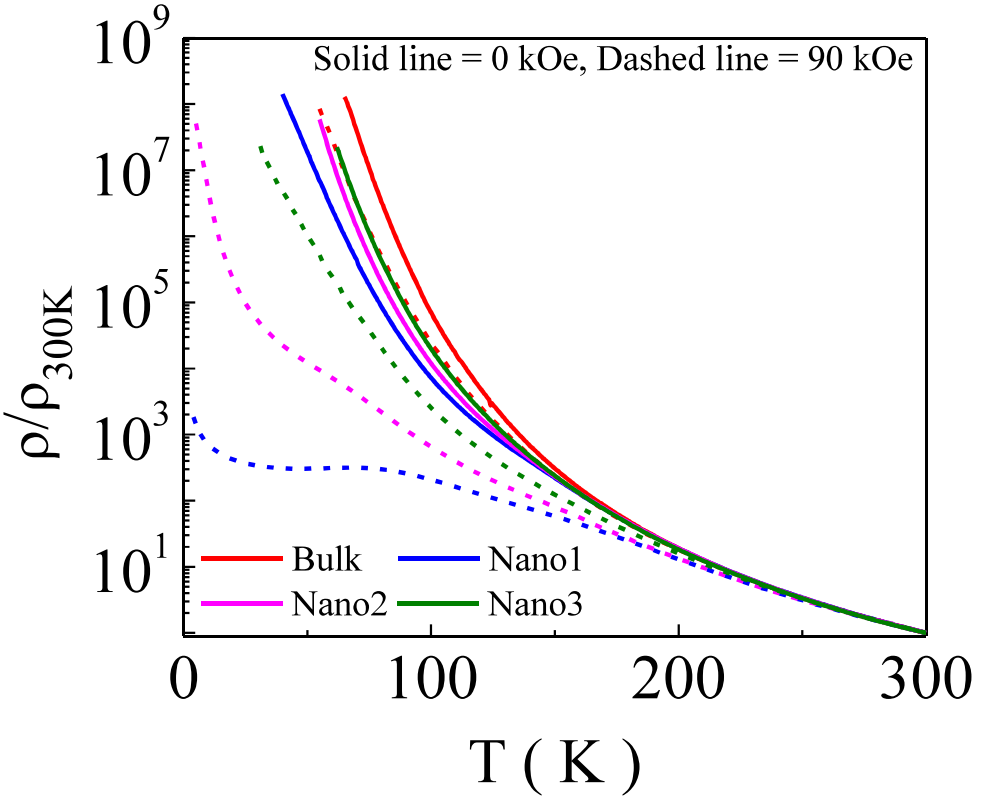


**Figure 5.3:** Temperature dependence of normalized resistivity of bulk and nanocrystalline samples. Here solid line is zero field resistivity data and dashed line is resistivity data measured at 90 kOe magnetic field and color code represents different samples.

From the magnetotransport study, the variation of magnetoresistance ($MR\%$) with temperature in bulk and nanocrystallite samples has been performed. The $MR\%$ has been calculated using $MR(\%) = \frac{R(H)-R(0)}{R(0)} \times 100$ which is commonly used for CMR materials and here where R(H) is the resistance in presence of magnetic field and R(0) is resistance in absence of magnetic field Through out the whole temperature range enhancement of MR has been observed in 'Nano1' sample compared with bulk and other nanocrystallite samples. The enhancement of MR is about $10^4$ order compared with bulk at 50 K temperature. To have more insight, magnetic field dependence of MR for all the samples has also been performed at different temperatures. In Fig. 5.4 dependence of MR with the external magnetic field at 80 K temperature has been presented. It is clearly seen that for all applied field value MR is larger in 'Nano1' compared with other and reaches at $3 \times 10^4\%$ for 90 kOe

magnetic field, whereas for 'Nano2', 'Nano3' and 'Bulk' it is only $9\times10^3\%$, $2\times10^3\%$ and $7\times10^2\%$ respectively for the same applied magnetic field.

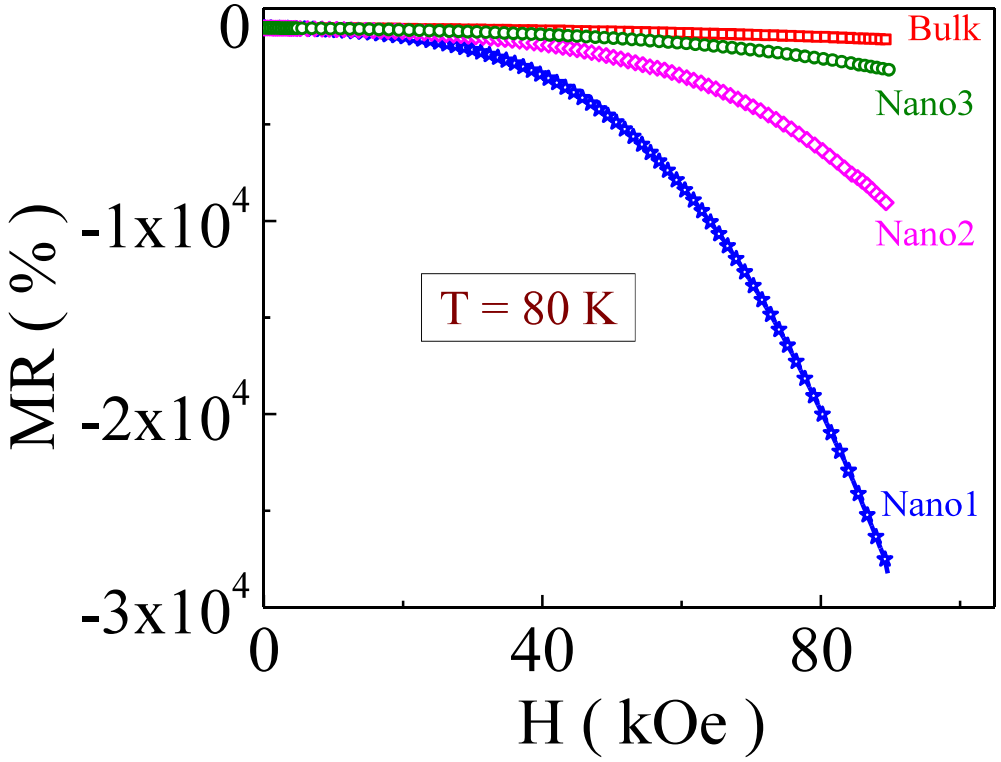


**Figure 5.4:** Magnetic field dependence of MR for bulk and nanocrystallite samples.

In order to explore the basic physics behind this huge enhancement of MR in 'Nano1' sample, magnetoresistance data of all the samples at different temperatures has been analyzed with the help of spin-polarized tunneling model (SPT) as proposed by Raychaudhuri et al [217]. This model describes the dependence of MR on the magnetic field by taking into account the slipping of domain walls across the grain boundary. According to this model, the expression of MR is

$$MR = -A' \int_0^H f(k)dk - JH - KH^3 \tag{5.1}$$

In this model it has been assumed, that in the absence of magnetic field ferromagnetic domains are pinned at the grain boundary. This pinning strength $k$ has the

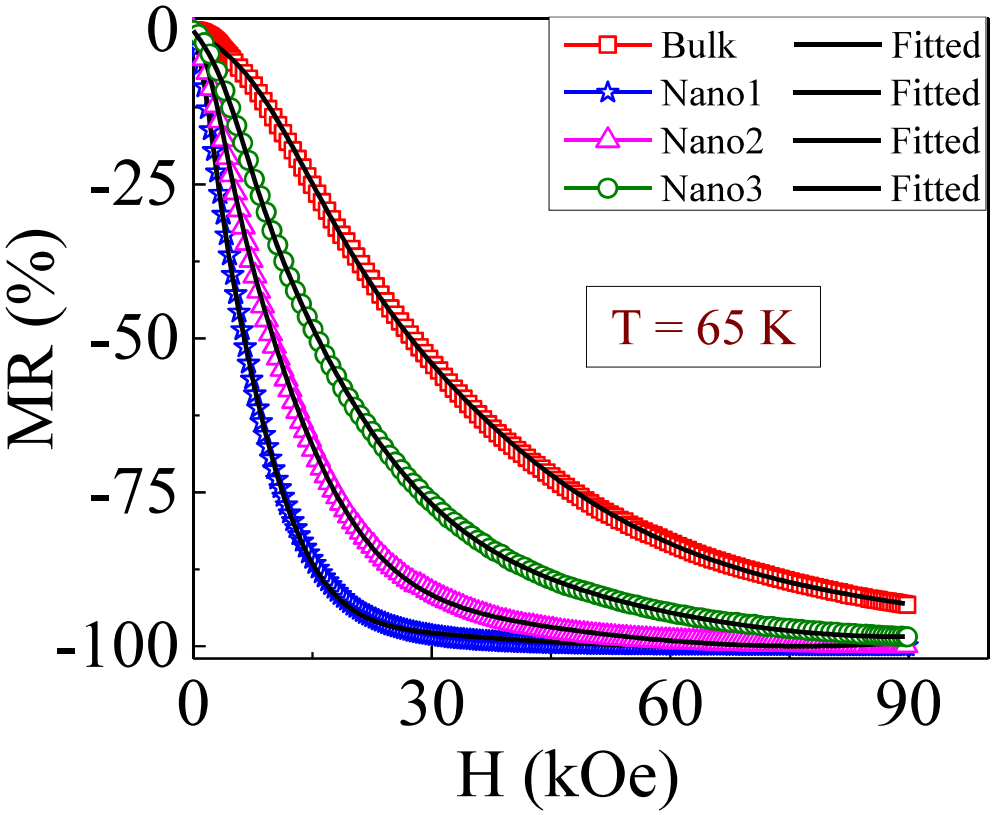


**Figure 5.5:** Variation of MR with magnetic field in 'Nano1', 'Nano2' and 'Nano3' sample at 65 K. Here corresponding black lines are the fitting with the SPT model. Here $MR\%$ has been calculated using the conservative definition of MR i.e. $MR(\%) = \frac{R(H)-R(0)}{R(0)} \times 100$.

following distribution

$$f(k) = Aexp(-Bk^2) + Cexp(-Dk^2) \tag{5.2}$$

Determining all these adjustable fitting parameters $MR_{SPT}$ and $MR_{INT}$ can be determined which are given by

$$MR_{SPT} = -\int_0^H f(k)dk MR_{INT} = -JH - KH^3 \tag{5.3}$$

The experimental MR versus H curves were fitted with equation 5.1 and from fitting parameters $MR_{SPT}$ has been determined. As a representative figure in Fig. 5.5, MR at 65 K of all the nanocrystallite samples along with fitted data has been plotted.

It shows excellent fit with the experimental data for the entire magnetic field range. The evolution of $MR_{SPT}$ with temperature for different particle sizes have been shown in Fig. 5.6. With the increase of temperature, $MR_{SPT}$ decreases in all the nanocrystallite samples and it is expected because of the enhancement of thermal fluctuation with the increase of temperature. The most unusual observation here is that with decreasing particle sizes $MR_{SPT}$ decreases. Normally with reduction of grain sizes, $MR_{SPT}$ increases because of the enhanced surface area. As discussed in the previous electrical transport section that in the present case two competing features are playing role in determination of resistivity. In 'Nano1' sample surface contribution was minimal whereas in 'Nano3' sample it is the dominating one. Depending on these observations together with relatively unusual variations of $MR_{SPT}$ with particle size, it can be argued that the pinning centers resisting the growth of the ferromagnetic domains are not at the grain boundary surface but also in the core of the sample. In other words, there is a possibility of short-range correlation in the core of 'Nano1' sample with a minimal surface disorder. Whereas in 'Nano3' sample surface disorder is dominating compare to inner short-range correlated regions. Based on this result, it has also been assumed that 'Bulk' sample may also consist of these short range correlated regions. So, SPT model was applied to it, but no realistic fitting parameters were obtained. At the same time $MR_{SPT}$ is almost independent with temperature, though MR data at different temperature shows different low field slope. It implies that either there are no FM correlated regions or together with the FM correlated regions some other kind of interactions is present in the 'Bulk' sample.

### 5.3.3 Dc magnetisation study

Temperature dependence of dc magnetization in the presence of 1 kOe external magnetic field was measured in all the samples in zero field cooled warming (ZFCW)

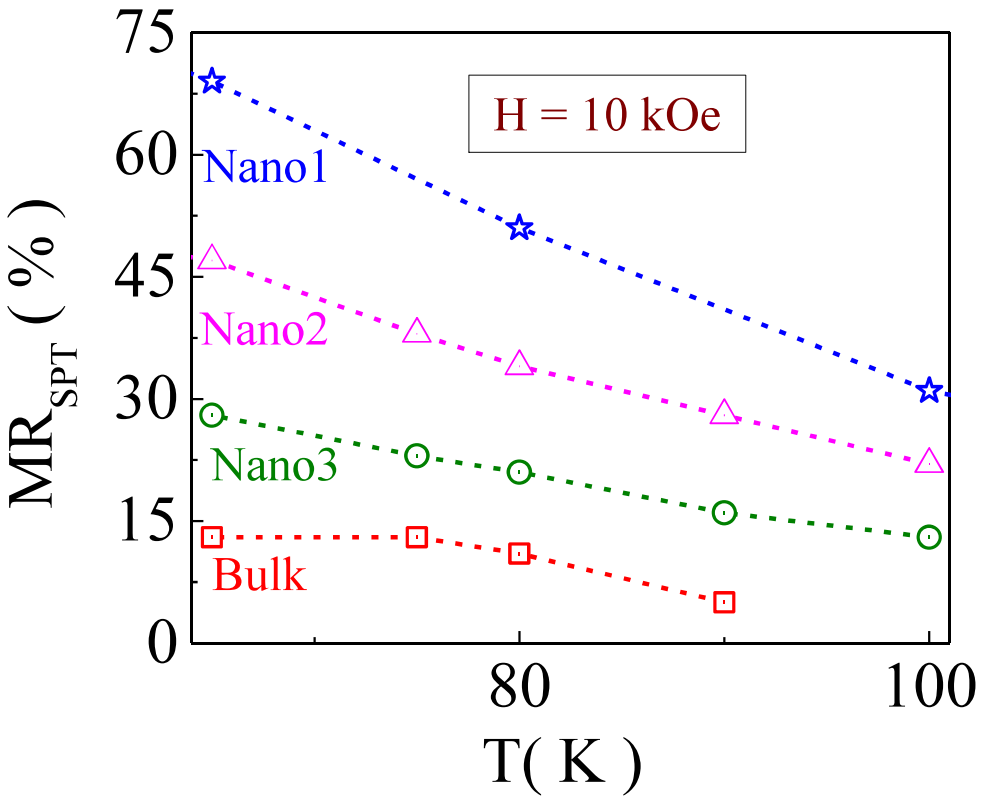


**Figure 5.6:** Temperature dependence of $MR_{SPT}$ in 'Nano1', 'Nano2' and 'Nano3' sample in effect of 10 kOe external magnetic field.

and field cooled warming (FCW) protocol. At low temperature, enhancement of magnetization has been observed in 'Nano1' particle whereas with further decrease of particle sizes magnetization decreases. Here all the samples show the ZFCW and FCW bifurcation at low temperatures which is a typical characteristic of the probable existence of spin glass phase [193, 194]. For all the samples ZFCW curve shows a broad maximum around 30 K, called freezing temperature and denoted as $T_f$. The reduction of $T_f$ with increase of applied magnetic field (inset of Fig. 5.7) for 'Bulk' is observed which is another signature of spin glass phase [218]. The ZFCW and FCW curves start to deviate below a certain temperature known as irreversible temperature ($T_{irr}$). The ($T_{irr}$) increases with the decrease of particle sizes. Canonical spin glass systems usually shows $T_{irr}$ very close to the $T_f$ [193, 194] which is observed for 'Bulk' sample but in nanoparticles $T_{irr} \gg T_f$. This feature resembles in some respects the cluster-glass characteristics [219] of the nanoparticles. With

the reduction of particle sizes a new magnetic phase appears at high temperature (near 200 K). Usually it may appear, that appearance of new peak is associated with superparamagentism coming from the surface of the nanoparticles as reported earlier in literature. If it is the reason, then with the decrease of particle sizes this phase should have increased but here further decrease of particle sizes, magnetization decreases which imply that only surface superparamagnetism is not the case here.

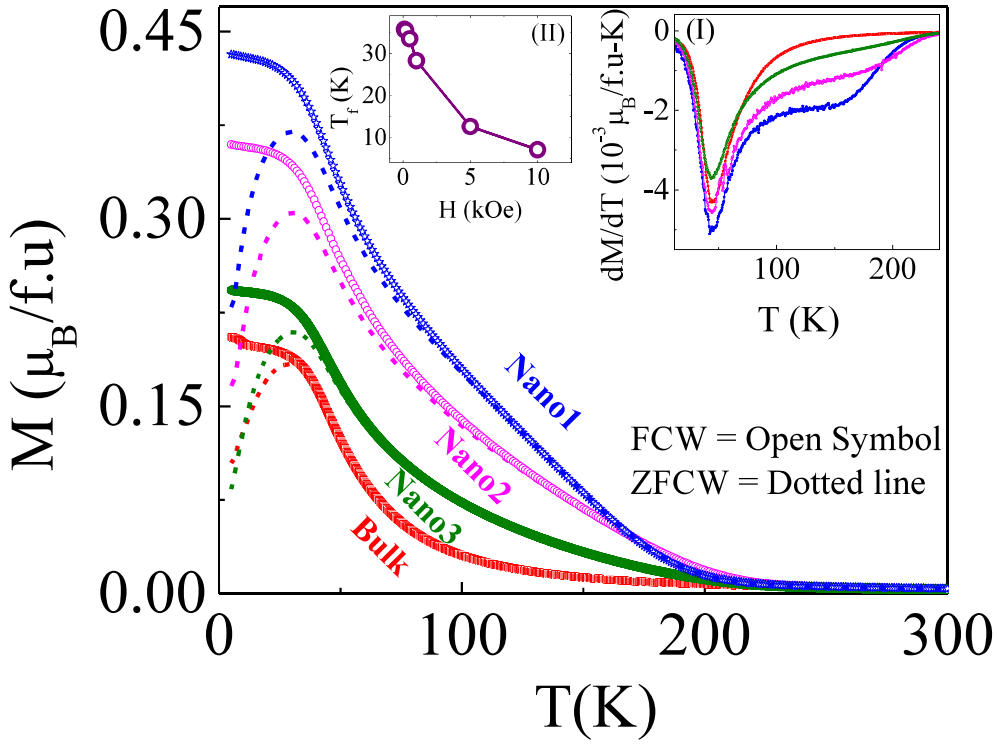


**Figure 5.7:** Evolution of magnetization in 'Bulk', 'Nano1', 'Nano2' and in 'Nano3' samples as a function of temperature in 1kOe magnetic field in ZFCW and FCW protocol. Inset (I) represents the dM/dT versus T curves of the FCW magnetization data of the samples. Inset (II) shows the variation of freezing temperature ($T_f$) in the 'Bulk' sample for different applied magnetic field.

To get further insight, magnetic field dependence of magnetization has been measured at various temperatures. Field variation of magnetization at 5 K temperature has been shown in Fig. 5.8. Here no saturation tendency is observed in any one of the sample but there is a decrease of $M_{90kOe}$ with decrease of particle sizes which is the signature of enhanced surface disorder with the reduction of particle sizes.

With initial size reduction, i.e. in 'Nano1' sample enhancement of magnetization compared with 'Bulk' sample is seen up to 20 kOe magnetic field and above which magnetization decreases. With further particle size reduction i.e. in 'Nano2' and 'Nano3' samples, these enhancement of magnetization appears up to 12 kOe and 3 kOe field. At the same time coercive field value ($H_C$) decreases from 1.17 kOe for 'Bulk' to 1.023 kOe in 'Nano1' and in the successive particles its value are 1.032 kOe and 1.176 kOe. $H_C$ is a measure of anisotropic strength as well as abundance of pinning centers present in the sample. The reduction of $H_C$ in 'Nano1' indicates the reduction of anisotropy or strength of pinning centres. From this result it is clear that in 'Nano1' sample surface contribution is minimal and enhanced magnetization is coming from the core by enhancing of ferromagnetic interaction. This can be also correlated with the reduction of orthorhombic distortions in 'Nano1' compared with 'Bulk' as reduced distortions enhance the ferromagnetic double exchange (DE) interactions.

To understand the appearance of new magnetic phase (around 200 K) with the reduction of particle sizes, isothermal magnetization has also been measured at 150 K, 180 K and 200 K temperatures for all the samples. From the Arrott plot [180] ($M^2$ versus H/M shown in Fig. 5.9) no signature of spontaneous magnetization is observed at 180 K temperature which suggests the absence of long-range ferromagnetic ordering in the samples. Thus the high-temperature phase of the nanoparticles ($250K > T > 100K$) consists of ferromagnetic clusters. Considering these clusters to be nearly noninteracting and to get a qualitative idea about these clusters sizes, M versus H data (150 K, 180 K and 200 K) for all the samples has been fitted with Wohlfarth's model [204]

$$M = N\langle\mu\rangle L(\frac{\langle\mu\rangle H}{k_B T}) \tag{5.4}$$

where 'N' is the cluster density i.e. number of cluster per unit volume, '$\langle\mu\rangle$' is the

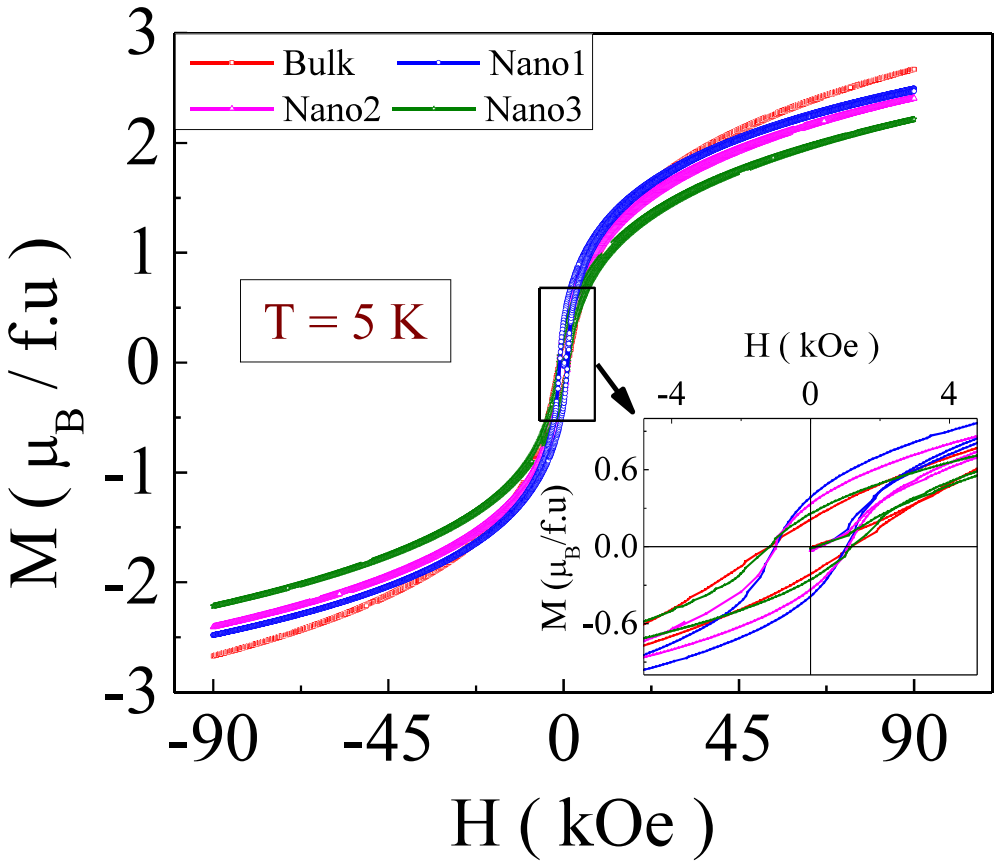


**Figure 5.8:** Isothermal magnetization at 5 K temperature in all the samples and in the inset zoomed portion near the origin of the MH curves has been shown.

average magnetic moment of the clusters and L(x) is the Langevin function and good fitting has been observed. One of the representative M versus H data (180 K) fitted with Wohlfarth's model is shown in the inset of Fig. 5.9.

The extracted average cluster size '$\langle\mu\rangle$' and cluster density 'N' obtained from the fitting of M(H) data using equation 5.4 for the 'Bulk' and nanoparticles at 180 K is shown in Fig. 5.10. It indicates that with the reduction of particle sizes cluster size increases and the cluster density decreases. At the same time the effect of temperature is to decrease the cluster sizes and as a representative figure in the inset of Fig. 5.10 evolution of $\langle\mu\rangle$ with temperature is shown. The observed large value of $\langle\mu\rangle$ in nanoparticles is because each cluster contains large number of atomic spins with magnetic moment of few $\mu_B$. As $\langle\mu\rangle = M_S V$, where V is the volume of the clusters and $M_S$ is the saturation magnetization. Assuming these clusters to be

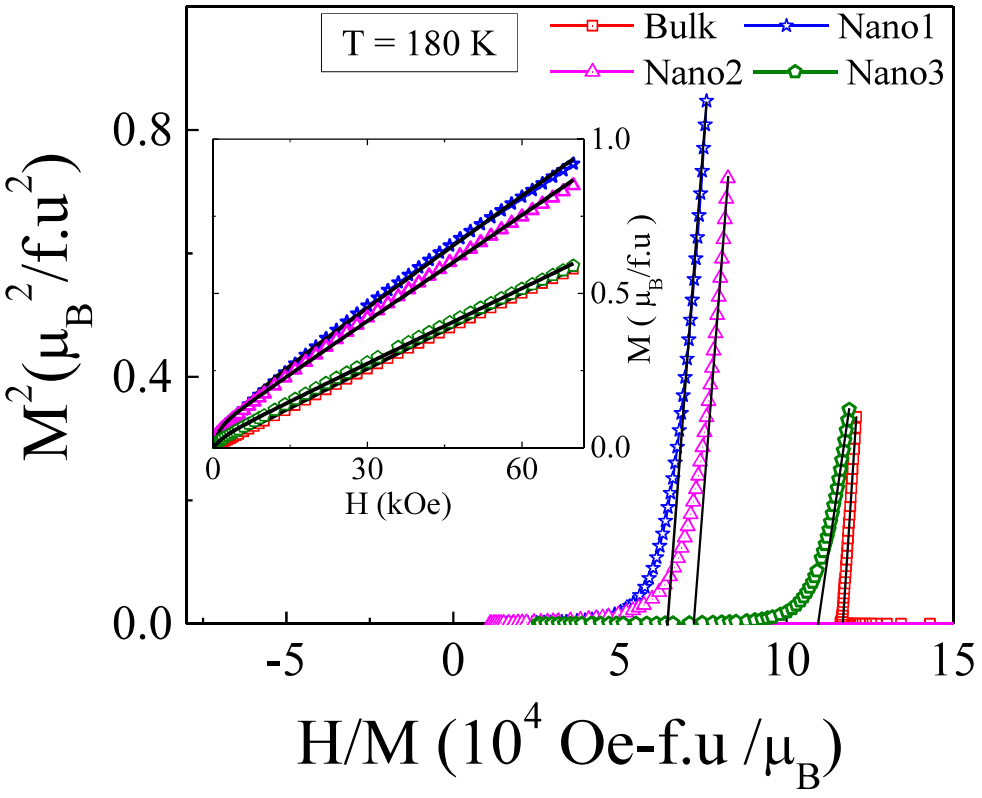


**Figure 5.9:** $M^2$ versus H/M curves of the samples at 180 K. In the inset, fitting of MH data at 180K with Wohlfarth's model has been shown where black lines are the corresponding fitted lines.

spherical the typical size of these clusters comes around $\sim 7nm$ for 'Nano1' sample at 180 K. The average size of these clusters is much lower than the smallest particle ($\approx$ 65 nm from SEM measurement) and it implies that each nanoparticle consists of several ferromagnetic clusters.

To get a deeper view of these qualitative descriptions about clusters, temperature dependence of inverses dc susceptibility (H/M) has been measured at the different applied magnetic field from 100 Oe to 10 kOe in ZFCW protocol for 'Bulk' and 'Nano1' sample. At high temperature the (H/M) data was fitted with Curie-Weiss law $\chi = C/(T - \theta_{CW})$ where $C = \mu_{eff}^2/3k_B$ , $\mu_{eff}$ is effective magnetic moment in Bohr magnetron, $\theta_{CW}$ is paramagnetic Curie temperature and $\lambda(\lambda = \theta_{CW}/C)$ is the molecular field constant. For 'Bulk' sample good fitting of (H/M) data at $T > 250K$ was observed (Fig. 5.11(a)). From the Curie-Weiss fitting, obtained effective para-

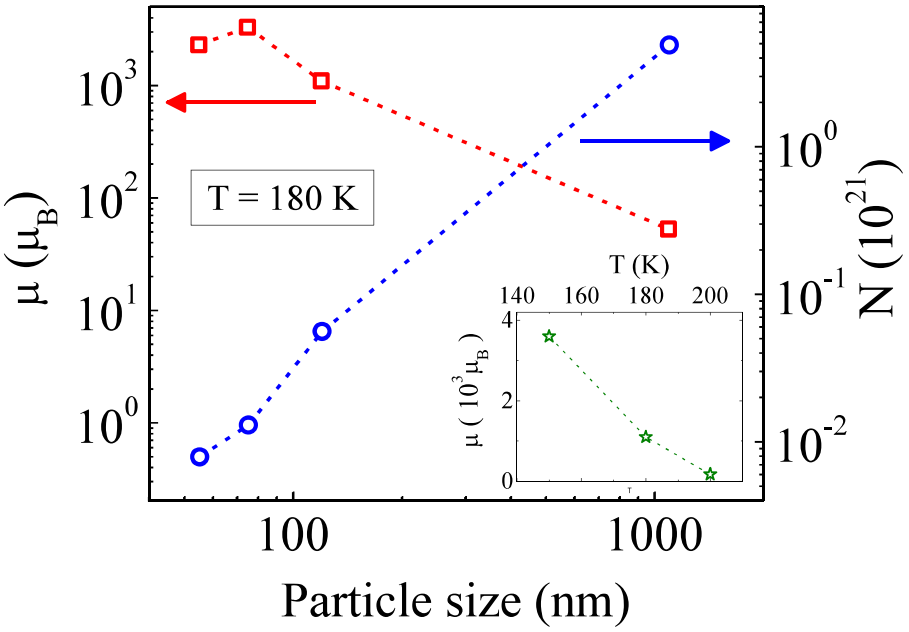


**Figure 5.10:** Evolution of average cluster moment $\langle\mu\rangle$ and cluster density N with particle sizes and in the inset variation of $\langle\mu\rangle$ with T for 'Nano1' sample is shown.

magnetic moment $\mu_{eff} = 5.43\mu_B$ is larger than the theoretically expected value of $4.62\mu_B$ for the spin only moment of Mn ions with appropriate $Mn^{3+}/Mn^{4+}$ ratio, suggesting that high-temperature paramagnetic phase consists of individual magnetic entities containing more than one Mn ions [195]. The obtained Curie-Weiss temperature value is $\theta_{CW} = 108K$ and molecular field constant is $\lambda = 0.55$. The positive values of $\theta_{CW}$ and $\lambda$ indicates the presence of dominant ferromagnetic correlation in the ordered state. A very important aspect is that for the bulk sample the inverse of dc susceptibility data shows an upward deviation from the Curie-Weiss law for temperature $T^* \leq 200K$ and this deviation is almost independent of applied magnetic field (measured up to 10 kOe from 100 Oe). At the same time there is no presence of spontaneous magnetization as observed from the Arrot plot at 180 K(Fig. 5.9).

This upward deviation of $\chi^{-1}(T)$ from CW behavior in 'Bulk' is rather different from the Griffiths phase where field dependent downward deviation arises because of the existing of short-range ferromagnetic clusters. Again, the presence of ferro-

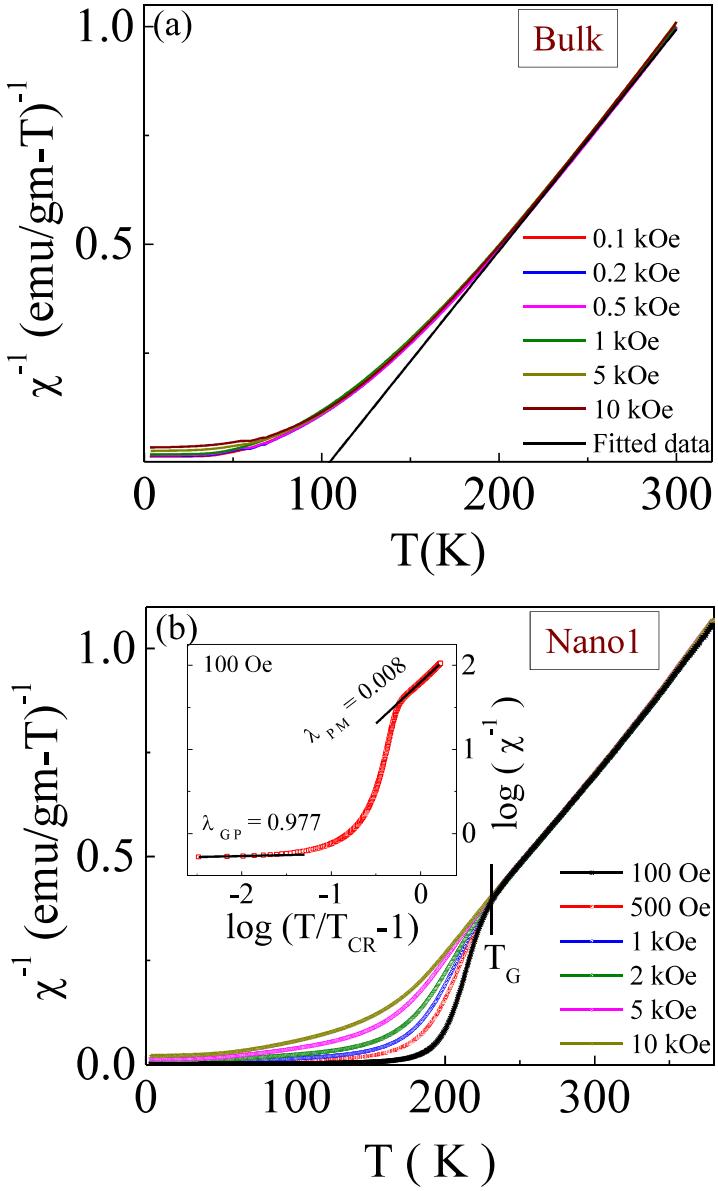


**Figure 5.11:** (a) In 'Bulk' temperature dependence of $\chi^{-1}$ for applied magnetic fields 100 Oe, 200 Oe, 500 Oe, 1 kOe, 5 kOe and 10 kOe. The black line show the Curie-Weiss fitting for $T > 250K$. (b) Variation of $\chi^{-1}$ with temperature in 'Nano1' sample for applied fields 100 Oe, 500 Oe, 1 kOe, 2 kOe, 5 kOe and 10 kOe. Inset shows the plot of $log(\chi^{-1})$ versus $log(t_m)$ at H= 100 Oe and solid lines represents the linear fitting both PM and GP regions with the power law.

magnetic cluster as discussed earlier suggest that this upward deviation is somehow related to these ferromagnetic clusters. For further understanding about these clusters, Curie-Weiss fitting has also been performed below $T^*$ down to $(T^* - 50)$K. This fitting gives the values $\theta_{CW}$ and $\lambda$ to be 85 K and 0.37. This value of $\mu_{eff}$ and $\lambda$, calculated in the temperature range $(T^* - 50)$ is higher and lower respec-

tively than that the calculated from the temperature above $T^*$ ($T > 250$). It indicates that the intracluster coupling is ferromagnetic(enhancement of $\mu_{eff}$) and intercluster coupling is possibly antiferromagnetic (decrease value of $\lambda$) [66]. Recently, this kind of upward deviation from CW law or non-Griffiths phase has been observed in various manganites [171], cobaltites [169], double perovskites [214] and in antiperovskites [198]. For instance in $La_{1-x}Sr_xCoO_3$ [169] this upward deviation of $\chi^{-1}(T)$ has been attributed to the possible existence of antiferromagnetic interactions between neighboring clusters which results in suppression of $\chi$. Recently in antiperovskite $Cu_{1-x}NMn_{3+x}(0.1 \leq x \leq 0.4)$ [198] the observed upward deviation of $\chi^{-1}(T)$ is described by the presence of short-range antiferromagnetic correlations, obtained from electron spin resonance spectra. In phase separated manganite $(La_{1-y}Pr_y)_{0.7}Ca_{0.3}MnO_3(0 \leq y \leq 1)$ [220] the observed upward deviation is explained by the presence of dominance of antiferromagnetic phase fraction over ferromagnetic phase fraction, calculated from neutron diffraction data. The presence of this deviation well above Curie temperature has also been observed in $Sm_{0.5}Sr_{0.5}MnO_3$ [221] due to the predominance of short-range antiferromagnetic charge ordered state. Thus the observed non-Griffiths phase in 'Bulk' sample is possibly the presence of antiferromagnetic correlations between ferromagnetic clusters.

On contrary to the 'Bulk' sample, in case of 'Nano1' sample the CW fitting for $T > 250K$ (Fig. 5.11(b)) gives the effective paramagnetic moment $\mu_{eff} = 5.86\mu_B$ and Curie-Weiss temperature $\theta_{CW} = 144K$. Compared to 'Bulk' sample, the increased $\theta_{CW}$ implies the enhanced ferromagnetic interactions and at the same time enhanced $\mu_{eff}$ indicates the increase in the size of the high temperature ($T > 250K$) paramagnetic entities. The most distinct observation here is that the inverse dc susceptibility shows a field dependent downward deviation from the CW law below a certain temperature in contrast to upward deviation in the 'Bulk' one. This downward deviation together with absence of spontaneous magnetization (Arrot plot (Fig. 5.9) implies the formation of short-range ferromagnetic clusters much above the or-

dering temperature. In addition to that, field induced suppression of the downturn of inverse dc susceptibility has been observed which is because of the masking of ferromagnetic signal by increasing the background paramagnetic signal as suggested by Deisenhofer et al [163]. for manganite systems. The onset of this downturn is indicated as $T_G$ ($\simeq 235K$) below which short-range ferromagnetic cluster formation take place and this downward deviation below $T_G$ is a typical characteristic of Griffiths phase. Normally Griffiths singularity is unambiguously characterized by the magnetic susceptibility exponent ($\lambda$) obtained from the power law $\chi^{-1} \propto (T - T_{CR})^{1-\lambda}$, where $T_{CR}$ is the critical temperature of the random FM clusters where susceptibility tends to diverge and $0 < \lambda < 1$. In order to determine $\lambda$, $\chi^{-1}(T)$ versus reduced temperature $t_m = (T - T_{CR})/T_{CR}$ has been plotted on $log_{10} - log_{10}$ scale (inset of Fig. 5.11 (b)) and slope of the fitted straight lines with power law in the Griffiths and paramagnetic regions gives the corresponding $\lambda_{GP}$ and $\lambda_{PM}$ respectively. Here it is to be noted that an incorrect value of $T_{CR}$ will give rise to an unphysical fitting which leads to an inaccurate determination of $\lambda$. To estimate $T_{CR}$ accurately, the method followed by Jiang et al [211]. has been used. The obtained value of $\lambda_{PM} = 0.008$ in the paramagnetic region which is closed to the ideal value of '0' and in Griffiths region $\lambda_{GP} = 0.977$ which is good agreement with the expected range $0 < \lambda < 1$ and comparable with other manganites [222–224]. Moreover large value of $\lambda_{GP}$ indicates that, Griffiths phase is strong in the 'Nano1' sample. Thus upon particle size reduction, non-Griffiths phase, possibly arising from antiferromagnetic correlations above Curie temperature, convert to Griffiths phase because of the suppression of AFM interactions. This scenario is also correlated with the reduction of orthorhombic distortions in 'Nano1' compared with 'Bulk', as reduction of distortions enhance the ferromagnetic interactions.

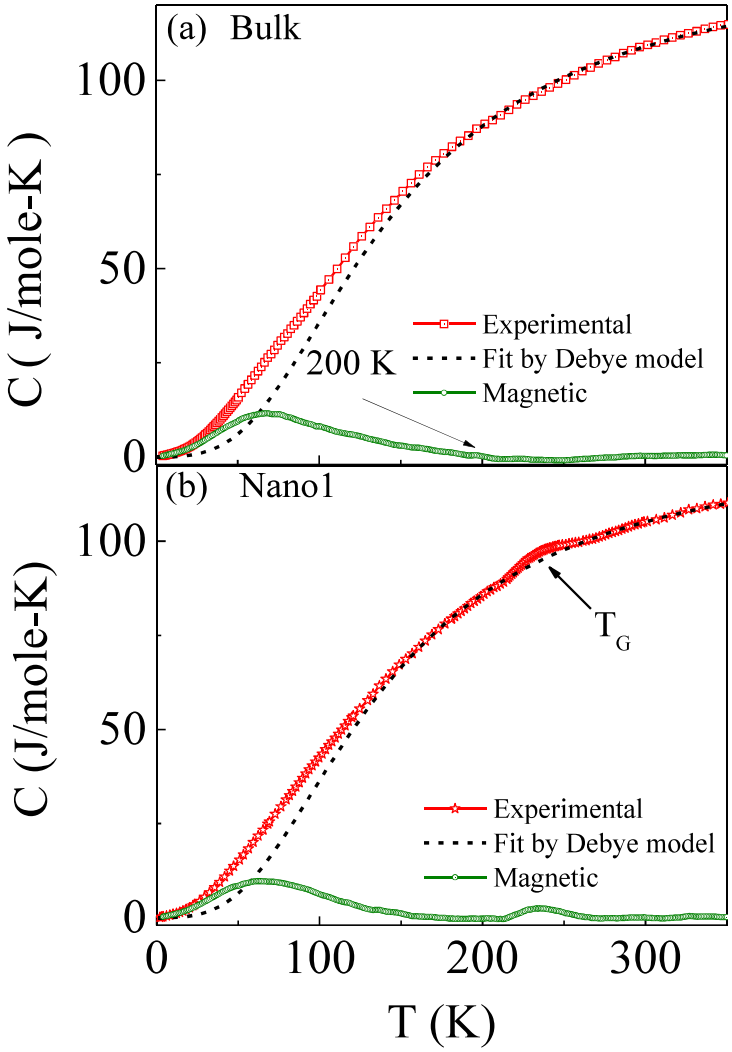


**Figure 5.12:** Plot of C vs T for (a) 'Bulk' and (b) 'Nano1' samples in zero field. Black dotted lines are the fitted data by using debye model and magnetic contribution is obtained by subtracting fitted data from experimental data.

### 5.3.4 Heat Capacity study

To have a clear vision of this conversion from non-Griffiths phase for 'Bulk' to Griffiths phase in 'Nano1' sample, zero field heat capacity as a function of temperature ($3K < T < 350K$) has been performed for both 'Bulk' (Fig. 5.12(A)) and 'Nano1' (Fig. 5.12(B)). High-temperature heat capacity data ($T > 250K$) for both samples have been fitted with Debye model of heat capacity by considering only lattice contributions. According to Debye model, heat capacity is expressed as

$C = 9nR(\frac{T}{\theta_D})^3 \int_0^{\frac{\theta_D}{T}} \frac{x^4 e^x}{(e^x-1)^2} dx$, where R is gas constant, n is the number of atoms per molecule and $\theta_D$ is the Debye temperature. The magnetic contributions have been obtained by subtracting the lattice part from the obtained experimental data. The observed peak of the magnetic contributions comes around the same temperature as obtained from MT measurements. The most distinct feature observed here is that in 'Nano1' sample around 235 K there is a kink and around the same temperature development of Griffiths phase has been observed from $\chi^{-1}$ versus temperature data. Thus the heat capacity data conclusively support the Griffiths singularity in 'Nano1' sample [160, 225]. Although in 'Bulk' sample no kink has been observed which together with previous discussions support the absence of Griffiths phase in it.

### 5.3.5 Low temperature ground state

The dc magnetization and transport data show the presence of magnetic disorder in all the samples at low temperature ($T < 50K$). Although in 'Nano1' the reduction of this disorder is observed compared to both 'Bulk' and 'Nano2' sample. To find out the origin of this magnetic disorder, low-temperature Heat capacity study, magnetic memory effect, relaxation study as well as ac susceptibility measurement has been performed.

#### 5.3.5.1 Low temperature Heat Capacity study

To enlighten the low-temperature magnetic phase, zero field as well as in field (H = 70 kOe) heat capacity has been measured for 'Bulk' and 'Nano1' samples. Fig. 5.13 shows the plot of $C/T$ vs $T^2$ of the investigated samples in the temperature range 2-14 K. With initial reduction of particle size i.e. in 'Nano1' sample, reduction of heat capacity is observed. However, field-induced suppression of heat capacity

has been observed in each of the samples. In order to elucidate these results and to estimate the different contributions to the specific heat, low-temperature data of each sample has been fitted with the following expression of specific heat [226, 227]:

$$C(T) = \gamma T + \beta T^3 + \delta T exp(-\Delta/T) \tag{5.5}$$

Here the linear coefficient $\gamma$ usually represents the free charge carriers density and is directly proportional to the density of states at the fermi level. The lattice contributions is represented by $\beta T^3$ and the higher order lattice term ($\propto T^5$) has been neglected as $T < 15K$. The last term $\delta T exp(-\Delta/T)$ is a phenomenological expression to account for the downward curvature and has been used previously by Martin et al. to justify the downturn and attributes it to the presence of spin glass contribution. It is worth mentioning here, that an attempt to fit the low-temperature specific heat data by including the ferromagnetic term ($\propto T^{3/2}$) with other contributions gives no proper fitting (specially below 5 K) and for this reason the term ($\propto T^{3/2}$) has not been taken into account to fit these data.

**Table 5.1:** Summary of the fitting parameters obtained by using Eq. 5.5 and the units of the different fitting parameters are $\gamma(mJmole^{-1}K^{-2})$, $\beta(mJmole^{-1}K^{-4})$, $\delta(10^{-2}Jmole^{-1}K^{-2})$ and $\Delta(K)$.

| Sample | H (kOe) | $\gamma$ | $\beta$ | $\delta$ | $\Delta$ |
|---|---|---|---|---|---|
| Bulk | 0 | 39.3 | 0.169 | 9.9 | 4.3 |
| Bulk | 70 | 6.5 | 0.159 | 12.1 | 2.9 |
| Nano1 | 0 | 18.2 | 0.103 | 8.1 | 2.0 |
| Nano1 | 70 | 3.7 | 0.011 | 10.1 | 2.4 |

The best fitting parameters obtained from fitting the specific heat data with the Eq. 5.5 are presented in Table. 5.1. The most striking feature here is that the appearance of the unexpectedly large linear term in all the sample in zero field, though they are the insulator as observed from transport properties. In ferromagnetic metallic systems $\gamma$ comes in the range 5-7mJ/mole$K^2$ which is associated with conduction electrons [229]. Another aspect here is that with applying magnetic field the value

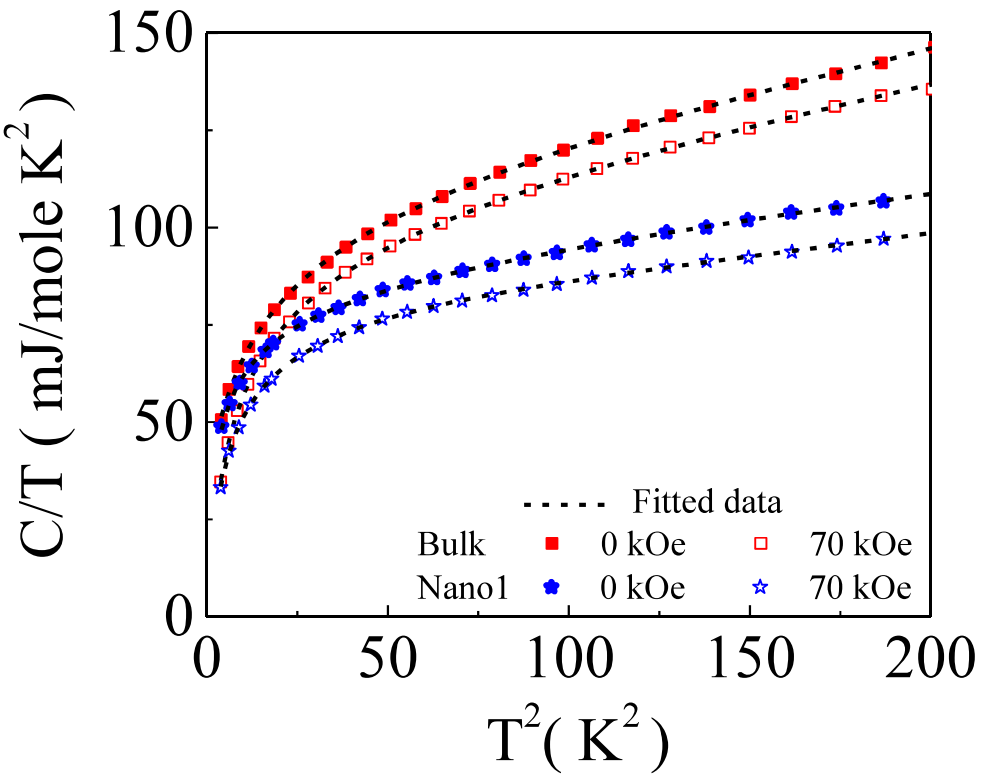


**Figure 5.13:** Variation of C/T versus $T^2$ for 'Bulk' and 'Nano1' samples in zero field and 70 kOe applied magnetic field. The corresponding black dotted lines represents the fitted data using Eq. 5.5.

of $\gamma$ decreases in all the samples. Thus the large linear coefficient $\gamma$ is not related to conduction electrons but with the magnetic disorder which is also suggested in previously reported literatures [226–228]. Therefore, reduction of $\gamma$ in 'Nano1' compared with 'Bulk' implies the presence of minimum magnetic disorder in it. The non-appearance of ferromagnetic spin wave contributions ($\propto T^{3/2}$) can be regarded as the consequence of this magnetic disorder [229, 230]. The decrease in $\beta$ with particle size reduction as well as on the application of external magnetic field is likely due to the decrease in unit cell volume which reduces the lattice contributions ($\beta T^3$) [231]. The decrease in unit cell volume in 'Nano1' has already been observed in structural section. Another point needs to be mentioned here is that without considering the phenomenological term ($\delta T exp(-\Delta/T)$) the qualitative descriptions inferred from the fitting parameters (not shown here) remains unaltered.

#### 5.3.5.2 Magnetic memory effect

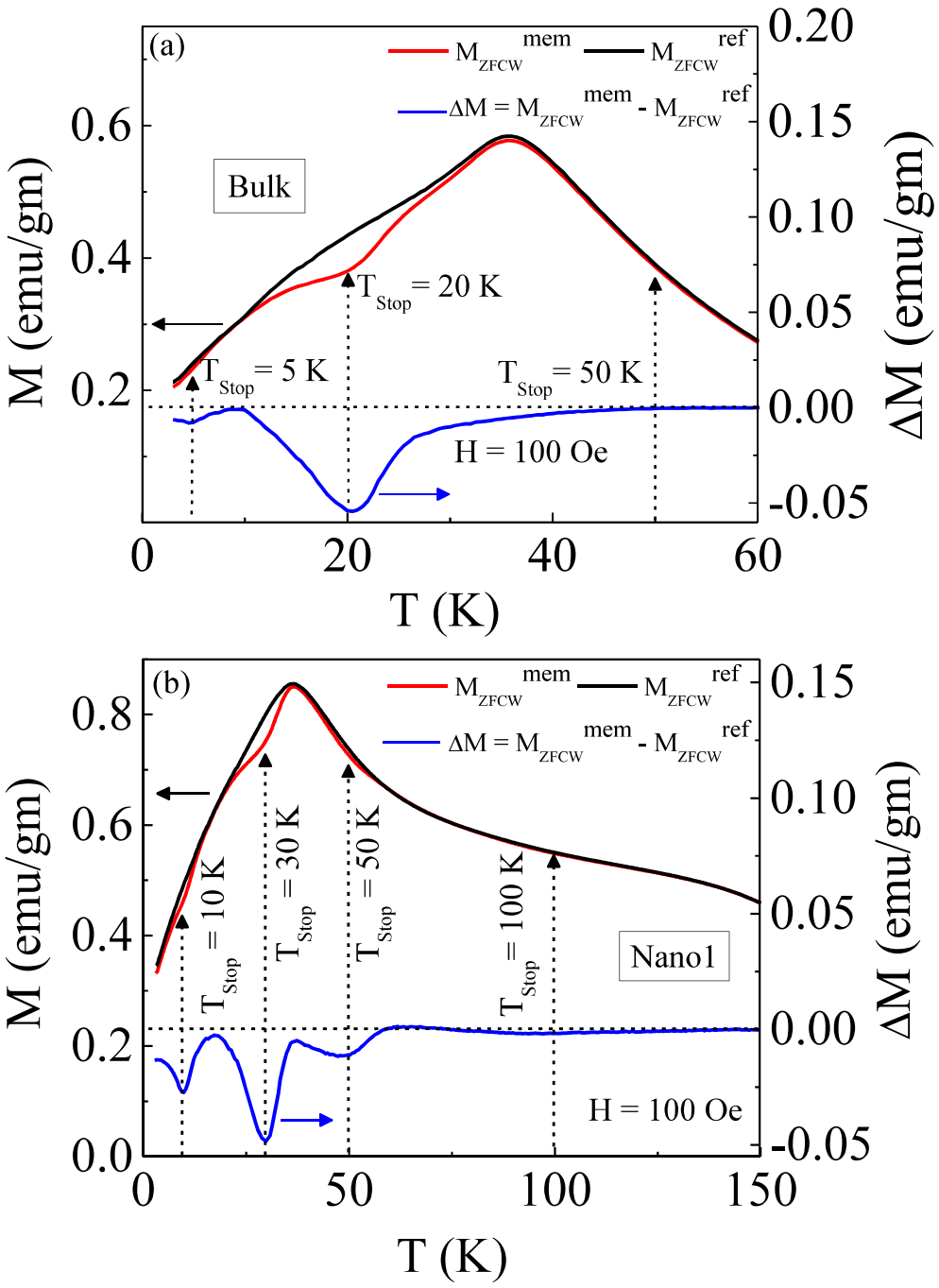


**Figure 5.14:** Memory effect measured in ZFC protocol for (a) Bulk and (b) Nano1 samples.

The previous discussions, like, overlapping of $T_f$ and $T_{irr}$ in ZFCW magnetization data for 'Bulk' and downturn at low temperature in C/T vs $T^2$ data for the samples suggests the possible existence of low-temperature spin glass phase. Usually, the

memory effect can be seen for superparamagnetic and phase separated systems in field cooled (FC) protocol but not in zero field cooled (ZFC) protocol [232]. Only spin glass systems show the memory effect in ZFC protocol. To confirm the possible spin glass phase, memory effect has been performed for 'Bulk' and 'Nano1' samples in the ZFC protocol followed by sun et al [233]. To measure the ZFC memory effect, samples has been cooled from the high temperature paramagnetic region ($T \geq 250K$) to the lowest temperature (2 K) with some intermediate stops at $T_{Stop}$ =50K, 20 K and 5 K for 'Bulk' (Fig. 5.14(a)) and 100 K, 50 K, 30 K and 10 K for 'Nano1' (Fig. 5.14(b)) and there the temperature has been maintained for $t_w = 1$ hour. Once the systems reache at 2 K, samples have been heated back to the paramagnetic region by applying a magnetic field (100 Oe) and magnetization has been recorded which is designed as $M^{mem}_{ZFCW}$. The normal ZFCW magnetization for the same magnetic field (100 Oe) has also been recorded which is depicted as $M^{ref}_{ZFCW}$ and is shown in Fig. 5.14(a) and Fig. 5.14(b) for 'Bulk' and 'Nano1' respectively. And the difference $\Delta M = M^{mem}_{ZFCW} - M^{ref}_{ZFCW}$ for both sample shows the dip at the corresponding stopping temperatures for $T < T_f$. Whereas for $T > T_f$, though no memory dip is observed for the 'Bulk' sample but for 'Nano1' sample memory dip is observed at the higher temperature. The existence of these memory dips confirms the presence of spin glass phase at the low temperature in the samples [232]. The presence of the dip in 'Nano1' at the higher temperature (100 K) is arising due to the surface spin glass behavior of the nanoparticle although its strength is very small as observed from the dip.

#### 5.3.5.3 Relaxation study

The presence of spin glass phase in the samples does not give any information about the individual entities between which cooperative interactions makes the systems glassy. To have a qualitative idea about these systems the time evolution of magne-

tization M(t) has been investigated in 'Bulk' and 'Nano1' samples at low temperatures ($T < T_f$). The measurements have been performed in the ZFC protocol. In the ZFC protocol, samples have been cooled from paramagnetic region ($T > 250K$) to the desired temperature (20 K for both 'Bulk' and 'Nano1') and after that applying a small measuring magnetic field (here 50 Oe) the time evolution of magnetization M(t) has been recorded (Fig. 5.15).

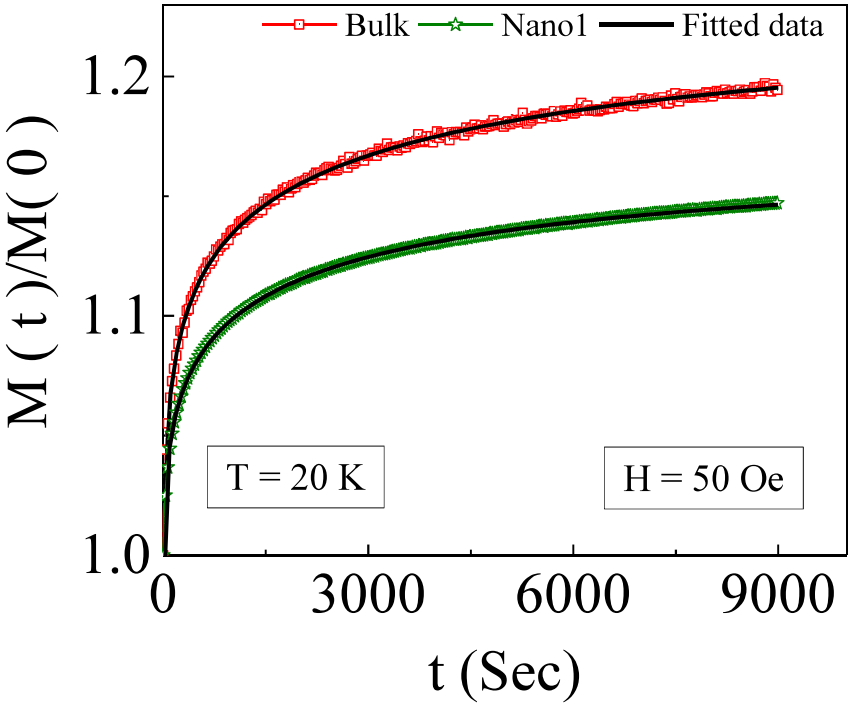


**Figure 5.15:** Relaxation of magnetization measured in zero field cooled (ZFC) protocol at 20 K temperatures for Bulk and Nano1 samples. Here solid line represents the fit to Eq. 5.6.

The time dependence of magnetization M(t) has been analyzed on the basis of standard stretched exponential of the form [234, 235]

$$M(t) = M_0 - M_r exp[-(\frac{t}{\tau_r})^{\beta}] \tag{5.6}$$

where $M_0$ relates to the intrinsic ferromagnetic component, $M_r$ to the glassy component of magnetization, $\tau_r$ is the characteristic relaxation time and $\beta$ is the stretching exponent. The exponent $\beta$ implies the number of states through which system

evolves and its values lies between 0 and 1 and it approaches to 1 as intermediate state diminishes [236, 237]. The best fitting parameters have been presented in Table. 5.2.

**Table 5.2:** Fitting parameters obtained by using Eq. 5.6 and the units of the different fitting parameters are $M_0$(emu/gm), $M_r$ (emu/gm), $\tau_r$ (Sec) and $\beta$ is dimensionless.

| Sample | T(K) | $M_0$ | $M_r$ | $\tau_r$ | $\beta$ |
|---|---|---|---|---|---|
| Bulk | 20 | 0.23 | 0.055 | 790 | 0.29 |
| Nano1 | 20 | 0.43 | 0.070 | 1015 | 0.35 |

The observed enhanced intrinsic ferromagnetic component $M_0$ in 'Nano1' compared with 'Bulk' is in agreement with the strong FM behavior. Again, the increase of $M_r$ in 'Nano1' than 'Bulk' is either due to the increase of cluster number or the cluster sizes which can also be the reason for the increases of $\tau_r$ with decreasing particle size because the increase of $\tau_r$ suggest the stiffening of the spin relaxation [234]. The diminishing of intermediate states with decrease of particle size is clear from the obtained values of $\beta$ and it is also known that the number of states depends mainly on the density of clusters. Thus from these results, it can be argued that the cluster size in 'Nano1' is more than 'Bulk' and is taking the dominating role in the relaxation process.

#### 5.3.5.4 ac susceptibility study

Ac susceptibility measurements in 'Bulk' as well as in 'Nano1' samples have been performed in an excitation field of 3 Oe for different frequencies. The evolution of real part of the ac susceptibility ($\chi'$) with temperature for different frequencies (f) for both 'Bulk' and 'Nano1' samples has been shown respectively in Fig. 5.16(a) and Fig. 5.16(b). Here another point needs to mention that, for 'Nano1' sample frequencies higher than 13.3 Hz gives too much scattered data, so they have not been presented here, although data corresponding to the 1 Hz and 13.3 Hz frequencies gives a qualitative idea about the system. The shifting of characteristic temperature

($T_f$) has been observed (inset I of Fig. 5.16(a) and (b)) with increasing frequencies (37.9 K for 1 Hz to 38.2 K for 997.3 Hz in Bulk sample and 37.1 K for 1 Hz to 37.7 K for 13.3 Hz in Nano1 sample), which again confirms the spin glass behavior of the systems. Usually, the relative shift in $T_f$ per decade of frequency for glassy system is given by [238]

$$\phi = \frac{\Delta T_f}{T_f \Delta log_{10}(f)}. \tag{5.7}$$

Here, $T_f$ is the mean value of the freezing temperatures associated with the measuring frequencies and $\Delta T_f$ is the difference between $T_f$ corresponding at frequencies separated by $\Delta log_{10}(f)$. For 'Bulk' and 'Nano1' samples the obtained values of $\phi$ are 0.003 and 0.014 respectively which falls within the range reported for canonical and classical spin glass systems [238].

For spin glass system near the freezing temperature ($T_f$), the correlation time $\tau$ diverges as $\tau \propto \xi^z$, where $z$ and $\xi$ are the dynamic scaling exponent and correlation length respectively. For continuous phase transition near $T_f$, there is a divergence of $\xi$ with temperature as $\xi = t^{-\nu'}$ where $\nu'$ is static critical exponent and $t = (T_f - T_{SG})/T_{T_{SG}}$ and $T_{SG}$ is the spin glass transition temperature for $f = 0$. Thus the evolution of correlation time with $T_f$ is given by [239]

$$\tau = \tau_0 (\frac{T_f - T_{SG}}{T_{SG}})^{-z\nu'} \tag{5.8}$$

where $\tau_0$ is the spin-flip characteristic time. The variation of reduced temperature (t) with the correlation time ($\tau$) in a log-log plot (with $T_{SG} = 37.8K$) has been shown in the inset (IV) of Fig. 5.16(a). The linear fit of this data with Eq. 5.8 yields $z\nu' = 5.6$ and $\tau_0 = 10^{-13}$ which lies within the range reported for established canonical spin glass systems [240]. The dynamics of spin glass freezing has also been analyzed using empirical Vogel-Fulcher law [241], where the dependence of freezing

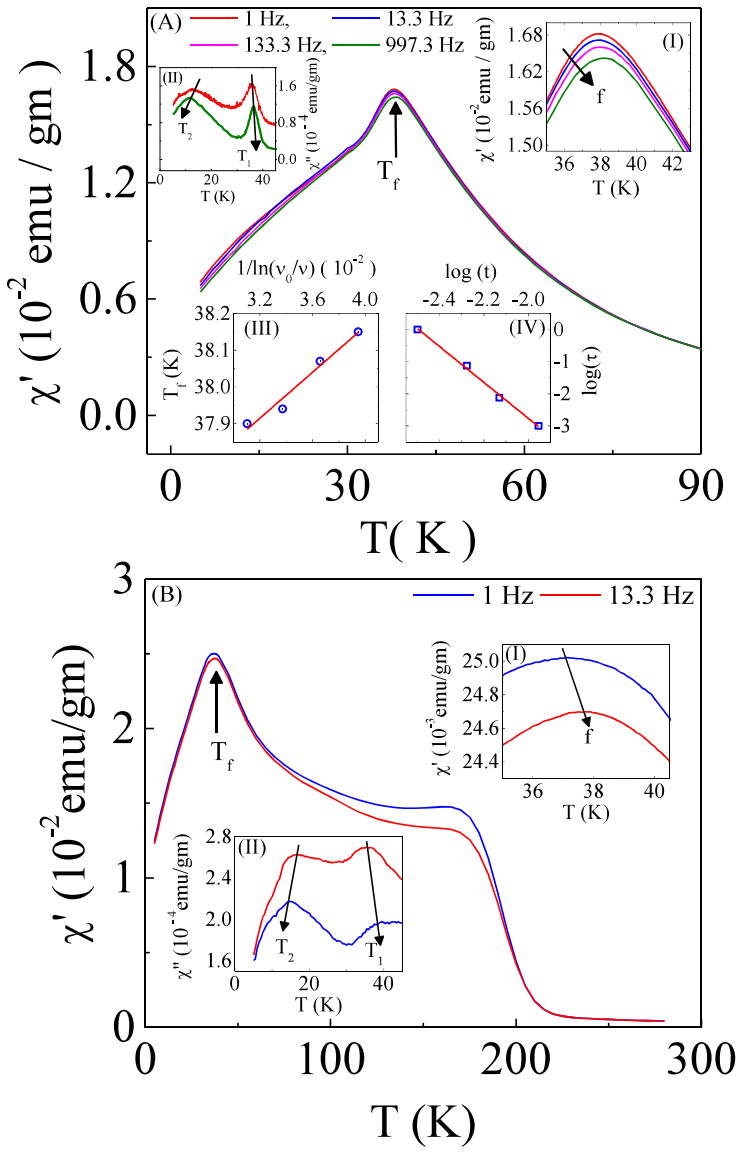


**Figure 5.16:** (A) The variation of real part of ac susceptibility ($\chi'$) with temperature of 'Bulk' sample for 1 Hz, 13.3 Hz, 133.3 Hz and 997.3 Hz frequencies with driving ac field $H_{ac} = 3Oe$ where $H_{dc} = 0Oe$. In the inset (I) an enlarged region near $T_f$ is shown. Inset (II) represents the variation of imaginary part of ac susceptibility ($\chi''$) with temperature. Inset (III) shows the plot of $T_f$ vs $1/ln(\nu_0/\nu)$ and solid line is the fit to Eq. 5.10. Inset (IV) represents the $log(\tau)$ vs $log(t)$ plot and the solid line is the fit to Eq. 5.8. (B) Temperature dependence of the real part of the susceptibility ($\chi'$) of 'Nano1' sample for 1 Hz and 13.3 Hz frequencies. An enlarged view near $T_f$ is shown in the inset (I). Inset (II) shows the temperature dependence of $\chi''$.

temperature with frequencies is given by

$$\tau = \tau_0 exp(\frac{E_A}{k_B(T_f - T_0)}), \tag{5.9}$$

where $\tau_0$ is same as in Eq. 5.8 and $T_0$ is the Vogel-Fulcher temperature which often represents the strength of intercluster interaction. After rearranging Eq. 5.9, the relative variation of $T_f$ with driving frequencies is represented by

$$T_f = \frac{E_A/k_B}{ln(\nu_0/\nu)} + T_0, \tag{5.10}$$

The plot of $T_f$ with $1/ln(\nu_0/\nu)$ has been shown in the inset (III) of Fig. 5.16(A) and the linear fit to the data with Eq. 5.10 yields $E_A/k_B = 36.9$ and $T_0 = 31.9K$. Normally, the ratio between activation energy ($E_A$) and $T_0$ i.e. $E_A/k_BT_0$, which is a measure of the strength of interactions between freezing entities, generally found to be close to 1 for canonical spin glass systems and for spin cluster glass systems it is relatively larger. Thus the obtained value of $\sim 1.2$ confirms the canonical spin glass behavior of Bulk sample.

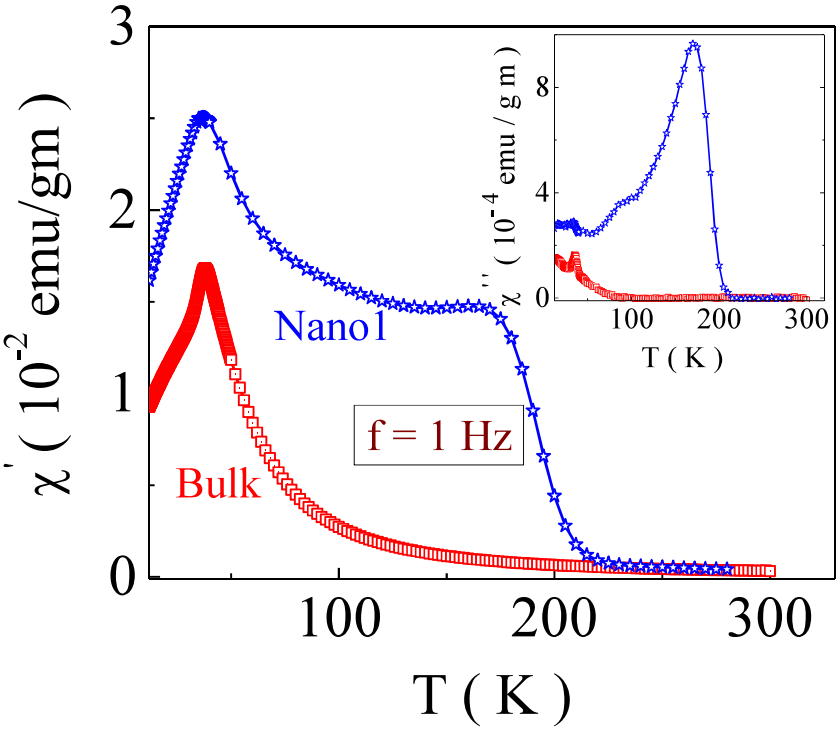


**Figure 5.17:** Variation of $\chi'$ with temperature for 'Bulk' and 'Nano1' samples in 1Hz driving frequency of amplitude $H_{ac} = 3Oe$. In the inset evolution of $\chi''(T)$ for the samples has been shown.

Here another point needs to mention that, together with the peak around $T_f$ (which

is also observed in $\chi'$ versus T data) another low-temperature peak ($T_2$) for both the samples are observed in the temperature dependence of the imaginary part ($\chi''$) of the susceptibility data which are presented in the inset of Fig. 5.16(a) and (b) respectively. Most striking feature here is the shifting of the peak (at $T_2$) towards lower temperature with increasing frequencies. This kind of reverse trend in peak shift at $T_2$ with frequencies arises may be due to the presence of slow and fast relaxing components in the freezing process. Thus the negative shifting implies the presence of ferromagnetic clusters in the samples [242–244]. Moreover, the positive shifting at $T_1$ implies the canonical and classical spin glass behavior of 'Bulk' and 'Nano1' samples.

Thus, ac data suggest the coexistence of ferromagnetic clusters and spin glass components in both 'Bulk' and 'Nano1' samples at low temperature ($T < T_f$). It is also needed to enlighten the high temperature magnetic phase of the samples. In this regard, ac susceptibility of both 'Bulk' and 'Nano1' has been measured in the temperature range 5 K to the paramagnetic region (280 K). The evolution of real part of ac susceptibility ($\chi'$) and out of phase of susceptibility ($\chi''$) for 'Bulk' and 'Nano1' has been shown in Fig. 5.17 and in its inset where 3 Oe excitation ac field with 1 Hz driving frequency has been used. Astonishingly, around 200 K in 'Nano1' sample a kink appears, although in 'Bulk' no signature of this kink is observed from $\chi'(T)$. Generally, the $\chi''(T)$ denotes the energy dissipation in the sample which is proportional to the hysteresis loop area at an equilibrium temperature for a complete period of the driving ac field. Therefore, the peak in $\chi''(T)$ indicates the onset of ferromagnetism where energy dissipation is maximum and becomes zero in the paramagnetic region. Thus the peak in 'Nano1' at 200 K is because of growth of ferromagnetic clusters and surprisingly this temperature corresponds to $T^*$ where $1/\chi(T)$ of 'Bulk' shows upturn from CW line. Therefore, it can be argued that the reason which was behind the CW upturn in 'Bulk', possibly antiferromagnetic correlation between tiny clusters, is suppressed in nanoparticle because of reductions

of distortion and forms small ferromagnetic clusters.

### 5.3.6 Phenomenological picture

Based on the above results a phenomenological picture can be proposed. According to this picture, all the samples consists of ferromagnetic clusters and growth of the clusters take place on particle size reduction which also brings with it surface disorder. The nanoparticles are of core-shell type, where in the core there is appearance of ferromagnetic clusters and shell is carrying surface disorder because of uncompensated spins and different defect. Competition between this two counteracting phenomenon determines the magnetization, transport and magnetotransport properties of nanoparticles. In the temperature range $T_{SG} < T < T^*$, the ferromagnetic clusters are in the host paramagnetic background which converts to the spin glass state as temperature goes below the freezing temperature ($T_{SG}$)(the spin glass nature of the system has been discussed in supplementary section). Again, the enhancement of magnetization and reduction of coercive field in 'Nano1' compared with bulk and other reduced size nanoparticles is observed. Another point here needs to mention that within the temperature span $T_{SG} < T < T^*$, in the 'Bulk' sample there is the presence of antiferromagnetic correlation between the ferromagnetic clusters. This antiferromagnetic correlation subsequently vanishes in the nanoparticles due to the reduced lattice distortions. Among the nanoparticles in 'Nano1', surface disorder is minimum and cluster density is maximum which combined with magnetic field helps to polarize the cluster moment and creates easier path for electronic transport and results in large MR. On the other hand, in 'Nano3' particle cluster density decreases and surface disorder increases which leads to suppression of MR.

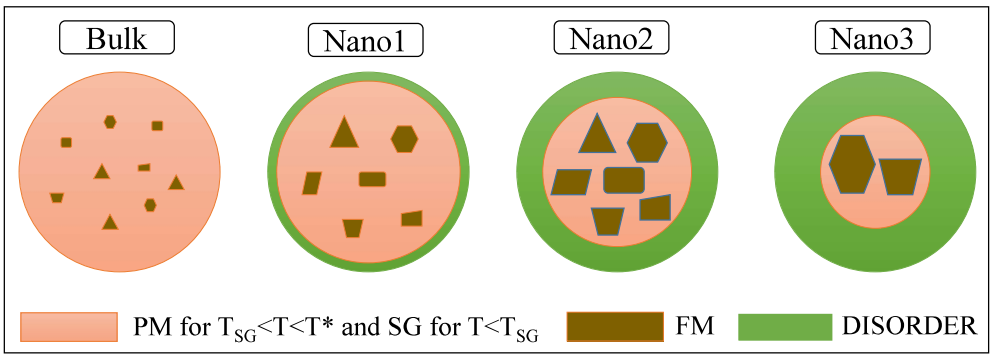


**Figure 5.18:** A schematic representation of the samples to explain the physical properties exhibited by them.

## 5.4 Summary

In summary, here we have investigated the possible connection between the presence of Griffiths phase and colossal magnetoresistance in hole doped LYCMO manganites using temperature dependent XRD, magnetization, heat capacity, ac susceptibility and magnetotransport studies. The progressive reduction of orthorhombic distortion with lowering the crystallite size has been observed, though there is no change in space group symmetry from 'Pnma'. Thus, the analysis of the heat capacity, dc magnetization, magnetotransport and ac susceptibility data confirms the existence of Griffiths phase in nano LYCMO sample. While on the contrary, dc susceptibility of bulk LYCMO indicates the absence of GP or presence of non-Griffiths phase in it. An enhancement of CMR in Nano1 compared with bulk has been observed over a wide temperature range due to the reduced lattice distortion which favors the formation of ferromagnetic clusters responsible for the development of GP. The observed phenomenon of enhancement of MR due to the conversion of non-GP to GP is in the rare category and is important for the developing further CMR materials with enhanced magnetoresistive property.

# CHAPTER 6

# Magnetocaloric properties of some selected compounds

## 6.1 Introduction

The magnetocaloric effect (MCE) has recently drawn several attentions due to the possible application in magnetic refrigeration technique which is energy efficient as well as environment-friendly and can be the alternative of the conventional gas-compressor based refrigeration [21, 22, 60–64]. The MCE is defined as the isothermal entropy change due to the application of external magnetic field i.e. $\Delta S_M (= S_M(T,H) - S_M(T,0))$ under adiabatic condition. Generally, MCE is obtained in the proximity of a magnetic phase transitions [245–248]. Together with the isothermal magnetic entropy change ($\Delta S_M$), another important parameter for magnetic refrigerants is the relative cooling power (RCP). In an ideal refrigeration cycle, the amount of heat transfer between hot and cold end is determined by RCP and it is defined as the twice the area under the $\Delta S_M$ versus T curve. The strategy to enhance the RCP is either by getting large $\Delta S_M$ or by enhancing the span of $\Delta S_M$ over a wide temperature range. Recently, an increasing attention has been

paid to look for magnetic refrigerants with large RCP [185, 249–251].

Among the different magnetic refrigerants, the doped perovskite manganites have attracted increasing attentions because of several advantages such as relatively large magnetic entropy change [66,67], tunable $T_C$ [68], chemical stability, low production cost and relatively large resistivity [183] which favors the reduction of loss due to the eddy current heating [70]. The physical properties of doped perovskite manganites with the general formulae $R_{1-x}A_xMnO_3$ (R= rare earth ion, A=divalent ion) are governed by the three factors [120]: the hole doping level $x$, average A-site ionic radius $\langle r_A \rangle$ and its disorder. For manganites, electronic bandwidth is directly proportional to the A-site ionic radius $\langle r_A \rangle$ [99, 104] as with the increase of $\langle r_A \rangle$, $Mn - O - Mn$ bond angle increases which favors the electronic conduction. On the other hand, A-site disorder is quantified by the variance of the A-site ionic distribution [252] $\sigma^2 = \sum y_i r_i^2 - \langle r_i \rangle^2$, where $\langle r_i \rangle$ is the average A-site ionic radius, $y_i$ is the fractional occupancies of the $i^th$ ion in A-site. The materials with higher electronic bandwidth usually show higher curie temperature [19, 231]. Hwang et al [19]. has described that at 30% hole doping, with decreasing $\langle r_A \rangle$ from 1.24$\mathring{A}$ to 1.18$\mathring{A}$ the PM to FM transition temperature ($T_C$) decreases from 360 K to 50 K and below $\langle r_A \rangle = 1.18\mathring{A}$ system converts from ferromagnetic to spin glass state. Again, systems showing ferromagnetic transition are usually metallic. Thus, from eddy current point of view ferromagnetic system is not suitable for the refrigerant material. On the other hand, enhanced A-site disorder converts the FM metallic systems into the cluster glass state which is insulating in nature [253, 280]. Disorder also increase the distribution of the ferromagnetic double exchange interactions strength which results in the broadening in $T_C$ [253]. Therefore, to have a refrigerant near room temperature with reduced eddy current loss and large RCP, one needs a system with large electronic bandwidth (near 1.24$\mathring{A}$) together with the quenched disorder to make the system insulating. Though the study on MCE in manganites have been reported earlier [21, 22, 60–64] but to the best of our knowledge, the effect of $\sigma^2$ on

large bandwidth manganites system has been rarely addressed.

Among the different magnetic materials, one of the most well-known manganites with relatively large electronic bandwidth is $La_{0.7}Sr_{0.3}MnO_3$ [255, 256] with PM to FM ordering temperature at 360 K. To study the effect of A-site disorder on MCE for large bandwidth manganite system, we have chosen $\langle r_A \rangle = 1.24\mathring{A}$ of $La_{0.7}Sr_{0.3}MnO_3$ to be fixed and prepared other samples with the same $\langle r_A \rangle$ but with different $\sigma^2$. In this regard, we have prepared $Pr_{0.7}Sr_{0.14}Ba_{0.16}MnO_3$ and $Nd_{0.7}Sr_{0.07}Ba_{0.23}MnO_3$ compounds with $\sigma^2 = 1.85 \times 10^{-3}$ and $1.17 \times 10^{-2}$ respectively. The detailed MCE study of the compounds has been addressed here. The study shows the enhancement of RCP with increasing $\sigma^2$. The origin of this enhancement has been explained from critical analysis of the compounds.

Generally, large magnetocaloric effect and large magnetoresistance is observed at the proximity of the magnetic phase transitions [257–261]. Previously, observation of CMR and MCE near the paramagnetic to ferromagnetic phase transition has been described in literature [72, 142, 143, 258]. Another important criterion for applicability of the MCE material is that the material must have high resistivity, so that eddy current loss minimize [70]. On the other hand, material showing PM-FM transitions is of low resistance. Therefore, to have a material for MCE application material must be insulating in nature even below magnetic phase transitions. Again, it is well known that near the magnetic phase boundary phase fluctuation dominates. suppression of this phase fluctuation on application of magnetic field gives rise to large magnetoresistance. Therefore, to serve the purpose for having both large MR and large MCE one needs a sample near the phase boundary. Moreover to have a high resistive material the sample have to be chosen near ferromagnetic insulator phase boundary.

Recently, ferromagnetic insulating material has drawn notable scientific interests because of its application in spin filter [262]. Usually FMI state is observed at the

low hole doped regime of manganites and normal double exchange (DE) phenomenon can not explain the behavior of it. A strong electron-phonon coupling is believed to play the crucial role for the formation of FMI state [263]. Kundu et al. [222, 276] has recently described that by making nanoparticles, FMI states of $Pr_{0.8}Sr_{0.2}MnO_3$ and $Nd_{0.8}Sr_{0.2}MnO_3$ can be destabilized which can give rise to the enhancement of MR. Again, the compound $Pr_{0.7}Sr_{0.3}MnO_3$ shows paramagnetic to ferromagnetic phase transition around 260 K [277]. It is also reported that the manganites with $Pr_{1-x}Sr_xMnO_3$ shows FMM-FMI transition at $x = 0.25$ [277]. Therefore, the compound $Pr_{0.775}Sr_{0.225}MnO_3$ has been chosen and studied for the magnetoresistive and magnetocaloric perspectives.

Here the study shows that the enhancement of MR occurs in $Pr_{0.775}Sr_{0.225}MnO_3$ compound because of enhanced phase fluctuation near the FMM-FMI phase boundary and the increase in RCP is because of the formation of short range ferromagnetic clusters above the ordering temperature ($T_C$).

## 6.2 Effect of A-site ionic disorder on magnetocaloric properties in large band width manganite systems

### 6.2.1 Sample Preparation and Characterization

The bulk polycrystalline manganites samples with compositional formulae $Ln_{0.7}D_{0.3}MnO_3$ (where Ln = La, Pr, Nd and D = Sr, Ba) has been prepared by the polymeric precursor sol gel method, also known as Pechini method. As a first step, the corresponding amounts of $La_2O_3$ (or $Pr_6O_{11}$ or $Nd_2O_3$), $MnO_2$ and $SrCO_3$ (or $BaCO_3$ or both) of purity 99.9% has been dissolved separately in nitric acid and mixed together in

citric acid to convert in citrates. The pH of the solutions has been adjusted between $6.5 - 7$. After getting a sol on slowly evaporating the citrate solution at $80 - 90^0C$, an equal amount of ethylene glycol has been added as a promoter of citrate polymerization and heated on a hot plate at $180^0C$ to form gel and subsequently has been heated at $250^0C$ until a black porous powder is formed as a complete removal of water molecules. Finally, the decomposed gels has been pelletized and sintered in air $1300^0C$ for 36 hours to make bulk samples.

### 6.2.2 Experimental Results and Discussion

The phase purity of the samples has been checked from x-ray diffraction patterns, recorded at room temperature using Rigaku-TTRAX-III with 9 kW rotating anode Cu-source of wavelength $\lambda = 1.54\mathring{A}$. The magnetic measurements has been performed over the temperature region 5-380 K at applied magnetic fields up to 70 kOe by employing VSM-SQUID (Quantum design).

The room temperature x-ray diffraction pattern of the samples has been shown in Fig. 6.1. The crystal structure determination has been performed from Rietveld analysis using FULLPROF software which indicates the rhombohedral structure of the $La_{0.7}Sr_{0.3}MnO_3$ sample with $R\overline{3}C$ space group symmetry whereas $Pr_{0.7}Sr_{0.14}Ba_{0.16}MnO_3$ and $Nd_{0.7}Sr_{0.07}Ba_{0.23}MnO_3$ possesses orthorhombic ($Pbnm$) structure. The relatively larger intensity peaks has also been indexed with the corresponding lattice planes in the figures. The extracted lattice parameters with calculated average A-site ionic radius $\langle r_A \rangle$ and A-site ionic distribution ($\sigma^2$) has been presented in Table. 6.1.

With increasing $\sigma^2$ for a fixed ionic radii (1.244 $\mathring{A}$), the crystal structure evolves from $R\overline{3}C$ to $Pbnm$. Although, the same structural evolution has also been observed on reduction of ionic radii from 1.244 $\mathring{A}$ for $La_{0.7}Sr_{0.3}MnO_3$ to 1.218 $\mathring{A}$ in

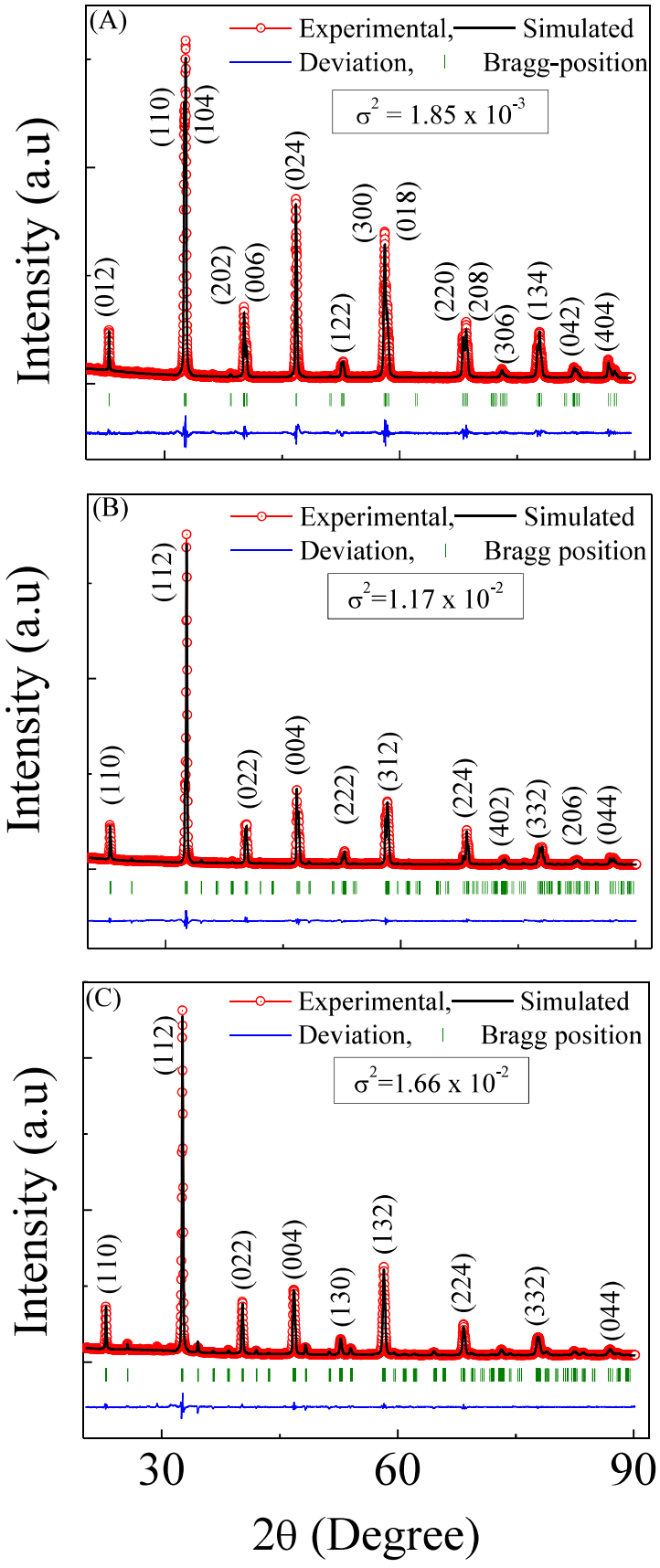


**Figure 6.1:** Room temperature XRD data with its profile fitted data for the samples with A-site ionic disorder (A) $1.85 \times 10^{-3}$ for $La_{0.7}Sr_{0.3}MnO_3$ (B) $1.17 \times 10^{-2}$ for $Pr_{0.7}Sr_{0.14}Ba_{0.16}MnO_3$ and (C) $1.66 \times 10^{-2}$ for $Nd_{0.7}Sr_{0.07}Ba_{0.23}MnO_3$ respectively.

**Table 6.1:** The lattice parameters in $\mathring{A}$, A-site ionic distribution ($\sigma^2$), unit cell volumes V ($\mathring{A}^3$) of the samples and goodness of fit ($\chi^2$)

| *Sample* | $\sigma^2(10^{-2})$ | a | b | c | V | $\chi^2$ |
|---|---|---|---|---|---|---|
| $La_{0.7}Sr_{0.3}MnO_3$ | 0.185 | 5.404(1) | 5.504(0) | 13.377(3) | 351.03(1) | 1.42 |
| $Pr_{0.7}Sr_{0.14}Ba_{0.16}MnO_3$ | 1.17 | 5.474(1) | 5.510(1) | 7.732(1) | 233.29(1) | 0.75 |
| $Nd_{0.7}Sr_{0.07}Ba_{0.23}MnO_3$ | 1.66 | 5.484(2) | 5.502(2) | 7.743(2) | 233.70(1) | 0.93 |

$La_{0.7}Sr_{0.1}Ca_{0.2}MnO_3$ as reported by Phan et al [264]. Thus superstructure type depends upon both $\langle r_A \rangle$ and ($\sigma^2$) [265].

Manganites being strongly correlated in nature, the effect of this A-site variance will also be reflected in magnetic properties. To elucidate the effect of this A-site variance, magnetization measurements as a function of temperature [M(T)] in presence 100 Oe external magnetic field has been performed in all the samples in zero field cooled warming (ZFCW) and field cooled warming (FCW) protocols (Fig. 6.2). For the samples with $\sigma^2 = 1.85 \times 10^{-3}$ and $1.17 \times 10^{-2}$ there is almost negligible bifurcation between ZFCW and FCW, but for further increase in variance to $1.66 \times 10^{-2}$ this bifurcation increases relatively which implies the presence of magnetic disorder in the system. In all the samples with lowering the temperature, paramagnetic to ferromagnetic transition ($T_C$) is observed. From the temperature derivative of magnetization data the curie temperature ($T_C$) of the samples has been determined and its corresponding variations with $\sigma^2$ has been presented in the inset of Fig. 6.2. The curie temperature $T_C$ decreases from 368 K to 105 K with increase of $\sigma^2$ from $1.85 \times 10^{-3}$ to $1.66 \times 10^{-2}$. Thus DE ferromagnetic interaction strength decreases with increase of $\sigma^2$. Previously, Dong et al [280]. has showed that upon increasing the variance from 0.0003 to 0.015 for a fixed A-site ionic radius $\langle r_A \rangle = 1.20\mathring{A}$, the curie temperature decreases from 228.7 K to 105.7 K and on further increase in variance the ground state transforms from ferromagnetic metal to cluster glass insulator. Attfield et al [265]. has also shown the effect of $\sigma^2$ on the curie temperature.

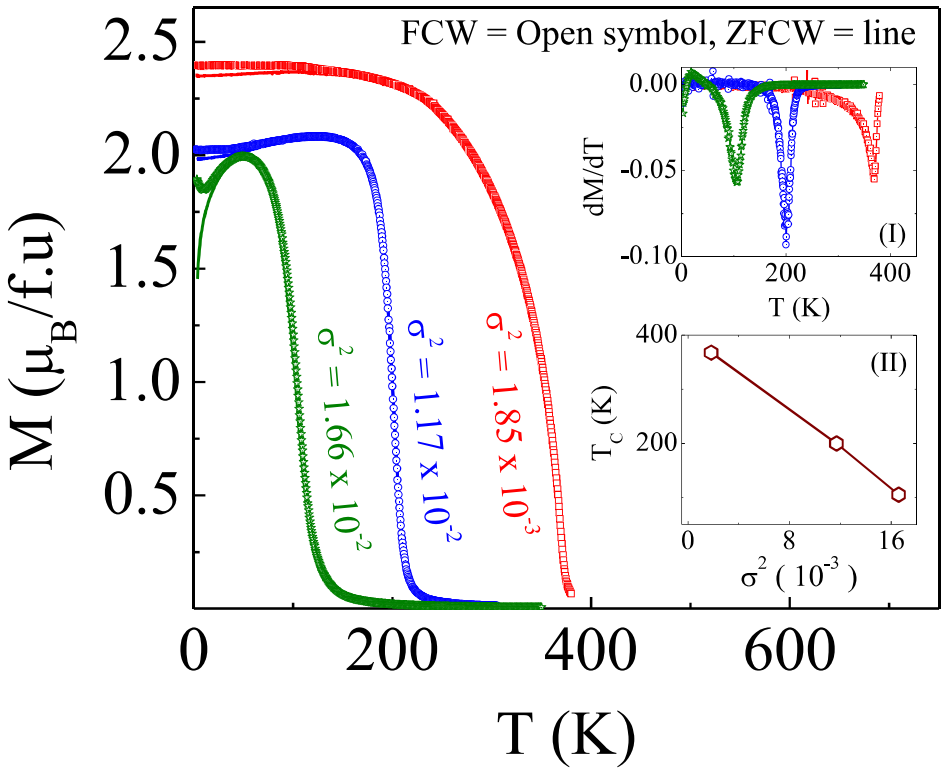


**Figure 6.2:** Variation of magnetization with temperature for different A-site disordered samples ($\sigma^2 = 1.85 \times 10^{-3}, 1.17 \times 10^{-2}$ and $1.66 \times 10^{-2}$) . Inset (I) represents dM/DT Versus T of the FCW magnetization data and (II) shows the evolution of curie temperature of the samples with ($\sigma^2$).

For further investigating the effect of the variance, the high temperature (paramagnetic region) inverse dc susceptibility (H/M) versus temperature data measured in presence of 100 Oe external magnetic field has been analyzed with the Curie-Weiss law $\chi = C/(T - \theta_{CW})$ where $C = \mu_{eff}^2/3k_B$ and $\mu_{eff}$ & $\theta_{CW}$ are the effective paramagnetic moment and paramagnetic curie temperature respectively. The temperature dependence of H/M data and its corresponding Curie-Weiss fitted curves has been presented in Fig. 6.3 which shows that with increasing $\sigma^2$ the paramagnetic curie temperature ($\theta_{CW}$) decreases and its values are 369 K, 209 K and 159 K for variance $1.85 \times 10^{-3}$, $1.17 \times 10^{-2}$ and $1.66 \times 10^{-2}$ respectively. Usually in a system having long range ferromagnetic order the curie temperature ($T_C$) and paramagnetic curie temperature ($\theta_{CW}$) values remains almost same. However, here the occurrence of deviation of $\theta_{CW}$ from $T_C$ comes with increase of A-site ionic distribution ($\sigma^2$) and deviates around 54 K in the sample of $\sigma^2 = 1.66 \times 10^{-2}$ and it can also be seen

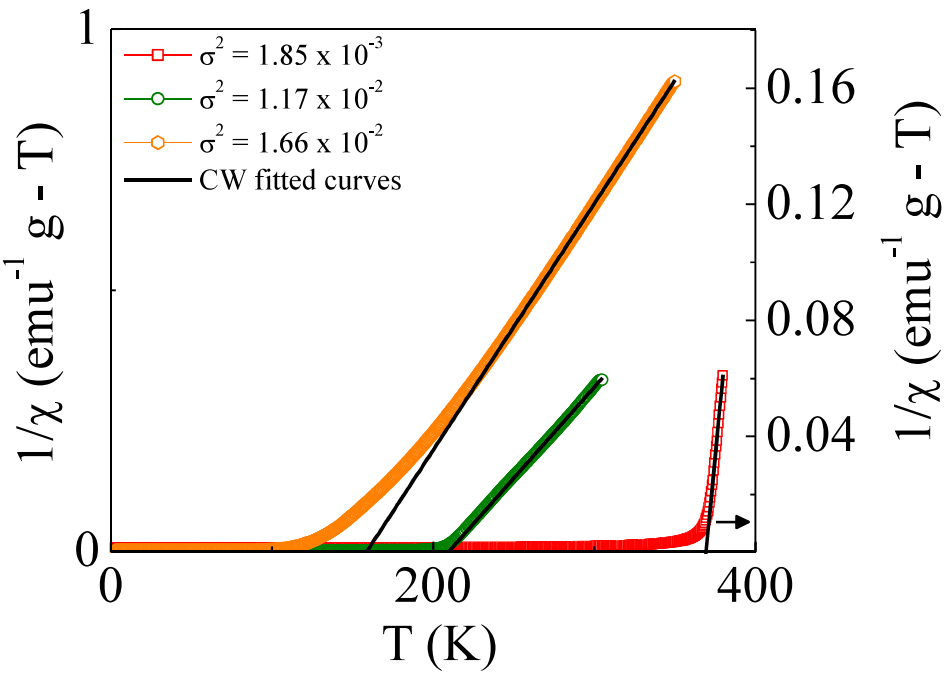


**Figure 6.3:** Variation of inverse dc susceptibility ($\chi^{-1}$) with temperature in presence of 100 Oe external magnetic field for the samples with ($\sigma^2 = 1.85 \times 10^{-3}, 1.17 \times 10^{-2}$ and $1.66 \times 10^{-2}$) respectively. The Curie-Weiss fitted line in the high temperature paramagnetic region of all the samples ($T > 200K$) has been presented by the black solid line in the corresponding figures.

from the upward deviation of the susceptibility data from the Curie-Weiss behavior. Again, the experimental value of the $\mu_{eff}$ of the samples are $5.59\mu_B$, $7.4\mu_B$ and $6.4\mu_B$ respectively, which are larger than the theoretically calculated effective magnetic moment of $4.62\mu_B$ for an effective Mn ion. This upward deviation, larger value of effective magnetic moment than the theoretical value and different value of $\theta_{CW}$ and $T_C$ is a signature of formation of ferromagnetic clusters [183]. Thus increasing A-site ionic distribution is basically breaking the long range ferromagnetic DE interaction which results in the formation of ferromagnetic clusters.

The effect of this A-site cationic distribution should also be reflected in magnetocaloric response. In this regard, magnetocaloric study of all the samples has been performed. Normally, magnetic entropy change ($\Delta S_M$) is determined from Maxwell thermodynamic relation $\Delta S_M(H,T) = \int_0^H (\frac{\partial M}{\partial T}) dH$. To calculate $\Delta S_M$ isothermal

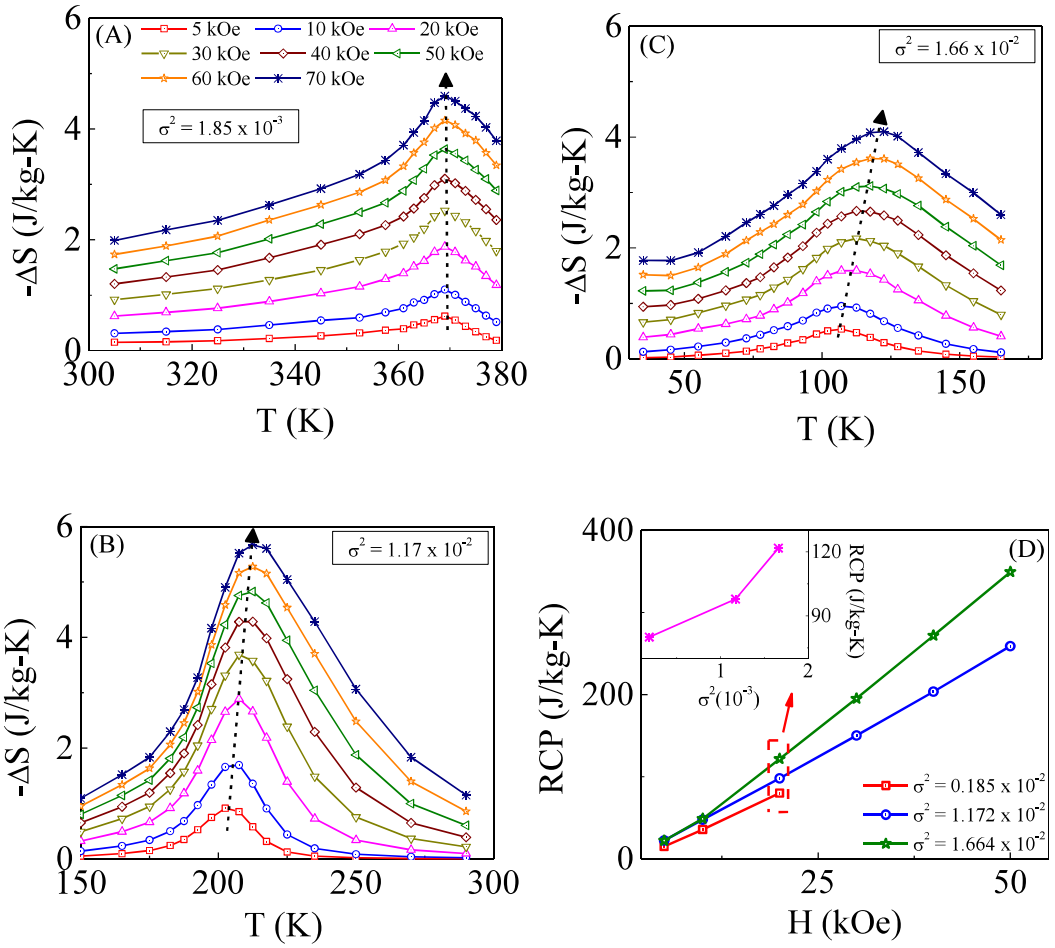


**Figure 6.4:** Temperature dependence of isothermal magnetic entropy change of the samples with A-site disorder (A) $1.85 \times 10^{-3}$ (B) $1.17 \times 10^{-2}$ and (C) $1.66 \times 10^{-2}$ for different applied magnetic field. (D) RCP versus H of the samples. Inset shows the RCP of the samples for H = 20 kOe field.

magnetization measurements [M(H)] has been performed for all the samples. All the M(H) data has been taken in zero field cooled (ZFC) protocol and before each successive isothermal M(H) measurements system has been taken to paramagnetic region to destroy the magnetic history. The plot of the temperature dependence of $-\Delta S_M$ of all the samples is shown in Fig. 6.4. Expectedly, the negative magnetic entropy change ($-\Delta S_M$) increases with lowering temperature in the paramagnetic region and shows a maximum value around their corresponding $T_C$. The maximum values of $-\Delta S_M$ are 4.6 J/kg-K, 5.7 J/kg-K and 4.1 J/kg-K in effect of 70 kOe applied magnetic field value for the samples with $\sigma^2 = 1.85 \times 10^{-3}$, $1.17 \times 10^{-2}$ and $1.66 \times 10^{-2}$ respectively. Usually with increasing $\sigma^2$ the maximum of $|\Delta S_M|$ gets

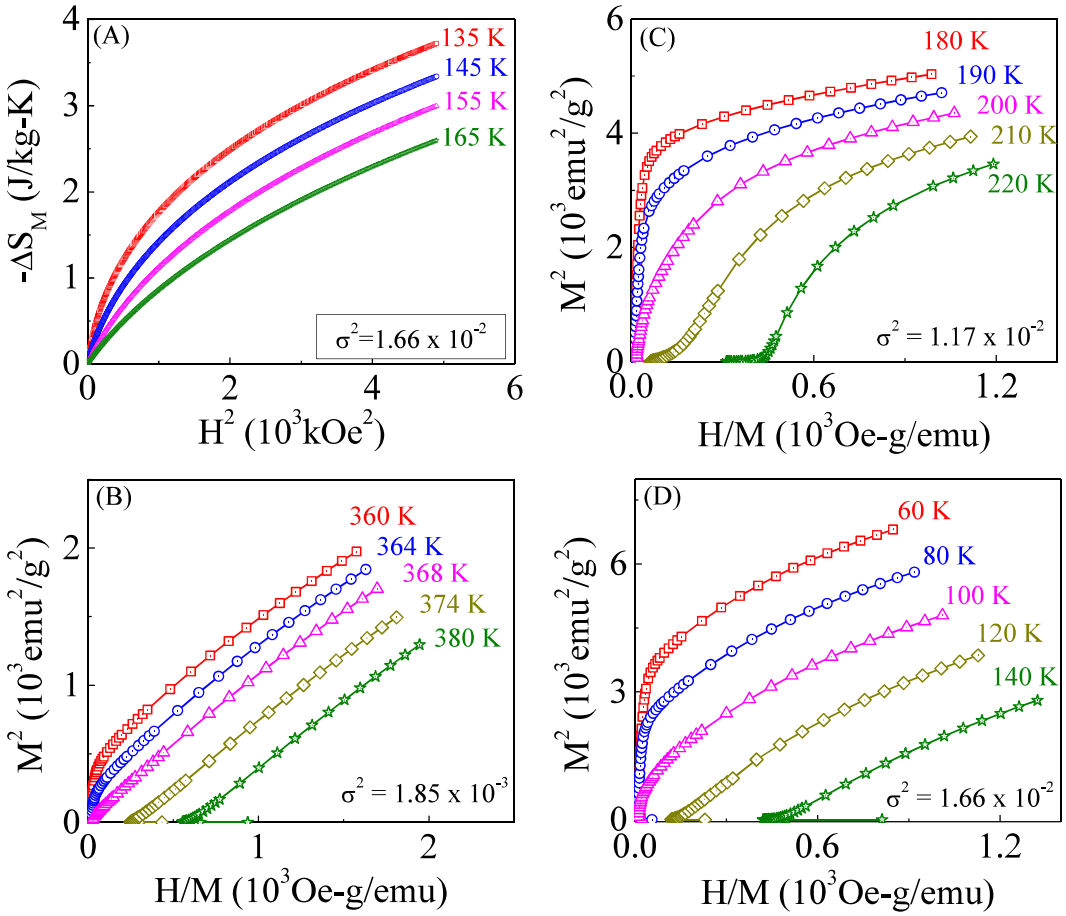


**Figure 6.5:** (A) Plot of $-\Delta S_M$ versus $H^2$ at different temperatures for the sample with $\sigma^2 = 1.66 \times 10^{-2}$. The Arrot plot ($M^2$ versus $H/M$) for the samples with $\sigma^2 =$ (B) $1.85 \times 10^{-3}$ (C) $1.17 \times 10^{-2}$ and (D) $1.66 \times 10^{-2}$ respectively.

suppressed, but here for $\sigma^2 = 1.17 \times 10^{-2}$ an anomaly is observed. Moreover, in the sample of lower A-site cationic distribution i.e. for ($\sigma^2$=$1.85 \times 10^{-3}$) the peak positions of the maximum magnetic entropy ($-\Delta S_{M,max}$) remains independent of applied magnetic field but with increasing $\sigma^2$ the position of $-\Delta S_{M,max}$ gets shifted with the applied magnetic field value. This feature suggest the distribution of ferromagnetic interaction strength in the higher $\sigma^2$ sample. In addition to $-\Delta S_{M,max}$, another important parameter for magnetocaloric materials is relative cooling power (RCP), defined as $RCP = -\Delta S_{M,max} \times \delta T_{FWHM}$ where $\delta T_{FWHM}$ is the full width at half maximum of $|\Delta S_{M,max}|$. The magnetic field dependence of RCP for the samples has been depicted in Fig. 6.4(D). Increase in RCP with applied magnetic field has been observed for all the samples because of the increase in $|\Delta S_M|$ with field.

**Table 6.2:** Comparison the values of $-\Delta S_M(J/kg-K)$ and $RCP(J/kg)$ of $La_{0.7}Sr_{0.3}MnO_3$, $Pr_{0.7}Sr_{0.14}Ba_{0.16}MnO_3$ and $Nd_{0.7}Sr_{0.07}Ba_{0.23}MnO_3$ with some other manganites reported in literature.

| *Sample* | $T_C(K)$ | $\Delta H$ | $-\Delta S_M$ | $RCP$ | Reference |
|---|---|---|---|---|---|
| $La_{0.7}Sr_{0.3}MnO_3$ | 368 | 15 | 1.45 | 57 | This work |
| $Pr_{0.7}Sr_{0.14}Ba_{0.16}MnO_3$ | 202 | 15 | 2.30 | 74 | This work |
| $Nd_{0.7}Sr_{0.07}Ba_{0.23}MnO_3$ | 100 | 15 | 1.25 | 86 | This work |
| $Pr_{0.7}Sr_{0.14}Ba_{0.16}MnO_3$ | 202 | 50 | 4.80 | 258 | This work |
| $Nd_{0.7}Sr_{0.07}Ba_{0.23}MnO_3$ | 100 | 50 | 3.10 | 350 | This work |
| $La_{0.8}Ca_{0.2}MnO_3$ | 230 | 15 | 5.5 | 72 | [67] |
| $La_{0.55}Ca_{0.45}MnO_3$ | 238 | 15 | 1.9 | 68 | [67] |
| $La_{0.75}Sr_{0.25}MnO_3$ | 340 | 15 | 1.5 | 65 | [75] |
| $La_{0.67}Ca_{0.33}MnO_3$ | 257 | 50 | 2.06 | 175 | [77] |
| $La_{0.87}Sr_{0.13}MnO_3$ | 197 | 50 | 5.80 | 232 | [76] |
| $La_{0.84}Sr_{0.16}MnO_3$ | 244 | 50 | 5.85 | 240 | [76] |
| $La_{0.67}Sr_{0.33}MnO_3$ | 348 | 50 | 1.69 | 211 | [77] |
| $La_{0.67}Ba_{0.33}MnO_3$ | 292 | 50 | 1.48 | 161 | [77] |

Moreover, an enhancement of RCP from 80 J/kg to 120 J/kg for 20 kOe applied magnetic field has been achieved with increase in the variance from $1.85 \times 10^{-3}$ to $1.66 \times 10^{-2}$. Even the RCP values of the presently studied compounds are comparable or even larger than the reported manganite materials and a comparison has been presented in Table. 6.2. Such enhancement of RCP is because of the increasing spreading of $|\Delta S_M|$ with $\sigma^2$.

To inspect the origin of this increased spreading with $\sigma^2$, magnetic field dependence of $|\Delta S_M|$ for the sample of maximum $\sigma^2$ ($1.66 \times 10^{-2}$) has been investigated (Fig. 6.5). According to the mean field theory, in the paramagnetic region $-\Delta S_M \propto H^2$ for a fixed temperature. From Fig. 6.5(A) it can be clearly seen that even at 165 K which is far away from the curie temperature (105 K) the $H^2$ dependence $|\Delta S_M|$ is not followed. It implies the presence of ferromagnetic interactions in the paramagnetic region though there is no spontaneous magnetization as observed from Arrot plot [248] (Fig. 6.5(D)). Thus the high temperature paramagnetic state is not pure paramagnetic but consists of short range small ferromagnetic clusters which has raised due to the increased A-site cationic distribution and is responsible to

enhance the RCP.

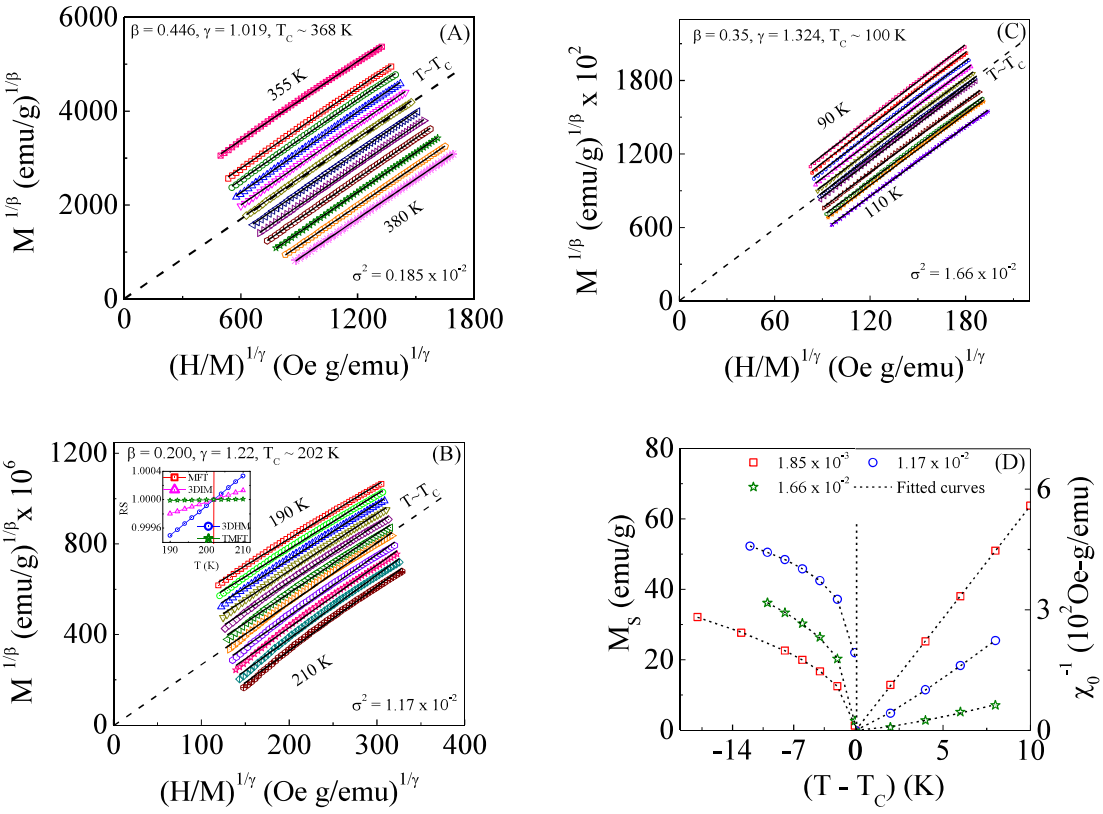


**Figure 6.6:** The modified Arrot Plot ($M^{1/\beta}$ versus $(H/M)^{1/\gamma}$) for the samples with $\sigma^2$ = (A) $1.85 \times 10^{-3}$ (B) $1.17 \times 10^{-2}$ and (C) $1.66 \times 10^{-2}$ respectively. The inset in (B) shows the relative slope (RS) versus T plot for different models of the corresponding sample. (D) Spontaneous magnetization $M_S$ (left axes) and inverse of the initial magnetic susceptibility $\chi_0^{-1}$ (right axes) versus $(T - T_C)$ along with the fit to the power laws.

Thus, though the presence of ferromagnetic clusters can explain the enhanced RCP in the maximum A-site cationic disorder sample but the anomaly in $|\Delta S_{M,max}|$ in $\sigma^2 = 1.17 \times 10^{-2}$ sample is still not clear. To clear this anomaly, critical analysis of the samples has been performed. Generally, critical temperature and critical exponents can be easily determined from analyzing the Arrot plot ($M^2$ versus H/M) around $T_C$. According to the Banerjee criterion [68], the order of a magnetic transition is determined from the high field slope of the $M^2$ versus H/M curves, where positive slope corresponds to the second order phase transition and negative slope stands for the first order transition. Fig. 6.5(B), (C) and (D) shows the Arrot plot of the samples around their corresponds $T_C$ where positive slopes in

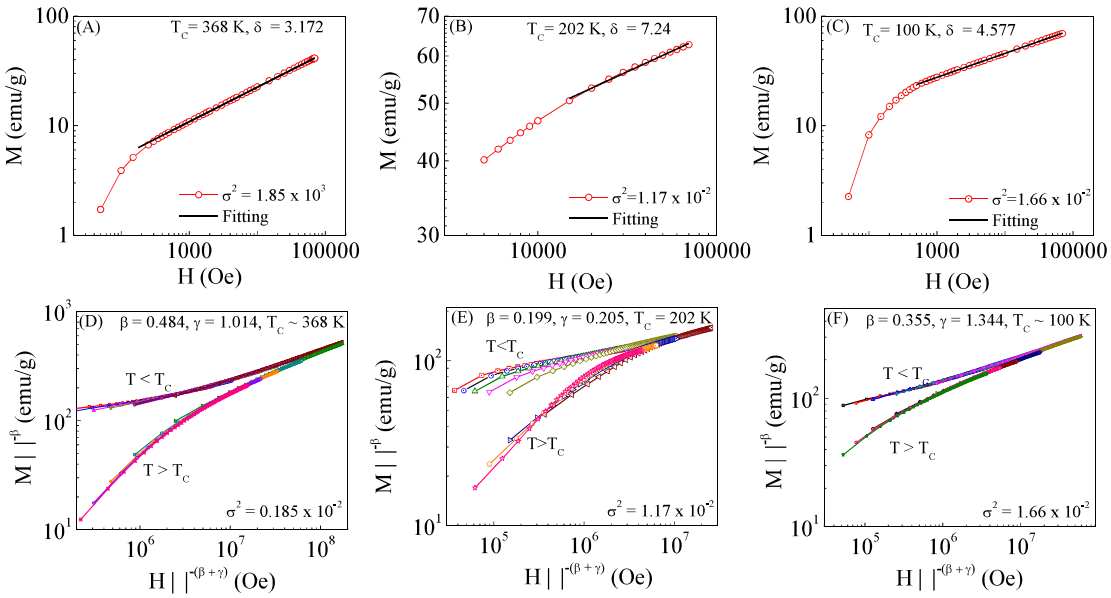


**Figure 6.7:** Critical isotherm M(H) in log-log scale at the temperature closest to $T_C$ for the samples with $\sigma^2$ = (A) $1.85 \times 10^{-3}$ (B) $1.17 \times 10^{-2}$ and (C) $1.66 \times 10^{-2}$ respectively. Plot (D), (E) and (F) represents the scaling plot for the above mentioned samples in log-log scale respectively.

each case implies the second order nature of the ferromagnetic transitions. Here, though for the sample $\sigma^2$=$1.85 \times 10^{-3}$ Arrot plot are linear but in other two sample nonlinear behavior of the Arrot plot is observed which implies the non applicability of the Landau mean field theory in the higher cationic disorder sample. Hence the modified Arrot plot, based on the Arrot-Noakes equation of state [266] $(H/M)^{1/\gamma} = (T - T_C)/T_C + (M/M_1)^{1/\beta}$, has been used to obtain the correct value of $\beta$ and $\gamma$. It is well known that, for a second order ferromagnetic transition near the critical temperature, the initial magnetic susceptibility $[\chi_0 = \partial M/\partial H_{H=0}]$ and spontaneous magnetization $[M_S = M_{H=0}]$ show the power law dependence with the reduced temperature $[\varepsilon = (T - T_C)/T_C]$ with the critical exponents $\gamma$ and $\beta$. According to scaling hypothesis [78] in the asymptotic region, these relations are $M_S(T) = M_0|\varepsilon|^\beta$ for $\varepsilon < 0$ and $\chi_0(T)^{-1} = (h_0/M_0)\varepsilon^\gamma$ for $\varepsilon > 0$ and $M = DH^{1/\delta}$ for $\varepsilon = 0$. To confirm the suitable model to fit the data, the relative slope (RS), defined as the degree of parallelism among the different $M^{1/\beta}$ versus $(H/M)^{1/\gamma}$ lines around $T_C$, for all the models has been calculated for the samples. The most appropriate

model is the one for which RS is same for all temperature near the $T_C$ and corresponding $\beta$ and $\gamma$ values has been used as an initial values in the modified Arrot plot. One of the representative RS versus T plot has been presented in the inset of Fig. 6.6(B). The modified Arrot plot using the optimal values of $\beta$ and $\gamma$ determined by iterative approximation method (explained below) has been shown in the Fig. 6.6 (A), (B) and in (C) respectively for the samples with variance $1.85 \times 10^{-3}$, $1.17 \times 10^{-2}$ and $1.66 \times 10^{-2}$. As in the high field region the effect of charge, orbital and lattice degrees of freedom gets suppressed, the high field region data has been used for the analysis. According to the asymptotic critical behavior, plot of $M^{1/\beta}$ versus $(H/M)^{1/\gamma}$ is linear and each isothermal curves becomes parallel to each other. The intercepts of the isothermal lines with x and y axis gives the values of $1/\chi^{1/\gamma}$ and $M_S^{1/\beta}$ at each temperatures and the resulting $M_S$ versus T and $\chi^{-1}$ versus T for the samples has been shown in the Fig. 6.6. The fitting of $M_S$ versus T and $\chi^{-1}$ versus T yields the values for $\beta$ and $\gamma$ which again has been used for the new modified Arrot plot and iterated until their values becomes consistent. This process yields the critical exponents which has been listed in Table. 6.3 where for comparison the values of the exponents for some other manganites and from standard theoretical models has been listed. The third critical exponent $\delta$ can be determined from the isothermal magnetization curves at $T_C$ by using the relation [78] $M = DH^{1/\delta}$. From linear fitting at high magnetic field of $log(M) - log(H)$ plot the exponent $\delta$ of the samples has been obtained and corresponding fitting has been presented in Fig. 6.7. These three critical exponents also obey the widom scaling relation [274] $\delta = 1 + \gamma/\beta$ which has been used to check the reliability of the obtained critical exponents and also been listed in the Table. 6.3. The close values of $\delta$ for the samples determined in these two ways proves that obtained exponents are reliable.

The reliability of the obtained critical exponents can also be ascertained from the scaling hypothesis. According to the hypothesis [78], equation of state can be written as $M(H, \varepsilon) = \varepsilon^{\beta} f_{\pm}(H/\varepsilon^{\beta+\gamma})$, where $f_{\pm}$ is the scaling functions with $f_-$ for $T < T_C$

**Table 6.3:** Comparison the values of the critical exponents of $La_{0.7}Sr_{0.3}MnO_3$, $Pr_{0.7}Sr_{0.14}Ba_{0.16}MnO_3$ and $Nd_{0.7}Sr_{0.07}Ba_{0.23}MnO_3$ with the various theoretical models and other manganites reported in literature.

| *Sample* | $T_C(K)$ | $\beta$ | $\gamma$ | $\delta$ | Reference |
|---|---|---|---|---|---|
| $La_{0.7}Sr_{0.3}MnO_3$ | 368 | 0.446 | 1.019 | 3.28 | This work |
| $Pr_{0.7}Sr_{0.14}Ba_{0.16}MnO_3$ | 202 | 0.200 | 1.22 | 7.1 | This work |
| $Nd_{0.7}Sr_{0.07}Ba_{0.23}MnO_3$ | 100 | 0.350 | 1.324 | 4.78 | This work |
| Mean field model | | 0.5 | 1 | 3.0 | [78] |
| 3D-Heisenberg model | | 0.365 | 1.386 | 4.797 | [78] |
| 3D-Ising model | | 0.325 | 1.24 | 4.82 | [78] |
| Tricritical mean-field model | | 0.25 | 1 | 5 | [267] |
| $La_{0.8}Sr_{0.2}MnO_3$ | 315 | 0.5 | 1.08 | 3.13 | [268] |
| $La_{0.67}Ba_{0.33}MnO_3$ | 306 | 0.356 | 1.120 | 4.15 | [269] |
| $Pr_{0.67}Ba_{0.33}MnO_3$ | 201 | 0.246 | 1.030 | 5.069 | [270] |
| $La_{0.9}Te_{0.1}MnO_3$ | 239 | 0.201 | 1.27 | 7.14 | [271] |
| $Nd_{0.5}Sr_{0.5}MnO_3$ | 239 | 0.5 | 1.02 | 4.02 | [272] |
| $Nd_{0.7}Pb_{0.3}MnO_3$ | 148 | 0.361 | 1.325 | 4.62 | [273] |

and $f_+$ for $T > T_C$. Thus plot of $M|\varepsilon|^{-\beta}$ versus $H|\varepsilon|^{-(\beta+\gamma)}$ will forms two universal curves for $T > T_C$ and $T < T_C$. From the isothermal magnetization around $T_C$, $M|\varepsilon|^{-\beta}$ versus $H|\varepsilon|^{-(\beta+\gamma)}$ for the samples has been plotted in Fig. 6.7 which proves the universality nature of the curves above and below $T_C$ and indicates the further reliability of the exponents.

The obtained critical exponents for $\sigma^2 = 1.85 \times 10^{-3}$ sample is close to the mean field model whereas for $\sigma^2 = 1.66 \times 10^{-2}$ sample critical exponents are close to 3D-Heisenberg model. The long range attractive interactions in a system is of the form [275] $J(r) \sim 1/r^{d+\sigma}$ where $d$ is the dimension of the system and $\sigma$ is the interaction range. For 3d system this relation becomes $J(r) \sim 1/r^{3+\sigma}$ with $3/2 \leq \sigma \leq 2$. When $\sigma = 2$, the 3D-Heisenberg exponents are valid which implies that $J(r)$ decays as $1/r^5$ and for $\sigma = 3/2$ the mean field exponents are valid which tells that $J(r)$ decreases as $1/r^{4.5}$. Therefor, in the lower cationic disorder sample the interaction strength is long range compared with the sample of maximum cationic disorder. On the other way to say, disorder breaks the long range interaction which is responsible to enhance RCP as discussed earlier. In the intermediate values of $\sigma$, the expo-

**Table 6.4:** The lattice parameters, average A-site ionic radii $\langle r_A \rangle$, A-site ionic distribution ($\sigma^2$) and unit cell volumes of the samples

| *Sample* | a ($\AA$) | b ($\AA$) | c ($\AA$) | $T_C(K)$ | $T_{MI}(K)$ | Reference |
|---|---|---|---|---|---|---|
| $Pr_{0.8}Sr_{0.2}MnO_3$ | 5.478 | 5.474 | 7.738 | 160 | - | 29 |
| $Pr_{0.775}Sr_{0.225}MnO_3$ | 5.477 | 5.471 | 7.738 | 175 | 100 | This work |
| $Pr_{0.7}Sr_{0.3}MnO_3$ | 5.450 | 5.483 | 7.714 | 260 | 262 | 33 |

nents follows different universality class such as Tricritical mean field theory where exchange interaction $J(r)$ ranges in between $1/r^{4.5}$ and $1/r^5$ and this kind of universality has been observed for the $\sigma^2 = 1.17 \times 10^{-2}$ sample. Thus, $\sigma^2 = 1.17 \times 10^{-2}$ sample being lie in the tricritical region large value of $|\Delta S_{M,max}|$ has been observed compared with other $\sigma^2$ sample.

## 6.3 Large magnetoresistance and relative cooling power in polycrystalline $Pr_{0.775}Sr_{0.225}MnO_3$ compound

### 6.3.1 Sample Preparation and Characterization

The bulk polycrystalline $Pr_{0.775}Sr_{0.225}MnO_3$ compound was prepared by the conventional sol-gel route with $Pr_6O_{11}$, $SrCO_3$ and $MnO_2$ as the starting materials of purity 99.9%. For the bulk sample preparation, decomposed gels were pelletized and subsequently sintered at $1300^0C$ for 36 hours.

### 6.3.2 Experimental Results and Discussion

For phase confirmation of the sample, the room temperature x-ray diffraction measurements was carried out using Rigaku-TTRAX-III diffractometer of 9kW rotating

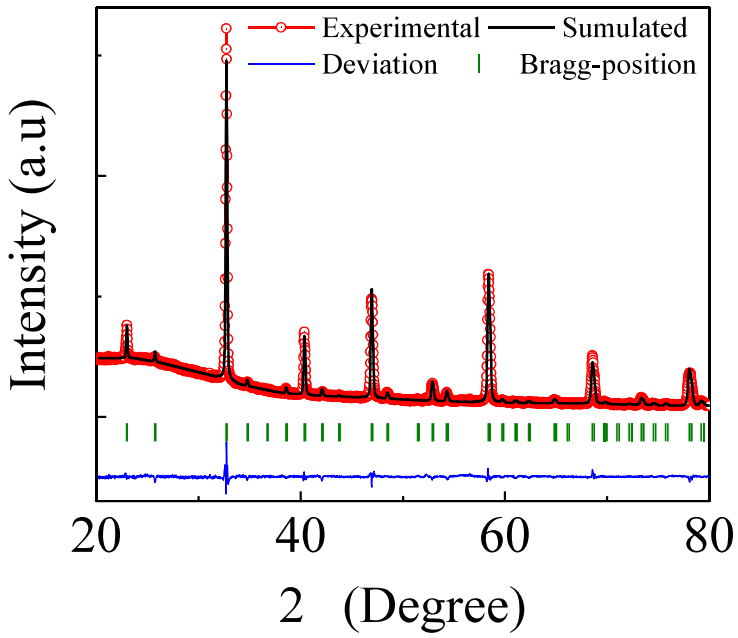


**Figure 6.8:** Room temperature XRD data with its profile fitted data.

anode cu source. The magnetic measurements was performed by employing quantum design SQUID-VSM. The transport and magnetotransport measurements was carried out by four probe method in longitudinal geometry using Cryogenic set up.

The x-ray diffraction study (Fig. 6.8) shows the single phase nature of the sample. Using FULLPROF software, Rietveld refinement of the xrd data has been performed which indicates the orthorhombic structure of the sample having 'Pnma' space group. The extracted lattice parameters has been summarized in Table. 6.4. It can be clearly seen that for the sample with 'Sr' composition $x = 0.2$ and $x = 0.225$ the lattice parameters are very close to each other but for $x = 0.3$ deviation of lattice parameters is observed.

In manganite system, magnetic and magnetotransport properties are strongly coupled with structure [183]. Thus, though there is a very little change in lattice parameters in $x = 0.225$ from $x = 0.2$, but the effect of little change in 'Sr' concentration can be seen from magnetic measurements as $x = 0.225$ is near the FMM-FMI phase boundary. In this regard, magnetization has been measured in presence of 1 kOe magnetic field in zero field cooled warming (ZFC) and field cooled warming (FCW)

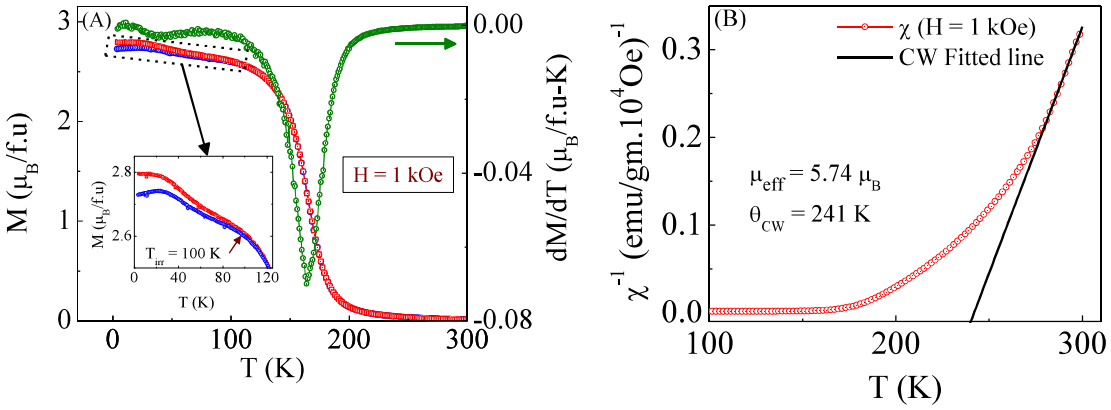


**Figure 6.9:** (A) Left axes: Variation of zero field cooled magnetization warming (blue curve) and field cooled warming magnetization (red curve) with temperature in presence of 1 kOe external magnetic field. Right axes: Temperature derivative of field cooled warming magnetization. Inset shows the zoomed portion of the magnetization data for $T < 100K$. (B) $\chi^{-1}$ versus T plot along with Curie-Weiss fitted line.

protocols and has been shown in Fig. 6.9(A). The ZFC and FCW curves starts to bifurcates around 100 K which is the irreversibility temperature. The signature of paramagnetic to ferromagnetic transition at $T_C$ = 175 K is observed from dM/dT vs. T data. At low temperature (at 50 K) another ordering is visible which is due to the 'Pr' ordering. Another point here has to be noted that with increasing 'Sr' concentration from $x = 0.2$ to $x = 0.225$, $T_C$ has increased from 160 K to 175 K which implies the increase in strength of the ferromagnetic interactions. For further understanding, high temperature ($T > 270K$) inverse dc susceptibility (H/M) data has been analyzed with the Curie-Weiss (CW) law and corresponding plot is shown in Fig. 6.9(B). According to CW law, $\chi = C/(T - \theta_{CW})$ where $C = \mu_{eff}^2/3k_B$ and $\mu_{eff}$, $\theta_{CW}$ are effective magnetic moment in Bohr magnetron and paramagnetic curie temperature respectively. The CW fitting gives $\theta_{CW}$ = 241 K and $\mu_{eff}$ = $5.74\mu_B$. The occurrence of $\theta_{CW} > T_C$ and larger value of $\mu_{eff} = 5.74\mu_B$ compared with theoretical value of $4.688\mu_B$ implies the presence of ferromagnetic clusters at higher temperature [171].

To see the effect of phase boundary on electrical transport measurements, temperature dependent resistivity for $x = 0.225$ compound has been measured in absence

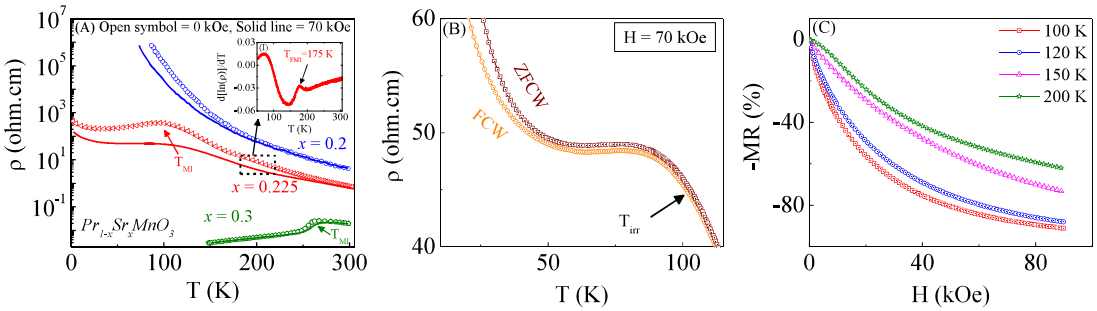


**Figure 6.10:** Variation of temperature dependent resistivity for the compounds $Pr_{1-x}Sr_xMNO_3(x = 0.2, 0.225, 0.3)$ measured during warming cycle in zero field and in presence of 70 kOe magnetic field. Inset shows the temperature derivative of $ln(\rho)$. (B) Temperature dependent resistivity for $x = 0.225$ compound measured in zero field cooled warming and field cooled warming protocol in presence of 70 kOe magnetic field. (C) MR versus H curves at 100 K, 120 K, 150 K and 200 K.

as well as in presence of 70 kOe external magnetic field (Fig. 6.10(A)) and measurement has been carried out during warming cycles. Resistivity data for $x = 0.2$ and $x = 0.3$ has been collected from literature [276, 280] and has been presented in the Fig. 6.10(A). Here it can be clearly seen that with increase of '$x$' from $x = 0.2$ to $x = 0.3$ the room temperature resistivity decreases from $7 ohm.cm$ to $0.02 ohm.cm$. The zero field resistivity of $x = 0.2$ sample shows the insulating nature down to the measurable temperature limit and in effect of 70 kOe external magnetic field resistivity decreases but the effect is not so pronounced and it also shows insulating behavior down to the low temperature. In contrast to $x = 0.2$, $x = 0.225$ shows spontaneous metal insulator transition at 100 K. A little hump is observed around 175 K which is clearly visible from $d[ln(\rho)]/dT$ vs. T data and this transition is the PM-FMI transition as from M vs T data it can be clearly seen that at 175 K PM-FM transition occurs. Thus, though sample undergoes FMI transition at 175 K but there is a metal-insulator transition at 100 K which is little bit fuzzy. To understand this apparent discrepancy, resistivity of the sample in presence of 70 kOe magnetic field has been measured in ZFC and FCW protocols which shows irreversibility around 100 K as observed from M vs T curve. This irreversibility is because of the coexistence of FMM and FMI phase. Thus, at 175 K sample undergoes PM-FMI phase transition and for $T < 100K$ there is the phase coexistence (FMM-FMI) and this

FMM phase creates the percolation path for the electrical transport which results in the insulator to metal transition. On application of 70 kOe magnetic field, there is the creation of more percolation path by suppressing the phase fluctuations of FMI and FMM phase and results in the huge suppression of resistivity compared with $x = 0.2$ sample. On the other hand, $x = 0.3$ sample undergoes metal insulator transition around 260 K which is close to the PM-FM ordering temperature. Thus in this sample there is no phase coexistence and for this reason magnetic field has very minute effect on resistivity. Therefore, $x = 0.225$ sample being lie near the FM-FMI phase boundary, phase separation occurs and as a result of which huge suppression of resistivity occurs which leads to the enhancement of magnetoresistance (MR).

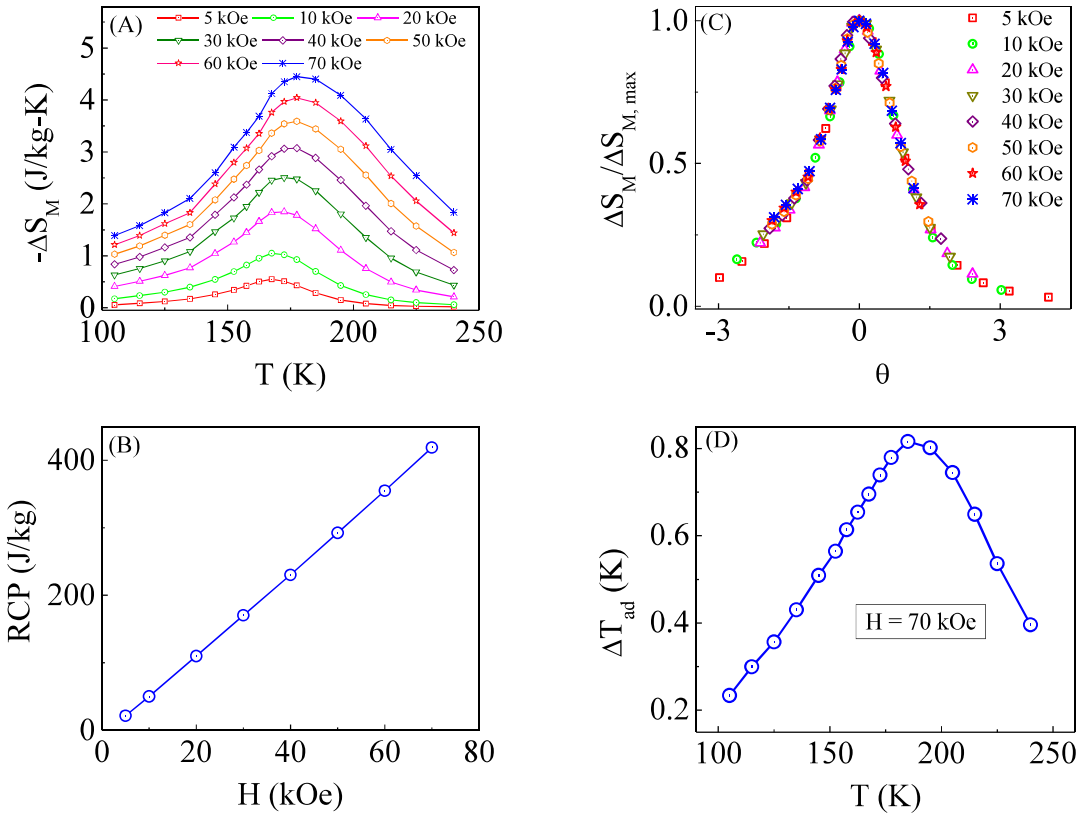


**Figure 6.11:** (A) Plot of $-\Delta S_M$ versus T for different applied magnetic field values. (B) variation of relative cooling power (RCP) versus H. (C) Universal curve of $\Delta S_M$ of $Pr_{0.775}Sr_{0.225}MnO_3$ under various applied magnetic fields. (D) Plot of the adiabatic temperature change $\Delta T_{ad}$ with temperature in presence of 70 kOe magnetic field.

To see the effect of magnetic field on MR, magnetic field dependence of MR at different temperatures (100 K, 120 K, 150 K and 200 K) has been measured (Fig.

6.10(C)) where MR has been defined as $MR(\%) = (R(H) - R(0))/R(0)$. Huge magnetoresistance of 87% has been observed in 70 kOe applied magnetic field at 100 K temperature whereas in $x = 0.3$ only 46% MR has been reported for 50 kOe applied magnetic field at 260 K [280] and 77% MR has been reported in $x = 0.2$ sample for 90 kOe magnetic field at 100 K temperature [276]. Thus the phase separation enhances the MR in $x = 0.225$ sample.

Together with the magnetotransport property the magnetocaloric (MCE) response of the sample have also been investigated. According to maxwell thermodynamic relation, magnetic entropy change $[\Delta S_M(H,T)]$ is determined as $\Delta S_M(H,T) = \int_0^H (\frac{\partial M}{\partial T})dH$. To determine $\Delta S_M$, isothermal magnetization [M(H)] has been measured at different temperatures in ZFC protocol and before each successive M(H) measurements sample has been taken to the paramagnetic region to destroy any magnetic history present in the sample. The temperature dependence of magnetocaloric entropy change ($\Delta S_M$) for different applied magnetic fields has been presented in Fig. 6.11(A). In the paramagnetic region negative magnetic entropy change (-$\Delta S_M$) increases with lowering the temperature and exhibits a maximum near the ferromagnetic ordering temperature (175 K) and the maximum value of -$\Delta S_M$ is $4.44 J/kg - K$ for 70 kOe applied magnetic field. Moreover, the peak positions of the maximum magnetic entropy change $[\Delta S_{M,max}]$ gets shifted towards higher temperature with increase in the applied magnetic field. It suggest the distribution of ferromagnetic interaction strength which occurs mainly in second order phase transition. To address the nature of the magnetic phase transition, universal behavior of $\Delta S_M$ has been studied as proposed by Franco et al [281]. The construction of the universal curve has been done by normalizing all the $\Delta S_M(T)$ curves with their corresponding peak value $\Delta S_{M,max}$ and rescaling the temperature axes as

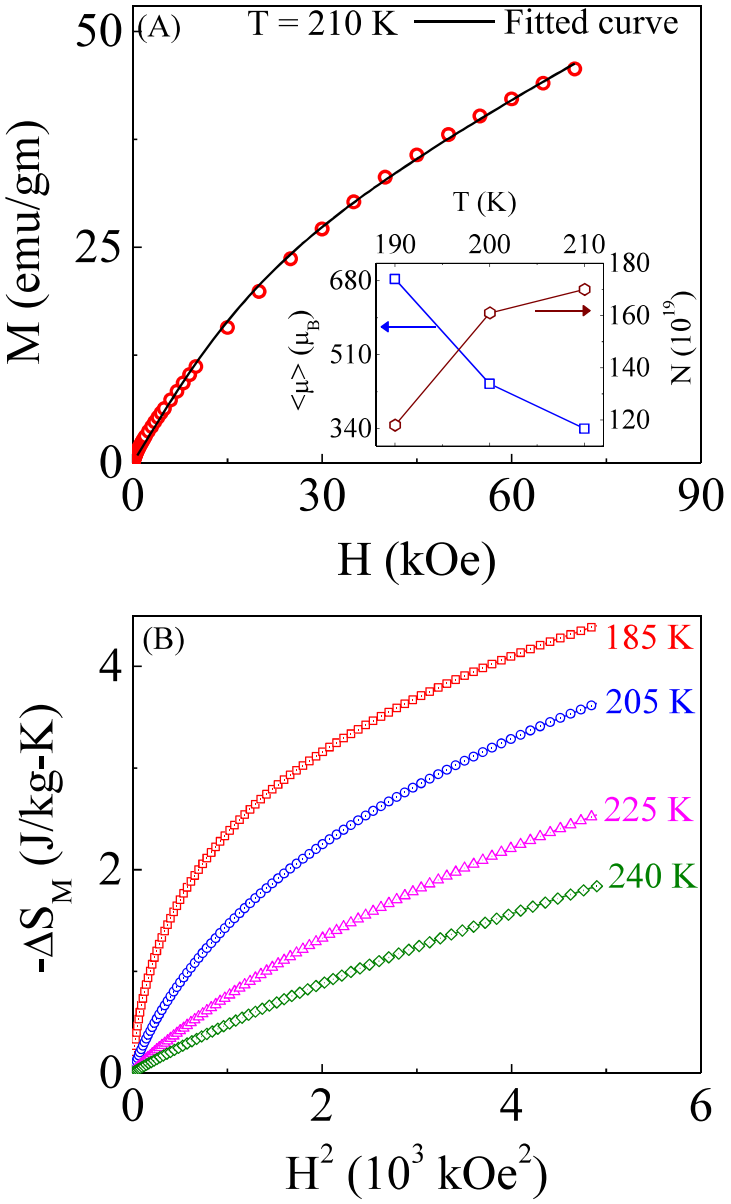


**Figure 6.12:** (A) Fitting of the isothermal (210 K) M versus H data with the modified Langevin function where black solid line represents the fitted line. Inset shows the temperature variation of average cluster moment (left axes) and average cluster density (right axes). (B) Plot of $-\Delta S_M$ versus $H^2$ at 185 K, 205 K, 225 K and 240 K temperatures.

$$\theta = \begin{cases} -(T - T_C)/(T_{r1} - T_C) & T \leq T_C \\ (T - T_C)/(T_{r1} - T_C) & T \geq T_C \end{cases} \tag{6.1}$$

Here $T_C$ is the temperature corresponding to the maximum entropy change and $T_{r1}$

& $T_{r2}$ are the reference temperature corresponding to a certain fraction $f$ such that $\Delta S_M(T_{r1})/\Delta S_M(T) = \Delta S_M(T_{r2})/\Delta S_M(T) = f$. Here we have used $f = 0.5$. The normalized entropy change with rescaled temperature [Fig. 6.11(C)] shows that all the curves superimposes on a single curve which indicates the second order nature of the PM-FMI magnetic phase transition. Besides the magnetocaloric entropy change, the adiabatic temperature change on application of the 70 kOe magnetic field has been calculated using the relation $\Delta T_{ad} = -\int_0^H (\frac{T}{C_P}\frac{\partial M}{\partial T})dH$, where $C_P$ is the zero field heat capacity of the sample. The variation of $\Delta T_{ad}$ with temperature on application of 70 kOe magnetic field has been shown in Fig. 6.11(D) which indicates $\sim 0.8K$ temperature change around the PM-FMI phase transition. In addition to $-\Delta S_{M,max}$, another important parameter for refrigerant materials from application point of view is relative cooling power (RCP), which is the amount of heat transfer from hot end to cold end in an ideal refrigerant cycle and is defined as $RCP = -\Delta S_{M,max} \times \delta T_{FWHM}$ where $\delta T_{FWHM}$ is the full width at half maximum of $-\Delta S_M$ vs. T curve. The magnetic field variation of RCP of the sample has been depicted in Fig. 6.11(B). The estimated values of RCP are $290J/kg$ and $418J/kg$ on application of 50 kOe and 70 kOe magnetic field values respectively. These values are quite large compared to many other magnetic refrigerant materials reported in literature and the comparison has been presented in Table. 6.2.

To investigate the microscopic origin of this large RCP, isothermal magnetization data in the paramagnetic region ($T > 180K$) has been analyzed with modified Langevin function [183] $M(H) = N\mu L(\frac{\mu H}{k_B T}) + AH$, where 'L(x)' is the Langevin function, 'N' is the number density of the clusters and '$\mu$' is the average magnetic moment of the clusters. A reasonable good fittings of the M(H) data with the function are observed and one of the fittings (190 K) is represented in Fig. 6.12(A). From the fittings, extracted '$\mu$' and 'N' at different temperatures have been presented in the inset of Fig. 6.12(A). With decrease in temperature, in the paramagnetic region, increase in cluster moment and at the same time decrease in cluster density

are observed. Again, according to the mean field theory, in the paramagnetic region [184, 185] $-\Delta S_M \propto H^2$. From Fig. 6.12(B) it can be clearly seen that even at 240 K, which is far away from $T_C$, no $H^2$ dependence is observed. It indicates the presence of ferromagnetic clusters in the paramagnetic region. Thus, presence of ferromagnetic clusters in the PM region is responsible for this large RCP value. In this context, it may be mentioned that presence of clusters has also been observed in some other magnetic materials [282–284]. Thus the study shows, that the procedure described here to enhance the cooling efficiency is a general one and can also be applicable to any magnetic materials.

## 6.4 Summary

In summary, we have investigated the structural, magnetic and magnetocaloric properties of isoelectronic perovskite manganites ($La_{0.7}Sr_{0.3}MnO_3$, $Pr_{0.7}Sr_{0.14}Ba_{0.16}MnO_3$ and $Nd_{0.7}Sr_{0.07}Ba_{0.23}MnO_3$) with larger A-site ionic radius or electronic bandwidth. The results show that with increasing $\sigma^2$ from $1.85 \times 10^{-3}$ to $1.66 \times 10^{-2}$ the ferromagnetic ordering temperature $T_C$ decreases from 360 K to 100 K. Interestingly, on the other hand the increase of RCP is observed with the increase of $\sigma^2$. To find out the underlying reason behind the enhancement in RCP with $\sigma^2$, a detailed critical analysis has been performed. Critical analysis shows that the sample with lower $\sigma^2$ =$1.85 \times 10^{-3}$ follow the mean field model, implies the long range nature of the interactions responsible for sharper $-\Delta S_M$ and the system with $\sigma^2$ =$1.66 \times 10^{-2}$ follow the 3D-Heisenberg model, tells about the short range nature of the interactions responsible for broadening the $-\Delta S_M$ and the system with $\sigma^2$ =$1.17 \times 10^{-2}$ follow the Tricritical mean-field model i.e. system lie in the tricritical region and is the reason behind the apparent anomaly in the value of $-\Delta S_M$. This study shows a possible way to increase RCP. To bring the ordering temperature near the room temperature for practical application further fine tuning of $\sigma^2$ is needed and is the

scope for further work.

In the last part of the chapter, we have investigated the magnetic, magnetotransport and magnetocaloric properties of $Pr_{0.775}Sr_{0.225}MnO_3$ compound, resides close to bi critical region interfacing the ferromagnetic metallic and ferromagnetic insulator phases. The results show that due to the suppression of enhanced phase fluctuation near the phase boundary, enhancement of magnetoresistance occurs in the sample compared to the samples resides on both sides of the bi-critical region. Again, the magnetization study suggest the presence of the ferromagnetic clusters above the ordering temperature which leads to an increase in the RCP of the compound.

# CHAPTER 7

# Summary and scope for future work

## 7.1 Summary

In this thesis work, a detailed and systematic study to understand the magnetic and magnetocaloric properties of rare earth based manganites have been carried out. Some exciting and powerful method of enhancing different functional aspects of the systems are also explored. The major findings of the thesis work along with the possible scope of future study has been discussed in this chapter.

The major findings of the work here is the extreme colossal magnetoresistance along with the ultrasharp metamagnetic transition in half doped $Sm_{0.5}Ca_{0.25}Sr_{0.25}MnO_3$ manganite compound. The parent compound $Sm_{0.5}Ca_{0.5}MnO_3$ (SCMO) is a very stable charge ordered antiferromagnetic (CO-AFM) compound and $\sim$ 500 kOe (at 4 K) critical magnetic field ($H_{CR}$) is required to destabilize the CO state. On the other hand CO-AFM and FM metallic phases coexist in $Sm_{0.5}Sr_{0.5}MnO_3$ and is metallic at low temperature. In our case we prepare $Sm_{0.5}Ca_{0.25}Sr_{0.25}MnO_3$ by replacing half of the $Ca^{2+}$ ions by $Sr^{2+}$ ions. By suitably tuning the volume fraction of the competing phases the obtained magnetoresistance value is as large as $\sim 10^{13}$% and $\sim 10^{15}$% at 10 K on application of 30 kOe and 90 kOe external

# CHAPTER 7

# Summary and scope for future work

## 7.1 Summary

In this thesis work, a detailed and systematic study to understand the magnetic and magnetocaloric properties of rare earth based manganites have been carried out. Some exciting and powerful method of enhancing different functional aspects of the systems are also explored. The major findings of the thesis work along with the possible scope of future study has been discussed in this chapter.

The major findings of the work here is the extreme colossal magnetoresistance along with the ultrasharp metamagnetic transition in half doped $Sm_{0.5}Ca_{0.25}Sr_{0.25}MnO_3$ manganite compound. The parent compound $Sm_{0.5}Ca_{0.5}MnO_3$ (SCMO) is a very stable charge ordered antiferromagnetic (CO-AFM) compound and $\sim$ 500 kOe (at 4 K) critical magnetic field ($H_{CR}$) is required to destabilize the CO state. On the other hand CO-AFM and FM metallic phases coexist in $Sm_{0.5}Sr_{0.5}MnO_3$ and is metallic at low temperature. In our case we prepare $Sm_{0.5}Ca_{0.25}Sr_{0.25}MnO_3$ by replacing half of the $Ca^{2+}$ ions by $Sr^{2+}$ ions. By suitably tuning the volume fraction of the competing phases the obtained magnetoresistance value is as large as $\sim 10^{13}$% and $\sim 10^{15}$% at 10 K on application of 30 kOe and 90 kOe external

magnetic field. This magnetoresistance value is several orders of magnitude higher than any other observed magnetoresistance value reported so far. In an external magnetic field the inhomogenous disorder, arising from the A-site disorder, seeds the ferromagnetic-metallic clusters into the system and as a result resistivity decreases at low temperatures which gives rise to large magnetoresistance. We also find an ultrasharp metamagnetic transition1 below 10 K which has been explained using martensitic scenario.

The remarkable reduction of the critical magnetic field ($H_{CR}$) in $Sm_{0.5}Ca_{0.25}Sr_{0.25}MnO_3$ compound is observed compared with the parent $Sm_{0.5}Ca_{0.5}MnO_3$ compound. To find out the origin of reduction of $H_{CR}$, we have studied the magnetic and magnetotransport properties in detail for the compounds $Sm_{0.5}(Ca_{0.5-x}Sr_x)MnO_3$ ($x$ = 0, 0.1, 0.2, 0.25, 0.3, 0.5). Study shows that there is an increase in phase separation with 'Sr' doping or in other words with increase in the average A-site ionic radius $\langle r_A \rangle$. Again 'Sr' substitution increase the A-site ionic disorder $\sigma^2$. This increased $\sigma^2$ together with increased $\langle r_A \rangle$ enhance the size of the ferromagnetic clusters in the AFM matrix and helps to decrease the $H_{CR}$ with 'Sr' doping as the clusters are acting as the nucleation center for the metamagnetic transition.

We have also achieved an extraordinarily large magnetoresistance in $La_{0.7}Ca_{0.3}MnO_3$ compound by introducing optimal disorder via yttrium ($Y^{3+}$) substitution in place of $La^{3+}$. In the optimum $Y^{3+}$ doped compound i.e. in $(La_{0.5}Y_{0.5})_{0.7}Ca_{0.3}MnO_3$, large magnetoresistance value as high as $1.5 \times 10^7\%$ at 50 K temperature and $3.6 \times 10^4\%$ at 80 K temperature has been achieved on application of 90 kOe external magnetic field. This enhancement of magnetoresistance in $x = 0.5$ compound has been obtained due to the creation of the percolation path by increasing the size of the ferromagnetic clusters on application of field.

A evolution from Griffiths (GP) like phase to non-Griffiths (non-GP) phase with yttrium substitution (i.e. $x$) has also been found from the detail analysis of the temper-

ature dependent dc susceptibility data of the polycrystalline $(La_{0.4}Y_{0.6})_{0.7}Ca_{0.3}MnO_3$ compounds. The existence of non-Griffiths phase is revealed from the upward deviation of the inverse susceptibility $(1/\chi)$ vs. T plot from the Curie weiss behavior for the compounds with $x \geq 0.5$. Whereas Griffiths like phase is identified from the downturn of $(1/\chi)$ versus T plot from the Curie weiss line in the compounds with $x = 0.3, 0.4$. With increase in $x$ the lattice distortions increases which in turn enhances the effective antiferromagnetic superexchange interactions between $Mn^{3+}/Mn^{3+}$ and $Mn^{4+}/Mn^{4+}$ ions. The evolution from GP like to non-GP phase is due to this enhancement of the effective short range antiferromagnetic interactions.

An enhancement of Colossal magnetoresistance in the minimal surface disorder nanoparticle ($\sim 120nm$) of $(La_{1-x}Y_x)_{0.7}Ca_{0.3}MnO_3$ compound has also been achieved due to the conversion from non-Griffiths phase to Griffiths phase. On the other hand, an enhancement of low field magnetoresistance has been obtained in the $(La_{0.5}Y_{0.5})_{0.7}Ca_{0.3}MnO_3$ nanoparticle and this enhancement has been attributed to the increase in the spin polarized tunneling component due to the increase in the ferromagnetic clusters size with reduction of particle size.

The study of magnetocaloric properties of some manganites systems also provides some interesting results. We have investigated the effect of A-site ionic disorder on magnetocaloric properties in large bandwidth manganite systems. The study shows the enhancement of relative cooling power with the A-site ionic disorder. The effect of the phase boundary of ferromagnetic metallic and ferromagnetic insulator state (FMM-FMI) on magnetocaloric properties in the $Pr_{0.775}Sr_{0.225}MnO_3$ compound has also been discussed. The results highlights that these low cost and chemically stable materials can be considered as appropriate alternatives of the intermetallic compounds for the refrigeration technology in a wide temperature regime.

## 7.2 Future prospects

In the thesis we have investigated the magnetotransport and magnetocaloric properties of some manganite systems. In chapter 3 we have observed that the charge ordered state of $Sm_{0.5}Ca_{0.5}MnO_3$ is drastically modified with 'Sr' doping in place of 'Ca' and gives rise to extreme colossal magnetoresistance. There is also a future scope of further modifying the charge ordered state of $Sm_{0.5}Ca_{0.25}Sr_{0.25}MnO_3$ by making nanoparticles and core-shell nanostructure with ferromagnetic compound in the core and charge ordered $Sm_{0.5}Ca_{0.25}Sr_{0.25}MnO_3$ compound in the shell to reduce the requirement of the critical field and having low field magnetoresistance. In this regard, neutron diffraction, electron diffraction study will also be helpful to visualize the evolution of the magnetic phases which is responsible for the enhancement of the magnetoresistance. Besides this, study of dielectric properties as well as ferroelectric properties of the materials may also give further insight into the system.

In chapter 4 and 5 we have shown that enhancement of magnetoresistance due to the evolution from non-Griffiths phase to Griffiths phase from magnetization and heat capacity study. Measurements of higher harmonics in ac susceptibility as well as electron spin resonance will give the direct picture of this evolution and is also the further scope of the work.

In chapter 6 we have shown the effect of the ferromagnetic metallic and ferromagnetic insulator state on magnetotransport and magnetocaloric properties. There is further scope of modifying the ferromagnetic insulator state by enhancing the chemical pressure in the ferromagnetic insulator state and study the corresponding magnetotransport and magnetocaloric properties.

# Bibliography


[1] Colossal Magnetoresistance, Charge ordering and Related Properties of Manganese Oxides, edited by C. N. R. Rao and R. Raveau, World Scientific, Singapore, (1998).

[2] Y. Tokura, Reports Prog. Phys. **69**, 797 (2006).

[3] M.B. Salamon and M. Jaime, Rev. Mod. Phys. **73**, 583 (2001).

[4] E. Dagotto, T. Hotta, and A. Moreo, Phys. Rep. **344**, 1 (2001).

[5] B. Raveau, C. Martin, A. Maignan and M. Hervieu, Phys. Rev. B **60**, 12191 (1999).

[6] S. Srivastava, N.K. Pandey, P. Padhan, and R.C. Budhani, Phys. Rev. B **62**, 13868 (2000).

[7] H. Tanaka, J. Zhang, and T. Kawai, Phys. Rev. Lett. **88**, 27204 (2001).

[8] S.Q. Liu, N.J. Wu, and A. Ignatiev, Appl. Phys. Lett. **76**, 2749 (2000).

[9] X. Hong, J.B. Yau, J.D. Hoffman, C.H. Ahn, Y. Bason, and L. Klein, Phys. Rev. B - Condens. Matter Mater. Phys. **74**, 1 (2006).

[10] C. Cui and T.A. Tyson, Phys. Rev. B - Condens. Matter Mater. Phys. **70**, 1 (2004).

[11] A. Das, P.D. Babu, S. Chatterjee, and A.K. Nigam, Phys. Rev. B - Condens. Matter Mater. Phys. **70**, 1 (2004).

[12] S. Kumar and A.P. Kampf, Phys. Rev. Lett. **100**, 76406 (2008).

[13] L.M. Rodriguez-Martinez and J.P. Attfield, Phys. Rev. B **63**, 24424 (2000).

[14] Y. Moritomo, H. Kuwahara, Y. Tomioka, and Y. Tokura, Phys. Rev. B **55**, 7549 (1997).

[15] R. Mathieu, M. Uchida, Y. Kaneko, J.P. He, X.Z. Yu, R. Kumai, T. Arima, Y. Tomioka, A. Asamitsu, Y. Matsui, and Y. Tokura, Phys. Rev. B **74**, 20404 (2006).

[16] Y. Moritomo, a. Asamitsu, H. Kuwahara, and Y. Tokura, Nature **380**, 141 (1996).

[17] P.K. Siwach, H. Singh, and O.N. Srivastava, J. Phys. Condens. Matter **20**, 273201 (2008).

[18] A. Asamitsu, Y. Tomioka, H. Kuwahara, and Y. Tokura, Nature **388**, 50 (1997).

[19] H. Hwang, S. Cheong, P. Radaelli, M. Marezio, and B. Batlogg, Phys. Rev. Lett. **75**, 914 (1995).

[20] C. Jooss, L. Wu, T. Beetz, R.F. Klie, M. Beleggia, M. a Schofield, S. Schramm, J. Hoffmann, and Y. Zhu, Proc. Natl. Acad. Sci. U. S. A. **104**, 13597 (2007).

[21] A. M. Tishin and Y. I. Spinchkin, The Magnetocaloric Effect and its Applications (IOP, Bristol, 2003).

[22] K.A. GschneidnerJr, V.K. Pecharsky, and A.O. Tsokol, Reports Prog. Phys. **68**, 1479 (2005).

[23] M.H. Phan, M.B. Morales, N.S. Bingham, H. Srikanth, C.L. Zhang, and S.W. Cheong, Phys. Rev. B **81**, 94413 (2010).

[24] T.L. Phan, P. Zhang, N.H. Dan, N.H. Yen, P.T. Thanh, T.D. Thanh, M.H. Phan, and S.C. Yu, Appl. Phys. Lett. **101**, (2012).

[25] B. Raveau, M. Hervieu, A. Maignan, and C. Martin, J. Mater. Chem. **11**, 29 (2001).

[26] E. O. Wollan and W. C. Koehler, Phys. Rev., **100**, 545 (1955).

[27] J. B. Goodenough, Phys. Rev., **100**, 564 (1955).

[28] G. H. Jonker and J. H. van Santen, Physica (Utrecht), **16**, 337 (1950).

[29] S. Jin, T.H. Tiefel, M. McCormack, R. a Fastnacht, R. Ramesh, and L.H. Chen, Science., **264**, 413 (1994).

[30] R. D. Shannon and C. T. Prewitt, Acta Crystallogr. B **25**, 725 (1969).

[31] R. Ruddlesden and P. Popper, Act. Cryst., **11** (1958).

[32] P. W. Anderson and H. Hasegawa, Phys. Rev. **100**, 67 (1955).

[33] P. de Gennes, Phys. Rev. B, **118**, 141 (1960).

[34] A. J. Millis, B. I. Shraiman, and R. Mueller, Phys. Rev. Lett. **77**, 175 (1996).

[35] C. P. Adams, J. W. Lynn, Y. M. Mukovskii, A. A. Arsenov, and D. A. Shulyatev, Phys. Rev. Lett. **85**, 3954 (2000).

[36] T. Mizokawa, D. I. Khomskii, and G. A. Sawatzky, Phys. Rev. B **60**, 7309 (1999).

[37] Colossal Magnetoresistive Oxides, edited by Y. Tokura (Gordon and Breach Science, Amsterdam, 2000).

[38] E. Dagotto, Nanoscale Phase Separation and Colossal Magnetoresistance (Springer-Verlag, Berlin, 2002).

[39] Y. Tokura, Y. Tomioka J. Magn. Magn. Mater., **200**, 1 (1999).

[40] R. Kajimoto, H. Yoshizawa, Y. Tomioka, and Y. Tokura, Phys. Rev. B **66**, 180402 (2002).

[41] Y. Tomioka and Y. Tokura, Phys. Rev. B **70**, 014432 (2004).

[42] D. Akahoshi, M. Uchida, Y. Tomioka, T. Arima, Y. Matsui and Y. Tokura, Phys. Rev. Lett. **90**, 177203 (2003).

[43] M. Uehara, S. Mori, C. H. Chen and S. W. Cheong, Nature **399**, 560-563 (1999).

[44] R. M. Kusters, J. Singleton, D. A. Keen, R. Mcgreevy and W. Hayes, Physica B, **155**, 362 (1989).

[45] G. C. Xiong, S. M. Bhagat, Q. L. M. Dominguez, H. L. Ju, R. L. Greene, T. Venkatesan, J. M. Byers and M. Rubinstein, Sol. Stat. Comn., **97**, 599 (1996).

[46] S. H. Park, Y. H. Jeong, B. K. Lee and S. Kwon, Phys. Reb. B, **56**, 67 (1997).

[47] C. S. Ting, X. Chen, Z. Weng, Mod. Phys. Lett., **3**, 1267 (1989).

[48] Y. Jia, L. Lu, K. Khazeniu, A. Zettl, Sol. Stat. Comn., **94**, 917 (1995).

[49] G. Jacob, W. Westerburg, F. Martin and H. Adrian, Phys. Rev. B, **58**, 14966 (1998).

[50] N. Mott and E. Davis, Electronic Process in Non-crystalline Materials (Clarendon Press, Oxford) (1971).

[51] M. Viret, L. Ranno and J. M. D. Coey, Phys. Rev. Lett., **55**, 8067 (1997).

[52] A. Banerjee, S. Pal, E. Rozenberg and B. K. Chaudhuri, J. Phys. Cond.Mat., **13**, 9489 (2001).

[53] G. Snyder, R. Hiskes, S. Dicarolis, M. R. Beasley and T. H. Geballe, Phys. Rev. B, **53**, 14434 (1996).

[54] K. Kubo and N. Ohata, J. Phys. Soc. Jpn., **33**, 21 (1972).

[55] A. Alexandrov and A. Brakovsky, J. Appl. Phys., **85**, 4349 (1999).

[56] P. Lin, S. H. Chun, and M. B. Salamon, J. Appl. Phys., **87**, 5825 (2000).

[57] J. E. Gordon, R. A. Fisher, Y. X. Xia, N. E. Phillips, S. F. Reklis, D. A. Wright and A. Zettl, Phys. Rev. B, **59**, 127 (1999).

[58] J. Lopez, O. Lima, P. Lisboa-Filho and F. Araujo-Moreira, Phys. Rev. B, **66**, 214402 (2002).

[59] V. Hardy, A. Wahl, C. Martin and C. Simon, Phys. Rev. B, **63**, 224403 (2001).

[60] N.A. de Oliveira and P.J. von Ranke, Phys. Rep. **489**, 89 (2010).

[61] A.O. Pecharsky, K.A. Gschneidner, and V.K. Pecharsky, J. Appl. Phys. **93**, 4722 (2003).

[62] A. Biswas, S. Chandra, T. Samanta, B. Ghosh, S. Datta, M.H. Phan, A.K. Raychaudhuri, I. Das, and H. Srikanth, Phys. Rev. B **87**, 134420 (2013).

[63] O. Tegus, E. Brck, K.H.J. Buschow, and F.R. de Boer, Nature **415**, 150 (2002).

[64] S. Chandra, A. Biswas, S. Datta, B. Ghosh, V. Siruguri, A.K. Raychaudhuri, M.H. Phan, and H. Srikanth, J. Phys. Condens. Matter **24**, 366004 (2012).

[65] V. K. Pecharsky and K. A. Gschneidner Jr, Phys. Rev. Lett., **78**, 4494 (1997).

[66] P. Sarkar, P. Mandal, and P. Choudhury, Appl. Phys. Lett. **92**, 182506 (2008).

[67] Z.B. Guo, Y.W. Du, J.S. Zhu, H. Huang, W.P. Ding, and D. Feng, Phys. Rev. Lett. **78**, 1142 (1997).

[68] Y. Zhang, P.J. Lampen, T.-L. Phan, S.-C. Yu, H. Srikanth, and M.-H. Phan, J. Appl. Phys. **111**, 63918 (2012).

[69] S. Banik and I. Das, RSC Adv. **7**, 16575 (2017).

[70] M. Moumen, A. Mehri, W. Cheikhrouhou-Koubaa, M. Koubaa, and A. Cheikhrouhou, J. Alloy. Compd. **509** (2011) 9084.

[71] N.T. Hien and N.P. Thuy, Phys. B Condens. Matter **319** 168 (2002).

[72] M.H. Phan, S.C. Yu, N.H. Hur, and Y.H. Jeong, J. Appl. Phys. **96** 1154 (2004).

[73] M.H. Phan, S. Tian, S.C. Yu, and A.N. Ulyanov, J. Magn. Magn. Mater. **256** 306 (2003).

[74] P. Sande, L.E. Hueso, D.R. Miguens, J. Rivas, F. Rivadulla, M.A. Lopez-Quintela, Appl. Phys. Lett. **79** 2040 (2001).

[75] Z.B. Guo, W. Yang, Y.T. Shen, and Y.W. Du, Solid State Commun. **105**, 89 (1998).

[76] A. Szewczyk, H. Szymczak, A. Wisniewski, K. Piotrowski, R. Kartaszynski, B. Dabrowski, S. Kolesnik, Z. Bukowski, Appl. Phys. Lett. **77** 1026 (2000).

[77] D.T. Morelli, A.M. Mance, J. V Mantese, and A.L. Micheli, J. Appl. Phys. **79**, 373 (1996).

[78] H. Eugene Stanley, Introduction to Phase Transitions and Critical Phenomena (Oxford University Press, New York, 1971).

[79] A. J. C Wilson, Proc. Phys. Soc. london., 80, 286 (1962).

[80] B. E. Warren, X-ray Diffraction (Addison-Wesley, New York, 1969).

[81] R. Mahendiran, A. Maignan, S. Hbert, C. Martin, M. Hervieu, B. Raveau, J.F. Mitchell, and P. Schiffer, Phys. Rev. Lett. **89**, 286602 (2002).

[82] C. Autret, A. Maignan, C. Martin, M. Hervieu, V. Hardy, S. Hbert, and B. Raveau, Appl. Phys. Lett. **82**, 4746 (2003).

[83] L.M. Fisher, A. V. Kalinov, I.F. Voloshin, N.A. Babushkina, D.I. Khomskii, Y. Zhang, and T.T.M. Palstra, Phys. Rev. B **70**, 212411 (2004).

[84] V. Hardy, S. Majumdar, S.J. Crowe, M.R. Lees, D.M. Paul, L. Herv, A. Maignan, S. Hbert, C. Martin, C. Yaicle, M. Hervieu, and B. Raveau, Phys. Rev. B **69**, 20407 (2004).

[85] J. Krishna Murthy, K.D. Chandrasekhar, H.C. Wu, H.D. Yang, J.Y. Lin, and A. Venimadhav, EPL (Europhysics Lett. **108**, 27013 (2014).

[86] Z.W. Ouyang, H. Nojiri, and S. Yoshii, Phys. Rev. B **78**, 104404 (2008).

[87] S.B. Roy, M.K. Chattopadhyay, P. Chaddah, and A.K. Nigam, Phys. Rev. B **71**, 174413 (2005).

[88] S. Velez, J.M. Hernandez, A. Fernandez, F. Maci, C. Magen, P.A. Algarabel, J. Tejada, and E.M. Chudnovsky, Phys. Rev. B **81**, 64437 (2010).

[89] Y.J. Choi, C.L. Zhang, N. Lee, and S.-W. Cheong, Phys. Rev. Lett. **105**, 97201 (2010).

[90] S. Danjoh, J.-S. Jung, H. Nakamura, Y. Wakabayashi, and T. Kimura, Phys. Rev. B **80**, 180408 (2009).

[91] V. Hardy, A. Maignan, S. Hbert, C. Yaicle, C. Martin, M. Hervieu, M.R. Lees, G. Rowlands, D.M.K. Paul, and B. Raveau, Phys. Rev. B **68**, 220402 (2003).

[92] T. Wu and J.F. Mitchell, Phys. Rev. B **69**, 100405 (2004).

[93] D. Liao, Y. Sun, R. Yang, Q. Li, and Z. Cheng, Phys. Rev. B **74**, 174434 (2006).

[94] G. Cao, J. Zhang, S. Cao, C. Jing, and X. Shen, Phys. Rev. B **71**, 174414 (2005).

[95] C. Bordel, J. Juraszek, D.W. Cooke, C. Baldasseroni, S. Mankovsky, J. Minr, H. Ebert, S. Moyerman, E.E. Fullerton, and F. Hellman, Phys. Rev. Lett. **109**, 117201 (2012).

[96] Y.K. Tsui, C.A. Burns, J. Snyder, and P. Schiffer, Phys. Rev. Lett. **82**, 3532 (1999).

[97] R. Flint, H.-T. Yi, P. Chandra, S.-W. Cheong, and V. Kiryukhin, Phys. Rev. B **81**, 92402 (2010).

[98] V. Hardy, S. Hbert, A. Maignan, C. Martin, M. Hervieu, and B. Raveau, J. Magn. Magn. Mater. **264**, 183 (2003).

[99] R. Mathieu, M. Uchida, Y. Kaneko, J.P. He, X.Z. Yu, R. Kumai, T. Arima, Y. Tomioka, A. Asamitsu, Y. Matsui, and Y. Tokura, Phys. Rev. B **74**, 20404 (2006).

[100] S. Banik, K. Das, and I. Das, J. Magn. Magn. Mater. **403**, 36 (2016).

[101] Y. Tomioka, H. Hiraka, Y. Endoh, and Y. Tokura, Phys. Rev. B **74**, 104420 (2006).

[102] S. Hebert, A. Maignan, V. Hardy, C. Martin, M. Hervieu, and B. Raveau, Solid State Commun. **122**, 335 (2002).

[103] S. Banik, K. Das and I. Das, RSC Adv. **7**, 16575 (2017).

[104] Y. Moritomo, A. Asamitsu, H. Kuwahara & Y. Tokura, Nature **380**, 141-144 (1996).

[105] Y. Shimakawa, Y. Kubo and T. Manako, Nature **379**, 53-55 (1996).

[106] M. N. Ali et al., Nature **514**, 205-208 (2014).

[107] F. F. Tafti, Q. D. Gibson, S. K. Kushwaha, N. Haldolaarachchige and R. J. Cava, Nat. Phys. **12**, 272-277 (2015).

[108] Y. Tokura, Reports Prog. Phys. **69**, 797-851 (2006).

[109] A. Mukherjee, K. Pradhan and P. Majumdar, Europhys. Lett. **86**, 27003 (2009).

[110] A. Arulraj et al., J. Phys. Condens. Matter **10**, 8497-8504 (1998).

[111] Y. Tokura and Y. Tomioka, J. Magn. Magn. Mater. **200**, 1-23 (1999).

[112] A. Das, P. D. Babu, S. Chatterjee, and A. K. Nigam, Phys. Rev. B **70**, 224404 (2004).

[113] K. R. Mavani and P. L. Paulose, Appl. Phys. Lett. **86**, 1-3 (2005).

[114] C. Martin et al., Phys. Rev. B **63**, 174402 (2001).

[115] R. Mahendiran, B. Raveau, M. Hervieu, C. Michel and A. Maignan, Phys. Rev. B **64**, 64424 (2001).

[116] K. Das, P. Dasgupta, A. Poddar and I. Das, Nat. Publ. Gr. 1-12 (2016). doi:10.1038/srep20351

[117] S. Dong, F. Gao, Z. Q. Wang, J. M. Liu and Z. F. Ren, Appl. Phys. Lett. **90**, 8-11 (2007).

[118] K. Das, R. Rawat, B. Satpati and I. Das, Appl. Phys. Lett. **103**, 1-6 (2013).

[119] Y. Tomioka, H. Hiraka, Y. Endoh and Y. Tokura, Phys. Rev. B **74**, 104420 (2006).

[120] Y. Tokura and Y. Tomioka, J. Magn. Magn. Mater. **200**, 1-23 (1999).

[121] L. Ghivelder et al. Phys. Rev. B - Condens. Matter Mater. Phys. **69**, 1-5 (2004).

[122] T. Tang, R. S. Huang and S. Y. Zhang, J. Magn. Magn. Mater. **321**, 263-266 (2009).

[123] D. S. Rana, R. Nirmala and S. K. Malik, Eur. Lett. **70** (3), 376-382 (2005).

[124] A. I. Kurbakov, A. V. Lazuta and V. A. Ryzhov, J. Phys. Conf. Ser. **200**, 12099 (2010).

[125] D. O'Flynn, C. V. Tomy, M. R. Lees, A. Daoud-Aladine and G. Balakrishnan, Phys. Rev. B **83**, 174426 (2011).

[126] A. Midya, S. N. Das, P. Mandal, S. Pandya and V. Ganesan, Phys. Rev. B **84**, 235127 (2011).

[127] E. Dagotto, Science. **309**, 257-262 (2005).

[128] B. Maji, K. G. Suresh and A. K. Nigam, Europhysics Lett. **91**, 37007 (2010).

[129] D. Liao, Y. Sun, R. Yang, Q. Li and Z. Cheng, Phys. Rev. B **74**, 174434 (2006).

[130] N. Shankaraiah, K. P. N. Murthy, T. Lookman and S. R. Shenoy, Europhys. Lett. **92**, 36002 (2010).

[131] V. Hardy et al., Phys. Rev. B **68**, 220402 (2003).

[132] E. Dagotto, T. Hotta and A. Moreo, Phys. Rep. **344**, 1 (2001).

[133] S. Yunoki, J. Hu, A. L. Malvezzi, A. Moreo, N. Furusaki and E. Dagotto, Phys. Rev. Lett. **80**, 845 (1998).

[134] E. Dagotto, S. Yunoki, A. L. Malvezzi, A. Moreo, J. Hu, S. Capponi, D. Poilblanc and N. Furukawa, Phys. Rev. B **58**, 6414 (1998).

[135] S. Kumar and P. Majumdar, Eur. Phys. J. B **50**, 571 (2006).

[136] G. D. Mahan, *Quantum Many Particle Physics* (Plenum Press, New York, 1990).

[137] S. Kumar and P. Majumdar, Europhys. Lett. **65**, 75 (2004).

[138] E. Dagotto, T. Hotta and A. Moreo, Phys. Rep. **344**, 1 (2001).

[139] S. Yunoki, A. Moreo and E. Dagotto, Phys. Rev. Lett. **81**, 5612 (1998).

[140] K. Pradhan, A. Mukherjee and P. Majumdar, Phys. Rev. Lett. **99**, 147206 (2007).

[141] K. Pradhan and Y. Yunoki, Phys. Rev. B **96**, 214416 (2017).

[142] S. Jin, T.H. Tiefel, M. McCormack, R. a Fastnacht, R. Ramesh, and L.H. Chen, Science., **264**, 413 (1994).

[143] A.P. Ramirez, J. Phys. Condens. Matter., **9**, 8171 (1997).

[144] K. Das, P. Dasgupta, A. Poddar, and I. Das, Scientific Reports., **6**, 20351 (2016).

[145] K. Das, R. Rawat, B. Satpati, and I. Das, Appl. Phys. Lett., **103**, 202406 (2013).

[146] L.M. Rodrguez-Martnez and J.P. Attfield, Phys. Rev. B., 2000, **63**, 24424.

[147] K.F. Wang, Y. Wang, L.F. Wang, S. Dong, D. Li, Z.D. Zhang, H. Yu, Q.C. Li, and J.-M. Liu, Phys. Rev. B., **73**, 134411 (2006).

[148] M. Otero-Leal, F. Rivadulla, and J. Rivas, Phys. Rev. B., **76**, 174413 (2007).

[149] De Teresa JM, M. Ibarra, J. Garca, J. Blasco, C. Ritter, P. Algarabel, C. Marquina, and del Moral A, Phys. Rev. Lett. **76**, 3392 (1996).

[150] N.G. Bebenin, R.I. Zainullina, N.S. Bannikova, V. V. Ustinov, and Y.M. Mukovskii, Phys. Rev. B., **78**, 64415 (2008).

[151] Y. Tomioka, A. Asamitsu, and Y. Tokura, Phys. Rev. B., **63**, 24421 (2000).

[152] R. Mahesh, R. Mahendiran, A.K. Raychaudhuri, and C.N.R. Rao, Appl. Phys. Lett., **68**, 2291 (1996).

[153] T. Terai, T. Kakeshita, T. Fukuda, T. Saburi, N. Takamoto, K. Kindo, and M. Honda, Phys. Rev. B., **58**, 14908 (1998).

[154] M.M. Saber, M. Egilmez, A.I. Mansour, I. Fan, K.H. Chow, and J. Jung, Phys. Rev. B., **82**, 172401 (2010).

[155] M.B. Salamon, P. Lin, and S.H. Chun, Phys. Rev. Lett., **88**, 197203 (2002).

[156] A. Biswas, I. Das, and C. Majumdar, J. Appl. Phys., **98**, 1 (2005).

[157] L. Jia, G.J. Liu, J.Z. Wang, J.R. Sun, H.W. Zhang, and B.G. Shen, Appl. Phys. Lett., **89**, 122515 (2006).

[158] R.B. Griffiths, Phys. Rev. Lett. **23**, 17 (1969).

[159] R.F. Yang, Y. Sun, W. He, Q.A. Li, and Z.H. Cheng, Appl. Phys. Lett. **90**, 6 (2007).

[160] A.H. Castro Neto, G. Castilla, and B.A. Jones, Phys. Rev. Lett. **81**, 3531 (1998).

[161] M.C. de Andrade, R. Chau, R.P. Dickey, N.R. Dilley, E.J. Freeman, D.A. Gajewski, M.B. Maple, R. Movshovich, A.H. Castro Neto, G. Castilla, and B.A. Jones, Phys. Rev. Lett. **81**, 5620 (1998).

[162] M. Randeria, J.P. Sethna, and R.G. Palmer, Phys. Rev. Lett. **54**, 1321 (1985).

[163] J. Deisenhofer, D. Braak, H.-A. Krug von Nidda, J. Hemberger, R.M. Eremina, V.A. Ivanshin, A.M. Balbashov, G. Jug, A. Loidl, T. Kimura, and Y. Tokura, Phys. Rev. Lett. **95**, 257202 (2005).

[164] M.B. Salamon, P. Lin, and S.H. Chun, Phys. Rev. Lett. **88**, 197203 (2002).

[165] W. Jiang, X. Zhou, G. Williams, Y. Mukovskii, and K. Glazyrin, Phys. Rev. B **77**, 64424 (2008).

[166] L.M. Rodriguez-Martinez and J.P. Attfield, Phys. Rev. B **54**, R15622 (1996).

[167] K. Hirota, N. Kaneko, A. Nishizawa, and Y. Endoh, J. Phys. Soc. Japan **65**, 3736 (1996).

[168] S. Paul, R. Pankaj, S. Yarlagadda, P. Majumdar, and P.B. Littlewood, Phys. Rev. B **96**, 195130 (2017).

[169] C. He, M.A. Torija, J. Wu, J.W. Lynn, H. Zheng, J.F. Mitchell, and C. Leighton, Phys. Rev. B **76**, 14401 (2007).

[170] S.M. Zhou, Y.Q. Guo, J.Y. Zhao, S.Y. Zhao, and L. Shi, Appl. Phys. Lett. **96**, 2 (2010).

[171] M.M. Saber, M. Egilmez, A.I. Mansour, I. Fan, K.H. Chow, and J. Jung, Phys. Rev. B **82**, 172401 (2010).

[172] S.M. Zhou, Y.Q. Guo, J.Y. Zhao, L.F. He, and L. Shi, EPL (Europhysics Lett. **98**, 57004 (2012).

[173] N. Zhang, W. Ding, W. Zhong, D. Xing, and Y. Du, Phys. Rev. B **56**, 8138 (1997).

[174] J. Rivas, L.E. Hueso, A. Fondado, F. Rivadulla, and M.A. Lpez-Quintela, J. Magn. Magn. Mater. **221**, 57 (2000).

[175] P. Dey and T.K. Nath, Phys. Rev. B **73**, 214425 (2006).

[176] C. Zener, Phys. Rev. **82**, 403 (1951)

[177] S. Paul, R. Pankaj, S. Yarlagadda, P. Majumdar, and P.B. Littlewood, Phys. Rev. B **96**, 195130 (2017).

[178] S. Banik, N. Banu, and I. Das, J. Alloys Compd. **745**, 753 (2018).

[179] A.J. Millis, Phys. Rev. B **53**, 8434 (1996).

[180] A. Arrott, Phys. Rev. **108**, 1394 (1957).

[181] D. Kumar and A. Banerjee, J. Phys. Condens. Matter **25**, 216005 (2013).

[182] J. Lin, P. Tong, D. Cui, C. Yang, J. Yang, S. Lin, B. Wang, W. Tong, L. Zhang, Y. Zou, and Y. Sun, Sci. Rep. **5**, 7933 (2015).

[183] S. Banik, K. Das, and I. Das, RSC Adv. **7**, 16575 (2017).

[184] H. Oesterreicher and F.T. Parker, J. Appl. Phys. **55**, 4334 (1984).

[185] S. Pakhira, C. Mazumdar, R. Ranganathan, S. Giri, and M. Avdeev, Phys. Rev. B **94**, 104414 (2016).

[186] J.L. Garcia-Munoz, J. Fontcuberta, M. Suaaidi, and X. Obradors, J. Phys. Condens. Matter **8**, (1996).

[187] T.L. Phan, T.A. Ho, T. V. Manh, N.T. Dang, C.U. Jung, B.W. Lee, and T.D. Thanh, J. Appl. Phys. **118**, 0 (2015).

[188] K. Das and I. Das, J. Appl. Phys. **119**, 0 (2016).

[189] A. Banerjee, S. Pal, E. Rozenberg, and B.K. Chaudhuri, J. Phys. Condens. Matter **13**, 9489 (2001).

[190] Y. Sun, X. Xu, and Y. Zhang, J. Phys. Condens. Matter **12**, 10475 (2000).

[191] S. Banik, K. Das, and I. Das, J. Magn. Magn. Mater. **403**, 36 (2016).

[192] P. Raychaudhuri, K. Sheshadri, P. Taneja, S. Bandyopadhyay, P. Ayyub, A.K. Nigam, R. Pinto, S. Chaudhary, and S.B. Roy, Phys. Rev. B **59**, 13919 (1999).

[193] K. Mydeen, P. Mandal, D. Prabhakaran, and C.Q. Jin, Phys. Rev. B **80**, 14421 (2009).

[194] D.N.H. Nam, R. Mathieu, P. Nordblad, N. V. Khiem, and N.X. Phuc, Phys. Rev. B **62**, 8989 (2000).

[195] R.P. Borges, F. Ott, R.M. Thomas, V. Skumryev, J.M.D. Coey, J.I. Arnaudas, and L. Ranno, Phys. Rev. B **60**, 12847 (1999).

[196] M.B. Salamon, P. Lin, and S.H. Chun, Phys. Rev. Lett. **88**, 197203 (2002).

[197] S.M. Zhou, Y.Q. Guo, J.Y. Zhao, S.Y. Zhao, and L. Shi, Appl. Phys. Lett. **96**, 2 (2010).

[198] J. Lin, P. Tong, D. Cui, C. Yang, J. Yang, S. Lin, B. Wang, W. Tong, L. Zhang, Y. Zou, and Y. Sun, Sci. Rep. **5**, 7933 (2015).

[199] W. Jiang, X. Z. Zhou, G. Williams, Y. Mukovskii, and K. Glazyrin, Phys. Rev. Lett. **99**, 177203 (2007).

[200] N. Rama, M.S. Ramachandra Rao, V. Sankara narayanan, P. Majewski, S. Gepraegs, M. Opel, and R. Gross, Phys. Rev. B 70, 224424 (2004).

[201] P. Tong, B. Kim, D. Kwon, T. Qian, S.-I. Lee, S. W. Cheong, and B.G. Kim, Phys. Rev. B 77, 184432 (2008).

[202] V.N. Krivoruchko, M.A. Marchenko, and Y. Me likhov, Phys. Rev. B 82, 064419 (2010).

[203] J. Kumar, S.N. Panja, S. Dengre, and S. Nair, Phys. Rev. B 95, 054401 (2017).

[204] E.P. Wohlfarth, J. Appl. Phys. **29**, 595 (1958).

[205] N. Rama, M.S. Ramachandra Rao, V. Sankaranarayanan, P. Majewski, S. Gepraegs, M. Opel, and R. Gross, Phys. Rev. B 70, 224424 (2004).

[206] P. Tong, B. Kim, D. Kwon, T. Qian, S.-I. Lee, S.-W. Cheong, and B.G. Kim, Phys. Rev. B 77, 184432 (2008).

[207] V.N. Krivoruchko, M.A. Marchenko, and Y. Melikhov, Phys. Rev. B 82, 064419 (2010).

[208] J. Kumar, S.N. Panja, S. Dengre, and S. Nair, Phys. Rev. B 95, 054401 (2017).

[209] M.B. Salamon, P. Lin, and S.H. Chun, Phys. Rev. Lett. **88**, 197203 (2002).

[210] R.F. Yang, Y. Sun, W. He, Q.A. Li, and Z.H. Cheng, Appl. Phys. Lett. **90**, 6 (2007).

[211] W. Jiang, X. Z. Zhou, G. Williams, Y. Mukovskii, and K. Glazyrin, Phys. Rev. Lett. **99**, 177203 (2007).

[212] W. Jiang, X. Z. Zhou, G. Williams, Y. Mukovskii, and K. Glazyrin, Phys. Rev. B **77**, 064424 (2008).

[213] J. Burgy, A. Moreo, and E. Dagotto, Phys. Rev. Lett. **92**, 097202 (2004).

[214] S.M. Zhou, Y.Q. Guo, J.Y. Zhao, S.Y. Zhao, and L. Shi, Appl. Phys. Lett. **96**, 2 (2010).

[215] V.K. Shukla, S. Mukhopadhyay, K. Das, A. Sarma, and I. Das, Phys. Rev. B 90, 245126 (2014).

[216] P. Dey and T.K. Nath, Phys. Rev. B **73**, 214425 (2006).

[217] P. Raychaudhuri, K. Sheshadri, P. Taneja, S. Bandyopadhyay, P. Ayyub, A.K. Nigam, R. Pinto, S. Chaudhary, and S.B. Roy, Phys. Rev. B **59**, 013919 (1999).

[218] K. Binder and A.P. Young, Rev. Mod. Phys. **58**, 801 (1986).

[219] J. Wu and C. Leighton, Phys. Rev. B **67**, 174408 (2003).

[220] W. Jiang, X. Zhou, and G. Williams, EPL **84**, 47009 (2008).

[221] S.M. Zhou, Y.Q. Guo, J.Y. Zhao, L.F. He, and L. Shi, EPL . **98**, 57004 (2012).

[222] S. Kundu and T.K. Nath, J. Phys. Condens. Matter **22**, 506002 (2010).

[223] A.K. Pramanik and A. Banerjee, Phys. Rev. B **81**, 024431 (2010).

[224] S. Zhou, Y. Guo, J. Zhao, L. He, and L. Shi, J. Phys. Chem. C **115**, 1535 (2011).

[225] C.L. Lu, K.F. Wang, S. Dong, J.G. Wan, J.M. Liu, and Z.F. Ren, J. Appl. Phys. **103**, 6 (2008).

[226] V. Hardy, A. Maignan, S. Hebert, and C. Martin, Phys. Rev. B 67, 024401 (2003).

[227] V.N. Smolyaninova, A. Biswas, X. Zhang, K.H. Kim, B.-G. Kim, S.-W. Cheong, and R.L. Greene, Phys. Rev. B **62**, R6093 (2000).

[228] M.R. Lees, O.A. Petrenko, G. Balakrishnan, and D. McK. Paul, Phys. Rev. B **59**, 1298 (1999).

[229] L. Ghivelder, I. A. Castillo, M.A. Gusmao, J.A. Alonso, and L.F. Cohen, Phys. Rev. B **60**, 12184 (1999).

[230] J.J. Hamilton, E.L. Keatley, H.L. Ju, A.K. Raychaudhuri, V.N. Smolyaninova, and R.L. Greene, Phys. Rev. B 54, 14926 (1996).

[231] J.M. De Teresa, M.R. Ibarra, C. Marquina, P.A. Algarabel, and S. Oseroff, Phys. Rev. B **54**, R12689 (1996).

[232] M. Sasaki, P.E. Jonsson, H. Takayama, and H. Mamiya, Phys. Rev. B **71**, 104405 (2005).

[233] Y. Sun, M.B. Salamon, K. Garnier, and R.S. Averback, Phys. Rev. Lett. **91**, 167206 (2003).

[234] R.S. Freitas, L. Ghivelder, F. Damay, F. Dias, and L.F. Cohen, Phys. Rev. B **64**, 144404 (2001).

[235] N. Khan, P. Mandal, and D. Prabhakaran, Phys. Rev. B **90**, 024421 (2014).

[236] X. Du, G. Li, E.Y. Andrei, M. Greenblatt, and P. Shuk, Nat. Phys. **3**, 111 (2007).

[237] A. Bhattacharyya, S. Giri, and S. Majumdar, Phys. Rev. B **83**, 134427 (2011).

[238] J. A. Mydosh, Spin Glasses: An Experimental Introduction (Taylor & Francis, London, 1993), Chap. 3.

[239] P.C. Hohenberg and B.I. Halperin, Rev. Mod. Phys. 49, 435 (1977).

[240] J. Lago, S.J. Blundell, A. Eguia, M. Jansen, and T. Rojo, Phys. Rev. B 86, 064412 (2012).

[241] J. Souletie and J.L. Tholence, Phys. Rev. B 32, 516 (1985).

[242] C. Nayek, S. Samanta, K. Manna, A. Pokle, B.R.K. Nanda, P.S. Anil kumar, and P. Murugavel, Phys. Rev. B 93, 094401 (2016).

[243] P.J. Baker, T. Lancaster, S.J. Blundell, M.L. Brooks, W. Hayes, D. Prabhakaran, and F.L. Pratt, Phys. Rev. B 72, 104414 (2005).

[244] C. Sow, D. Samal, P. S. Anil Kumar, A.K. Bera, and S.M. Yusuf, Phys. Rev. B 85, 224426 (2012).

[245] A. Biswas, T. Samanta, S. Banerjee, and I. Das, Appl. Phys. Lett. **94**, 1 (2009).

[246] T. Samanta, I. Dubenko, A. Quetz, S. Temple, S. Stadler, and N. Ali, Appl. Phys. Lett. **100**, 5 (2012).

[247] X. Bohigas, J. Tejada, E. Del Barco, X.X. Zhang, and M. Sales, Appl. Phys. Lett. **73**, 390 (1998).

[248] Q. Ji, B. Lv, P.F. Wang, H.L. Cai, X.S. Wu, G.H. Liu, and G.S. Luo, J. Appl. Phys. **105**, 1 (2009).

[249] X.Q. Zheng, J. Chen, J. Shen, H. Zhang, Z.Y. Xu, W.W. Gao, J.F. Wu, F.X. Hu, J.R. Sun, and B.G. Shen, J. Appl. Phys. **111**, 7 (2012).

[250] N.S. Bingham, M.H. Phan, H. Srikanth, M.A. Torija, and C. Leighton, J. Appl. Phys. **106**, 1 (2009).

[251] N.S. Bingham, P.J. Lampen, T.L. Phan, M.H. Phan, S.C. Yu, and H. Srikanth, J. Appl. Phys. **111**, 2010 (2012).

[252] L.M. Rodriguez-Martinez and J.P. Attfield, Phys. Rev. B **54**, R15622 (1996).

[253] M. Otero-Leal, F. Rivadulla, and J. Rivas, Phys. Rev. B **76**, 174413 (2007).

[254] K.F. Wang, Y. Wang, L.F. Wang, S. Dong, D. Li, Z.D. Zhang, H. Yu, Q.C. Li, and J.-M. Liu, Phys. Rev. B **73**, 134411 (2006).

[255] P.G. Radaelli, G. Iannone, M. Marezio, H.Y. Hwang, S.-W. Cheong, J.D. Jorgensen, and D.N. Argyriou, Phys. Rev. B **56**, 8265 (1997).

[256] E.J. Moon, R. Colby, Q. Wang, E. Karapetrova, C.M. Schleptz, M.R. Fitzsimmons, and S.J. May, Nat. Commun. **5**, 5710 (2014).

[257] T. Krenke, E. Duman, M. Acet, E.F. Wassermann, X. Moya, L. Maosa, and A. Planes, Nat. Mater. **4** 450 (2005).

[258] A. Rostamnejadi, M. Venkatesan, J. Alaria, M. Boese, P. Kameli, H. Salamati, and J.M.D. Coey, J. Appl. Phys. **110** 43905 (2011).

[259] M. Quintero, J. Sacanell, L. Ghivelder, A.M. Gomes, A.G. Leyva, and F. Parisi, Appl. Phys. Lett. **97** 121916 (2010).

[260] C.N.R. Rao, A.K. Cheetham, and R. Mahesh, Chem. Mater. **8** 2421 (1996).

[261] J. Chen, X.Q. Zheng, Q.Y. Dong, J.R. Sun, and B.G. Shen, Appl. Phys. Lett. **99** 122503 (2011).

[262] J.S. Moodera, T.S. Santos, and T. Nagahama, J. Phys. Condens. Matter **19** 165202 (2007).

[263] T. Mizokawa, D.I. Khomskii, and G.A. Sawatzky, Phys. Rev. B **63** (2000) 24403.

[264] M.H. Phan, V. Franco, N.S. Bingham, H. Srikanth, N.H. Hur, and S.C. Yu, J. Alloys Compd. **508**, 238 (2010).

[265] L.M. Rodrguez-Martnez and J.P. Attfield, Phys. Rev. B **63**, 24424 (2000).

[266] A. Arrott and J.E. Noakes, Phys. Rev. Lett. **19**, 786 (1967).

[267] K. Huang, Statistical Mechanics, 2nd ed. (Wiley, New York, 1987).

[268] C. V Mohan, M. Seeger, H. Kronmller, P. Murugaraj, and J. Maier, J. Magn. Magn. Mater. **183**, 348 (1998).

[269] N. Moutis, I. Panagiotopoulos, M. Pissas, and D. Niarchos, Phys. Rev. B **59**, 1129 (1999).

[270] M. Baazaoui, S. Hcini, M. Boudard, S. Zemni, and M. Oumezzine, J. Magn. Magn. Mater. **401**, 323 (2016).

[271] J. Yang, Y. Lee, and Y. Li, Phys. Rev. B **76**, 54442 (2007).

[272] R. Venkatesh, R. Nirmala, G. Rangarajan, S.K. Malik, and V. Sankaranarayanan, J. Appl. Phys. **99**, 08Q311 (2006).

[273] N. Ghosh, S. Rler, U.K. Rler, K. Nenkov, S. Elizabeth, H.L. Bhat, K. Drr, and K.-H. Mller, J. Phys. Condens. Matter **18**, 557 (2006).

[274] B. Widom, J. Chem. Phys. **43**, 3898 (1965).

[275] M.E. Fisher, S. Ma, and B.G. Nickel, Phys. Rev. Lett. **29**, 917 (1972).

[276] P. T. Das, A. K. Nigam and T. K. Nath J. Adv. Phy., **8** 2084 (2015).

[277] B. Raveau, M. Hervieu, A. Maignan, and C. Martin, J. Mater. Chem. **11** 29 (2001).

[278] Z.M. Wang, G. Ni, Q.Y. Xu, H. Sang, Y.W. Du, J. Magn. Magn. Mater. **234** (2001) 371.

[279] Y. Sun, W. Tong, Y.H. Zhang, J. Magn. Magn. Mater. **232** 205 (2001).

[280] H.O. Wang, Z. Chu, K.P. Su, W.S. Tan, and D.X. Huo, J. Alloys Compd. **689** 69 (2016).

[281] C.M. Bonilla, J. Herrero-Albillos, F. Bartolome, L.M. Garcia, M. Parra-Borderias, and V. Franco, Phys. Rev. B **81**, 224424 (2010).

[282] M.H. Phan, M.B. Morales, C.N. Chinnasamy, B. Latha, V.G. Harris, and H. Srikanth, J. Phys. D. Appl. Phys. **42**, 115007 (2009).

[283] K. Das and I. Das, J. Appl. Phys. **119**, 093903 (2016).

[284] M. Balli, B. Roberge, P. Fournier, and S. Jandl, Crystals **7**, 44 (2017).